CORA Cork Open Research Archive
Cartlann Taighde Oscailte Chorcaí

Title	Piezoelectric energy harvesting using blood-flow-like excitation for implantable devices
Authors	O'Keeffe, Rosemary
Publication date	2015
Original Citation	O'Keeffe, R. 2015. Piezoelectric energy harvesting using blood-flow-like excitation for implantable devices. PhD Thesis, University College Cork.
Type of publication	Doctoral thesis
Rights	© 2015, Rosemary O'Keeffe. - http://creativecommons.org/licenses/by-nc-nd/3.0/
Download date	2026-10-31 04:00:02
Item downloaded from	https://hdl.handle.net/10468/2490

UCC
University College Cork, Ireland
Coláiste na hOllscoile Corcaigh

SCHOOL OF ENGINEERING, ELECTRICAL AND ELECTRONIC

TYNDALL NATIONAL INSTITUTE

UNIVERSITY COLLEGE CORK



PIEZOELECTRIC ENERGY HARVESTING USING BLOOD-FLOW-LIKE EXCITATION FOR IMPLANTABLE DEVICES

Rosemary O'Keeffe, B.E., M.Eng.Sc.

Submitted to the National University of Ireland, Cork for the degree of Ph.D.

October 2015

Head of School: Prof. Nabeel A. Riza

Supervisors: Dr. Kevin G. McCarthy

Dr. Alan Mathewson

Table of Contents

Chapter 1: Introduction and Motivation....1
1.1. Motivation....1
1.2. Transduction Mechanisms....6
1.2.1. Piezoelectric Transduction....8
1.3. Proposed Piezoelectric Energy Harvester....11
1.4. Piezoelectric Energy Harvesting Optimisation....13
1.5. Biocompatibility....16
1.6. Energy Harvesting Methods....19
1.4.1. Fluid Flow based Energy Harvesting....19
1.4.2. Human Based Energy Harvesting....24
1.4.3. Heel Stroke and Movement based Energy Harvesting....26
1.7. Creating Energy Efficient Systems....28
1.8. Thesis Contributions....29
1.9. Thesis Outline....29
Chapter 2: Piezoelectric Materials....31
2.1. Introduction....31
2.1.1. Process....37
2.2. Material Property Testing Procedures....39
2.3. Initial Results....41
2.4. DC Sputtering Test Wafer....47
2.2.1. Critical Parameters....47
2.2.2. Process Set-up for Quality and Repeatability....51
2.5. RF Sputtering Results....54
2.6. Material Quality Results from Device Testing....55
2.7. Process Stability Tests....58
2.8. Summary....65

Chapter 3: Finite Element Modelling 69
3.1. Introduction 69
3.1.2 Simulation Approaches 70
3.1.3 COMSOL Multiphysics 71
3.2. Confirming Model Accuracy 72
3.3. Broadening the Frequency Response 75
3.3.1. Device Geometry for Bandwidth Broadening 76
3.3.2. Device Arrays for Bandwidth Broadening 81
3.4. Power Output Modelling 84
3.4.1. Calculation of Device Output Power 85
3.4.2. Model Set-up 86
3.4.3. Device Testing 87
3.4.4. Measured and Modelled Results Compared 89
3.5. Summary 95
Chapter 4: Fluid-Actuated Energy Harvesting Devices 97
4.1. Introduction 97
4.2. Proposed Device Structures 98
4.3. FEM Fluid Flow Results 104
4.3.1. Introduction 104
4.3.2. Velocity Results 106
4.3.3. Turbulence Results 111
4.3.4. Device Stress Results 115
4.4. FEM Voltage Results 119
4.4.1. Hole Diameter 120
4.5. Experimental Results 121
4.5.1. Introduction 121
4.5.2. Perfusion Machine Results 124

4.5.3. Pressure Testing 127
4.6. Summary 128
Chapter 5: Polymer Materials 131
5.1. Introduction 131
5.2. AlN Growth on Polyimide 132
5.3. FEM Analysis of Polymer Material 137
5.3.1. FEM of Diaphragm with 2000µm Hole 137
5.3.2. FEM of Cross Structure 142
5.4. PVDF Material Growth 147
5.5. Summary 152
Chapter 6: Review of Energy Harvesting Circuits 155
6.1. Introduction 155
6.2 Energy Harvesting Circuit Approaches 159
6.3. Simulated and Bread-boarded Circuits 169
6.3.1. Op-Amp Circuits 169
6.3.2. Torah Circuit 171
6.3.1. Guilar Circuit 174
6.3.2. Romani Circuit 177
6.3.3. Analysing and Redesigning the Romani Circuit 182
6.4. Summary 188
Chapter 7: Conclusions and Future Work 191
7.1. Introduction 191
7.2. Summary of this Work 191
7.3. Conclusions 193
7.4. Recommendations for Future Work 195
Bibliography 197

Table of Figures

Figure 1.1: Evolution of pacemaker technology [3] 2
Figure 1.2: Battery size in pacemakers, (a) traditional [4] (b) current state of the art leadless pacemaker [9] 3
Figure 1.3: Power Density vs. Voltage for Energy Harvesting Technologies [12] 4
Figure 1.4: Electrostatic Transduction [16] 6
Figure 1.5: Electromagnetic Transduction [17] 7
Figure 1.6: Piezoelectric Modes and Voltage Generated 7
Figure 1.7: Frequency Response 9
Figure 1.8: Broadband Response 10
Figure 1.9: Piezoelectric Energy Harvesting through Pulsating Fluid Flow Scheme 12
Figure 1.10: (a) A unimorph cantilever, (b) A bimorph cantilever. 13
Figure 1.11: Piezoelectric "Cymbal" transducer 14
Figure 1.12: Two mass cantilever [33] 14
Figure 1.13: Effect on DC voltage from (a) Temperature and (b) Pressure [32] 16
Figure 1.14: Pressure cavity with diaphragm (a) schematic and (b) assembly [39] .. 16
Figure 1.15: Proliferation rates of cells subjected to PZT [43] 17
Figure 1.16: C-axis orientation of crystal structure [45] 18
Figure 1.17: Typical SEM cross section of good quality AlN material showing columnar (c-axis) growth 19
Figure 1.18: Piezoelectric wind harvester system [51] 20
Figure 1.19: Piezoelectric windmill showing arrangement of piezoelectric actuators [19] 20
Figure 1.20: Helmholtz resonator with piezoelectric energy converter [52] 21
Figure 1.21: Piezoelectric eel in stream [53] 22
Figure 1.22: (a) Triangular cantilever with point load at free end, (b) triangular cantilever with uniform load over full length [37] 23
Figure 1.23: Electromagnetic Energy Harvesting from Breathing [56] 24
Figure 1.24: Integration of Piezoelectric material into shoe [65] 27
Figure 1.25: Power electronics topology for energy-harvesting systems 28
Figure 2.1: Device Layers (not to scale) 32

Figure 2.2: SEM image (a) surface and (b) cross section 34
Figure 2.3: Principle of X-ray Diffraction [78] 35
Figure 2.4: 2Θ scan example (not to scale) 35
Figure 2.5: Example of Ω scan showing FWHM measurement 36
Figure 2.6: Process Steps for MEMS structures 38
Figure 2.7: AlN crystal structure for 002 and 100 orientation 39
Figure 2.8: LDV set-up 41
Figure 2.9: 2Θ and relative Ω scan results from first device wafers 42
Figure 2.10: AlN relative Ω scan results for initial test wafers 43
Figure 2.11: SEM images of (a) Wafer 3 and (b) Wafer 1 where the top image is the top surface and the bottom is the cross section showing (002) orientation. 44
Figure 2.12: EDX spectroscopy of wafer 3 and 1 45
Figure 2.13: Effect of sputtering pressure and distance on AlN crystal structure [46] 47
Figure 2.14: Effect of Interlayer on AlN film Orientation by Kamohara *et al*. [49] . 48
Figure 2.15: Device Wafer 2Θ and rocking curve scan results. 52
Figure 2.16: Device Wafer 2Θ and Rocking Curve results. 53
Figure 2.17: Rocking Curve scan of AlN on test wafers 53
Figure 2.18: Results from RF sputtering 55
Figure 2.19: Diaphragm Devices Tested for Material Quality 56
Figure 2.20: 2Θ scan diaphragm device 57
Figure 2.21: SEM image of Diaphragm Devices (cross section) 57
Figure 2.22: EDX analysis of diaphragm structure 58
Figure 2.23: Process Stability Test 2Θ Scan Results 61
Figure 2.24: Process Stability Test AlN Rocking Curve Scan 61
Figure 2.25: Process Stability Test Ti Rocking Curve Scan 62
Figure 2.26: 2Θ scan of redo of Wafer 5 (previous best process) 64
Figure 2.27: AlN Rocking Curve of redo of Wafer 5 64
Figure 2.28: Ti Rocking Curve of redo of Wafer 5 65
Figure 3.1: A two-layer cantilever. S is strain, V is voltage, M is mass and z is vertical displacement [90] 70
Figure 3.2: Equivalent Circuit of the piezoelectric generator [90] 70
Figure 3.3: COMSOL overview 72
Figure 3.4: Wafer of fabricated Devices 73

Figure 3.5: Initial Resonant Frequency Results 74
Figure 3.6: 2nd Generation Frequency Results 75
Figure 3.7: Example of multiple modes of resonant frequency of MEMS devices ... 77
Figure 3.8: Example of increased bandwidth response with overlapping modes 77
Figure 3.9: Cantilever with Gap on beam at anchor point. Colours indicate stress (in N/m^2) with red indicating maximum stress 78
Figure 3.10: Resonant frequency vs. Gap length for Modes 1 and 2 79
Figure 3.11: Resonant frequency vs. Gap width for Modes 1 and 2 79
Figure 3.12: Cantilever beam with spring at anchor end. Colours indicate stress (in N/m^2) with red indicating maximum stress 80
Figure 3.13: Spring network device LDV result 80
Figure 3.14: Diaphragm with 4 springs device LDV result 81
Figure 3.15 Fabricated arrays of devices (a) traditional cantilevers (b) triangular beam cantilevers 82
Figure 3.16: Frequency vs. mass length for modelled and fabricated cantilevers 82
Figure 3.17: Fabricated device with silicon under etch 83
Figure 3.18: Output voltage vs. frequency for 3 triangular beam cantilever devices 84
Figure 3.19: Triangular Beam showing Anchor at Base. 87
Figure 3.20: Electromagnetic Shaker Set-up. (a) Overview of full system showing magnet shaker and control hardware, (b) Device in place on shaker, (c) experimental set-up for measuring output power. 87
Figure 3.21: Power vs. Load Resistance for a device on a Magnetic Shaker 88
Figure 3.22: Power vs. acceleration for a single cantilever at resonance 89
Figure 3.23: Cantilever device under excitation. Colours indicate displacement (in mm) with maximum displacement in red 89
Figure 3.24: Triangular device under excitation. Colours indicate displacement (in mm) with maximum displacement in red 90
Figure 3.25: Power Measurement for Cantilever Device Wafer 2 91
Figure 3.26: Power Measurement for Cantilever Device Wafer 3 91
Figure 3.27: Experimental results showing the power generated vs. load resistance for 3 different cantilever structures operating at resonant frequency 92
Figure 3.28: Modelling results showing the power generated vs. load resistance for 3 different cantilever structures operating at resonant frequency 92
Figure 3.29: Power Measurement for Triangular Beam Device 94

Figure 3.30: Current Measurements 95
Figure 4.1: Suspended particles in blood [103] 98
Figure 4.2: Fluid flow (blue arrow), fixed points (red) and free points (green) for (a) empty artery, (b) cantilever, (c) diaphragm with 2000µm hole, (d) diaphragm, (e) fixed beam and (f) diaphragm with cross cut out 99
Figure 4.3: Cantilever Device 100
Figure 4.4: Diaphragm with 100µm hole 101
Figure 4.5: Diaphragm operation 102
Figure 4.6: Diaphragm with hole for placement in direct path of flow 102
Figure 4.7: Fixed Beam Device 103
Figure 4.8: Diaphragm with Cross 103
Figure 4.9: Typical artery pressure waveform and approximated waveform from equation for use in models 105
Figure 4.10: Empty Tube at t=0.6s. Velocity (in m/s) indicated by colours with maximum velocity in red 107
Figure 4.11: Cantilever at t=0.6s. Velocity (in m/s) indicated by colours with maximum velocity in red 108
Figure 4.12: Diaphragm at t=0.6s. Velocity (in m/s) indicated by colours with maximum velocity in red 108
Figure 4.13: Diaphragm with 100µm hole at t=0.6s. Velocity (in m/s) indicated by colours with maximum velocity in red 109
Figure 4.14: Diaphragm with 2000µm hole at t=0.6s. Velocity (in m/s) indicated by colours with maximum velocity in red 109
Figure 4.15: Fixed Beam at t=0.6s. Velocity (in m/s) indicated by colours with maximum velocity in red 110
Figure 4.16: Diaphragm with Cross. Velocity (in m/s) indicated by colours with maximum velocity in red 110
Figure 4.17: Empty Tube at t=0.6s. Arrows indicate disruption to flow 112
Figure 4.18: Cantilever at t=0.6s. Arrows indicate disruption to flow 112
Figure 4.19: Diaphragm at t=0.6s. Arrows indicate disruption to flow 113
Figure 4.20: Diaphragm with 100µm hole at t=0.6s. Arrows indicate disruption to flow 113
Figure 4.21: Diaphragm with 2000µm hole at t=0.6s. Arrows indicate disruption to flow 114

Figure 4.22: Fixed Beam at t=0.6s. Arrows indicate disruption to flow 114
Figure 4.23: Diaphragm with Cross. Arrows indicate disruption to flow 115
Figure 4.24: Cantilever. Stress (in N/m^2) indicated by colour with red indicating maximum stress 116
Figure 4.25: Diaphragm at t=0.6s. Stress (in N/m^2) indicated by colour with red indicating maximum stress 116
Figure 4.26: Diaphragm with 100µm hole at t=0.6s. Stress (in N/m^2) indicated by colour with red indicating maximum stress 117
Figure 4.27: Diaphragm with 2000µm hole at t=0.6s. Stress (in N/m^2) indicated by colour with red indicating maximum stress 117
Figure 4.28: Fixed Beam at t=0.6s. Stress (in N/m^2) indicated by colour with red indicating maximum stress 118
Figure 4.29: Diaphragm with Cross at t=0.6s. Stress (in N/m^2) indicated by colour with red indicating maximum stress 118
Figure 4.30: Hole Diameter from Device 120
Figure 4.31: Fabricated Devices for Implantable Energy Harvesting 121
Figure 4.32: Perfusion machine operation 122
Figure 4.33: Set-up for Devices in-flow 123
Figure 4.34: Set up for devices with flow on top 123
Figure 4.35: Perfusion Machine Set-up 124
Figure 4.36: Example of Pulsating Flow 125
Figure 4.37: PVDF sample for measuring pressure 127
Figure 4.38: COMSOL model of PVDF sample. Colour indicate stress with maximum stress in red. 128
Figure 5.1: AlN deposited on flexible material for use in biomedical applications [72] 133
Figure 5.2: 2Θ Scan of AlN and Ti on Polyimide 134
Figure 5.3: Results of Petroni *et al*. growth of AlN on polyimide [111] 134
Figure 5.4: Relative Ω scan of Titanium grown on Polyimide 135
Figure 5.5: Relative Ω scan of Aluminium Nitride grown on Polyimide 136
Figure 5.6: Diaphragm with 2000µm hole, Polyimide. Arrows indicate disruption to flow..... 138
Figure 5.7: Diaphragm with 2000µm hole, PVDF. Arrows indicate disruption to flow 139

Figure 5.8: Diaphragm with 2000µm hole, Polyimide. Velocity indicated by colours with maximum velocity in red…… 139

Figure 5.9: Diaphragm with 2000µm hole, PVDF. Velocity indicated by colours with maximum velocity in red…… 140

Figure 5.10: Diaphragm with a 2000µm hole, Polyimide. Stress (in N/m^2) is indicated by the colours with maximum stress in red 140

Figure 5.11: Diaphragm with a 2000µm hole, PVDF. Stress (in N/m^2) is indicated by the colour with maximum stress in red 141

Figure 5.12: Diaphragm with a cross, Polyimide. Arrows indicate disruption to flow 143

Figure 5.13: Diaphragm with a cross, PVDF. Arrows indicate disruption to flow . 143

Figure 5.14: Diaphragm with a cross, Polyimide. Velocity (m/s) indicated by colours with maximum velocity in red 144

Figure 5.15: Diaphragm with a cross, PVDF. Velocity (m/s) with maximum velocity in red 145

Figure 5.16: Diaphragm with a cross, Polyimide. Stress (in N/m^2) with maximum stress in red 145

Figure 5.17: Diaphragm with a cross, PVDF. Stress (in N/m^2) with maximum stress in red 146

Figure 5.18: Film Thickness vs. Spin Speed..... 149

Figure 5.19: Comparison of PVDF fabricated with different Swelling Agents using XRD …… 150

Figure 5.20: Comparison of sample with different THF Concentration..... 151

Figure 6.1: Full Bridge Rectifier..... 157

Figure 6.2: Input and Output voltages from Full Bridge Rectifier 158

Figure 6.3: Flexible energy harvesting diode rectifier circuit with integrated supercapacitor and energy harvester [124] 158

Figure 6.4: SSHI energy harvesting circuit [125]..... 159

Figure 6.5: Schematic Diagram of Energy Harvester with Self-Powered SSHI Interface [130]..... 160

Figure 6.6: Water bucket fountain strategy overview [140] 162

Figure 6.7: Full-Bridge Rectifier and Bias-flip circuit and output waveforms [143] 164

Figure 6.8: Synchronous Electric Charge Extraction (SECE) waveforms 165

Figure 6.9: SSPB Circuit [149] ……...167

Figure 6.10: Summing Amplifier [152] 170
Figure 6.11: Example of a typical Op-Amp Circuit for Multiple inputs 170
Figure 6.12: Output from Op-Amp Circuit (Blue) and Input (Pink) …….. 171
Figure 6.13: Voltage Multiplier Circuit Based on Torah *et al*. [153] 172
Figure 6.14: Simulated output from voltage multiplier circuit in blue. Input in red. 173
Figure 6.15: Output Voltage from Voltage Multiplier for Different Input Voltages 173
Figure 6.16: Block Diagram of Guilar *et al*. circuit for 3 inputs 174
Figure 6.17: Dual Input Guilar Circuit. One CCR is highlighted by dashed light grey line [123] 175
Figure 6.18: Simulated Output of Guilar *et al*. circuit for 3 inputs 176
Figure 6.19: Guilar *et al.* Circuit with microcontroller …….. 176
Figure 6.20: Romani *et al*. Circuit Block Diagram [122] 177
Figure 6.21: Passive Rectifying Circuit 178
Figure 6.22: Schematic of Wake-up Circuit. Voltage Regulator in yellow box 179
Figure 6.23: Interrupt Circuit 180
Figure 6.24: Main Switching Circuit. 180
Figure 6.25: Voltage Control across Inductor …… 181
Figure 6.26: Voltage signal for A (yellow) and B (green) to control voltage across Inductor 181
Figure 6.27: Bread-boarded Romani *et al*. Circuit 182
Figure 6.28: Vo Simulated Romani Circuit, 1 output …… 183
Figure 6.29: Vo (Yellow) and Voff (Green) from Bread-boarded Romani *et al.* Circuit, 1 output …… 183
Figure 6.30: Vo, Simulated Romani *et al*. Circuit, 1 output, zoomed 184
Figure 6.31: Simulation Results of altered Romani *et al*. circuit 185
Figure 6.32: Voltage output from active circuit capacitor for different inductor voltages 186
Figure 6.33: Control waveforms [122] 187
Figure 6.34: JK flip-flop using NAND logic gates [157] 188
Figure 6.35: JK timing Diagram [158] 188

Table of Tables

Table 1.1: Power density comparison on various energy harvesting sources [13] with corrections 5
Table 1.2: Typical Material Properties of Common Piezoelectric Materials 8
Table 1.3: Summary of power and energy available from everyday human body activity [67] 27
Table 2.1: Beam layer thicknesses 33
Table 2.2: Mass layer thicknesses 33
Table 2.3: AlN Deposition Process Steps 37
Table 2.4: Sputtering Conditions and Deposition Step Description for AlN Deposition 37
Table 2.5: Device Fabrication Process Steps 38
Table 2.6: Process Properties for Initial Test Wafers 42
Table 2.7: Properties changed during DC sputtering tests 48
Table 2.8: Properties changed and the description for testing AlN quality 49
Table 2.9: Properties changed and the description for testing AlN quality (cont.) 50
Table 2.10: Results of changing process set-up for DC sputtering 51
Table 2.11: AlN Deposition Test Parameters 2015 59
Table 2.12: AlN Deposition Test Parameters 2015 (Cont.) 60
Table 2.13: 2015 Process Stability Test Results 62
Table 3.1: Measured vs. Modelled Power Results for 3 devices 93
Table 4.1: Proposed energy harvesting devices and surface area 99
Table 4.2: Dimensions of Cantilever 100
Table 4.3: Dimensions of Diaphragm 101
Table 4.4: Dimensions of Diaphragm with 2000µm hole 102
Table 4.5: Dimensions of Fixed Beam 103
Table 4.6: Dimensions of Diaphragm with Cross 103
Table 4.7: Simulated resonant frequencies 106
Table 4.8: Modelled fluid velocity for each device placed in flow 107
Table 4.9: Maximum stress experienced by devices in flow 119

Table 4.10: Maximum Velocity of Fluid and Voltage of Device at t=0.6s 119
Table 4.11: Effect on Fluid Velocity and Voltage Output for Varying Hole Diameters 120
Table 4.12: Results of Measured vs. Modelled Voltage Results 126
Table 5.1: Comparison of Tyndall AlN deposited on Polyimide and State of the Art (SOA).....136
Table 5.2: Simulation voltage results for polymer material on diaphragm device..142
Table 5.3: Simulation voltage results for polymer material on cross device.....147
Table 5.4: Recipes for PVDF films.....148
Table 5.5: Results from Piezometer.....152
Table 6.1: Device Elecrical Parameters for a half pulse at 1Hz frequency……..156
Table 6.2: Summary of Energy Harvesting Circuit Literature Review……....168
Table 6.3: Inductor size and voltage output from 2 capacitor circuit simulations...186
Table 6.2: JK flip-flop operation 188

Declaration

This thesis was written entirely by the author, except where stated otherwise. The source of any material not created by the author has been clearly referenced. The work described herein was conducted by the author as part of the Hetrogenous Systems Integrations group in Tyndall and the School of Engineering in UCC, except where stated otherwise.

Rosemary O'Keeffe

Acknowledgements

Firstly I would like to thank my supervisors, Dr. Kevin McCarthy and Dr. Alan Mathewson, not only for all their tireless work overseeing, aiding, reading, editing, answering questions and suggesting improvements but also for keeping me on track and for their support and friendship. This thesis would not exist without them.

Also I'd like to thank my un-official supervisor, Dr. Nathan Jackson; he was always available to aid in my research and has, on more than one occasion, suggested experiments to improve the research. Mike O'Neill from Analog Devices also deserves to be acknowledged because it was through working with him that this work became a reality. Further thanks to Dr. Chris Ngwa for awarding me the funding to allow this work to be done and for supporting me over the entire process.

Next I'd like to acknowledge the support of my family, particularly my parents who supported me throughout this process and were always there with guidance. They instilled in me the importance of education and for this I will always be grateful.

To all my friends inside and outside of Tyndall who listened to my groans, helped me with experiments, answered stupid questions, drowned my sorrows, celebrated my triumphs and generally kept me sane. The nights in the pub and the days on the Tag pitch made all the difference and without them I would have gone mad before getting anywhere near a thesis. I'd especially like to thank the tea group (headed by Brian McCarthy and Aidan Daly) who bore the brunt of my frustrations and joys.

I'd also like to thank the many staff members of Tyndall who have fabricated devices, provided material, fixed computer problems and did countless other things which I can't even remember to make this work possible.

This work was funded by the Collaborative Centre for Applied Nanotechnology (CCAN) under Enterprise Ireland/IDA Ireland Technology Centres and the International Centre for Graduate Education in Micro- and Nano-Engineering (ICGEE).

Scientists dream of doing great things. Engineers do them.

James A. Michener

Abstract

The goal of this research is to produce a system for powering medical implants to increase the lifetime of the implanted devices and reduce the battery size. The system consists of a number of elements – the piezoelectric material for generating power, the device design, the circuit for rectification and energy storage. The piezoelectric material is analysed and a process for producing a repeatable high quality piezoelectric material is described. A full width half maximum (FWHM) of the rocking curve X-Ray diffraction (XRD) scan of between ~1.5° to ~1.7° for test wafers was achieved. This is state of the art for AlN on silicon and means devices with good piezoelectric constants can be fabricated. Finite element modelling (FEM) was used to design the structures for energy harvesting. The models developed in this work were established to have an accuracy better than 5% in terms of the difference between measured and modelled results. Devices made from this material were analysed for power harvesting ability as well as the effect that they have on the flow of liquid which is an important consideration for implantable devices. The FEM results are compared to experimental results from laser Doppler vibrometry (LDV), magnetic shaker and perfusion machine tests. The rectifying circuitry for the energy harvester was also investigated. The final solution uses multiple devices to provide the power to augment the battery and so this was a key feature to be considered. Many circuits were examined and a solution based on a fully autonomous circuit was advanced. This circuit was analysed for use with multiple low power inputs similar to the results from previous investigations into the energy harvesting devices. Polymer materials were also studied for use as a substitute for the piezoelectric material as well as the substrate because silicon is more brittle.

Glossary

AC – Alternating Current

Al – Aluminium

AlN – Aluminium Nitride

Ar – Argon

CCR – CMOS Controlled Rectifier

CMOS – Complementary Metal-Oxide Semiconductor

d_{xy} – Piezoelectric Coefficient

DC – Direct Current

DMF – Dimethylformamide

DRIE – Deep Reactive Ion Etch

EDX – Energy Dispersive X-ray Spectroscopy

EHD – Energy Harvesting Device

FEM – Finite Element Modelling

FIB – Focused Ion Beam

FPGA – Field Programmable Gate Array

FWHM – Full Width Half Maximum

GA – Genetic Algorithm

GUI – Graphical User Interface

HAPM – Harvesting Aware Power Management

HF – Hydrogen Fluoride

IC – Integrated Circuit

IMD – Implantable Medical Devices

LCR – Inductance, Capacitance, Resistance

LDV – Laser Doppler Vibrometer

LED – Light Emitting Diode

MEHC – Maximum Energy Harvesting Control

MEMS – Mircoelectromechanical Systems

$Mg(NO_3)_2.6H_2O$ – Magnesium Nitrate Hexahydrate

Mo – Molybdenum

MOSFET – Metal-Oxide Semiconductor Field-Effect Transistor

MPPT – Maximum Power Point Tracking

N_2 – Nitrogen

NMOS – N-Channel Metal-Oxide Semiconductor

O_2 – Oxygen

PCB – Printed Circuit Board

PEH – Piezoelectric Energy Harvester

PFM – Piezoelectric Force Microscopy

PMOS – P-Channel Metal-Oxide Semiconductor

PSCE – Pulsed Synchronous Charge Extraction

PVDF – Polyvinylidene Fluoride

PWM – Pulse Width Modulation

PZT – Lead Zirconate Titanate

RF – Radio Frequency

RoHS – Restriction on the use of Hazardous Substances

RPM – Revolutions Per Minute

SECE – Synchronous Electric Charge Extraction

SEM – Scanning Electron Microscopy

Si – Silicon

Si_3N_4 – Silicon Nitride

SiO_2 – Silicon Dioxide

SSPB – Single Supply Pre-Biasing

SSHI – Synchronous Switch Harvesting on Inductor

TEM – Transmission Electron Microscopy

THF - Tetrahydrofuran

Ti – Titanium

XRD – X-ray Diffraction

ZnO – Zinc Oxide

Author's Publications

- Wireless Accelerometers for Early Detection of Restenosis, *Jackson, Nathan; O'Keeffe, Rosemary; O'Leary, Robert; O'Neill, Mike; Moriarty, Micheal; Mathewson, Alan, Procedia Engineering, vol. 25, pp. 563-566, 2011*
- Influences of Titanium Underlayer on (002) Oriented Aluminium Nitride, *Jackson, Nathan; O'Leary, Robert; O'Keeffe, Rosemary; White, Mary; O'Neill, Mike; Waldron, Finbarr; Mathewson, Alan, International Workshop on Piezoelectric MEMS, Lausanne, September 2011*
- Practical Wireless Sensor Networks Power Consumption Metrics for Building Energy Management Applications, *Wang, W.S.; O'Keeffe, R.; Wang, N.; Hayes, M.; O'Flynn, B.; O'Mathuna, C., Forum Bauinformatik, Cork, September 2011*
- A Diaphragm based Piezoelectric AlN Film Quality Test Structure, *Jackson, Nathan; O'Keeffe, Rosemary; O'Leary, Robert; O'Neill, Mike; Waldron, Finbarr; Mathewson, Alan, ICMTS, San Diego, pp. 1-5, March 2012*
- Frequency response of variants of a cantilever beam, *Rivadeneyra, Almudena; O'Keeffe, Rosemary; Jackson Nathan; O'Neill, Mike; López-Villanueva, Juan A.; Mathewson, Alan, SMCD, Seville,pp. 177-180, September 2012*
- CMOS Compatible Piezoelectric Energy Harvester, *Jackson, Nathan; O'Keeffe, Rosemary; Waldron, Finbarr; O'Neill, Mike; Mathewson, Alan, Analog Devices Limerick Engineering Conference, Limerick, November 2012*
- Influence of Aluminium Nitride crystal orientation on MEMS energy harvesting device performance, *Jackson, Nathan; O'Keeffe, Rosemary; Waldron, Finbarr; O'Neill, Mike; Mathewson, Alan, J. Micromechanics and Microengineering, Vol. 23, Issue 7, pp. 1-7, 2013*
- Investigation of Devices for In-Vivo Energy Harvesting through Blood-Flow-Like Excitation, *O'Keeffe, Rosemary; Jackson, Nathan; McCarthy, Kevin G.; Mathewson, Alan, ICMTS, Osaka,pp. 19-24, March 2013*
- Investigation into Modelling Power Output for MEMS Energy Harvesting Devices using COMSOL Multiphysics, *O'Keeffe, Rosemary; Jackson, Nathan; Waldron, Finbarr; O'Neill, Mike; McCarthy, Kevin G.; Mathewson,*

Alan, IEEE International Conference on Thermal, Mechanical and Multi-Physics Simulation and Experiments in Microelectronics and Microsystems, Wroclaw, pp. 1-6, April 2013

- CMOS compatible Low-Frequency Aluminium Nitride MEMS Piezoelectric Energy Harvesting Devices, *Jackson, Nathan; O'Keeffe, Rosemary; Waldron, Finbarr; O'Neill, Mike; Mathewson, Alan, SPIE Microtechnologies Conference, Grenoble, April 2013*
- Evaluation of low-acceleration MEMS Piezoelectric Energy Harvesting Devices, *N. Jackson, R. O'Keeffe, F. Waldron, M. O'Neill, and A. Mathewson, J. Microsystem Technologies***,** *Vol. 20, Issue 4-5, pp. 671-680*
- The Health Benefits of Stress, *O'Keeffe, Rosemary, The Boolean, issue 4, pp. 133-137, 2014*
- Structural Health Monitoring of Reinforced Concrete Beam using Piezoelectric Energy Harvesting System, *Cahill, Paul; O'Keeffe, Rosemary; Mathewson, Alan; Jackson, Nathan; Pakrashi, Vikram EWSHM, Nantes, pp. 190 – 196, July 2014*
- A MEMS Silicon-Based Piezoelectric AC Current Sensor, *Olszewski, Zbigniew; Houlihan, Ruth; O'Keeffe, Rosemary; O'Neill, Mike; Waldron, Finbarr; Mathewson, Alan; Jackson, Nathan, Eurosensors Conference 2014, Vol. 87, pp. 1457-1480*
- Tuneable MEMS Piezoelectric Energy Harvesting Device, *Rivadeneyra, Almudena; Soto-Rueda, Juan Manuel; O'Keeffe, Rosemary; Banqueri, Jesus; Jackson, Nathan; Mathewson, Alan; Lopez-Villanueva, Juan Antonio, J. Microsystems Technology, February 2015, pp. 1-8*

Awards

- Awarded ICGEE scholarship for Ph.D. 2011
- "UCC Doctoral Showcase 2012" in the 3 minute Thesis category finalist.
- "UCC-Pfizer Award for Innovation through Teamwork" competition 2013 finalist.
- "Dynamic and Emerging Award" in the "UCC Young Entrepreneur of the Year" awards 2013 with a project on using piezoelectric material for gait analysis for runners.
- Runner up for best presentation at the "Tyndall Internal Conference 2013".
- Best 2 minute presentation at the "Tyndall Internal Conference 2014".
- Best poster in "Tyndall Student Poster Competition 2014".

Chapter 1:

Introduction and Motivation

1.1. Motivation

The first fully implantable cardiac pacemaker was implanted in 1958 [1] and used nickel-cadmium batteries to power it. Since that time much research has been conducted on improving the device itself in all areas (functionality, size, reliability) as well as the battery including using a radioisotope to extend the battery life [1] since radioisotopes were capable of powering the device for over 20 years but the original batteries lasted only a maximum of 2 years. The original device stimulated the heart at a constant rate which meant that changes due to resting or exercising were not taken into account and since then devices have improved to allow for pacing to be dependent on the demands of the patient in varying states, the size was also reduced making them easier to implant and different algorithms were designed which adapted to the changing heart rate needs [2]. The leads have also been improved from myocardial which were subject to breakage due to bending and stimulation threshold increasing over time to steroid-eluting leads which don't require a thoracotomy or anaesthesia to be implanted. More recent developments are

towards leadless pacemakers which means the pacemaker can be implanted in the heart and the issue of leads breaking is completely solved by having no leads [3]. Batteries have also advanced in terms of lifespan with traditional mercury zinc cells having a lifespan of 1 to 2 years [2] and current batteries, which are usually lithium-ion, lasting around 10 years [4]. Providing a safe and reliable method for increasing the battery life of implantable devices such as pacemakers provides an interesting problem because it is often the battery that is a critical feature in the size of implantable devices [5].



Figure 1.1: Evolution of pacemaker technology [3]

Figure 1.1 shows the evolution of the pacemaker from the first fully implantable device in 1958 to the top of the range leadless pacemaker in 2013 [3]. The largest element in the pacemaker is the battery and though the rest of the electronics has seen major improvements, the largest contributor to the size of the device is still the battery. This is illustrated in Figure 1.2 where it is seen that the battery percentage volume of the device has not decreased from the traditional pacemaker even when all the other electronics have become significantly miniaturised. It is clear here that the battery is getting proportionately bigger as improvements to the electronics are made. Increasing the lifetime of the battery through the use of energy harvesting and a rechargeable battery could provide a solution to further reduce the size of pacemakers. Another advantage would be that future research in implantable devices could benefit from having access to continuous power. Research into implantable health monitoring devices [6, 7] and

artificial pancreases [8] has been going on for decades and solving power issues through the kind of work described in this thesis could advance these fields even further.

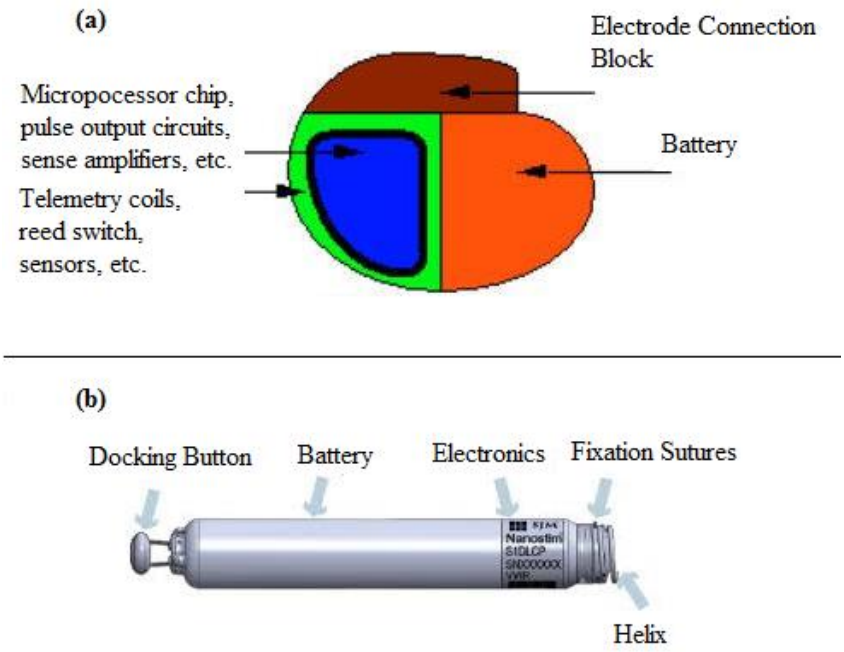


Figure 1.2: Battery size in pacemakers, (a) traditional [4] (b) current state of the art leadless pacemaker [9]

This thesis describes work on the development of a method for increasing battery lifespan through energy harvesting. Energy harvesting is the extraction of ambient energy (wasted energy from the environment) and converting it into usable power. One example of this concept is light from the sun which can be collected using solar panels and converted into electrical energy using solar cells on roofs or other areas where there is no flora or fauna to use the light. Another example is in the area of mechanical devices which always produce vibrations (kinetic energy) when they are being used and once again this energy is currently wasted. A vibrational energy harvester mounted on the engine might be able to convert this energy to a usable form to drive a sensor inside the engine cavity. There are many forms of energy harvesting including photovoltaic, thermal and vibrational.

Figure 1.3 shows typical power densities versus voltage for a number of energy harvesting technologies. Both solar and thermoelectric energy harvesting have higher power densities but they operate in a much smaller voltage region than

vibrational (piezoelectric and electromagnetic) energy harvesting. Solar power is a well developed form of energy harvesting, but for energy to be extracted it is essential that the solar conversion device has sufficient exposure to sunlight [10]. It is not practical when dealing with sensors that are to be implanted in the body because exposure to ambient light is often difficult to achieve in implanted devices. Thermal energy harvesters are also of limited interest for biomedical applications and were discussed by Ramadass and Chandrakasan [11]. However, these devices require a temperature gradient to operate and are more widely discussed for external devices, (i.e. devices which operate external to the body). For these reasons solar and thermal energy harvesting are not considered to be viable forms of energy harvesting for implantable devices.

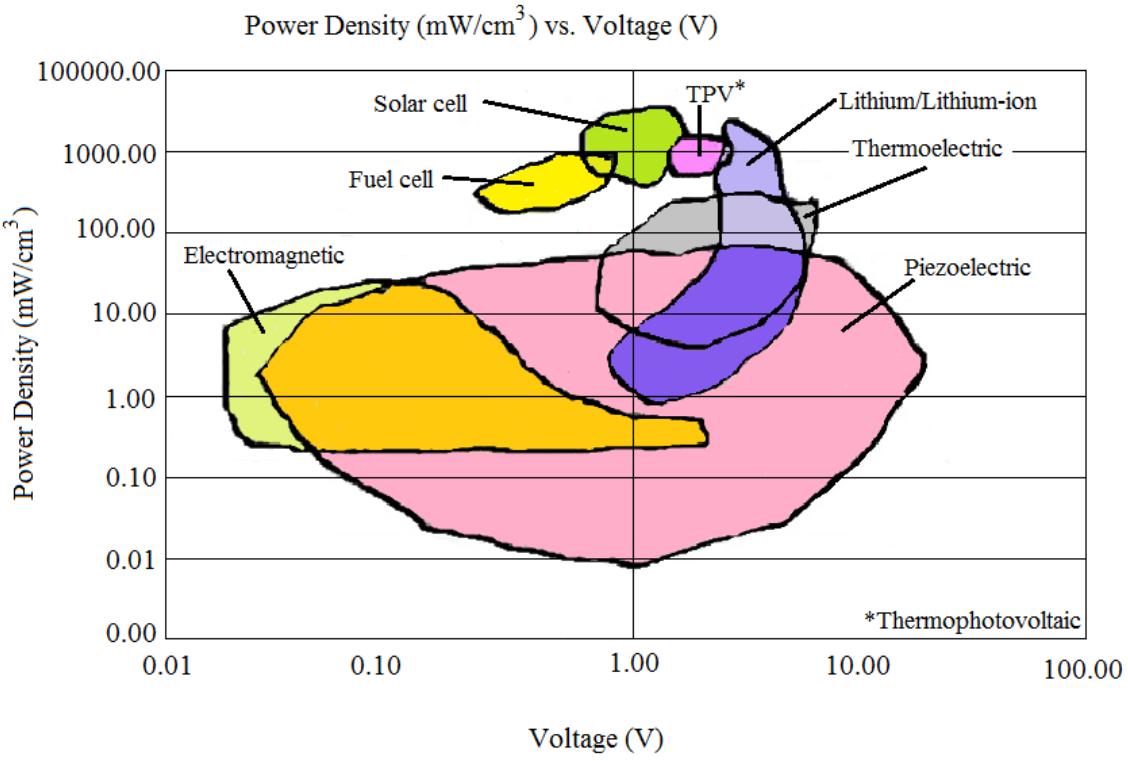


Figure 1.3: Power Density vs. Voltage for Energy Harvesting Technologies [12]

Table 1.1 shows a power density comparison for various energy harvesting technologies as described by Tan and Panda [13]. Here it is seen that vibrational energy harvesting was chosen for a blood pressure related system. Some of the values stated here seem to be exagerated with typical polycrystalline solar cell efficiencies usually around 13% - 16% [14] and in the case of blood pressure the

notes explain that expected values of μW are more usual when coupled with a piezoelectric generator.

Energy Source	**Power Density from Energy Source**	**Notes**
Solar (direct sunlight)	$100mW/cm^2$	Common polycrystalline solar cells are 16% - 17% efficient, while standard mono-crystalline cells approach 20%
Solar (illuminated office)	$100\mu W/cm^2$	
Thermoelectric	[a)] $60\mu/cm^2$ at 5°C gradient [b)] $135\mu W/cm^2$ at 10°C gradient	Typical efficiency of thermoelectric generators are ≤ 1% for $\Delta T < 40°C$ [a)]Seiko Thermic wristwatch at 5°C body heat, [b)]Quoted for a Thermo Life generator at $\Delta T = 10°C$
Blood Pressure	0.93W at 100mmHg	When coupled with piezoelectric generators, the power that can be generated is order of μW when loaded continuously and mW when loaded intermittently
Proposed Ambient airflow Harvester	$177\mu W/cm^3$	Typical average wind speed of 3m/s in the ambient
Vibrational Micro-Generators	$4\mu W/cm^3$ (human motion – Hz) $800\mu W/cm^3$ (machines – kHz)	Predictions for $1cm^3$ generators. Highly dependent on excitation (power tends to be proportional to ω, the driving frequency and y_o, the input displacement
Piezoelectric Push Buttons	50μJ/N	Quoted at 3V DC for the MIT Media Lab Device

Table 1.1: Power density comparison on various energy harvesting sources [13] with corrections

Vibrational energy harvesting responds to ambient vibrations in the environment. For instance when the engine of a car is turned on, vibrations can be felt even though the car is not moving. These vibrations are just wasted energy. There are many sources of ambient vibrations in the environment and it would seem that everything is vibrating at some frequency and even concrete beams have natural vibrations [15]. These vibrations can be used by vibrational energy harvesters in a number of ways. For natural vibrations (resonant vibrations) if the frequency is matched by the vibration energy harvesting device it will respond by moving and this will generate power. This is called resonant vibrational energy harvesting. A second form of vibrational energy harvesting would be using a medium to excite the

material, such as when fluid flows past or through it (water, wind, blood etc.). This can move the vibrational device and cause the transduction mechanisms discused in Section 1.2 to come into play.

1.2. Transduction Mechanisms

There are three transduction mechanisms associated with vibrational energy harvesting. These are electrostatic, electromagnetic and piezoelectric mechanisms [10]. In electrostatic transduction energy is generated through the relative movement of electrically isolated and charged capacitor plates as seen in Figure 1.4. Electromagnetic transduction is produced through the relative motion between a magnetic flux and a conductor or coil causing electromagnetic induction seen in Figure 1.5. Piezoelectric transduction is caused by the deformation of active piezoelectric material which produces electric charge.

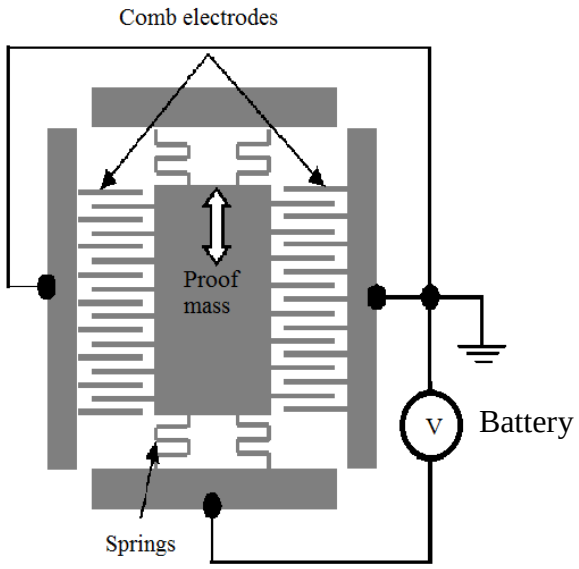


Figure 1.4: Electrostatic Transduction [16]

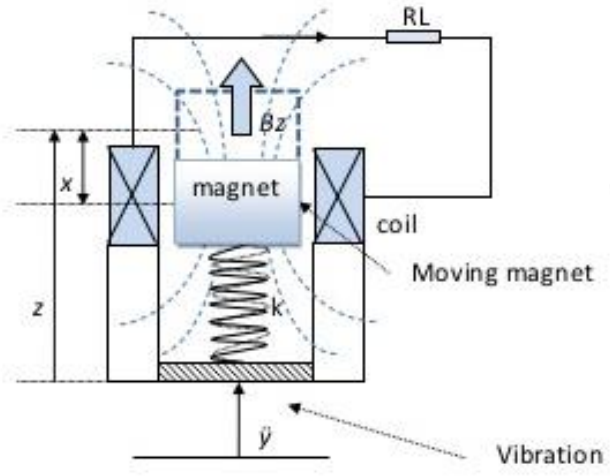


Figure 1.5: Electromagnetic Transduction [17]

This thesis will focus on the piezoelectric transduction mode which has been the focus of much research due to its high power density and ease of application [18]. Piezoelectric harvesting devices can be made to be the most efficient and smallest and they can generate approximately three times more energy than either electrostatic or electromagnetic energy sources [19]. Piezoelectric energy harvesting devices can also be relatively simple devices; the most common form is the cantilever in miroelectromechanical systems (MEMS) energy harvesting [20]. As seen from Figure 1.4 electrostatic transduction requires a battery and Figure 1.5 shows that electromagnetic transduction devices require the assembly of many parts whereas it is seen in Figure 1.6 that the piezoelectric device is a single element which does not require a battery. For these reasons it is considered to be the best choice for use in this work.

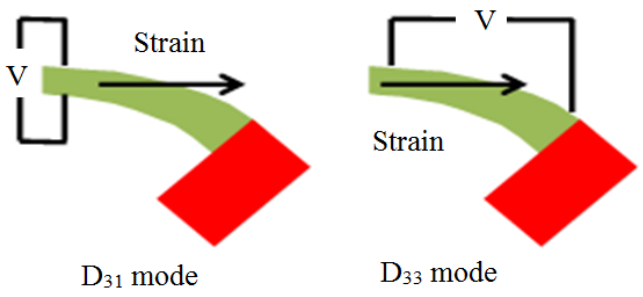


Figure 1.6: Piezoelectric Modes and Voltage Generated

1.2.1. Piezoelectric Transduction

Piezoelectric devices respond to a stress or strain by generating a voltage or will deflect when a voltage is applied to the material. There are two types of force associated with piezoelectric materials. Compressive force is a force perpendicular to the electrodes (d_{33} mode) and transverse strain is parallel to the electrodes (d_{31} mode) as shown in Figure 1.6. Typical values for material properties of most common piezoelectric materials are shown in Table 1.2 where $\varepsilon_{33,r}$ is the relative dielectric constant, Y is the Young's modulus and ρ is the mass density. Depending on the application the force may be applied in either the d_{33} or d_{31} modes. It is often constraints such as the geometry of the device or the nature and frequency of the vibrations available that determine which mode is chosen over the other. However, the transverse mode, d_{31}, is more common for vibrational energy harvesting because there is a lower resonance frequency in this mode [21] and more industrial systems and other target locations produce low frequency vibrations. The electrical energy stored in the material when exposed to compressive forces (d_{33}) is defined by [22]:

$$E_c = \frac{1}{2} Y^2 \frac{d_{33}^2 S^2}{\varepsilon} v \qquad (1.1)$$

where Y is Young's Modulus, S is the strain tensor, v is the volume of the piezoelectric element, ε is the permittivity and d_{33} is the piezoelectric constant. From this equation it is seen that the electrical energy available from a piezoelectric energy harvester is affected by the Young's modulus and the strain tensor of the material. For these reasons a flexible material which exhibits a low Young's modulus can harvest less power than a stiffer material like lead zirconate titanate (PZT).

Material	**d_{31} (pC/N)**	**d_{33} (pC/N)**	**$\varepsilon_{33,r}$**	**Y (GPa)**	**ρ (kg/m^3)**
PZT [23]	-130	290	1,300	96	7.7
AlN [23]	2.0	3.4	10.5	330	3.26
ZnO [23]	-4.7	12	12.7	210	5.6
PVDF [24]	22	-30	10-12	8.3	1780

Table 1.2: Typical Material Properties of Common Piezoelectric Materials

Piezoelectric transduction occurs with the use of piezoelectric materials which can be either ceramics or polymers. Ceramics, such as PZT [21], are brittle but can

provide greater energy with smaller deformation than polymers. Polymers, such as polyvinylidene fluoride (PVDF) [21], are more flexible but need much larger deflections to produce useful energy output.

Piezoelectric materials can be used in systems that respond to certain frequencies of vibration as discussed above. This occurs within a limited bandwidth around the resonant frequency. The resonant frequency and bandwidth that the device is active over are determined by the geometry of the device structure. The formula for calculating the resonant frequency of a cantilever based on the device geometry is [25]:

$$f_r = \left(\frac{1}{2\pi}\sqrt{\frac{3Y}{m_{proof}}}\right)\sqrt{\frac{wt^3}{L^3}} \qquad (1.2)$$

where f_r is the resonant frequency, Y is the Young's modulus of the material, m_{proof} is the mass of the proof mass, w, L and t are the width, length and thickness of the beam's rectangular cross section. It is clear from the equation that the geometric features (length, width, thickness) have a large effect on the resonant frequency and can be used to design a device to resonate at a specific frequency. Figure 1.7 shows an example of why this is necessary. The resonant frequency of a given device is shown in blue and highlighted by a box. If this is the same value as the target vibration source the device will resonate and generate power. If, however, the constant vibrations are not at the design frequency, as indicated by the black curve, no power will be generated.

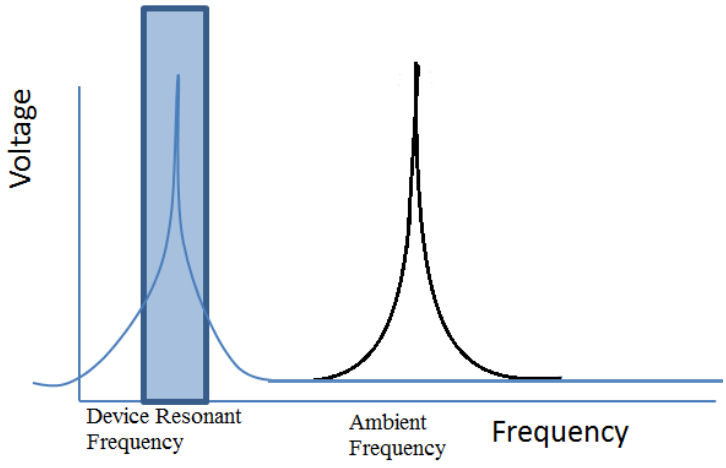


Figure 1.7: Frequency Response

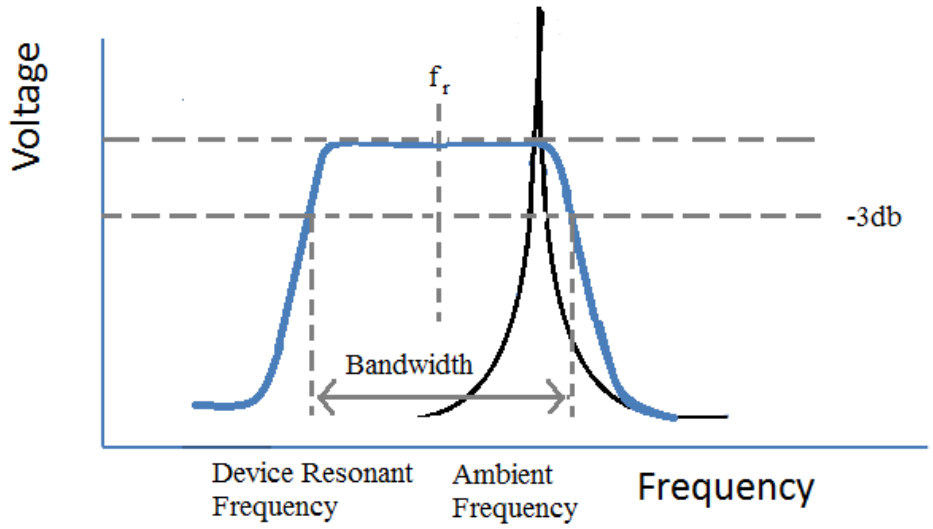


Figure 1.8: Broadband Response

The response shown in Figure 1.7 is typical for piezoelectric energy harvesters which tend to have very small bandwidth and a high Q value. Increasing the bandwidth is of considerable interest to researchers because if the bandwidth is widened then more frequencies will produce a response; however, the power obtained at any one frequency will be lower than that achieved by a smaller bandwidth device because the Q value is lowered. This is shown in Figure 1.8 where the voltage is reduced but the larger bandwidth means that the device would respond to the ambient frequency and energy could be harvested. There are many papers which discuss possible methods to increase bandwidth in energy harvesting devices [26-28]. Hariti *et al*. discuss partial depolarisation of the piezoelectric material to produce a broadened response [28]. In [26] Zhu *et al*. and in [27] Swee-Leong *et al*. provide good reviews of such methods including using a generator array and this method will be discussed more in Chapter 3. While this is a major consideration of piezoelectric energy harvesting in general resonant frequency response it is less important when dealing with fluid actuated piezoelectric energy harvesting devices.

1.3. Proposed Piezoelectric Energy Harvester

Implantable Medical Devices (IMDs), such as pacemakers, are being used more and more in patient care because they can be the key to longer and healthier life for many people [29]. These devices are particularly challenging because the devices need to be robust, biocompatible and long lasting due to the nature of the environment inside the body. Changing a battery in such a device could require invasive and dangerous surgery. This is a problem for doctors, patients and health insurance providers. It can also be an issue when deciding if a new device technology is worth further investment in research and qualification. By developing a method to recharge a battery inside a closed system (like the body), the battery lifetime can be increased and therefore the lifetime of the device that is to be implanted in the body of a patient is also increased. This, in turn, could eliminate the need for a second surgery to replace the battery and increase the use of implantable devices for monitoring of chronic conditions. A system like this could also lead to less time spent in hospital for patients with long term illnesses because a powered health monitoring device could be implanted in the body which would mean the patient could continue on with life and the doctor would have access to information on the patient's health.

To this end, an energy harvesting scheme that operates inside the body has been designed which converts movement of blood into electricity. The initial concept of this system is shown in Figure 1.9. This figure represents an artery with pulsating blood flow and the devices that are installed in the flow are moved back and forth by the flow. This pulsating blood flow will provide a constant source of stress for the piezoelectric energy harvesting cantilevers. The voltage generated from this stress will need to be rectified and stored or used to recharge an implantable device battery.

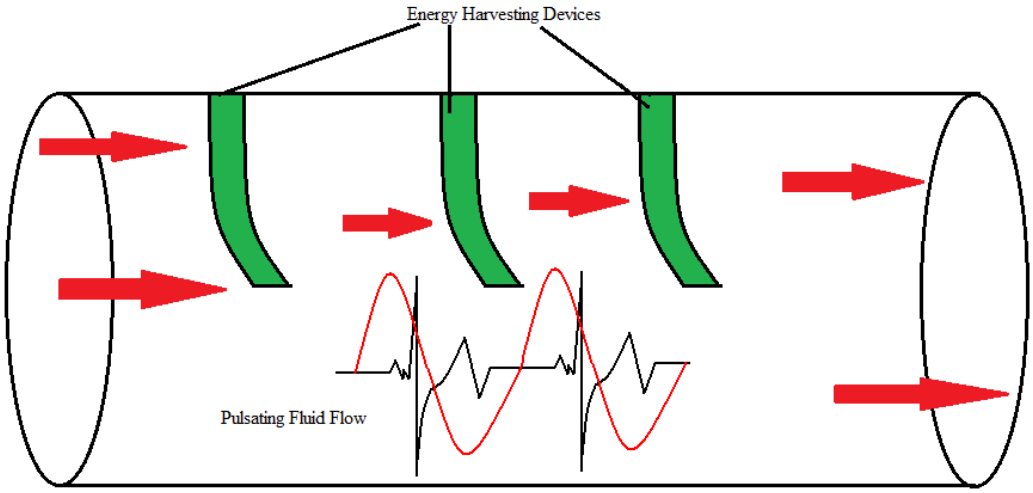


Figure 1.9: Piezoelectric Energy Harvesting through Pulsating Fluid Flow Scheme

The energy harvesting scheme described in this thesis can be broken down into a number of elements. Firstly, the piezoelectric material needs to be considered. The chosen material needs to be biocompatible and the piezoelectric properties of the material will need to be examined so that an efficient device can be created. The next factor is the design and layout of the devices. This is very important for implantable devices which are intended to operate in the bloodstream because obstructing blood flow could result in discomfort, pain and may even be fatal [30]. The other element to be considered is the energy harvesting circuit which needs to be designed to rectify and store the energy generated by the piezoelectric devices.

In this thesis the choice of material will be based on biocompatibility considerations and the device design will be based on the effect that the physical presence of the device has on blood flow in an artery. However, the fluid used in all models and experiments is water which will not take into account the suspended particles in blood but which can be compared to the experiments in which the available fluid was water. Previous work by Jackson *et al*. [31] also included studies into the use of water as a replacement fluid for blood and it was shown that the viscosity and flow characteristics are comparable and therefore water is an acceptable fluid to use in this work.

1.4. Piezoelectric Energy Harvesting Optimisation

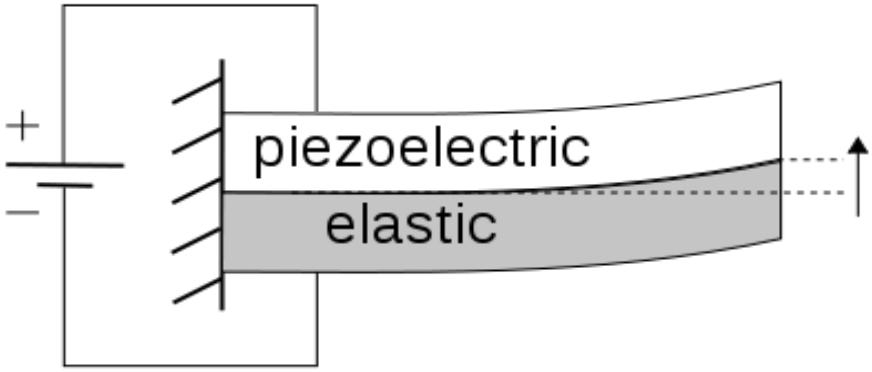


Figure 1.10a [32]

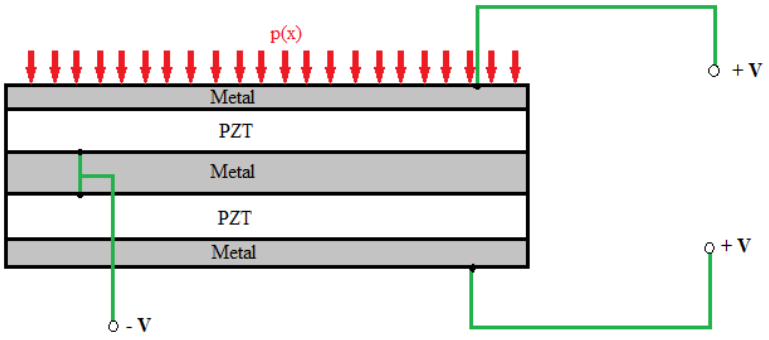


Figure 1.10b

Figure 1.10: (a) A unimorph cantilever, (b) A bimorph cantilever.

The traditional geometry for a piezoelectric energy harvester is the cantilever beam. This can be either a unimorph, i.e. 1 layer of piezoelectric material on elastic/composite substrate, or a bimorph i.e. 2 layers of piezoelectric material with elastic/composite between them. These are both illustrated in Figure 1.10. Both types of cantilever have been the focus of extensive research such as work reported by Ou *et al.* [33] which provides a model for a two mass unimorph validated with experimental results and Ting *et al*. [34] which examines the correlation between power and frequency for a unimorph. An experimentally validated model of a bimorph is provided by Erturk and Inman in [35]. To increase the power harvesting capabilities without weakening the structure metal caps (known as 'cymbals') are

used to strain piezoelectric material on the top and bottom faces by attaching the stressed metal caps which strain the material [21] shown in Figure 1.11.

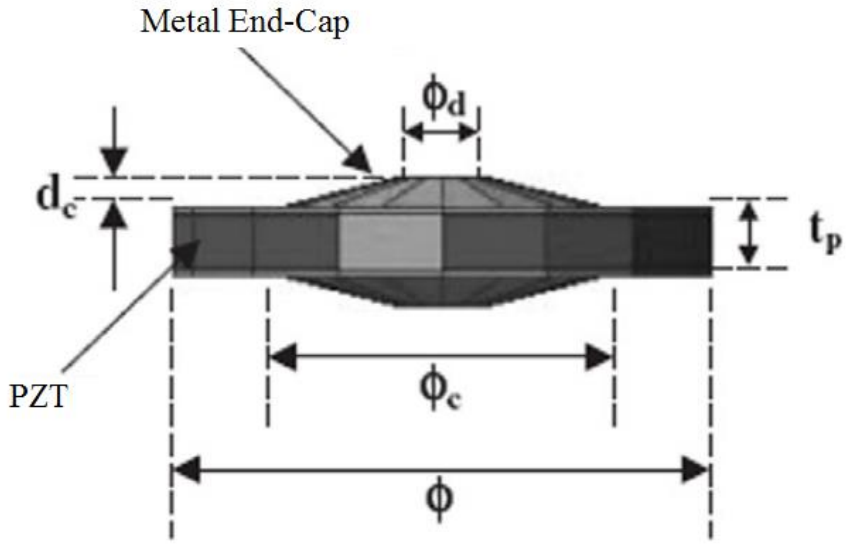


Figure 1.11: Piezoelectric "Cymbal" transducer

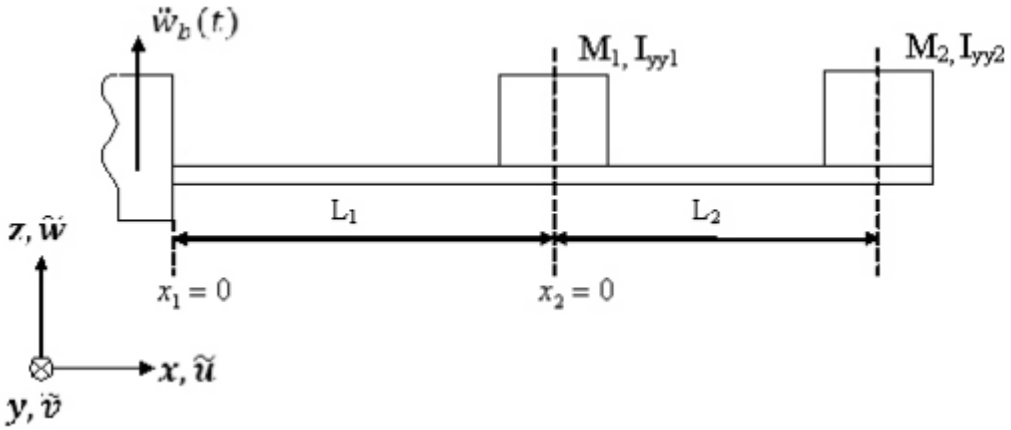
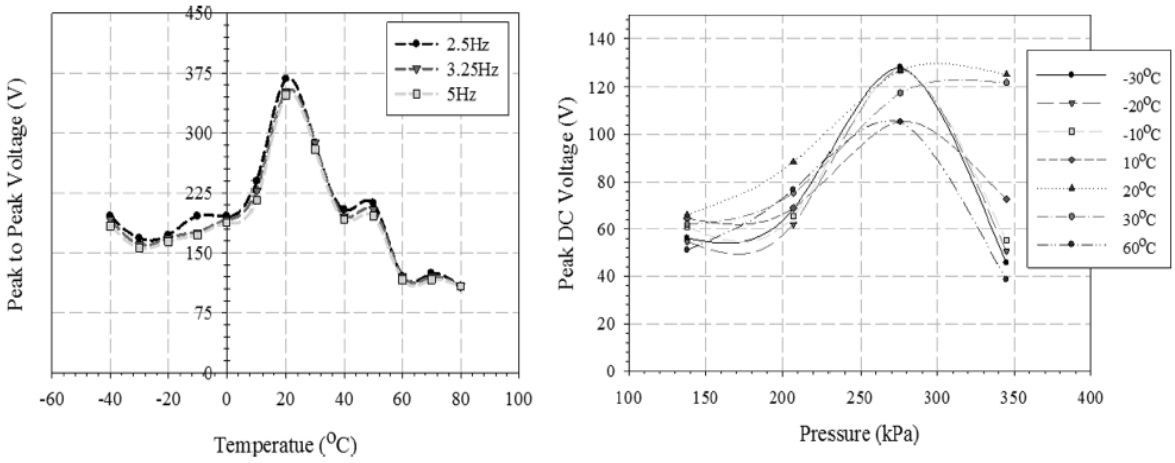


Figure 1.12: Two mass cantilever [33]

To widen the effective bandwidth multiple proof masses can be placed on the cantilever as shown by Ou *et al*. [33] (Figure 1.12) which increases the number of resonant modes in the same frequency range and this concept will be discussed further in Chapter 3. This means that a more effective energy harvester could be designed because a wider effective bandwidth means less fine tuning to find appropriate frequencies [33]. This was shown in Figure 1.8. Although increasing bandwidth often reduces the power available over a structure with a smaller bandwidth designed to operate at a specific frequency. Also, devices designed to

broaden the bandwidth often require a much larger area than small bandwidth devices. Other possible geometries have been discussed in many papers, such as the one by Erika *et al*. [36] where a circular membrane structure is examined and the one by Kuehne *et al*. [37] and Khaligh *et al*. [38] which both consider the merit of tapered device designs.

Power harvesting can also be improved through optimised environmental temperature and pressure, resonant frequency and load resistance (i.e. resistance matching) [39]. Mane *et al*. [39] found that at 20°C and a pressure of approximately 275kPa the tested PZT energy harvester produced its highest voltage and the voltage response dropped significantly away from these values as shown in Figure 1.13. These graphs show that the output voltage from a piezoelectric device can be affected by the temperature at three different frequencies (a) and for varying temperature the pressure also affects the output voltage (b). The tests were carried out using the set-up shown in Figure 1.14. These results show that there is a significant benefit that can be achieved if the pressure and temperature of the environment can be controlled with a peak to peak voltage increase of approximately 275V for optimal temperature and a peak DC voltage increase of approximately 90V at optimal pressure. These voltages are very high due to the large size of the material and the use of PZT and would be much too high for any implantable device with size constraints as well as constraints on safe voltages inside the body. Since this work relates to the provision of power supply for implantable devices the optimisation of devices through temperature will not be examined in this work because the environment inside the body cannot be altered and the temperature is 37° [40].



(a) **(b)**

Figure 1.13: Effect on DC voltage from (a) Temperature and (b) Pressure [32]

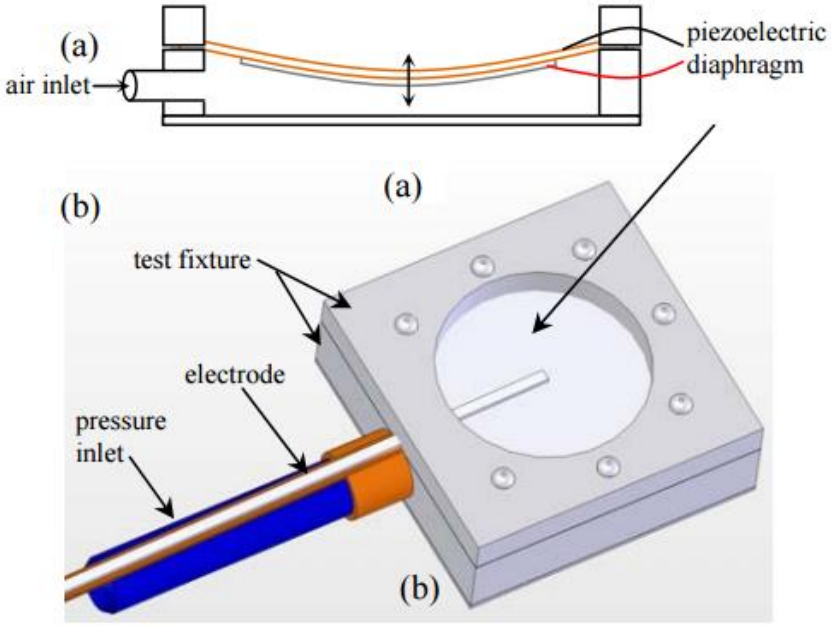


Figure 1.14: Pressure cavity with diaphragm (a) schematic and (b) assembly [39]

1.5. Biocompatibility

Due to the biocompatibility requirement of implantable medical devices (IMDs), Polyvinylidene Fluoride (PVDF), with its piezoelectric properties and thermal stability [41] accompanied by its biocompatibility characteristics, is a likely choice of material for many biomedical devices. Lead Zirconate Titanate (PZT) is a widely used piezoelectric ceramic for energy harvesting. However, due to the presence of

lead in the composition of the material it is not biocompatible. Furthermore there has been a movement away from the use of lead in all applications over the entire industry since the introduction of the Restriction on the use of Hazardous Substances (RoHS) [42] in July 2011. Lead is toxic and therefore if an application needs PZT to perform at the optimum level it needs to be sealed so that the lead cannot escape and poison the host. In 2006, Sakai, Hoshiai and Nakamachi [43] coated PZT crystals with a titanium thin film because titanium is a commonly used biocompatible material. The results were encouraging when examining the rate of proliferation of mouse fibroblast tissue origin L929 cells when compared to a Zinc Oxide (ZnO) and a control. Figure 1.15 shows the proliferation of cells subjected to PZT, ZnO and a control over 96 hours. In this figure it is shown that the cell growth in both the control and the PZT is equivalent over 96 hrs. and better than that of the ZnO which isn't even present at 96 hours. However, the rate of cell death, which is also an important factor as an indicator of the biocompatibility of a material, suggests that the Titanium coated PZT is still not biocompatible. These results show that there is a possibility of using coated PZT in in-vivo systems; however, this has not been achieved through the Ti coated PZT. Many new piezoelectric biomaterials are also being researched such as $MgSiO_3$ by Nakamachi [44] as the area of biomedical energy harvesting becomes more important.

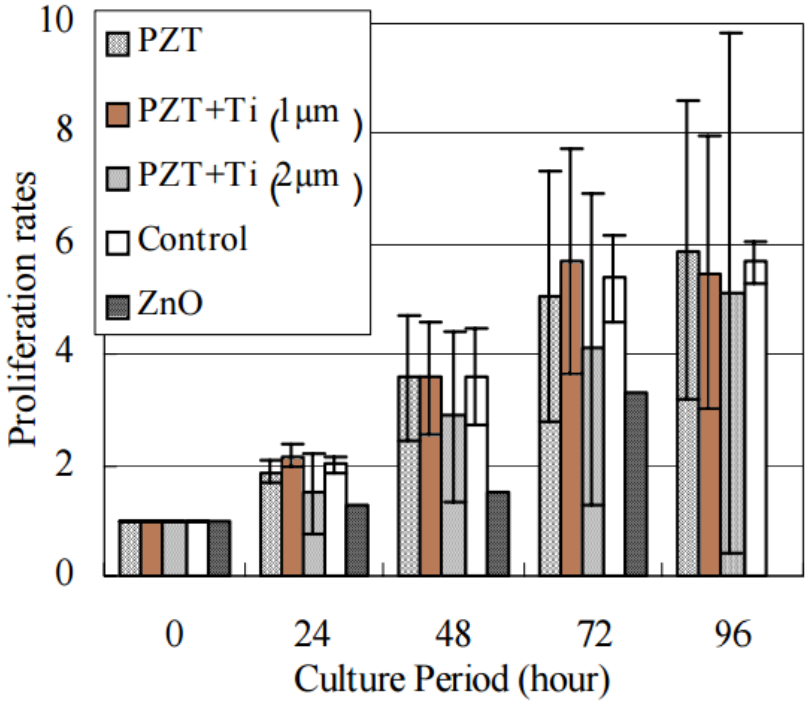


Figure 1.15: Proliferation rates of cells subjected to PZT [43]

Since PVDF is a very flexible material, with a low Young's modulus and stress, the power which can be harvested is less than that which can be generated with PZT as established using Equation (1.1) in 1.2.1. AlN is CMOS compatible as well as biocompatible and can achieve a high voltage output when its crystal structure is aligned in the c-axis orientation. This is different to PZT and PVDF which require poling (stretched mechanically).

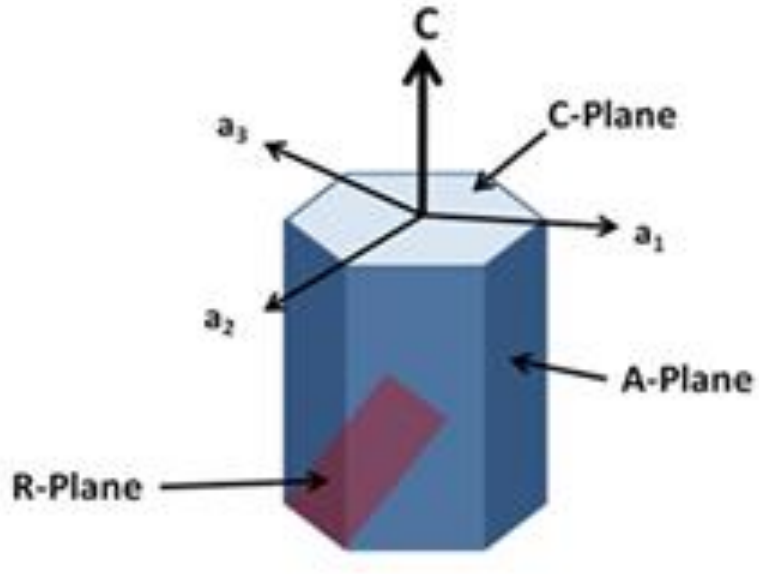


Figure 1.16: C-axis orientation of crystal structure [45]

In this work, c-axis growth of AlN is achieved by growing AlN on a Ti layer already aligned to the c-axis crystal plane. Figure 1.16 shows the c-axis crystal structure and Figure 1.17 shows what this growth looks like in a scanning electron microscope (SEM) micrograph of the material. This very columnar structure of the AlN shows good c-axis growth and is important for a good quality AlN piezoelectric material. This can be a difficult process to undertake and is very important because the piezoelectric properties of AlN are highly dependent on its orientation. Many papers have discussed the various methods for growing good quality AlN [46-50]. Xu *et al*. in [46] and Ababneh *et al*. [50] discuss the influence on the quality of the piezoelectric material of the pressure, temperature and distance from the target when sputtering the AlN. Kamohara *et al*. in [48] and [49] examine the use of Molybdenum for the bottom electrode on which AlN is grown and the effect of interlayers, respectively. These techniques will be discussed further in Chapter 2 where the AlN material is examined.

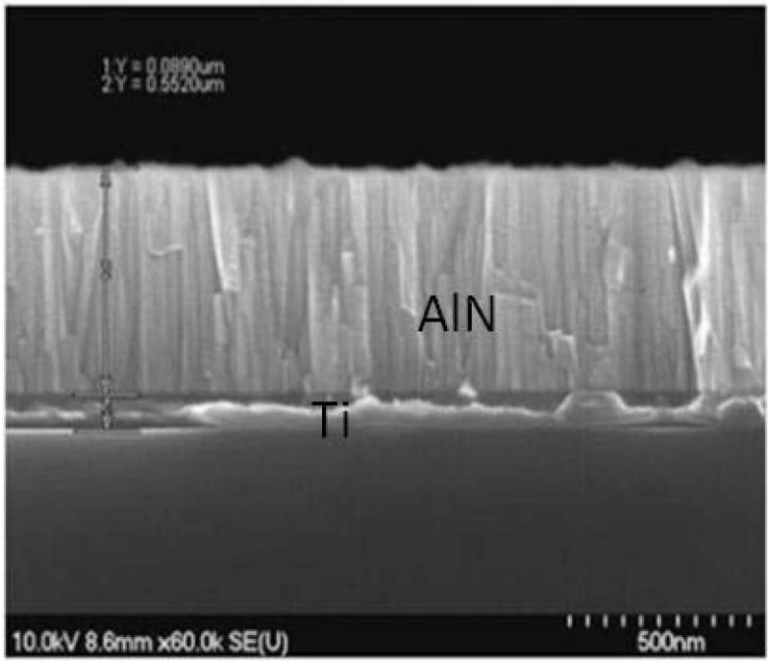


Figure 1.17: Typical SEM cross section of good quality AlN material showing columnar (c-axis) growth

1.6. Energy Harvesting Methods

1.6.1. Fluid Flow based Energy Harvesting

A traditional cantilever design (Figure 1.18) was used by Tan and Panda to measure wind speed [51]. An array of piezoelectric strips has been connected in a traditional windmill pattern as one possible configuration by Priya *et al.* [19] shown in Figure 1.19. The windmill was rotated by the force of the wind which caused the shaft to rotate and mounted onto the shaft were stoppers. The piezoelectric bimorphs were hit by the stoppers as the shaft rotated. Each bimorph measured $60x20x0.6mm^3$. The device was investigated for use as an early warning system for storm winds. This device had reliability issues because, for winds above 12mph (which would not be considered to be storm force) the structure became damaged from the impact of the piezoelectric bimorphs on the stoppers on the windmill shaft. However, it was capable of producing 6.9mW of output power. This device has not been proven to work for its intended purpose yet, but research is continuing into making a more robust design. When it is available this power will be used to supply a wind speed sensor for an early warning system for storms. This is an example of

energy harvesting from ambient fluid flows and could provide insights into possible methods of energy harvesting from fluid within the body.

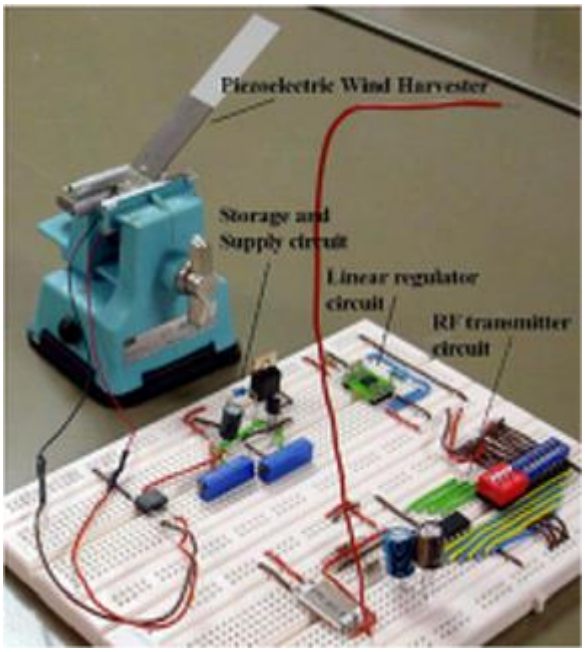


Figure 1.18: Piezoelectric wind harvester system [51]

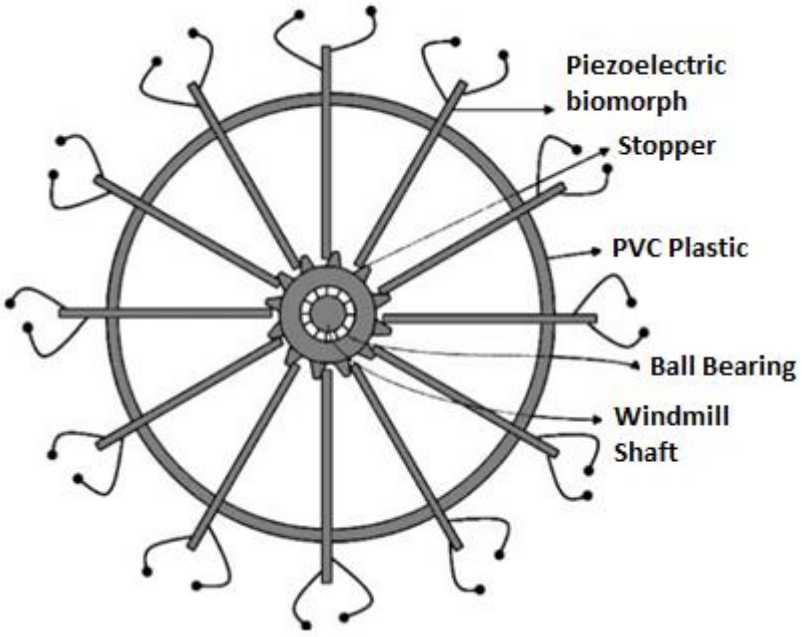


Figure 1.19: Piezoelectric windmill showing arrangement of piezoelectric actuators [19]

Motova *et al*. proposed a device [52] which uses a piezoelectric energy harvester in a Helmholtz resonator to harvest vibrational energy. In this system the resonant frequency is tuned by increasing the angle of the airflow into the device as well as changing the diameter of the neck and the length of the cavity. The piezoelectric device is placed on a membrane which resonates as a function of the airflow. This set-up is shown in Figure 1.20 where the energy harvester is placed on an adjustable plate so that the air cavity underneath the harvester can be altered. This is an interesting idea for harvesting energy through airflow because the resonant frequency can be tuned to deliver maximum available power. However, the device was quite large and the results could be very different if it was miniaturised. Also the effectiveness of the device was dependent on the angle of the airflow into the neck such that a slight change away from the optimum angle had a big effect on the effectiveness of the device. In many of the examples of turbine and windmill style vibration energy harvesting, the devices are often ineffective or have a low reliability such as in the situations discussed above where the devices were not reliable at high wind speeds.

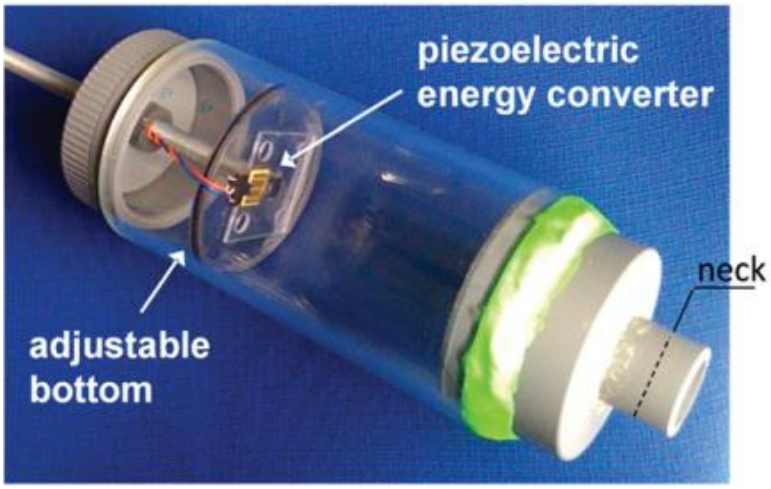


Figure 1.20: Helmholtz resonator with piezoelectric energy converter [52]

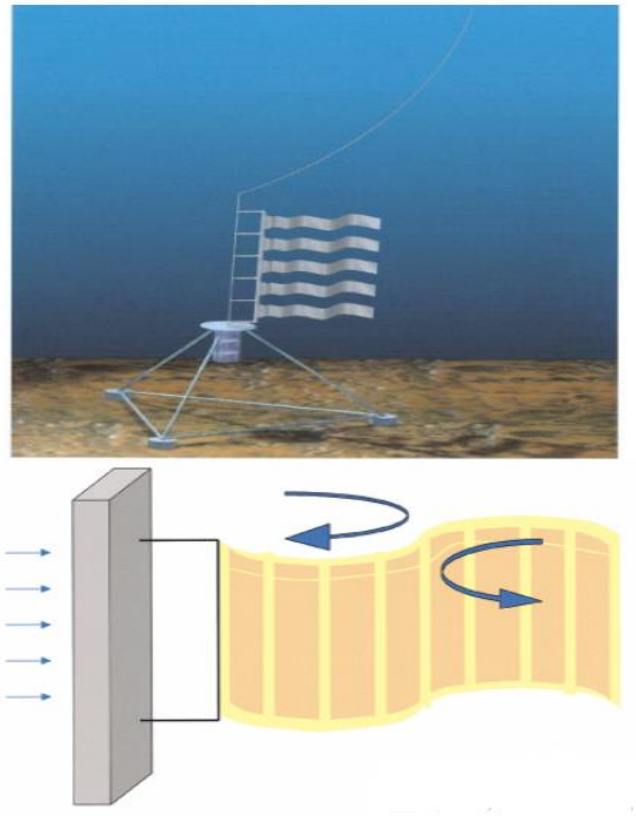


Figure 1.21: Piezoelectric eel in stream [53]

The piezoelectric eel designed by Taylor *et al*., shown in Figure 1.21, utilises a bluff body upstream of an energy harvesting device to create turbulent flows in calm rivers [53]. The water interacting with the bluff body causes eddies, which interact with a piezoelectric energy harvester downstream. Further studies by Pobering and Schwesinger on a device similar to the eel device and compared to a bimorph cantilever showed that a device similar to the eel in water flowing at 2m/s could produce between 11 and 32W/m^2 of power [54]. Various methods of fluid based piezoelectric energy harvesting have been discussed in that paper. These devices use wind and water to actuate the devices and have been shown to produce usable power levels. However, these devices have limitations and in most cases, there are little or no size restrictions or requirement to reduce their impact on flow. Energy harvesting from fluid flow is the central theme of this work. However, since the devices discussed here are to be actuated by blood flow through an artery or vein then the size and effect on flow become critical design parameters. This means that the various forms of energy harvesting discussed here would not be practical for use in the blood steam. However, they do provide an insight into the amount of energy that could be available to harvest as well as a possible starting point for designs.

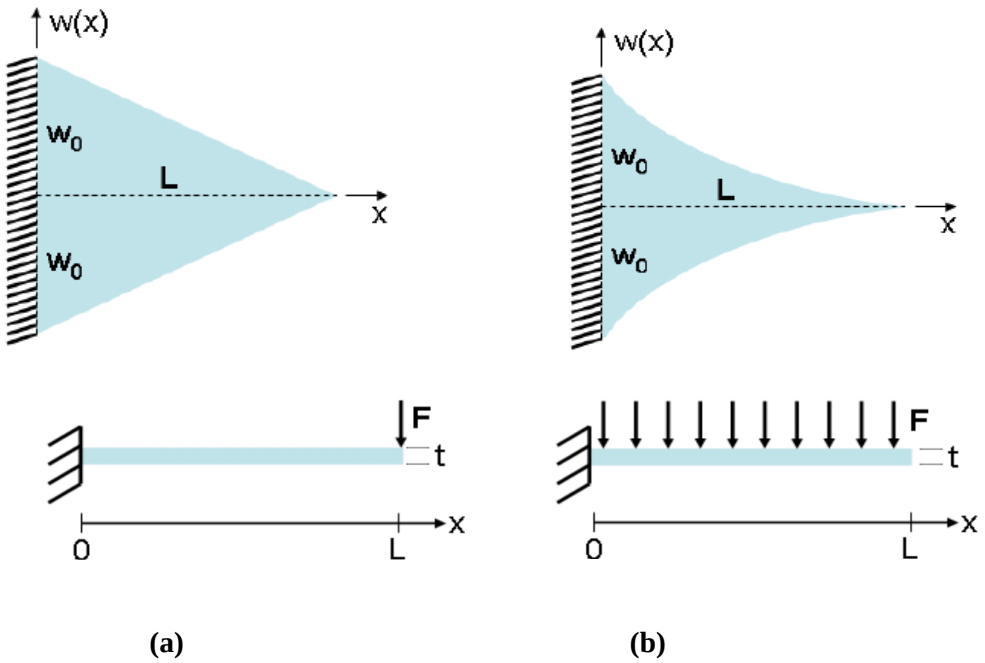


Figure 1.22: (a) Triangular cantilever with point load at free end, (b) triangular cantilever with uniform load over full length [37].

In order to discover the most effective geometry for fluid actuated energy harvesting Kuehne *et al*. [37] used two triangular piezoelectric cantilevers – triangular with point load and triangular with uniform load as illustrated in Figure 1.22 (a) and (b), respectively. Here the design of the devices creates the point load and uniform load as it is a function of w(x). The curved triangular geometry distributes the load uniformly compared to the straight-sided triangular geometry which generated a point load. These structures were compared with a rectangular piezoelectric cantilever of the same area. It was found that in all instances the triangular beam outperformed the rectangular cantilever. The triangular geometry allowed for greater deflection before mechanical destruction and also produced larger output voltage and better energy harvesting per mm^2. This was calculated at equivalent beam deflections for the cantilever and triangular beams and the better energy harvesting performance is due to the spatial distribution of the mechanical stress. For the maximum deflection of the rectangular cantilever, tested at 0.8mm of defection before mechanical failure, an output voltage of 0.1V and energy of approximately $1.67nJ/mm^2$ was achieved. At the same deflection the triangular geometry provided approximately 0.18V and $3.9nJ/mm^2$. These translate to 751.5nW and 1755nW for a $4.5mm^2$ rectangular and triangular cantilever,

respectively, at a frequency of 100Hz. The maximum deflection before breakage for the triangular beam occurred at 1.9mm and the beam was able to achieve 15.75μW of power maximum at 100Hz. These results show that device geometry plays a big role in the ability to harvest energy efficiently and must be taken into consideration with all other design parameters.

1.6.2. Human Based Energy Harvesting

Biomedical energy harvesting techniques can be categorised as either passive or active. Passive energy harvesting is defined by Joseph as energy harvesting in which the patient does not need to complete a task for energy to be harvested [55]. Harvesting energy from blood flow would be passive because blood flows independently of any interaction with the person. Active energy harvesting requires a certain task to be performed, i.e. walking, raising of arm, etc. Passive energy harvesting is of most interest in biomedical applications because the generation of power occurs independently of the activity of the host and doesn't interfere with the daily life of the patient.

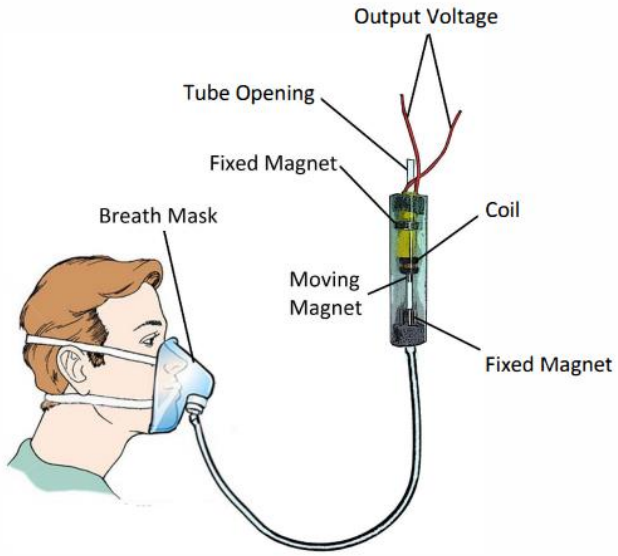


Figure 1.23: Electromagnetic Energy Harvesting from Breathing [56]

Breathing is another autonomic human process and research has been conducted into harvesting this energy. One device by Delnavaz and Voix [56] uses an electromagnetic element which was actuated by air flow out of the lungs and mouth (Figure 1.23). It was proposed for recharging mobile devices but it requires the user to wear a mask over their face and would be obtrusive and impractical for constant

energy harvesting. In 1984 a power of 17μW was achieved through the use of a PVDF device, which was excited through contraction/expansion of the ribcage and was implanted in-vivo in a dog, by Häsler *et al*. [57]. Further advances in this area may be facilitated by recent work by Qi *et al*. [22] who printed a piezoelectric ribbon onto flexible rubber. Previously the high temperature process required to form a ceramic piezoelectric material such as PZT made incorporation into flexible electric modules unfeasible but here the authors show high yield and good crystallinity. These devices would need to be tested for biocompatibility before they could be used for implantable devices but the results to date are encouraging.

In 2010, tests on a piezoelectric material placed in the blood flow were conducted by Khaligh *et al*. [38], the purpose of these experiments was to determine the amount of energy which can be harvested in this way. It was reported that for a square, 10mm x10mm, piezoelectric element of thickness 110μm located in the blood stream 0.03μW could be harvested and for a circular element of smaller size, 5.56mm radius with 9μm thickness, a higher value 0.61μW could be achieved but it was not stated over how many pulse cycles these power values were achieved. This experiment was based on finite element models (FEM) which were not validated using experimental results. These results seem to be anomalous based on the thick value of 110μm and the low power of 0.03μW. For fully validated models which take into account the size limitations of implanted devices, power levels significantly less than these would be much more typical of those available from blood flow.

However, there can be some disadvantages associated with harvesting energy from blood flow because there is a limit to how much energy can be harvested without subjecting the patient to additional unwanted strain. An important consideration is stenosis (plaque build-up on the vessel walls) or blood clots could be formed if the blood flow is obstructed. This is why the effect of devices on the fluid will be examined to avoid any disruption to the health of the patient which would render the technology unusable. However, there are other devices such as stents that are regularly implanted in the blood stream and they can cause blockages, but this happens rarely and properly using ultrasonics can help to alleviate any problems [58]. The insertion of an intravenous drip is another example where a needle is left inside a vein and causes a blockage. This is a fairly common medical procedure and not considered dangerous when infiltration is done properly.

Important factors to be considered when designing an implantable energy harvester are the biocompatibility and the effect on the flow but if these limitations could be overcome there would be a lot of potential for this form of energy harvesting. This would mean that implantable devices could possibly be recharged continuously in the future without the need for power from outside the body or intervention from doctors. This could significantly benefit research into implantable devices and the area of personalised health both of which have been identified as key areas for action by the NHS of Britain [59]. Recent research by Poon *et al*. in Stanford has developed an implantable medical device which travels through the bloodstream sampling the blood and is powered inductively when a reading is taken by a doctor [7]. This type of device requires external power from the inductive coupling and the work described in this thesis will focus on providing power to such a device without need of coupling to a device external to the body.

1.6.3. Heel Stroke and Movement based Energy Harvesting

As stated previously, human vibration energy harvesting can be divided into passive and active modes. Movement based energy harvesting is mostly active mode and has been the subject of a great deal of research, [10, 19, 21, 22, 36, 38, 51, 55, 60-64] and more. The results of some of these publications will be described here. However in most cases human activity such as arm movement, breathing, bending knees, etc., can be used to exploit the strain-driven operation mode for piezoelectric action [22].

Heel stroke energy harvesting (which is effectively harvesting energy from walking and running) has been discussed in great detail [10, 19, 21, 22, 63]. Figure 1.24 shows the design of such a system. A PZT bimorph is used at the heel and a PVDF stave (made from a multilayer laminate PVDF foil) is used in the front of the shoe underneath the ball of the foot. PVDF was chosen for this location because it is more flexible and will not break under the large deformations experienced in this location. PZT, which is more brittle but has a higher piezoelectric constant than PVDF, was placed in the heel of a US Navy work boot, due to the increased rigidity and the lower deformation, and was able to harvest 8.4mW of power into a 500kΩ load [65]. The PVDF stave which was placed into a trainer was shown to produce 1.3mW of power for a 250kΩ load at 0.9Hz [65].

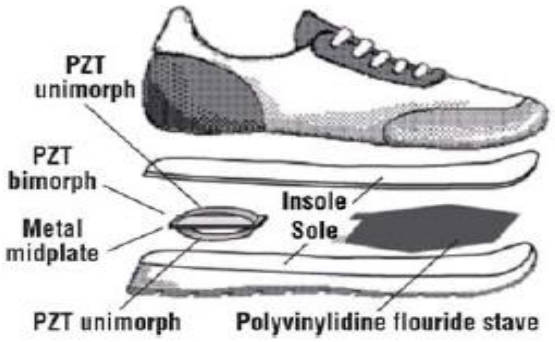


Figure 1.24: Integration of Piezoelectric material into shoe [65]

Other possible sources of movement-based energy harvesting are from replacement knee joints. In the work of Platt *et al*. [66] a sensor in a replacement knee, that was used to determine the wear and tear on the joint, was powered from the movement of the knee. 4.8mW of power was provided by the force on the joint from experiments which were done outside the body and over short time periods of 3 seconds. Table 1.3 provides a summary of the power available from various human movements as complied by González *et al*. [67]. From these results the possible powers which can be generated seem very high and these results are based on calculations rather than taken from experimental results.

Activity	**Mechanical Power Generated**	**Electrical Power Available**	**Electrical Energy Available Per Movement**
Blood flow	0.93W	0.37^{+}W	0.37J
Exhalation	1.00W	$0.40^{\#}$W	2.4J
Upper Limbs	3.00W	$0.33^{\sim}$ - 1.5^{+}W	1.5 – 6.7J
Breath	0.83W	$0.091^{\sim}$ - 0.42^{+}W	0.5 – 2.5J
Fingers (type)	6.9 – 19.00mW	$0.76^{\sim}$ - $2.1^{\sim}$W	143 - 266µJ
Walk	67.00W	$5^{\sim}$ - 8.4^{*}W	8.3 – 14.0J
$^{+}$ mechanical generator 50% efficiency; $^{\#}$ turbine + generator 40% efficiency; $^{\sim}$ piezoelectric generator 11% efficiency; * mechanical generator 12.5% efficiency			

Table 1.3: Summary of power and energy available from everyday human body activity [67]

1.7. Creating Energy Efficient Systems

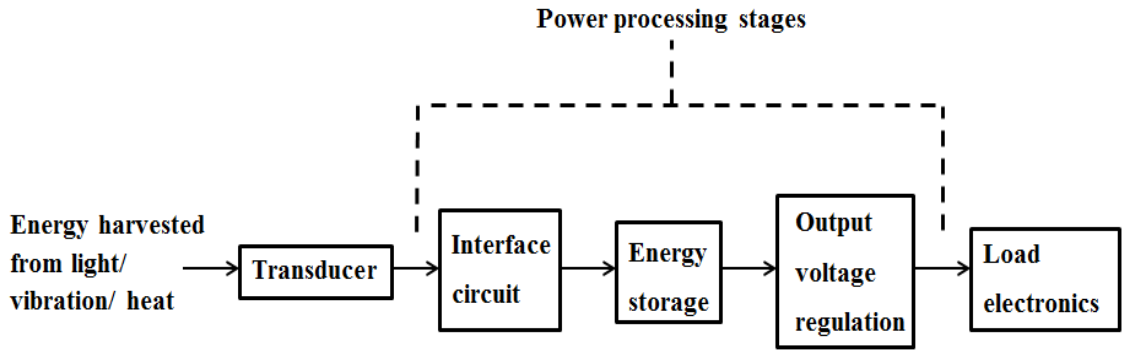


Figure 1.25: Power electronics topology for energy-harvesting systems

A complete energy harvesting system requires a source to harvest energy from, a transducer to convert the generated energy, and the power must then be processed and stored to be used by a system. This is shown in Figure 1.25. The power processing stages are very important to a complete system because it takes the generated power and creates a usable output for a load such as a pacemaker or other device. The interface circuit is required because the power generated is usually alternating current and is often unpredictable in nature. Most systems also require some form of energy storage because the individual power generated is too low to power a device or there is additional power generated which needs to be stored for later use. Depending on the system requirements output regulation to ensure the devices are provided with the correct voltage may also be required. These are all shown in Figure 1.25.

Most energy harvesting systems do not generate large amounts of power and it is important that the accompanying power management system be energy efficient. Energy efficient control and rectification systems are necessary to allow the maximum amount of energy to be harvested and to be used in the system, rather than being wasted in driving the control circuitry. A number of approaches that increase harvested energy and decrease the loss to the system will be discussed in this work. The ideal system to be powered would be an energy neutral system [68], i.e. a system that uses all the energy harvested and does not require an external power source. This would potentially give the system an infinitely long lifetime and would eliminate the need for further surgery once implanted. This is a key aspect for

implantable devices. To achieve this, not only does the harvesting circuitry need to be addressed, but also the energy storage and use in the sensors must be considered. In the work described in this thesis a fully efficient system which is coupled with a matched output load to extract maximum power will not be developed but an energy harvesting circuit which can be used for devices with multiple inputs will be examined and this system can be built on later.

1.8. Thesis Contributions

From this work 15 papers have been published including 3 journal papers. This work has contributed in the areas of material analysis, FEM, device design for energy harvesting and circuit design. State of the art in AlN grown on polyimide and on Si has been achieved and analysis of all the factors which contribute to the quality of the AlN have been investigated and assessed. FEM models with increased accuracy have been created and devices have been designed based on these models with excellent accuracy and these models can be updated to design future models. Experimental work was conducted on fabricated devices which provided information on the usefulness of various methods of analysing both devices and materials. This work has been awarded numerous prizes and has been used to inform other areas of energy harvesting including gait analysis and magnetic/piezoelectric combination energy harvesting devices. The circuit work has also been used in conjunction with structural health monitoring using piezoelectric devices.

1.9. Thesis Outline

Chapter 2 presents aluminium nitride (AlN) as a piezoelectric material. The reason for the choice of AlN as the piezoelectric material is explained. This chapter also includes a study of the material quality and the results of experiments performed to develop the best quality AlN material possible. Several different types of material and electrical analysis are considered and discussed in this chapter.

Chapters 3 and 4 deal with the finite element modelling (FEM) of the devices. Chapter 3 describes the approach taken to validate the models and the use of FEM to design devices to be fabricated. In Chapter 4 the chosen device geometries are elaborated and a discussion of the correlation between the models and fabricated devices is included. The choice of device geometries was greatly influenced by

these numerical simulations. The effect on fluid flow due to the presence of the devices in the blood vessel is also investigated in conjunction with the expected power capabilities.

The possible use of polymer materials, either as the piezoelectric material or in conjunction with AlN, is discussed in Chapter 5. Polymer material has been studied for this application because it is more flexible and less brittle than silicon or a crystalline piezoelectric material such as AlN.

Chapter 6 reviews different approaches for rectifying and storing the voltage produced by the piezoelectric material. Both single and multiple input circuits are investigated and results will be presented for simulated and bread-boarded circuits. There is a requirement in this work for the circuit to accept multiple inputs because individual inputs from the system are very low.

Discussion of future work and the conclusions which were reached based on the research undertaken are to be found in Chapter 7.

Chapter 2:

Piezoelectric Materials

2.1. Introduction

Table 1.2 from Chapter 1 shows the material properties of common piezoelectric materials. Here d_{31} and d_{33} are piezoelectric coefficients that show how much charge is generated as a function of pressure applied in either the vertical or lateral direction, $\varepsilon_{33,r}$ is the relative dielectric constant, Y is the Young's modulus and ρ is the mass density. As discussed in Chapter 1 the piezoelectric coefficient and Young's modulus have a direct effect on the electrical energy generation ability of the material. Of the most common piezoelectric materials PZT and PVDF are ferromagnetic and require poling (i.e. the introduction of mechanical strain in a specific direction) to produce a piezoelectric material. ZnO and AlN are wurtzite materials and have a piezoelectric response when grown in the c-axis [69]. PZT and ZnO both share contamination risks for tools shared with CMOS fabrication [70]. PZT contains lead and is therefore not biocompatible. PVDF has good thermal stability and excellent mechanical properties [71] but as a flexible material it requires large deformations to produce a good voltage response and its material

properties reflect the fact that its energy capabilities are much lower than that of PZT.

AlN is a very useful material because it is both CMOS compatible and biocompatible [72]. The quality of the film is highly dependent on how the film is deposited as well as its underlying layers [73] [48, 49, 74, 75]. As stated previously, single orientation c-axis films produce the best piezoelectric response and this is achieved by optimising the deposition parameters as well as the quality of the underlying layer. It has also been observed in the work of this thesis that an underlayer with good c-axis orientation seeds a better quality AlN film. It was, therefore, very important to determine the best conditions for the deposition of high quality, repeatable AlN films. This is discussed in this chapter.

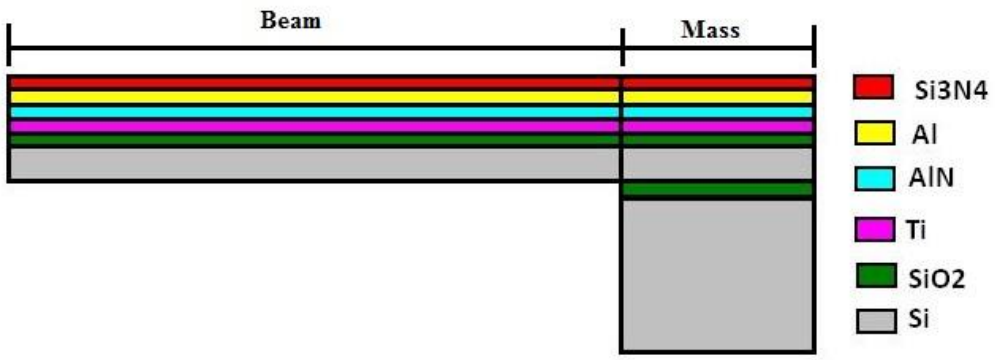


Figure 2.1: Device Layers (not to scale)

The layers of the devices are shown in Figure 2.1. The devices have been divided into 2 sections: beam (Table 2.1) and mass (Table 2.2). The mass has 2 extra layers and these are not included on all devices. The Si_3N_4 is a surface passivation layer which is required because the devices will be used in fluid. The layer thicknesses are given in Table 2.1 and Table 2.2.

Beam	
Layer	**Thickness**
Si_3N_4	200nm
Al	1µm
AlN	500nm
Ti	100nm
SiO_2	1µm
Si	25µm

Table 2.1: Beam layer thicknesses

Mass	
Layer	**Thickness**
Top 6 Layers remain the same as Table 2.1	
Bottom SiO_2	1µm
Bottom Si	530µm

Table 2.2: Mass layer thicknesses

As stated earlier, the piezoelectric material chosen for this work was AlN. The material thicknesses were chosen because good results have been obtained from simulations for devices fabricated with these dimensions. The optimisations of the fabrication process parameters was decided based on scanning electron microscopy (SEM) using a FEI Quanta FEG 650 [76], X-ray diffraction (XRD) using a Philips X'Pert Pro XRD system [77] and other methods to be described later. As stated previously the AlN film quality is based on growth in the c-axis orientation. To examine the best process parameters for sputtering the AlN, many (~ 100) Si wafers were fabricated and examined using experiments that vary the pressure and the distance from the target in the sputtering chamber. The grain size and the alignment were examined under a scanning electron microscope (SEM), which gave a good but qualitative indication of the quality of the film. SEM is the process of imaging a sample by scanning over the surface with an electron beam. The electrons interact with the atoms and the back scattered electrons from the sample produce signals which can be detected and from this an image is formed. The devices were imaged on the top surface and on a cross section as shown in Figure 2.2. When looking at

the surface SEM image the important features are to look for rounded grains dominating the surface as shown in Figure 2.2(a) and for the cross section (b) it is the columnar structure of the AlN material that is important for a high quality AlN material in the c-axis.

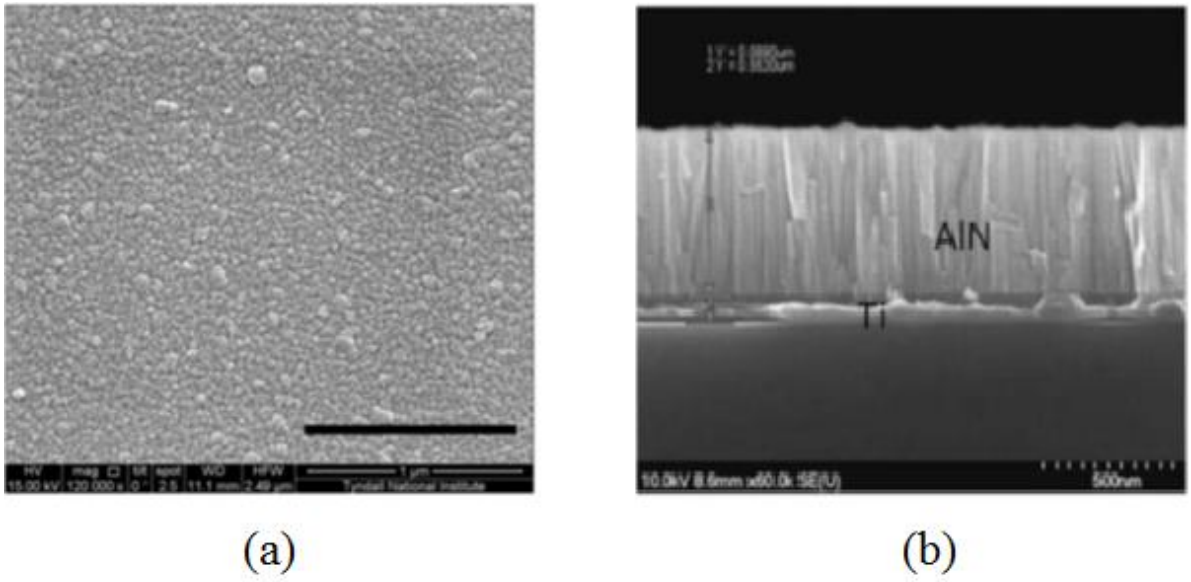


Figure 2.2: SEM image (a) surface and (b) cross section

To get a more quantitative analysis of the film crystallinity, X-ray diffraction (XRD) tests were carried out which provide information on the quality and homogeneity of the crystal orientation of the Ti and AlN films. The c-axis orientation will also be referred to as (002) orientation in this chapter because this is how it is defined for XRD. The c-axis orientation is also referred to as (0001) in many scholarly works. XRD analysis is carried out by focusing an X-ray beam of known intensity at a sample and measuring the diffraction of the beam under different illumination angles. The angles of the diffracted beam are then measured and the crystal structure of the sample can be established from this. This process is shown in Figure 2.3. In this work two types of XRD analysis was conducted. The first is a 2Θ long scan in the c-axis (002 in XRD) orientation over a wide angle from 30° to 70°. This is achieved by sweeping the detector through the angle while the sample is static. This analysis is performed to establish whether the AlN growth has single or multiple orientations. An example of a good 2Θ long scan is shown in Figure 2.4. In these scans the important features are a good AlN and Ti peak and no other peaks at higher degrees. Here it can be seen that the AlN peak should occur

around 36° but due to the alignment of the machine before every scan this peak may occur anywhere from 35.5° to 36.6°. The Ti peak occurs ideally at 38° but can be seen in scans between 37.5° and 38.5°. Another important feature to point out here is the y-axis. This axis shows the intensity of the scan but the actual value is not important because it shows the relative amount of X-rays detected above the baseline, hence it is shown in arbitrary units (a.u.). All the XRD scans will show arbitrary units for the y-axis.

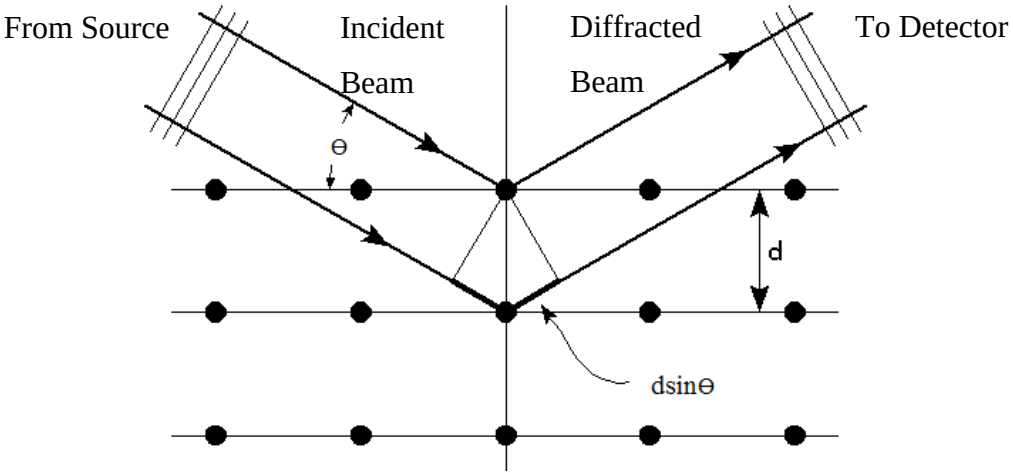


Figure 2.3: Principle of X-ray Diffraction [78]

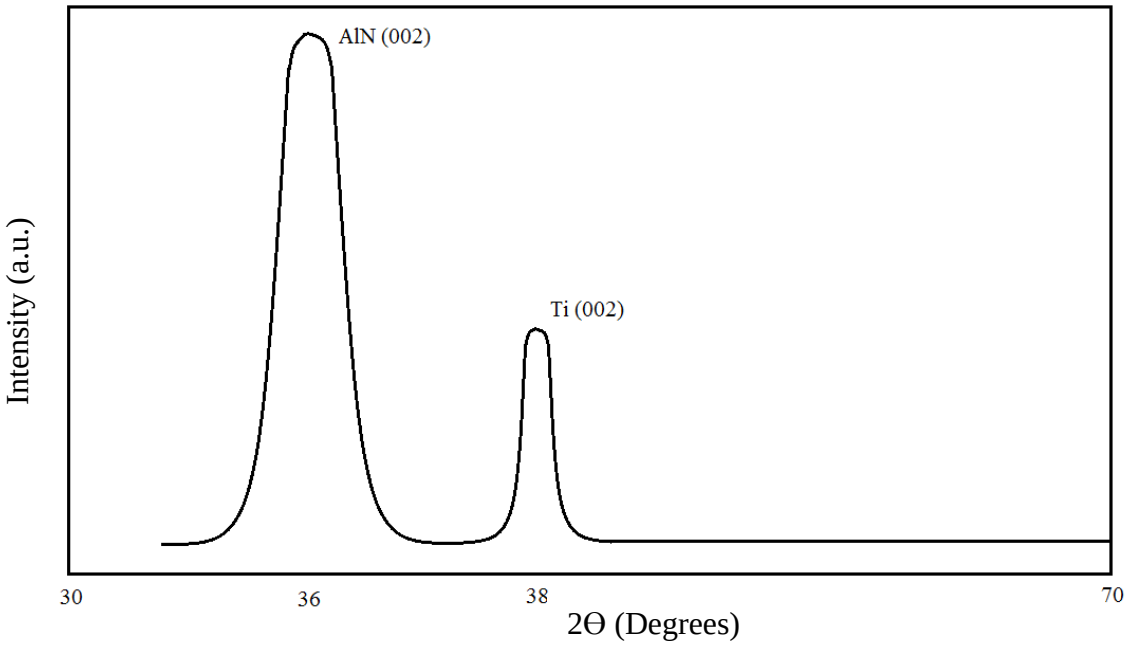


Figure 2.4: 2Θ scan example (not to scale)

Once the 2Θ scan has been performed then a relative Ω scan is carried out. In this scan, the 2Θ value which is found from the long 2Θ scan is set at the peak and

the Ω value is scanned around this point. This scan is done by sweeping the sample with respect to the source of the X-ray. From this scan the full width half maximum (FWHM) of the output is taken. The FWHM is a measure of the crystallinity of the AlN with a tighter peak indicating a higher quality material. This is taken by finding half the height of the peak response and at this point measuring the width as shown in Figure 2.5. The Ω scan range is determined by the centre (peak) value obtained from the 2Θ scan. The value of the Ω is half that of the 2Θ scan. This means that for a 2Θ scan of AlN with a peak at 36° the Ω scan will be centred at 18°. The FWHM is considered to be a good metric, along with the presence/absence of other orientations, of the quality of the AlN films. In this work the FWHM of the AlN and the Ti will be examined because the crystal quality of the Ti affects the quality of the AlN. A low value of FHWM is preferred to a high one for both materials. Typical values for AlN are <2° for high quality and >8° for low quality material and for the Ti layer the FWHM is typically higher than that of the AlN layer. The FWHM is an indicator of the quality and homogeneity of the material and the smaller the FWHM the better the alignment of the crystal orientation and therefore the higher the power output that can be achieved from the material.

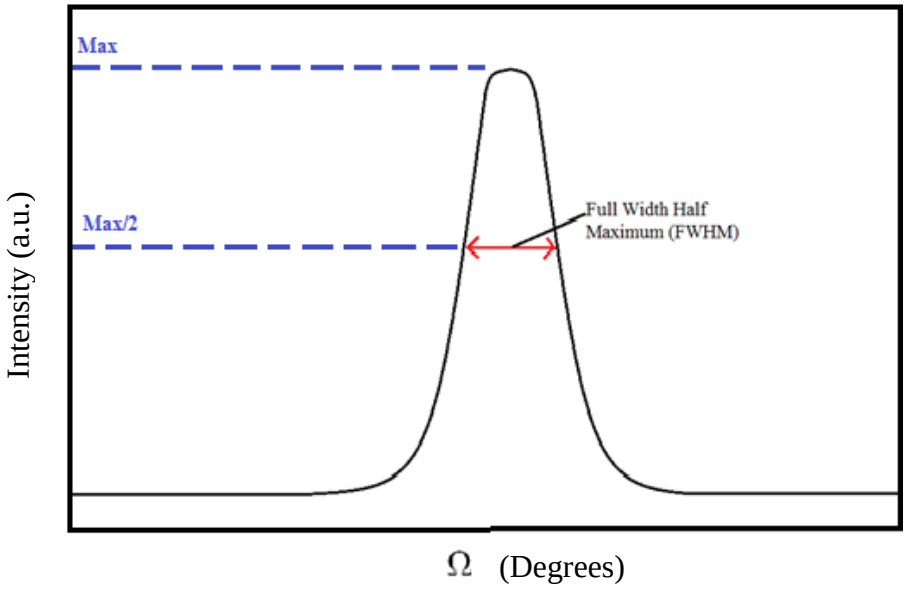


Figure 2.5: Example of Ω scan showing FWHM measurement

2.1.1 Process

The process used to deposit the AlN material is outlined in Table 2.3 and the sputtering conditions are given in Table 2.4.

Process Step	Description
1	Start with Si wafer; dip in HF for 10 seconds to remove native oxide.
2	Transfer to DC sputter, deposit Ti (100nm).
3	Followed by deposition of AlN (~500nm) without breaking vacuum. Done in 3 deposition steps at 2kW power and 260°C

Table 2.3: AlN Deposition Process Steps

Sputtering Conditions		
	Vacuum	6mTorr
	100% N_2	20sccm flow rate
	Target distance	~5cm
Deposition Step		**Time**
	Deposit time	16 mins
	Stop Depositing. Clean to avoid AlN build up	10 mins

Table 2.4: Sputtering Conditions and Deposition Step Description for AlN Deposition

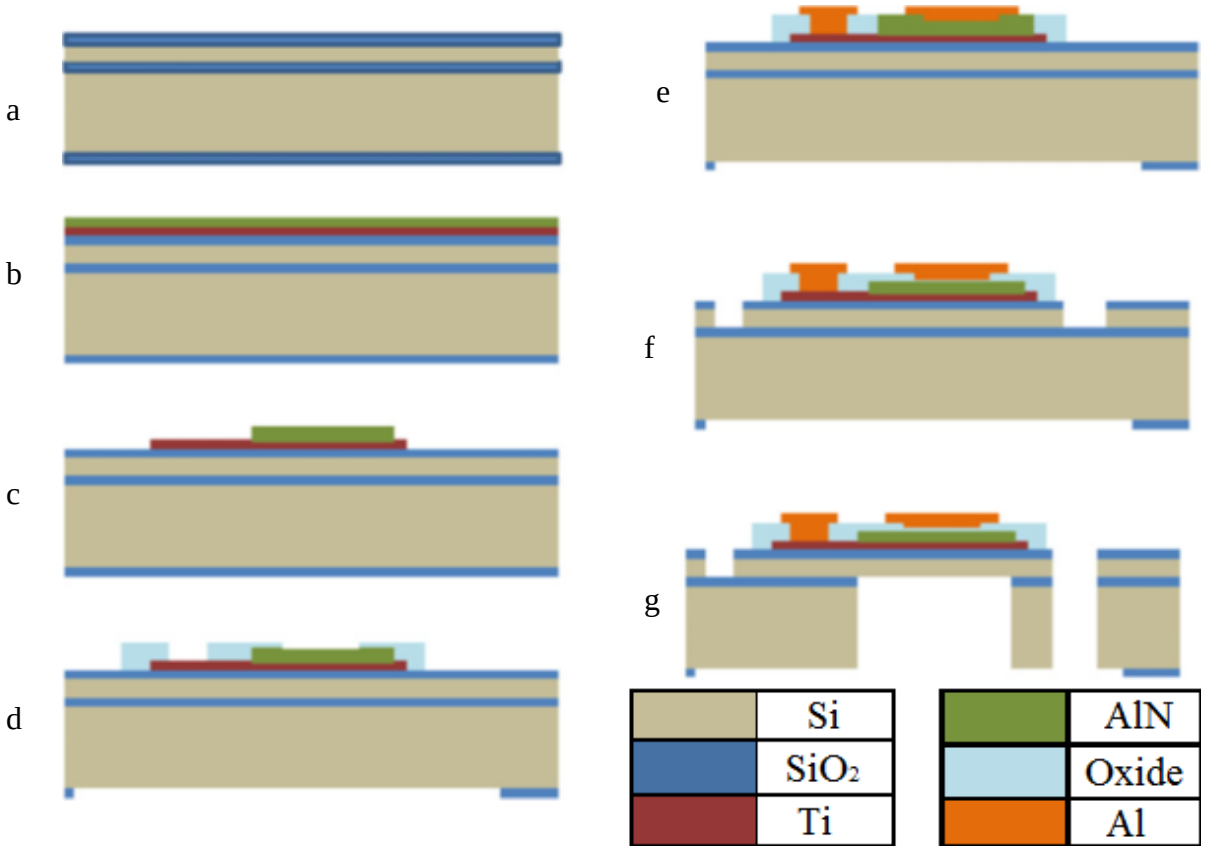


Figure 2.6: Process Steps for MEMS structures

Figure 2.6 shows the steps involved in creating the MEMS energy harvesting structures which are presented in Table 2.5.

Step	Description
a.	Thick SiO_2 is grown on an SOI wafer
b.	Titanium (Ti) and Aluminium Nitride (AlN) is deposited
c.	The Ti and AlN layers are patterned
d.	An oxide barrier layer is deposited and patterned
e.	Aluminium (Al) layer is deposited and patterned for the device electrodes and the bond pads
f.	The top oxide and silicon is etched to form the shape of the beam
g.	A backside deep reactive ion etch (DRIE) is performed to define the mass and the cavity

Table 2.5: Device Fabrication Process Steps

2.2. Material Property Testing Procedures

The crystal alignment of the (002) and (100) orientations of AlN are shown in Figure 2.7, the columnar structure of the (002) orientation is the orientation desired for the piezoelectric properties. This c-axis orientation was described in Chapter 1 and the importance of it has already been discussed. To achieve this, a number of test wafers were designed and tested using SEM, XRD, energy dispersive X-ray spectroscopy (EDX), probe station using LCR (inductance, capacitance and resistance) meter for the dielectric constant and laser Doppler vibrometry (LDV) to establish the piezoelectric constant. Initial tests also included transmission electron microscopy (TEM) and piezoelectric force microscopy (PFM). However it was found that the resolution of the TEM images available was not good enough and the PFM tests were time consuming and did not provide additional information once the other tests were verified. However, some PFM results will be discussed because these results confirmed the XRD results in the initial tests and established that the XRD is a good measure of film quality.

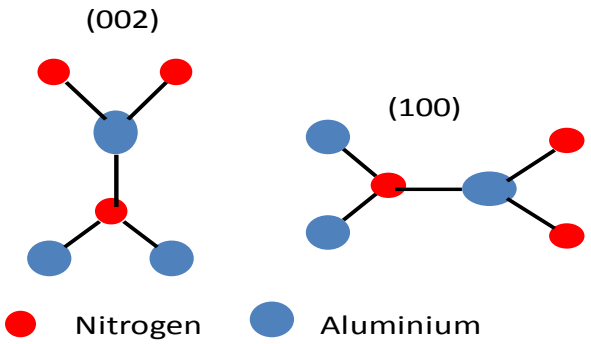


Figure 2.7: AlN crystal structure for 002 and 100 orientation

SEM and XRD have been described previously. EDX is similar to both in that it is the interaction of an X-ray beam with the characteristic X-rays emitted by elements when they react with an electron beam. EDX is used to determine the various elements in a sample and is based on the unique atomic structure of each element. In this work it is used to determine if other elements (besides those required) are present in the sample. This is very important to the quality of the film because it has been shown that the presence of oxygen in the sample can affect its piezoelectric constant [79, 80].

The capacitance measurement was conducted on a standard probe station using an LCR meter. A probe was connected with the top and bottom electrodes (i.e. the Al and Ti layers) and the capacitance was read. This value was used to measure the relative permittivity (ε_r) of the material using the formula:

$$\varepsilon_r = \frac{Ct}{\varepsilon_0 A} \qquad (2.1)$$

where C is the capacitance, t is the thickness of the AlN, ε_0 is the permittivity of free space and A is the surface area of the top electrode. The surface area of the top electrode is used because this determines the active surface area.

LDV (Polytech MSA-400) uses a dual laser method to determine displacement. The measuring laser is positioned at the end of the cantilever structure, while a reference laser is positioned on the stationary silicon frame. Figure 2.8 shows the measurement set-up. The method to calculate the d_{31} piezoelectric constant was based on the procedure described by Doll *et al*. [81]. Firstly, the resonant frequency is measured by attaching the structure to be measured to a vibration apparatus (a loud speaker) connected to the LDV. A frequency sweep was then applied and the point of maximum displacement was determined from this. The frequency at which maximum displacement occurs is the resonant frequency. To measure the piezoelectric constant (d_{31}) a sinusoidal bias is applied between the top and bottom electrodes and the displacement is measured. Three different bias voltages were used (0.25, 0.5 and 1V), which was amplified twenty times in order to measure the displacement of the AlN material. These values along with the thickness value obtained from the SEM images were used to calculate the d_{31} piezoelectric constant. To do this first the d_{33f} value is obtained using:

$$d_{33f} = \frac{\epsilon_3}{E_3} = \frac{\Delta t}{V_{bias}} \qquad (2.2)$$

where d_{33f} is the thin film piezoelectric coefficient, ϵ_3 and E_3 are the strain and electric field in the film, Δt and V_{bias} are the change in thickness and the voltage applied across the material. d_{33f} is related to d_{33} and d_{31} by:

$$d_{33} = d_{33f} + \frac{2s_{13}^E}{s_{11}^E + s_{12}^E}|d_{31}| \qquad (2.3)$$

where s^E_{11}, s^E_{12}, s^E_{13} are the elastic compliance parameters of the material. The elastic compliance parameters are found from the material properties of AlN and from Equation 2.3 d_{31} is found.

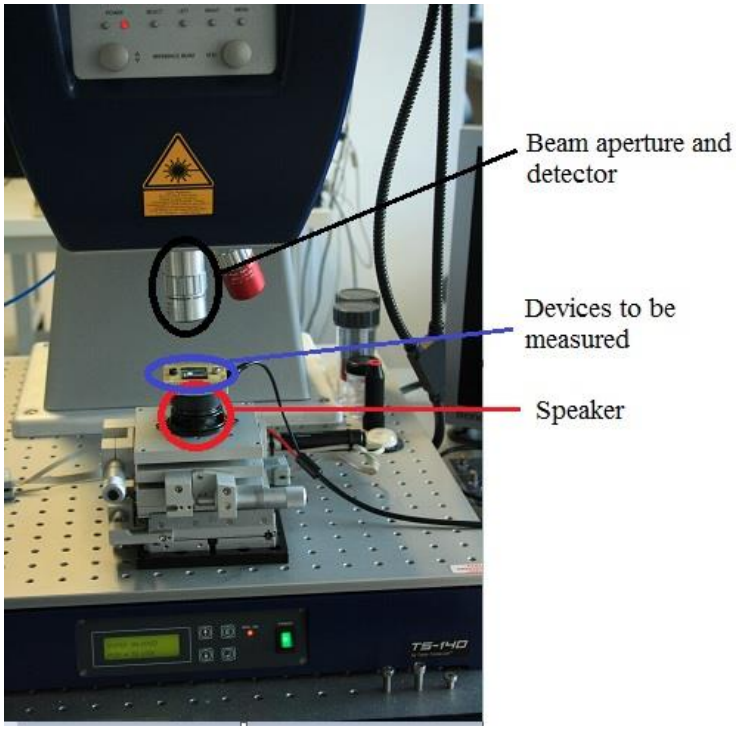


Figure 2.8: LDV set-up

2.3. Initial Results

The XRD results from the initial results are shown in Figure 2.9 and Figure 2.10. Figure 2.9 shows the 2Θ long scan of material from device wafers, i.e. wafers that were processed to create usable devices and the insert is the relative Ω scan (also referred to as rocking curve scan). Test wafers were fabricated by growing Ti and AlN on a Si wafer but device wafers require both bottom (Ti) and top (Al) electrodes to be present in order to function. In Figure 2.9 the peak at 38° is much higher than that shown in Figure 2.4 because it contains both Ti and Al. Figure 2.10 shows the relative Ω scan for the initial test wafers. Samples B to H were prepared by changing the oxide, the Ti and AlN thickness, as well as by using multiple and single stops in the AlN deposition and with a lower nitride concentration than normally used. The results show that these parameters directly affect the value of the FWHM of the material and hence its quality. There is a 160% increase in the FWHM over the different samples and this is due to depositing on different Si surfaces. The device wafers were subjected to more processing than the test wafers and this

affected the Si surface and therefore the quality of the Ti and AlN material. In the test samples the exposed Si layer came directly from the box (new wafer from manufacturer) and was already a good surface. The device wafers had to be etched to remove the oxide overlayer. This caused the difference in the material between the test and device wafers. The device wafers are numbered 1 to 3 to differentiate them from the test wafers which were referenced with letters B to H which is shown in Table 2.6. Properties of Sample E and F are omitted for intellectual property reasons.

Properties	Sample
Oxide, 10nm Ti, ~200nm AlN (single deposition)	B
Oxide, 10nm Ti, ~200nm AlN (multiple stops in deposition)	C
Oxide, 100nm Ti, ~200nm AlN (multiple stops in deposition)	D
Oxide, 100nm Ti, ~500nm AlN (multiple stops in deposition) with 50-75% N_2	G
Oxide 200nm Ti, 500nm AlN (multiple stops in deposition)	H

Table 2.6: Process Properties for Initial Test Wafers

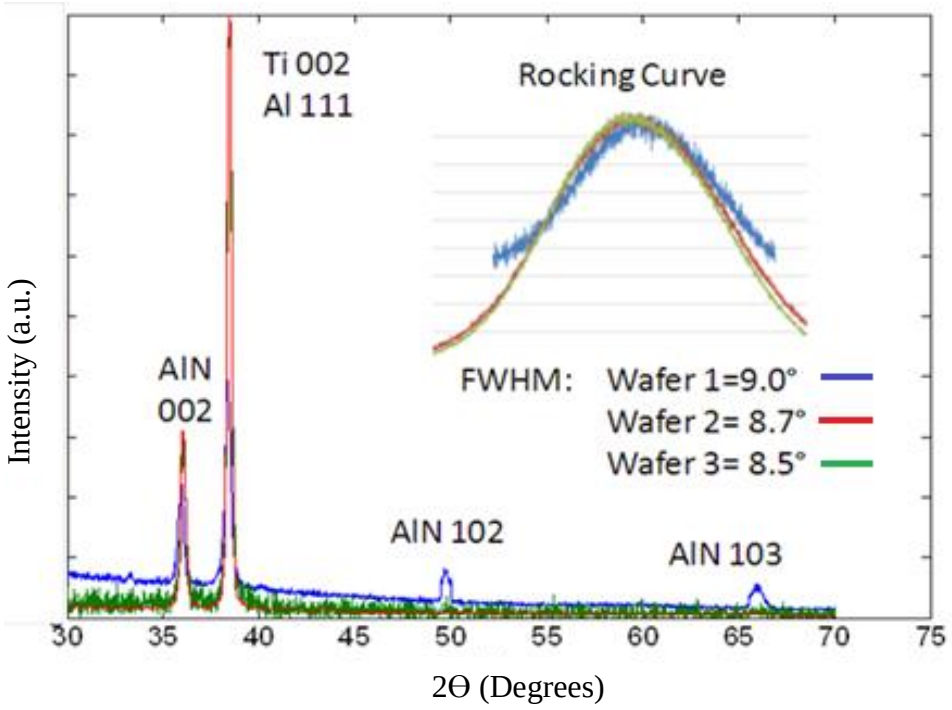


Figure 2.9: 2Θ and relative Ω scan results from first device wafers

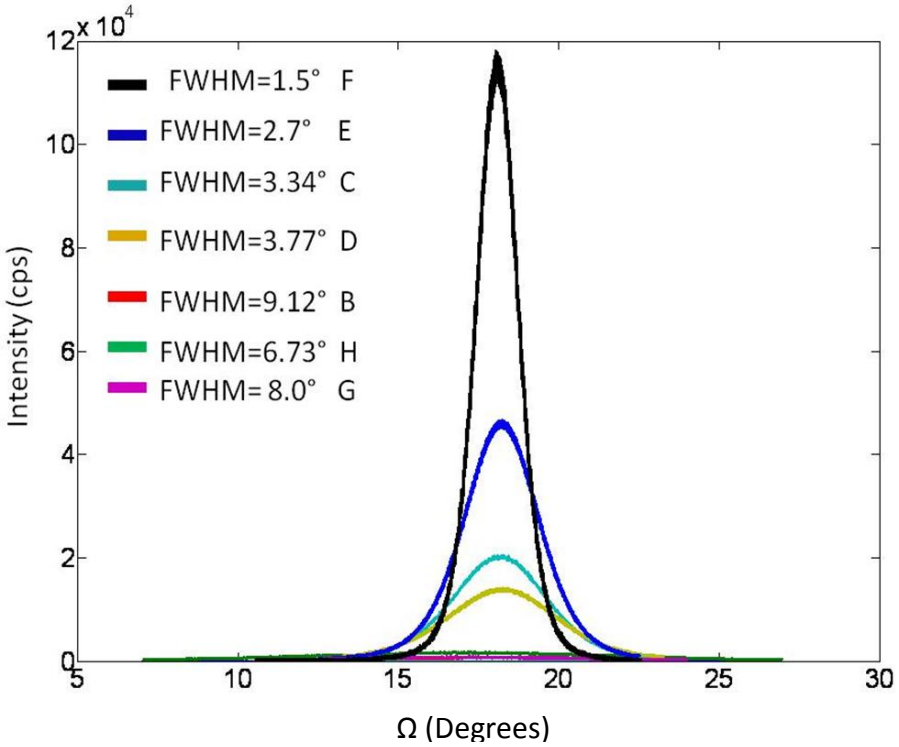
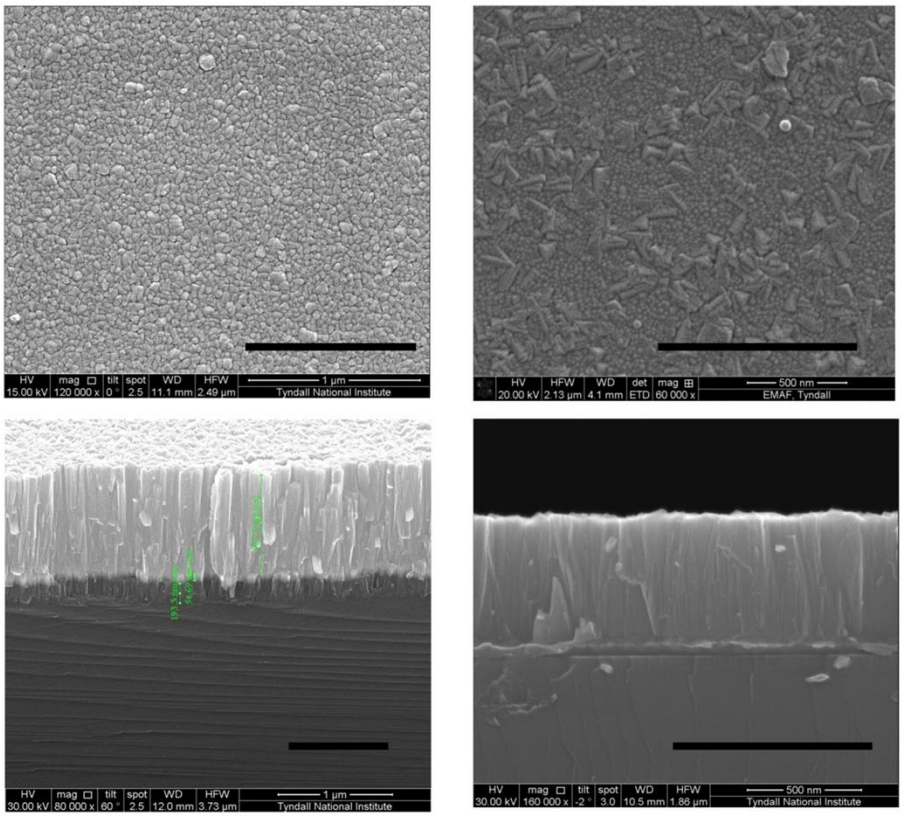


Figure 2.10: AlN relative Ω scan results for initial test wafers

The initial device wafers were also tested using PFM and SEM to determine the film quality. The columnar structure shown in Figure 2.2 represents the kind of piezoelectric film that was designed. Figure 2.11(a) is a top and cross section view of Wafer 3 which showed single (002) orientation of the AlN in the 2Θ long scan (Figure 2.9). These results are confirmed by the rounded grains in the top view and the highly columnar structure in the cross section. Figure 2.11(b) shows the results from Wafer 1. In the 2Θ long scan (Figure 2.9) multiple orientations of AlN showing tilted grains of (102) and (103) as well as (002) were seen and these results are consistent with the results of the SEM. The top view shows a network of small elongated islands, which represent the tilted grains, as well as the smaller rounded grains expected and the cross section does not show the single growth direction seen in (a). The results for Wafer 2 are not shown here because they were very similar to those of wafer 3 which once again is consistent with the XRD results shown in Figure 2.9.



(a) **(b)**

Figure 2.11: SEM images of (a) Wafer 3 and (b) Wafer 1 where the top image is the top surface and the bottom is the cross section showing (002) orientation.

From the EDX results, shown in Figure 2.12, it can be seen that Wafers 1 and 3 have similar composition of materials. Importantly, no significant oxygen content was found in any of the samples. Wafer 2 results are not shown because they were similar to Wafer 3. As previously stated, oxygen content has been shown to affect the material quality [80] and that is why this is an important parameter. In Figure 2.12 no significant differences are seen between Wafer 1 and Wafer 3. The peaks are of different heights but the compositions are the same and these peak differences are not significant.

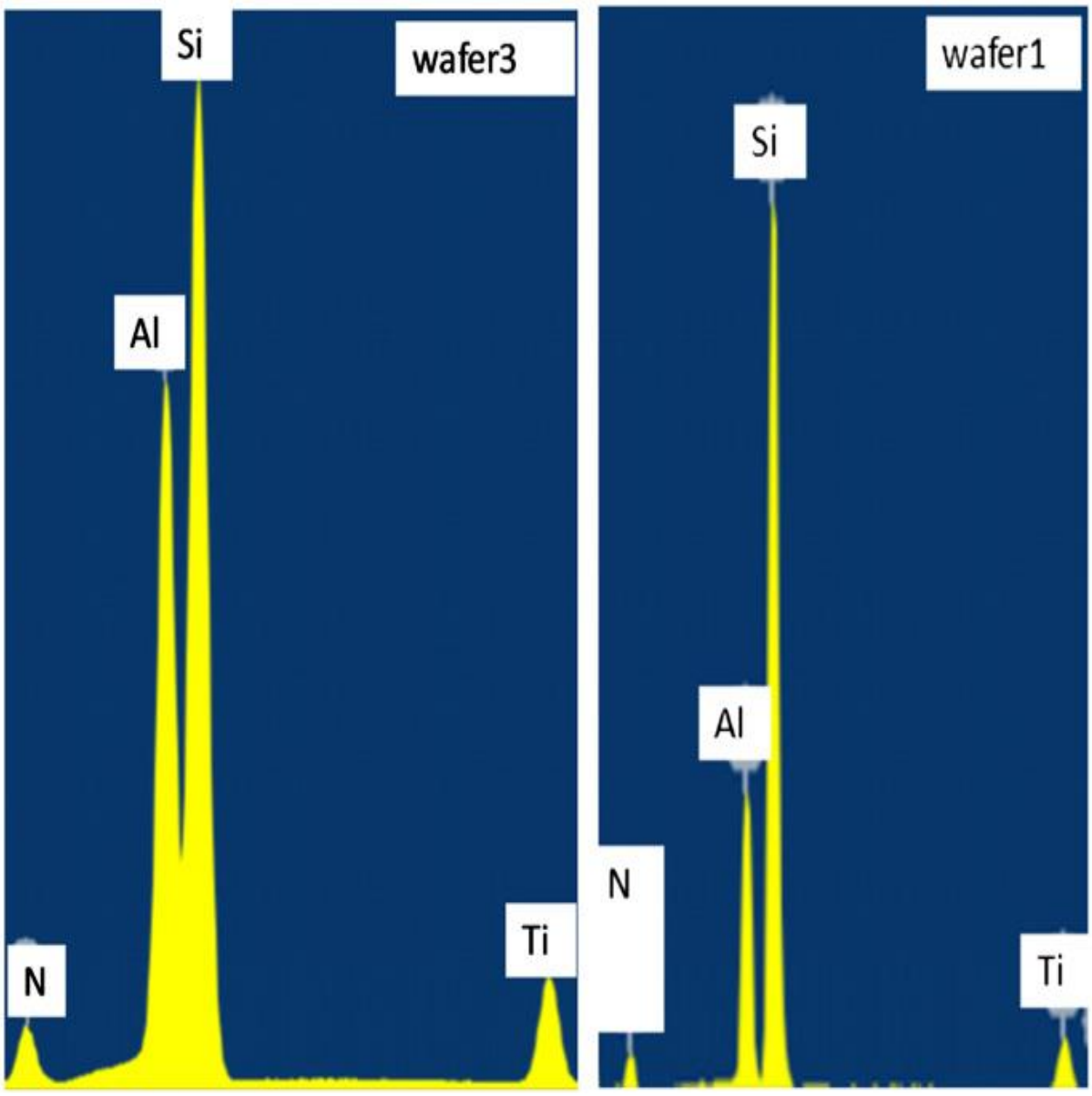


Figure 2.12: EDX spectroscopy of wafer 3 and 1

The results of the PFM showed that the film quality for Wafer 1 was significantly worse than that of Wafers 2 and 3. The FWHM of these devices were all approximately the same so this result showed that if other orientations were seen in the XRD 2Θ scan beyond the Ti (002) peak then the quality of the film was significantly decreased. This is shown for Wafer 1 in Figure 2.9 where peaks for AlN (102) and (103) were seen at 50º and 66º respectively. It was established that even for films with very small FWHM values if other peaks were present in the XRD spectrum then the PFM showed a significant decrease in the piezoelectric

quality of the material [70]. These results confirmed that single (c-axis) orientation was a critical factor for growing a high quality piezoelectric AlN material and also that XRD was an excellent test method for these films.

These wafers were also tested for the dielectric constant using the capacitive measurement described in Section 3.2. This is an important test as an increase in dielectric constant corresponds to a decrease in the power harvested [82]. The dielectric constants were found to be 8.83, 8.93 and 8.9 for Wafers 1, 2 and 3, respectively, so it is seen that the orientations did not have a significant effect on the dielectric constant. These results are close enough to conclude that crystallinity is not a major factor in the dielectric properties of the material.

The piezoelectric constant (d_{31}) was calculated using the SEM and LDV measurements and the results were 0.84pm/V, 1.97pm/V and 2.04pm/V for Wafers 1, 2 and 3 respectively. Here it is seen that Wafer 1 has a much lower piezoelectric constant than Wafers 2 or 3. The EDX showed that the three wafers had similar material make-up and the FWHM results from the Ω scan were equivalent. The piezoelectric constant and PFM results showed that the piezoelectric quality of the material was reduced. It can be deduced that the presence of (102) and (103) AlN orientations has a significant effect because these orientations interfere with the (002) growth of the film so that areas of the film with other orientations are present and this reduces the effective area of the material.

2.4. DC Sputtering Test Wafer

2.4.1. Critical Parameters

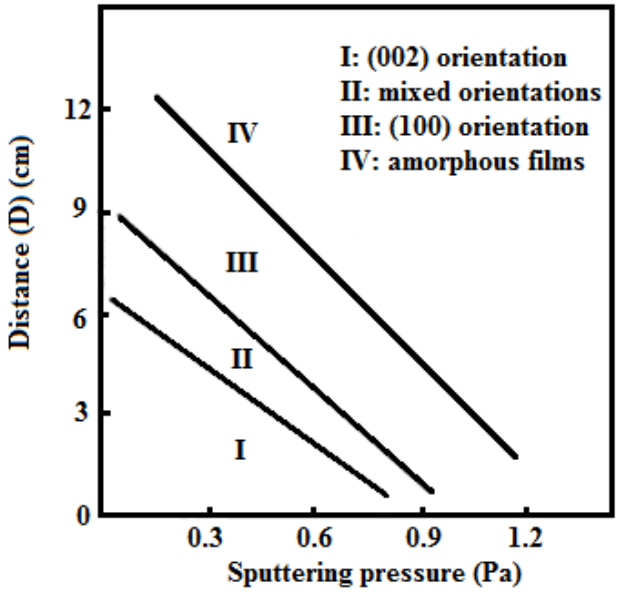


Figure 2.13: Effect of sputtering pressure and distance on AlN crystal structure [46]

In order to determine how to achieve a good quality AlN film an experimental matrix of sputtering set-ups was designed. Figure 2.13 shows the effect that pressure and distance between substrate and target using DC reactive magnetron sputtering has on AlN crystallinity as discovered by Xu *et al*. [46]. In this it was shown that the AlN film needs to be sputtered with low pressure and low distance to the target to achieve a (002) orientation. Figure 2.14 shows the effect of using a seeding interlayer in the film orientation described by Kamohara *et al*. [49]. Figure 2.14(a) shows the SEM results for AlN material grown on Si which is illustrated in Figure 2.14(d). The illustration Figure 2.14(d) as well as the SEM Figure 2.14(a) show that the AlN structure is not fully c-axis orientated. In Figure 2.14(b) and (e) a molybdenum (Mo) layer was grown before the AlN and the structure is much more columnar and is following the structure of the Mo. However, some grain tilt is still seen. Figure 2.14(c) and (f) shows an AlN interlayer grown on the Si. The Mo layer is more columnar than seen in Figure 2.14(e) and (b) and the AlN structure shows the most c-axis orientation. These studies by Xu *et al*. [46] and Kamohara *et al*. [49]

as well as the results from the initial wafer discussed in Section 2.3 determined the parameters that would be studied in this work.

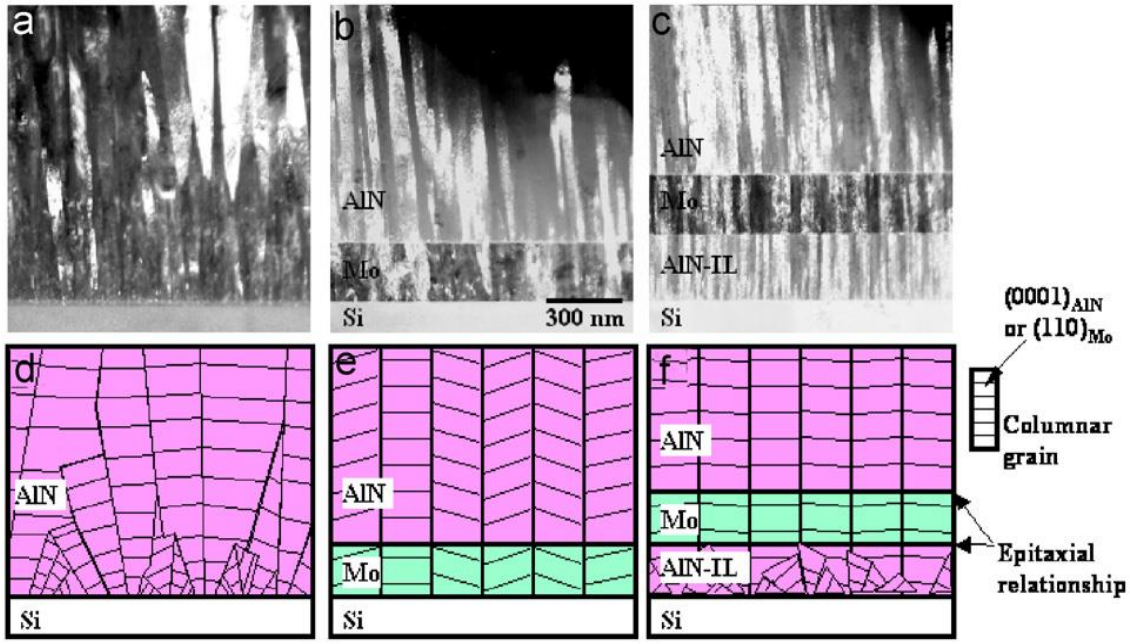


Figure 2.14: Effect of Interlayer on AlN film Orientation by Kamohara *et al*. [49]

Power	**Interlayer**	**Bias**
(A) High (3kW)	(D) AlN (200nm) interlayer	(F) – 28V
(B) Medium (2kW)	(E) No interlayer	(G) No Bias
(C) Low (1kW)		

Table 2.7: Properties changed during DC sputtering tests

The wafers were grown using combinations of the properties shown in Table 2.7 as well as varying the distance between the target and the substrate. The power referenced was for AlN deposition, all thicknesses of AlN were 500nm except for the interlayer experiments where a 200nm seed layer was deposited. This layer was deposited at 2kW power. All Ti layers were 100nm unless stated otherwise. In all cases the deposition was formed on bare Si wafers with oxide and native oxide removed unless specified. Twenty eight test wafers were fabricated and the details of each experimental structure made up of combinations of the parameters A to G are given in Table 2.8 and Table 2.9. In this work Ti was chosen as the metal layer because it was a material which could be processed in the onsite fab.

Number	Properties	Description
1	BDG	Pre sputter with Argon and Nitrogen
2	BDG	Remove oxide, deposit 200nm interlayer on Si, deposit 100nm Ti, deposit 500nm AlN at 2kW
3	AEG	Remove oxide, deposit 100nm Ti on Si, deposit 500nm AlN at 3kW
4	ADG	
5	CDG	
6	BEG	
7	BDF	
8	BEF	
9	BDG	oxide layer of a couple of hundred nm on the Si prior to deposition
10	BDG	Silicon Nitride on Si prior to deposition (a few hundred nm)
11	BEG	oxide layer on the Si
12	BEG	Silicon Nitride layer on Si
13	CEG	
14	ADF	
15	AEF	
16	CDF	
17	CEF	
18	BDG	deposit both AlN at 3mTorr pressure with flow rate of 10sccm N2
19	BDG	move target to 80mm
20	BDG	move target to 30mm
21	BEG	same as W18 low pressure 3mTorr 8sccm
22	BEG	same as W20 30mm target distance

Table 2.8: Properties changed and the description for testing AlN quality

Number	Properties	Description
23	BEG	low pressure 3mTorr and 30mm target
24	BEG	deposit polyimide on bare silicon then deposit BEG on cured polyimide
25	AEF	apply the RF bias to the seed layer as well as the top AlN
26	BEF	low pressure 3mTorr 8sccm
27	BEF	30mm Target
28	BDG	Pre sputter with Argon and Nitrogen

Table 2.9: Properties changed and the description for testing AlN quality (cont.)

Prime grade Si (100) was used for all test wafers and the native oxide was removed by dipping in HF. The length of the dip was kept constant at 30 seconds for all steps to ensure all native oxide was removed and this was done for all wafers except where it was necessary to retain the oxide layer. The wafers were transferred to the sputterer and put under vacuum as quickly as possible afterwards to stop the native oxide from reforming. The AlN interlayer was deposited at 2kW to a thickness of 200nm using multiple breaks and using the same number of breaks and time for each interlayer on each wafer in the experimental matrix that required an interlayer. Multiple breaks were used to reduce the stress on the target but the vacuum was not broken between the breaks. The other parameters are kept constant. The standard pressure and target distance were 5mTorr and 45mm, respectively, with a flow rate of 20sccm N_2.

Table 2.10 shows the results of the DC sputtering test wafers and from these results the optimum process was chosen. The best results show the lowest FWHM for AlN and no extra peaks which correspond to other orientations. From this table it is seen that the best results occur when there is no bias and no interlayer but the power seemed to have very little effect on the result and, in fact, the difference seen is within the precision limitations of the measurement. The best results are highlighted in yellow.

Test wafer	FWHM (AlN)	FWHM (Ti)	(102) peaks	(103) peaks	(100) peaks
BDG	4.77	2.8	Yes	Yes	No
AEG	1.62	1.92	No	No	No
ADG	6.03	3.36	Yes	Yes	No
CDG	3.7	2.36	No	No	No
BEG	1.67	1.93	No	No	No
BDF	6.11	3.57	No	No	Yes
BEF	5.8	3.1	No	No	Yes
BDG (oxide)	9	NA	Yes	Yes	No
BDG (nitride)	10	10	Yes	Yes	No
BEG (oxide)	4.36	3.88	No	No	No
BEG (nitride)	2.21	3.08	No	No	No
CEG	1.6	1.69	No	No	No
ADF	6.1	3.2	Yes	Yes	Yes
AEF	5.64	1.8	No	No	yes
CDF	4.7	2.48	Yes	No	Yes
CEF	6.8	NA	Yes	Yes	Yes
BDG (3mT)	8	6	Yes	Yes	No
BDG (80mm TD)	6.3	NA	Yes	Yes	Yes
BDG (30mm TD)	3.1	2.8	Yes	Yes	Yes
BEG (3mT)	1.76	2.12	No	No	No
BEG (30mm TD)	1.65	2.1	No	No	No
BEG (3mT & 30mm TD)	1.59	2.1	No	No	No
BEF (3mT)	4.3	NA	No	No	Yes
BEF (30mm TD)	3.9	NA	No	Yes	Yes
BEF (3mT & 30mm TD)	2.9	NA	No	Yes	Yes

Table 2.10: Results of changing process set-up for DC sputtering

2.4.2. Process Set-up for Quality and Repeatability

From the results of the DC sputtering tests it became clear that the best AlN results were achieved when using a medium power (2kW), no interlayer and no bias. The very best result was shown using low pressure, 3mTorr and low target, distance 30mm. However, it was found that this process took a much longer time and that the target degraded much quicker when using this process. For the standard process it was decided to set the distance to 50mm and the pressure to 6mTorr because this would mean that multiple wafers could be deposited using the same target.

The results of the 2Θ long scan and the rocking curve scan for device wafers using the standard process are shown in Figure 2.15 and Figure 2.16. Here it is seen that there are no additional AlN peaks and the FWHM results are much better than the results shown from the initial device wafers (Figure 2.9). The FWHM has been reduced by approximately 6.5° compared to the results from the initial device

wafers. The rocking curve scan of test wafers deposited using the optimum process is shown in Figure 2.17. The 2Θ long scans for these test wafers all showed similar results to the device 2Θ long scans. The rocking scan results show that the process is repeatable as FWHM results of between ~1.5º and ~1.7º were achieved over a number of wafers.

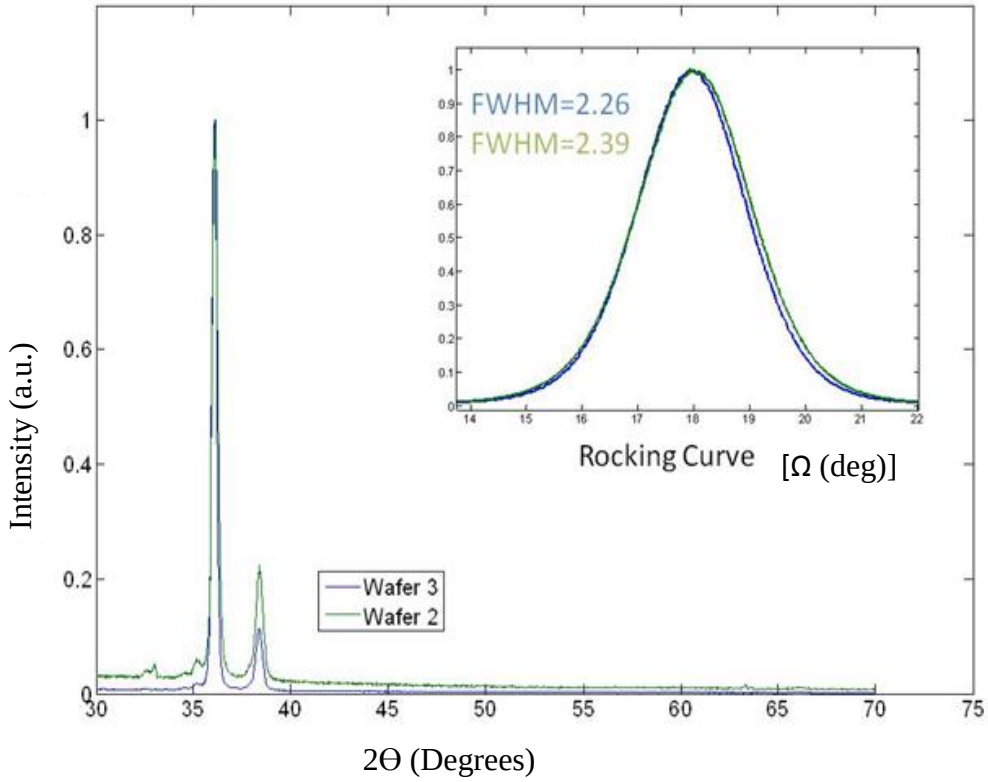


Figure 2.15: Device Wafer 2Θ and rocking curve scan results.

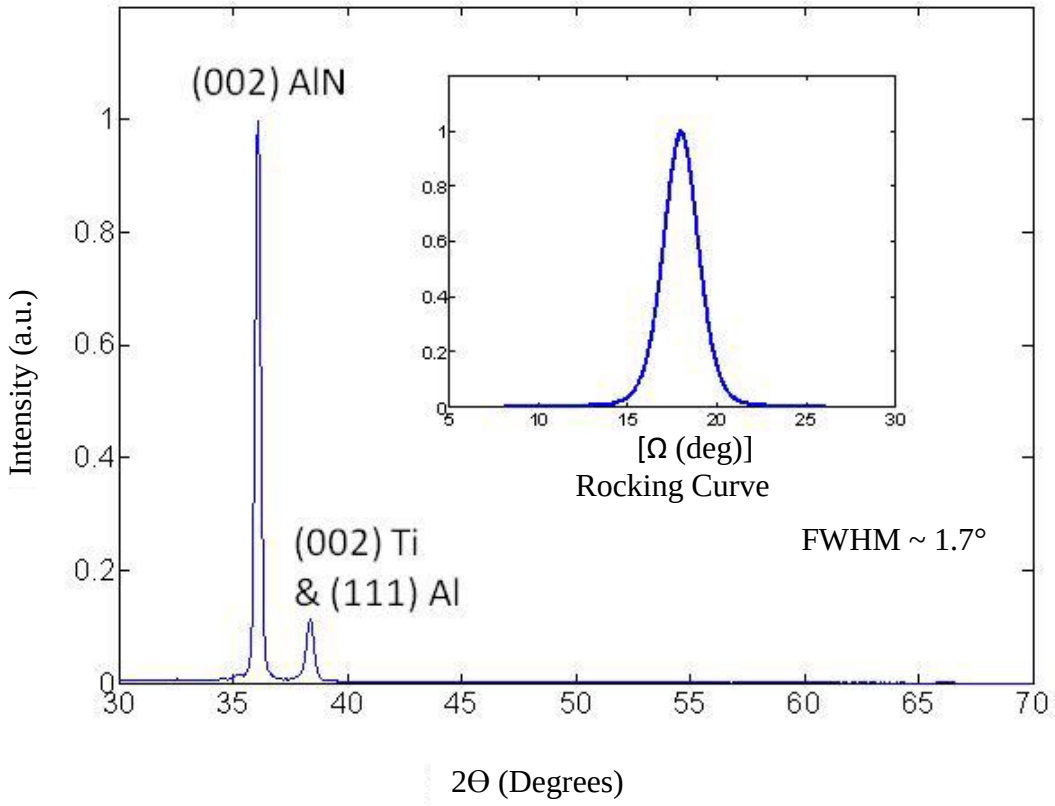


Figure 2.16: Device Wafer 2Θ and Rocking Curve results.

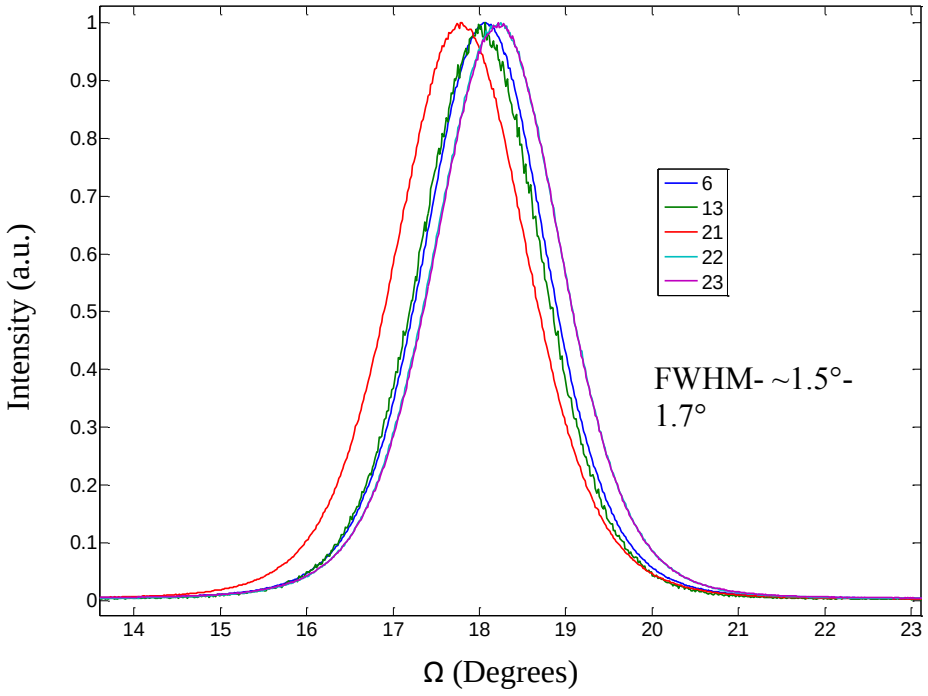


Figure 2.17: Rocking Curve scan of AlN on test wafers

2.5. RF Sputtering Results

RF sputtering was also considered as a technique to deposit high quality AlN films because Okano *et al*. [83] reported that it produced good quality film. XRD results for 2Θ scan were presented but the rocking curve scan was not shown so the FWHM could not be determined. Research by Cheng *et al*. [84] showed that the nitrogen (N_2) concentration was an important parameter in the production of (002) oriented AlN. In this work it was established that an N_2 concentration of 100% was best to produce only (002) orientations. Matsunami *et al*. [85] examined the growth of AlN on different substrates. Here it was seen that RF sputtering of AlN on a Si substrate did produce (002) orientated film. However, the FWHM result from the rocking curve was approximately 10° with the substrate temperature optimised for minimised FWHM. Saravanan *et al*. [86] examined the growth of AlN on Si (100) and Si (110) substrates. The FWHM for the Si (100) substrate was 3.3° which was better than the result obtained by Matsunami *et al*. but was much higher than the DC sputtering results obtained.

In this work, RF sputtering was investigated for varying pressure and distance from target. The results of these test wafers are shown in Figure 2.18. It is clear that the (002) AlN and Ti peaks are present and there are no extra peaks in the long scan after 40º. Comparing these results to those seen for the standard DC sputtering of device wafers (Figure 2.15) it is seen that the AlN (002) peak is very weak for all test wafers. The (002) Ti peak also contains AlN (101) and this additional peak would cause a reduction in the piezoelectric properties of the film. From these results it was determined that DC sputtering was preferable to RF.

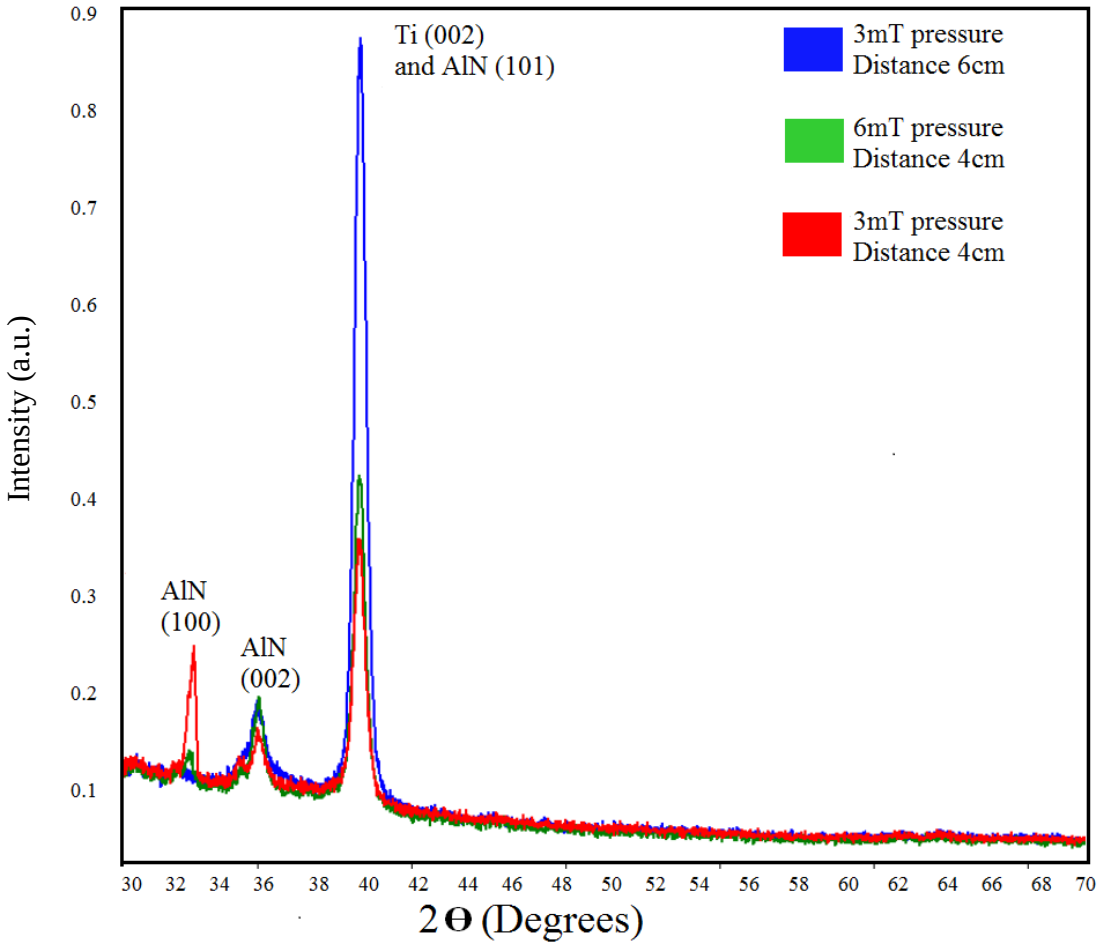


Figure 2.18: Results from RF sputtering

2.6. Material Quality Results from Device Testing

After establishing the required conditions for depositing an optimum film, tests were carried out on fabricated devices based on these conditions. Previous to this the device results were achieved by testing an unpatterned piece of the same wafer on which the devices were fabricated. This is the usual method for determining the quality of the AlN material because the fabricated devices are often too small to focus the XRD on the device and the SEM test is destructive because a cross section of the device is required. However, the ability to test the film quality of an actual device means that the true quality of the devices can be obtained.

The diaphragm devices are shown in Figure 2.19. Both devices were tested. However, it was found that while the smaller device had a large enough surface area to do an XRD, focusing the beam at the device was very difficult and time consuming. The results discussed here are for the larger diaphragm device shown to the front of the picture.

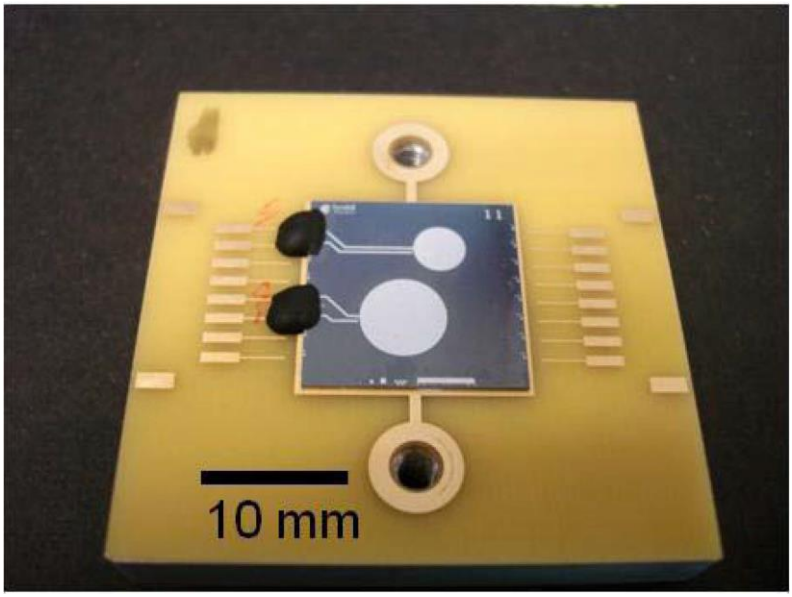


Figure 2.19: Diaphragm Devices Tested for Material Quality

After successfully fabricating the device the capacitance testing was performed. The relative dielectric constant (ε_r) of 9.65 $\pm$ 0.13 was obtained which is comparable to typical values of AlN from the literature of around 9-10. The LDV measurements were taken for three different voltages as explained in Section 2.2 and an average value of 2.25 $\pm$ 0.16m/V for piezoelectric constant (d_{31}) was found. Reported d_{31} results range from 0 up to around 3m/V. This value is usually the most important parameter in determining the quality of the film because increasing the piezoelectric constant increases the movement or voltage response of the device.

The XRD measurement from the 2Θ scan (Figure 2.20) shows two peaks; AlN (002) and Ti (002) and Al (111). No other peaks were visible in the sample which shows that there is a single AlN orientation. A rocking curve around the (002) oriented AlN film was investigated and a FWHM of 3.7° was measured. This result is higher than the FWHM seen for previous wafers but those results were not obtained from the actual device structures.

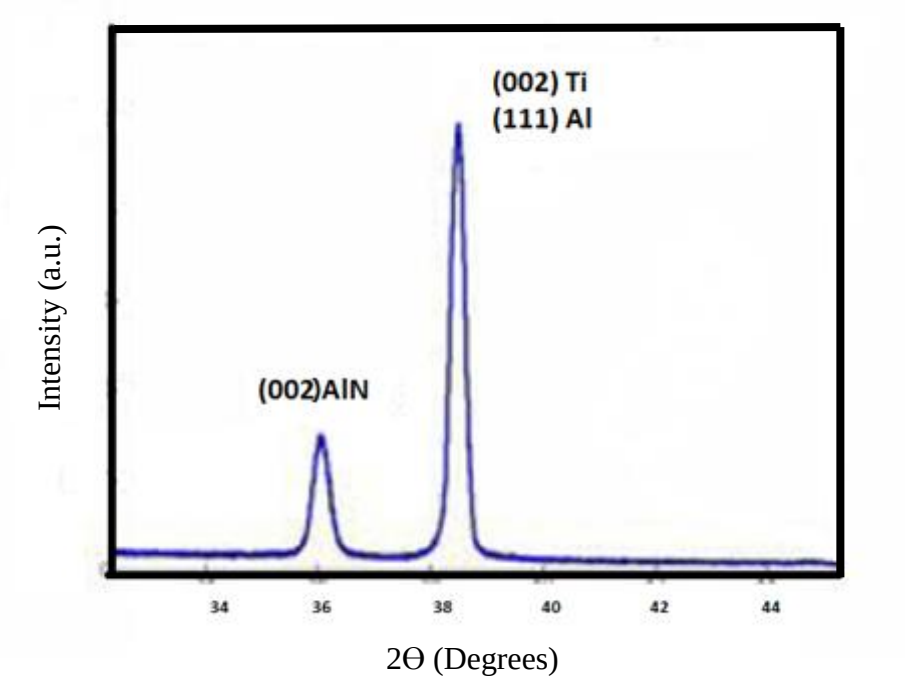


Figure 2.20: 2Θ scan diaphragm device

A cross section SEM image of the multiple layers in the diaphragm test structure is shown in Figure 2.21. The thickness of the different layers can be estimated from the SEM image, which is important for predicting the behaviour of the device and for process control during fabrication. This SEM image is not as clear as previous SEM images examined and this is due to the fact that the surface was polished which resulted in a smearing of the grain boundary; however, the device layers can be seen and from the SEM image the layer thicknesses could be found.

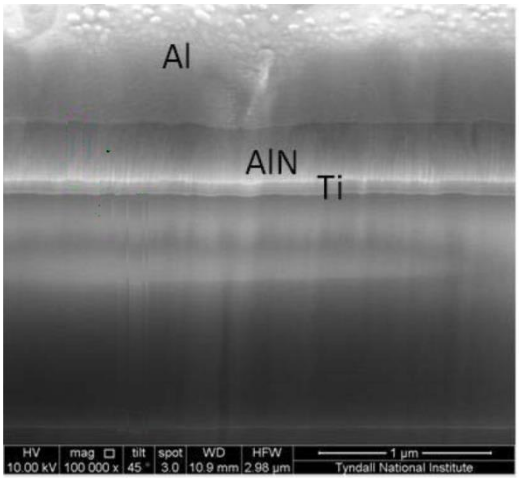


Figure 2.21: SEM image of Diaphragm Devices (cross section)

The results from the EDX are shown in Figure 2.22. The results show that Al, Si, Ti, N and O are present in the diaphragm structure. Oxygen is the only component that would want to be reduced or absent in order to obtain higher quality AlN film. The oxygen may have come from the oxide layer in the material or possibly it was present in the chamber and 100% nitrogen was not achieved. These results show that it is possible to use devices such as these to perform material analysis on AlN films and it could be useful to add these devices to a wafer in order to obtain accurate material properties on device wafers.

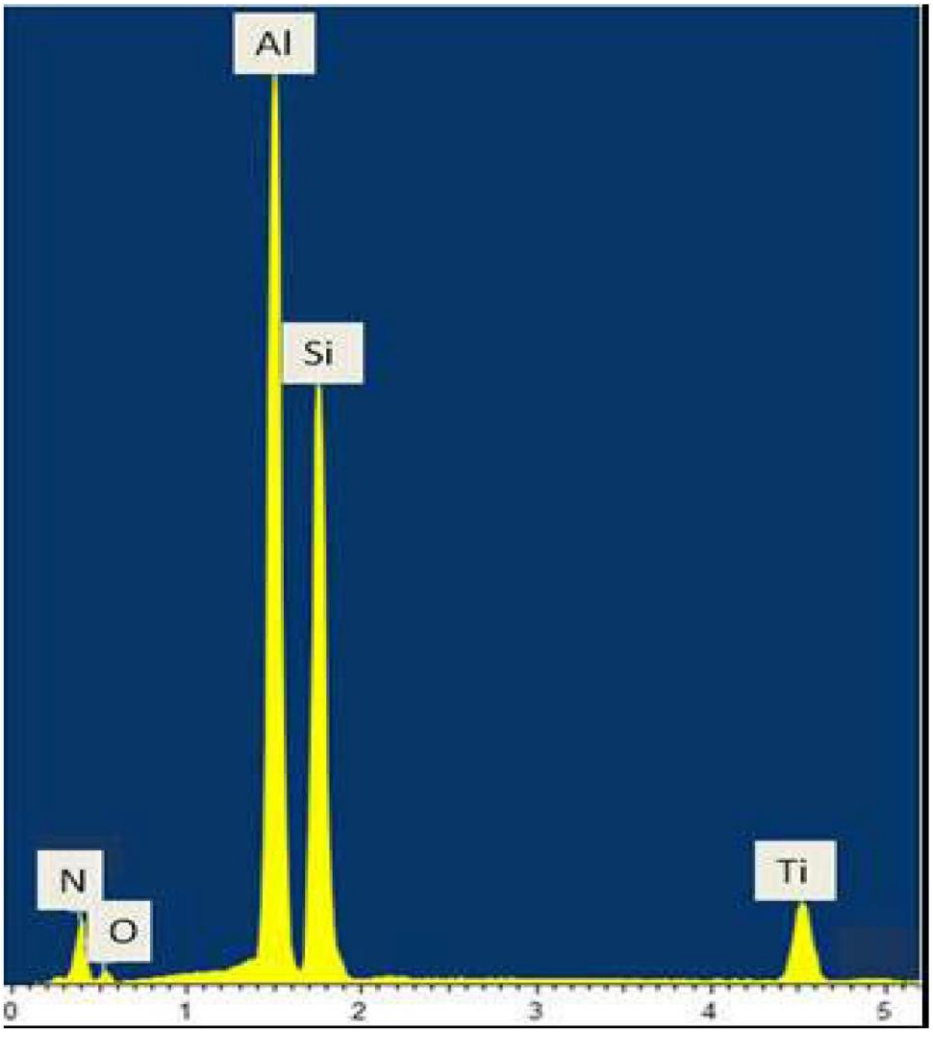


Figure 2.22: EDX analysis of diaphragm structure

2.7. Process Stability Tests

During the course of this work there were a number of gaps between fabricating new devices and test wafers and it was decided to do a series of tests to establish whether the process parameters had changed due to new targets/ machine

maintenance or other factors. To this end a matrix of test wafers was ordered using the process parameters as shown in Table 2.11 and Table 2.12.

Wafer No.	**Deposition Description**	**Ti Deposition Conditions**	**AlN Deposition Conditions**
1	Typical • (100) Si • HF dip • Ti/AlN (100nm/500nm)	• 80% Separation • Pressure 6mTorr • Argon Gas 100% 70sccm • Power 1kW	• Target Separation 50mm • Pressure 6mTorr • Power 2kW • N_2 gas (100% 20sccm)
2	Interlayer (thin) • (100) Si, • HF- dip • AlN/Ti/AlN (20nm/100nm/500nm)	• 80% Separation • Pressure 6mTorr • Argon Gas 100% 70sccm • Power 1kW	• Target Separation 50mm • Pressure 6mTorr • Power 2kW • N_2 gas (100% 20sccm)
3	Interlayer (medium) • (100) Si, • HF- dip • AlN/Ti/AlN (100nm/100nm/500nm)	• 80% Separation • Pressure 6mTorr • Argon Gas 100% 70sccm • Power 1kW	• Target Separation 50mm • Pressure 6mTorr • Power 2kW • N_2 gas (100% 20sccm)
4	Interlayer (thick) • (100) Si, • HF- dip • AlN/Ti/AlN (200nm/100nm/500nm)	• 80% Separation • Pressure 6mTorr • Argon Gas 100% 70sccm • Power 1kW	• Target Separation 50mm • Pressure 6mTorr • Power 2kW • N_2 gas (100% 20sccm)
5	Low pressure and target distance • (100) Si • HF dip • Ti/AlN (100nm/500nm)	• 80% Separation • Pressure 6mTorr • Argon Gas 100% 70sccm • Power 1kW	• Target Separation 30% • Pressure 3mTorr • Power 2kW • N_2 gas (100% 8sccm)
6	Interlayer, low pressure and target distance • (100) Si, • HF- dip • AlN/Ti/AlN (100nm/100nm/500nm)	• 80% Separation • Pressure 6mTorr • Argon Gas 100% 70sccm • Power 1kW	• Target Separation 30% • Pressure 3mTorr • Power 2kW • N_2 gas (100% 8sccm)

Table 2.11: AlN Deposition Test Parameters 2015

Wafer No.	Deposition Description	Ti Deposition Conditions	AlN Deposition Conditions
7	Increased breaks • (100) Si • HF dip • Ti/AlN (100nm/500nm)	• 80% Separation • Pressure 6mTorr • Argon Gas 100% 70sccm • Power 1kW	• 4 12min depositions instead of 3 16min • Target Separation 50mm • Pressure 6mTorr • Power 2kW • N_2 gas (100% 20sccm)
8	Chamber temp ~100°C • (100) Si • HF dip • Ti/AlN (100nm/500nm)	• 80% Separation • Pressure 6mTorr • Argon Gas 100% 70sccm • Power 1kW	• Chamber temp ~100°C • Target Separation 50mm • Pressure 6mTorr • Power 2kW • N_2 gas (100% 20sccm)
9	Chamber temp ~175°C • (100) Si • HF dip • Ti/AlN (100nm/500nm)	• 80% Separation • Pressure 6mTorr • Argon Gas 100% 70sccm • Power 1kW	• Chamber temp ~175°C • Target Separation 50mm • Pressure 6mTorr • Power 2kW • N_2 gas (100% 20sccm)

Table 2.12: AlN Deposition Test Parameters 2015 (Cont.)

The XRD results are shown in Figure 2.23, Figure 2.24 and Figure 2.25 and are summarised in Table 2.13. A wafer using the standard conditions is included in Table 2.13 for comparison. The test wafers were fabricated over a two month time period and the standard wafer was also fabricated during this time to ensure that the comparison is valid. The 2Θ long scan results (Figure 2.23), which are zoomed in so that the smaller peaks would be visible, show that there are extra peaks visible for Wafers 3, 4 and 7. The rocking curve scan results for the AlN (Figure 2.24) and Ti (Figure 2.25) show that the previous analysis still applies to the newer samples and the process is effected by the interlayer and pressure.

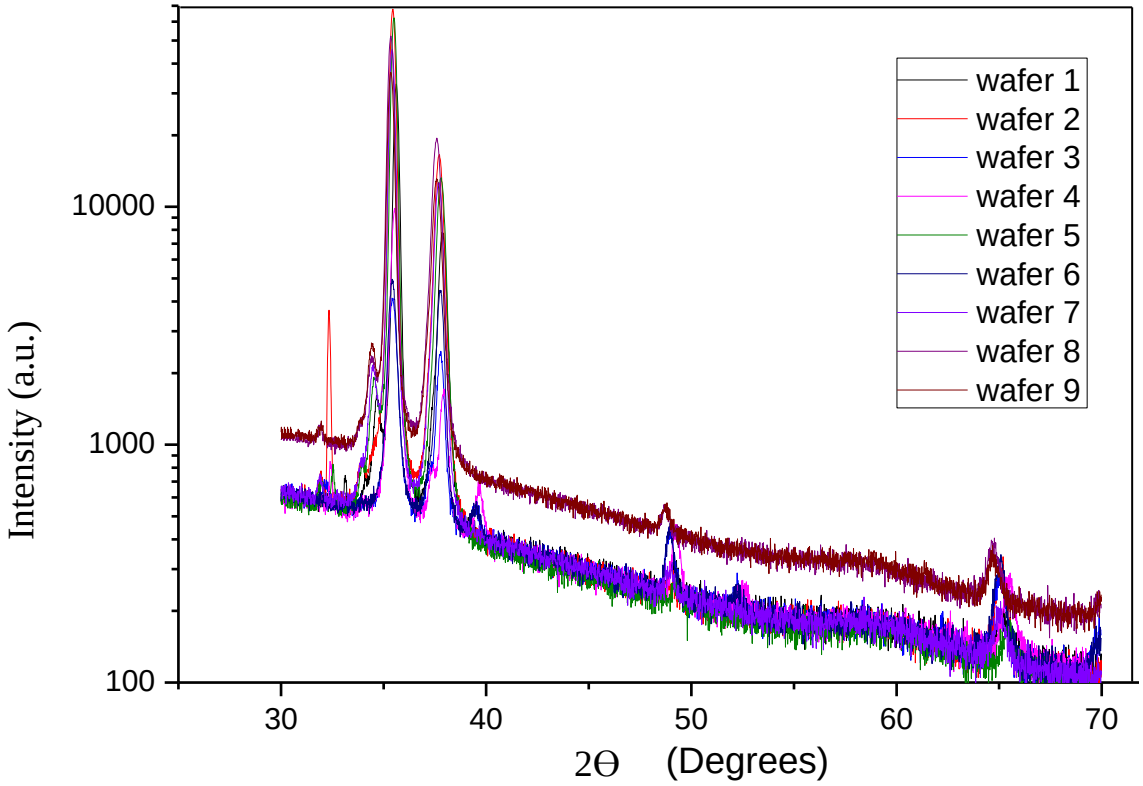


Figure 2.23: Process Stability Test 2Θ Scan Results

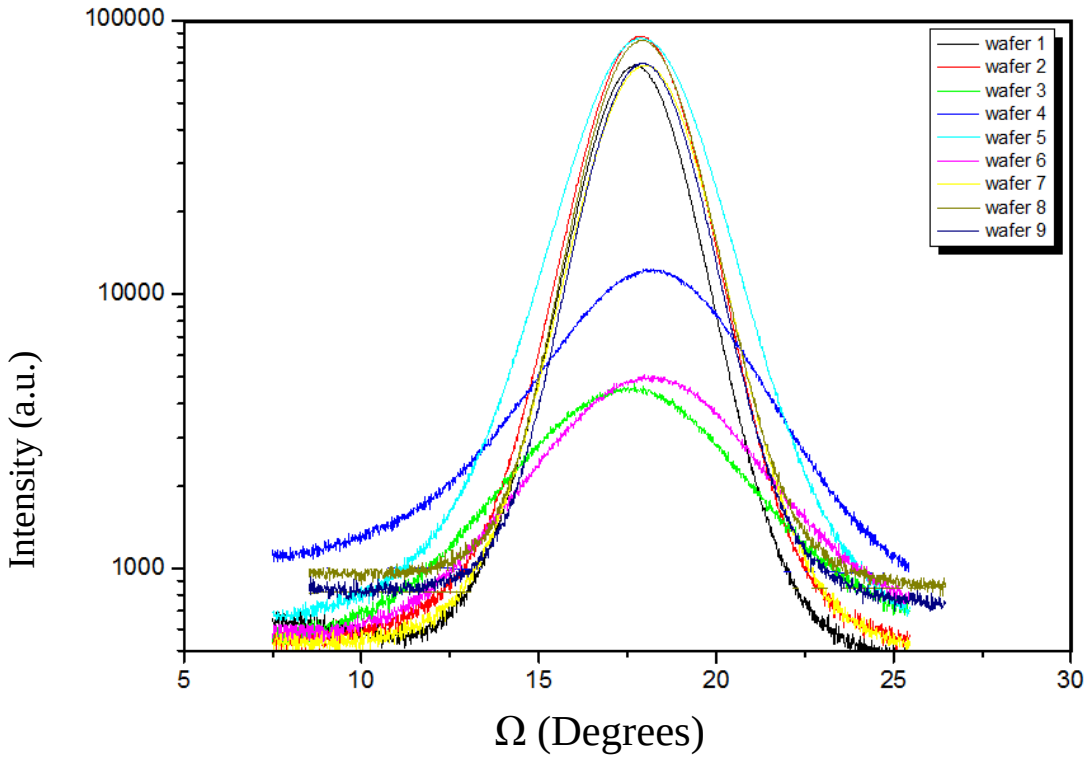


Figure 2.24: Process Stability Test AlN Rocking Curve Scan

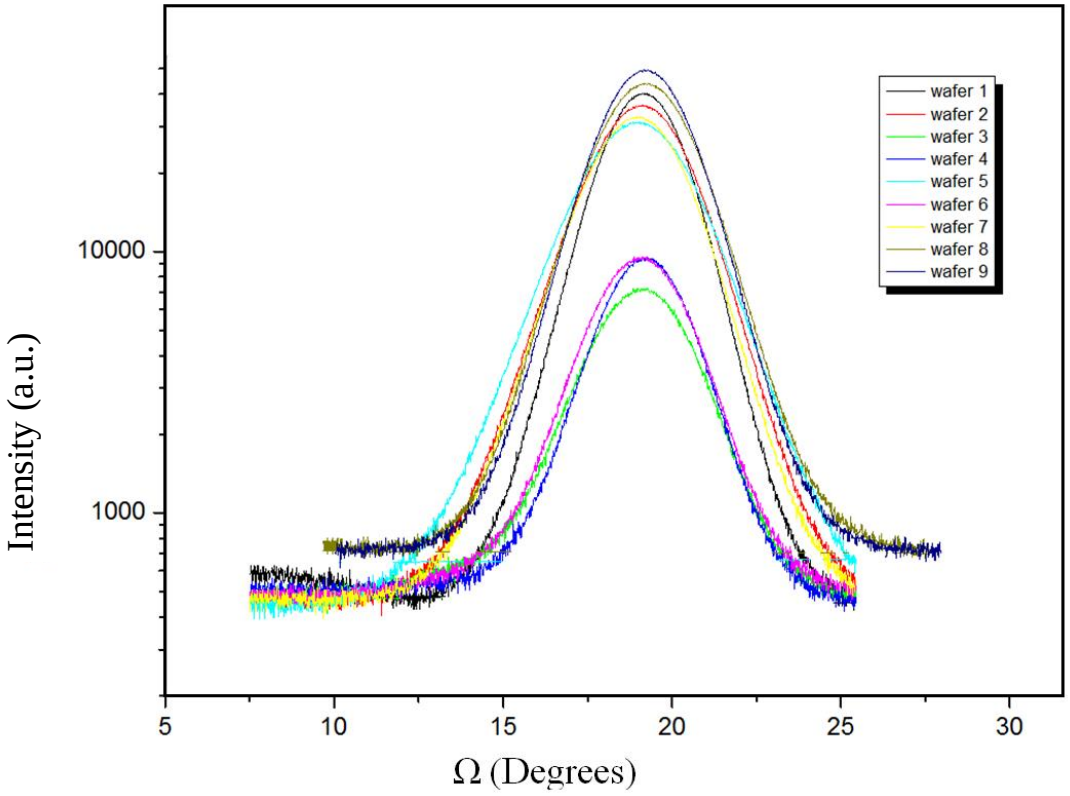


Figure 2.25: Process Stability Test Ti Rocking Curve Scan

Wafer Number	2Θ Scan Extra Peaks	Ti FWHM (Degrees)	AlN FWHM (Degrees)
1	No	2.86	2.44
2	No	3.42	2.58
3	Yes	3.41	5.6
4	Yes	2.99	4.98
5	No	3.85	3.09
6	Yes	3.27	5.43
7	No	3.43	2.68
8	No	3.35	2.58
9	No	3.15	2.54
Standard 2015	No	2.58	2.06

Table 2.13: 2015 Process Stability Test Results

The FWHM of the AlN is bigger than previous values and the quality of the film has reduced. Previous best quality results were 1.5° and from Table 2.13 it is seen that the best FWHM achieved was 2.06°. One further anomaly in the results was seen for Wafer 5 (which followed the previously determined best process). This process was used to grow another test wafer to see if this process no longer produced a good material. The results are shown in Figure 2.26 for a 2Θ long scan and Figure 2.27 and Figure 2.28 show the rocking curve scans for AlN and Ti respectively and the Gaussian fit curves in yellow boxes. These results show that the process is still a good process for deposition of AlN due to the lack of extra peaks. However, the FWHM of the 2.27° is much worse than previously obtained. However, the standard process (which was less destructive to the target) now shows the best results. These results are not as good as previously seen but many standard process wafers have been fabricated and the FWHM is around 2.06° to 2.1°. There are many reasons why the process is not achieving the previous results. Possible reasons include the target has been changed and the machine has been serviced. A usable piezoelectric layer can still be processed. However, these results do highlight the need to periodically test the piezoelectric material quality and to adjust the procedure based on these tests especially when dealing with older equipment.

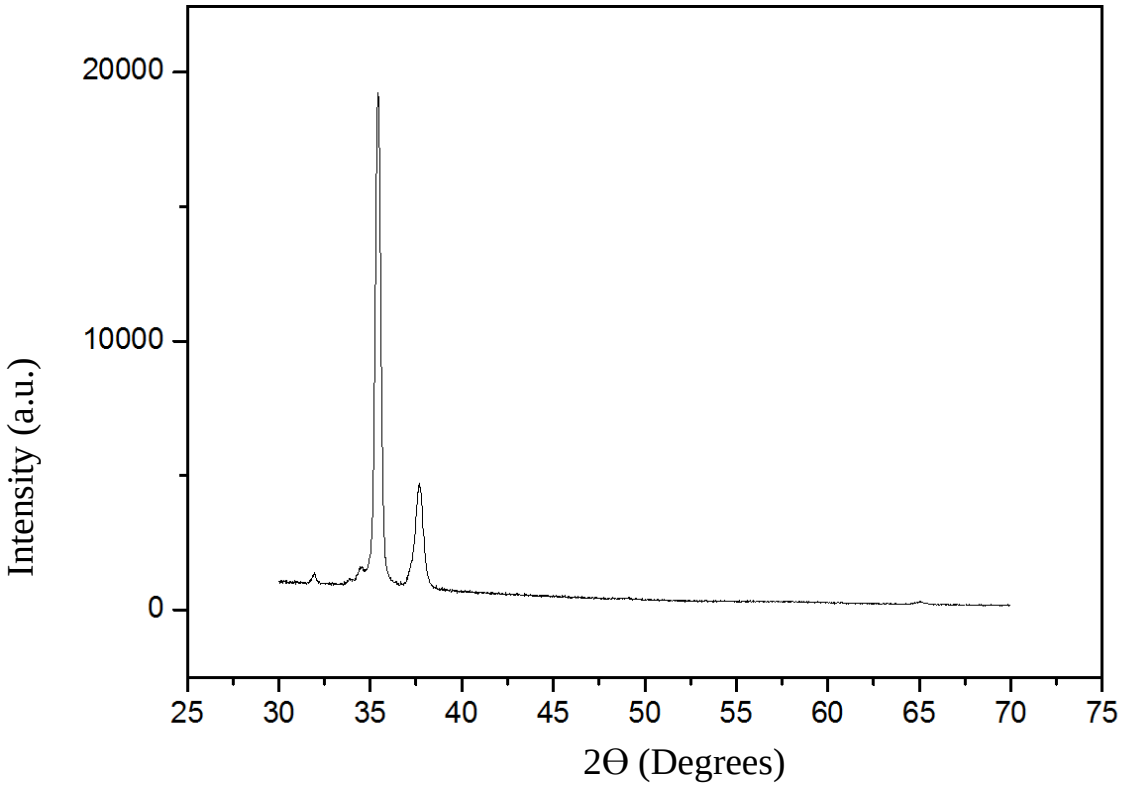


Figure 2.26: 2Θ scan of redo of Wafer 5 (previous best process)

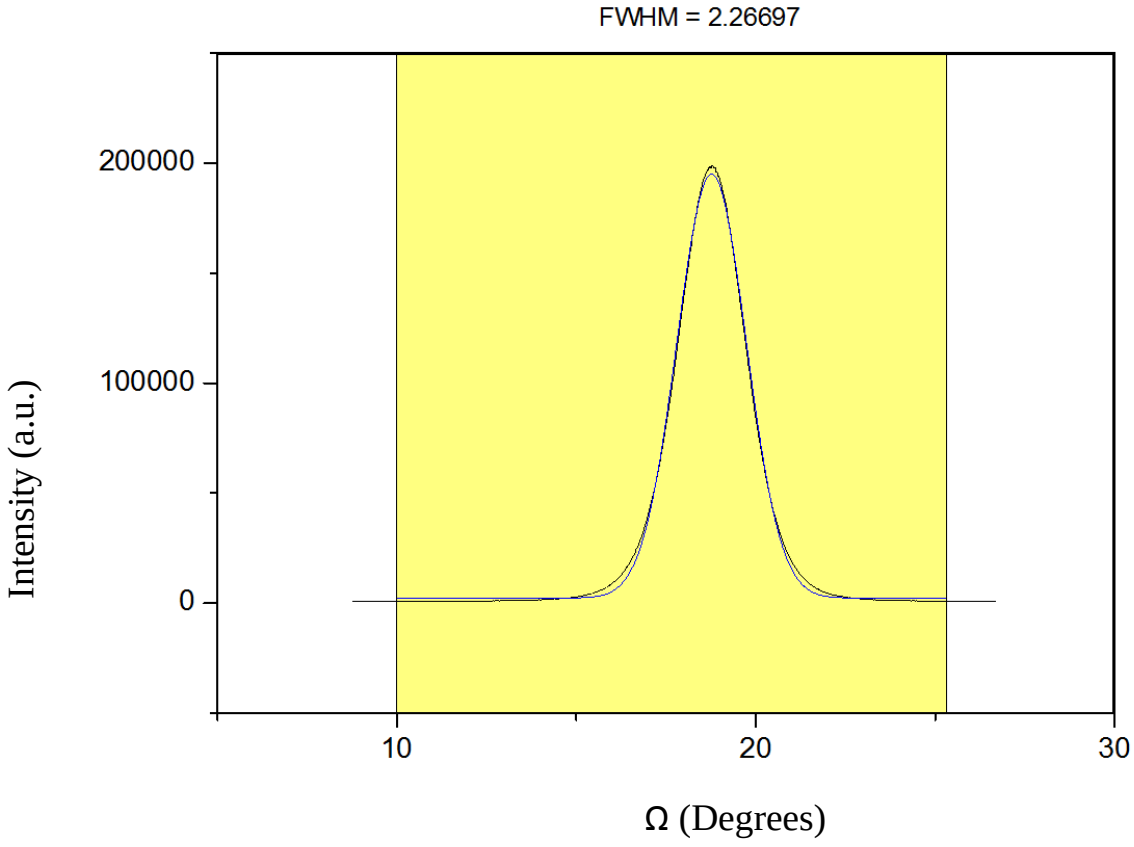


Figure 2.27: AlN Rocking Curve of redo of Wafer 5

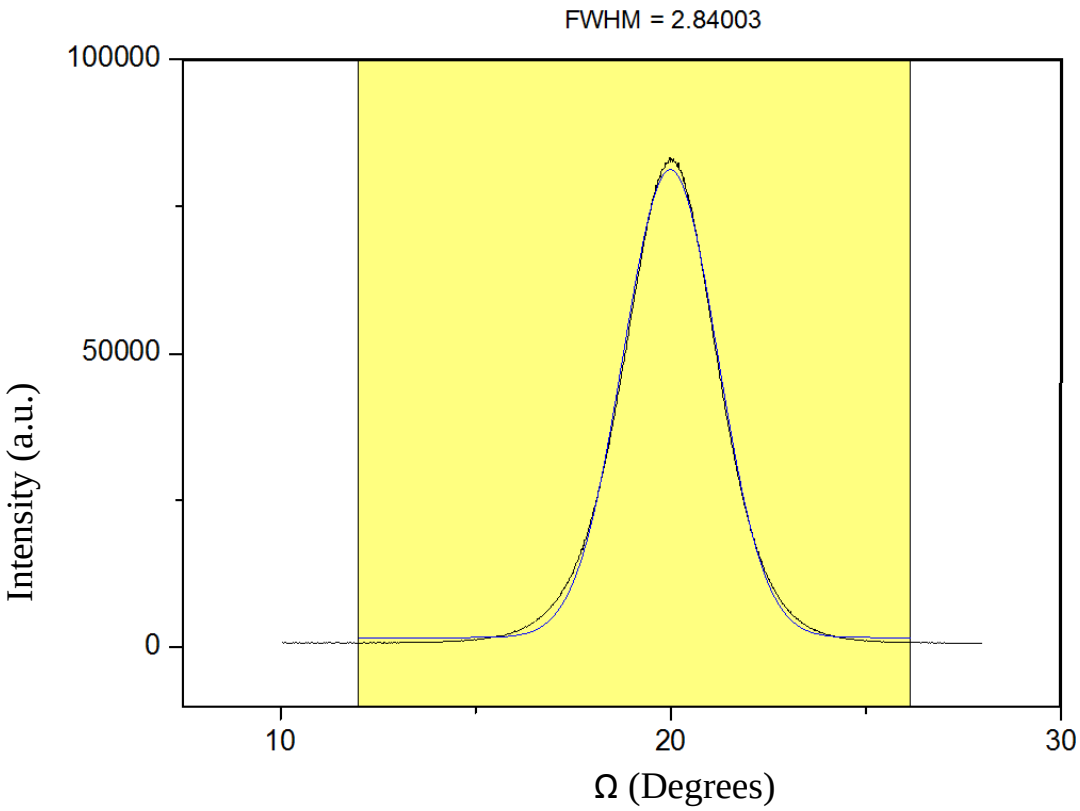


Figure 2.28: Ti Rocking Curve of redo of Wafer 5

2.8. Summary

A process for growing high quality piezoelectric AlN was described in this chapter. A number of different parameters and their effect on the piezoelectric quality of AlN have been examined. Tests were performed on both test wafers (where the material is grown over the whole wafer and no active devices are created) and device wafers (where the wafer is processed to contain MEMS devices). The growth of the AlN layers as well as the processes involved in the creation of piezoelectric devices is also elaborated.

The initial tests identified critical parameters required for obtaining a good quality film and these were investigated by growing a matrix of test wafers changing individual parameters as well as combinations of parameters. These tests included evaluating DC and RC sputtering as well as investigating the effects of power, interlayer and bias. The results provided a great understanding of the AlN material and how to grow it for piezoelectric properties. These tests also identified a previously unconsidered quality which was the effect of other orientations (apart

from the c-axis orientation) on the piezoelectric properties of the film. These results confirmed that single (c-axis) orientation was a critical factor for growing a high quality piezoelectric AlN material and also that XRD was an excellent test method for these films. From the matrix of test wafers it was seen that the best results occur when there is no bias and no interlayer but the power seemed to have very little effect on the result and, in fact, the difference seen is within the precision limitations of the measurement. A best method for AlN growth was identified which would give the highest quality film. However this process was destructive to the target. For the standard process it was decided to set the distance to 50mm and the pressure to 6mTorr because this would mean that multiple wafers could be deposited using the same target.

It was noticed that the FWHM of the AlN film had degraded and this prompted a second round of testing which investigated the critical parameters of the material and process stability. The possible reasons for the change in the film quality are that the target has been changed a number of times due to the high attrition experienced in the AlN deposition process, the sputterer has broken down and been repaired and the standard distance which is set initially in the machine may have changed when this maintenance was performed. Furthermore, there are other factors which could have contributed to this, such as not knowing the exact temperature of the deposition. The sputterer is also used for other processes, involving different materials and these may also be affecting the quality of the AlN film. All of these factors make a case for having a sputtering system that is dedicated solely to AlN deposition. There are a number of factors and unfortunately it is currently impossible to control all of these. These tests have, however, highlighted the issue of machine degradation and its effect on the process and further study is required to determine how best to combat this.

However, it is clear that the quality of the film is still of a high quality and can produce a high quality piezoelectric energy harvesting devices even though the quality of the film is not as high as previously obtained. This means that the film quality is still repeatable and its properties are predicable within a larger range and the optimum process chosen is still producing the best quality available with the current system.

This work has resulted in a number of publications in journals and conferences. Previous work by Sanz-Hervas at al. [87] showed that an AlN film with high FWHM can have a high piezoelectric constant if non-(002) peaks were not present and these results were confirmed by the work here. This work was published in the Journal of Micromechanics and Microengineering [70]. The investigation into the titanium underlayer was also presented at the International Workshop on Piezoelectric MEMS in Switzerland [74]. The design of a test structure which can be tested for piezoelectric material quality was presented at the International Conference on Microelectronic Test Structures in San Diego [88].

Chapter 3:

Finite Element Modelling

3.1. Introduction

In this chapter the use of finite element modelling for designing the energy harvesting devices will be examined. First an overview of simulation techniques will be provided and more specifically the use of the COMSOL Multiphysics [89] tool. The results of models created for this work will then be investigated along with the accuracy of such models when compared to fabricated devices. The initial results from fabricated materials were obtained from devices which were designed for extracting power from a vibrating cantilever in air. These devices were designed to investigate the effect of geometry on the power, resonant frequency and bandwidth response of microelectromechanical systems (MEMS) cantilever based energy harvesting devices and the results were used to inform the designs of the fluid excited devices.

3.1.1. Simulation Approaches

Most papers on simulating piezoelectric devices are concerned with developing the various methods for creating accurate coupled equations between the mechanical and electrical domains. There is also an additional requirement for determining the effects of assumptions made about the resonant frequencies of oscillation and the calculation of power. These methods include modelling the mechanical and electrical systems as electrical circuits with the electromechanical coupling being modelled as a transformer as expounded by Roundy and Wright [90]. This means that the equations that describe the system can be solved using Kirchhoff's current and voltage laws. The cantilever which was modelled is shown in Figure 3.1 and Figure 3.2 is its equivalent circuit.

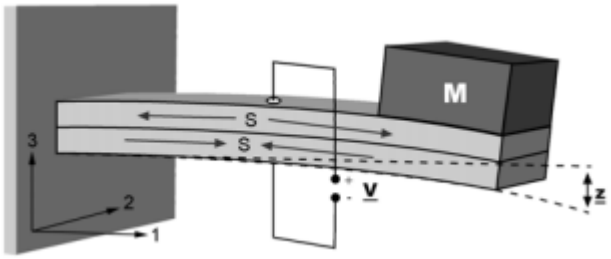


Figure 3.1: A two-layer cantilever. S is strain, V is voltage, M is mass and z is vertical displacement [90]

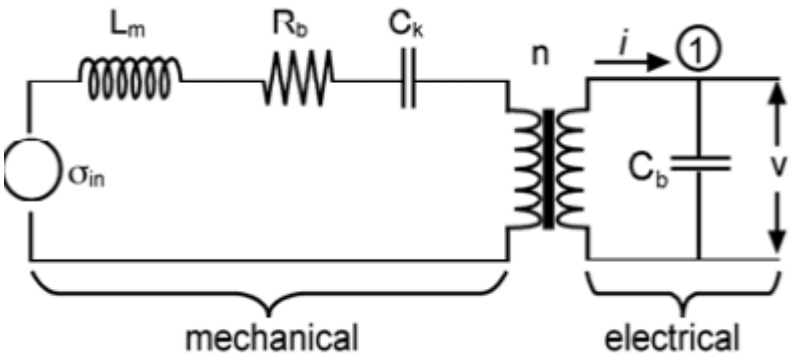


Figure 3.2: Equivalent Circuit of the piezoelectric generator [90]

Another example using FEM in conjunction with the analytical circuit simulation tool SPICE [91] was conducted by Elvin and Elvin [92] where a commercial FEM tool (ABAQUS [93]) is combined with SPICE to investigate the effect on a device from the coupling between the electrical and mechanical structures. The beam is generally approximated using the Euler-Bernoulli beam theory [25]. This theory is a

simplification of the linear theory of elasticity. It is a method of calculating the deflection and load carrying characteristics of beams for small deflections and lateral loads. Modelling the beam for its electrical-mechanical coupling is useful for investigating the power capabilities of the MEMS devices. This will be discussed in this chapter.

A further example of FEM is optimising the material properties of a device using FEM and a genetic algorithm (GA) as can be seen in the work of Farnsworth *et al*. [94]. A genetic algorithm inserts a mutation into the system (in this case changing a material property) and then propagates this mutation over various generations to see if it leads to an improvement or a degradation in performance. In this case COMSOL is used along with a GA to determine the resonant frequency of the device. Other FEM analyses of the beam in use are found in the work of Ekeom and Buchaillot [95] where FEM and a three dimensional numerical model were developed and Xin *et al*. [96] where static FEM computation is utilised. Using a commercial FEM tool has many of advantages and the choice of COMSOL Multiphysics will be discussed in the next section. Understanding how the resonant frequency and bandwidth of a cantilever are affected by various physical parameters is a large part of the work.

3.1.2. COMSOL Multiphysics

COMSOL Multiphysics is a finite element modelling program. It uses partial differential equations (PDEs) to create a model of a system. These equations can be user defined within COMSOL or alternatively there are a number of predefined modules which are available containing the standard PDEs required for specific analysis such as fluid dynamics and piezoelectric materials are also provided. This is illustrated in Figure 3.3. Both 3D and 2D modelling is possible using this program and modules can be combined by the user; that is, a device can be studied for its effect on fluid flow as well as its piezoelectric response to the flow by using two separate modules and coupling the output of one as an input to the second. There are also combinational modules, such as fluid structure interactions, which means that this coupling can be done by the software and in this way fully coupled models are possible. The modules which are used in this work are highlighted in yellow and the various physics and studies of these modules are also shown.

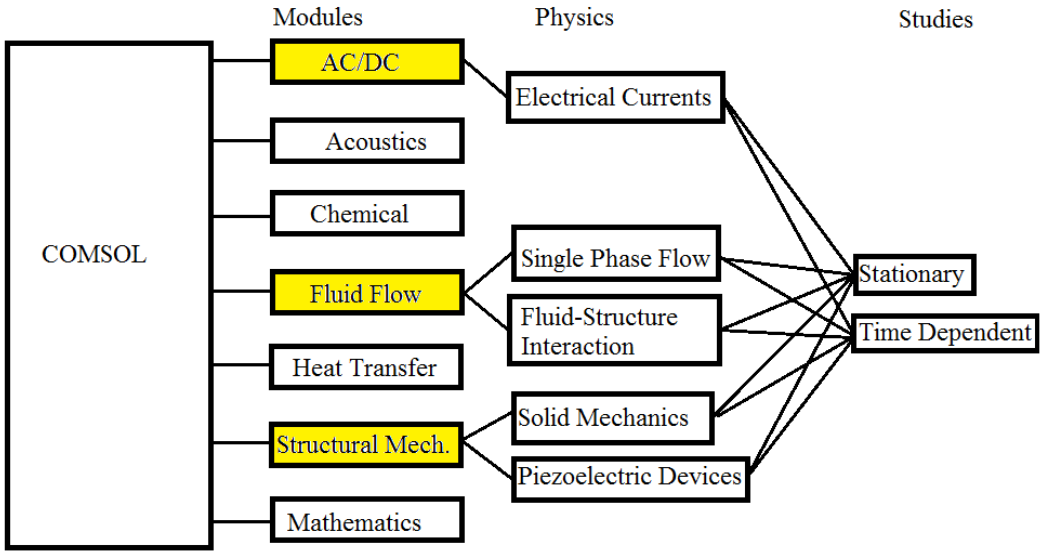


Figure 3.3: COMSOL overview

A number of iterative and direct solvers are also available within COMSOL. Direct solvers can be memory intensive because the problem is solved directly. However, iterative solvers first find an approximate solution and this is then improved with each iteration until the error is within the defined tolerance. This is not as memory intensive but can be very slow and needs to have a good preconditioner to get a good first approximation. Often, the best solver for the model will be chosen automatically by COMSOL, based on the amount of data entered, the analysis type and the information required. This functionality, as well as the ability to analyse the results in many different ways, such as through traditional line graphs, surface plots etc., makes COMSOL an ideal choice for the simulations to be performed in this work instead of numerous other programmes such as Nastran [97] or FlexPDE [98]. COMSOL is also user friendly because it uses a graphical user interface (GUI) and this ensures that models can be created easily. For more complex models it is also possible to create the model in another programme such as SolidWorks [99] and input this model for simulation and analysis. Also a link with MATLAB [100] is available for performing calculations based on the outcomes of the simulations.

3.2. Confirming Model Accuracy

A number of piezoelectric MEMS devices consisting of aluminium nitride (AlN) grown on a silicon (Si) wafer were fabricated. Figure 3.4 shows a wafer of the fabricated devices. This wafer includes cantilevers, wide beams and triangular

beams as well as more unusual devices. These MEMS devices were designed to be tested and compared to the finite element models (FEM) created using COMSOL Multiphysics. In order to simplify the process the mechanical structure was simulated before the active layers were added to predict performance. Comparing the fabricated results to FEM meant that the FEM accuracy could be determined. Once a calibrated simulator is available it becomes possible to inform future device designs. Initial tests, which modelled the devices in the absence of the AlN and dielectric films, provided the resonant frequency of the MEMS devices which was then compared to the results of fabricated devices. Figure 3.5 shows the initial results; the devices are labelled 1 to 12 as an example of different types of devices that were tested (this is true for the devices in Figure 3.6 also). What is important to note here is the fit between the modelled and the measured frequencies.

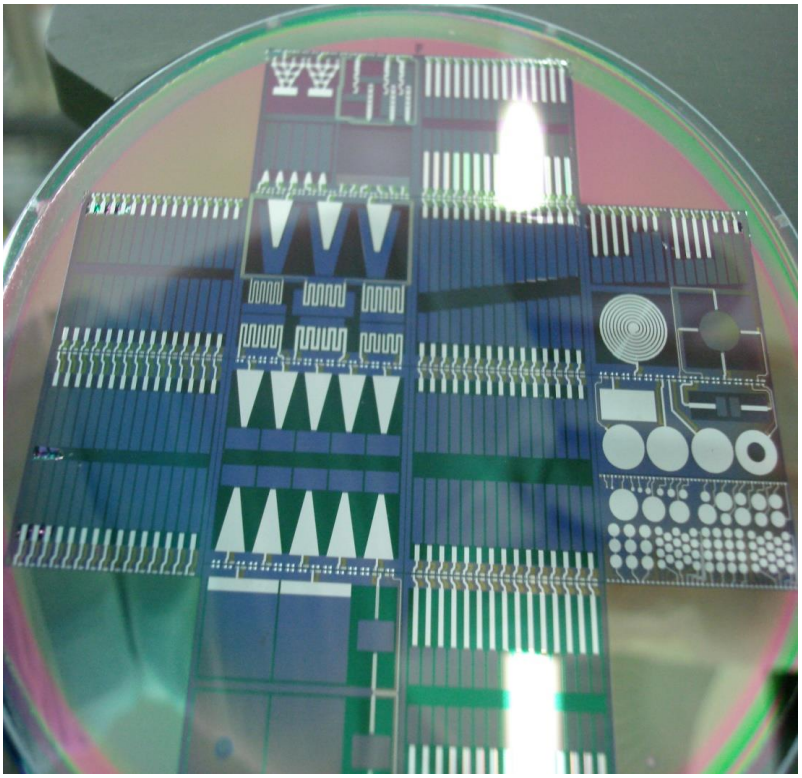


Figure 3.4: Wafer of fabricated Devices

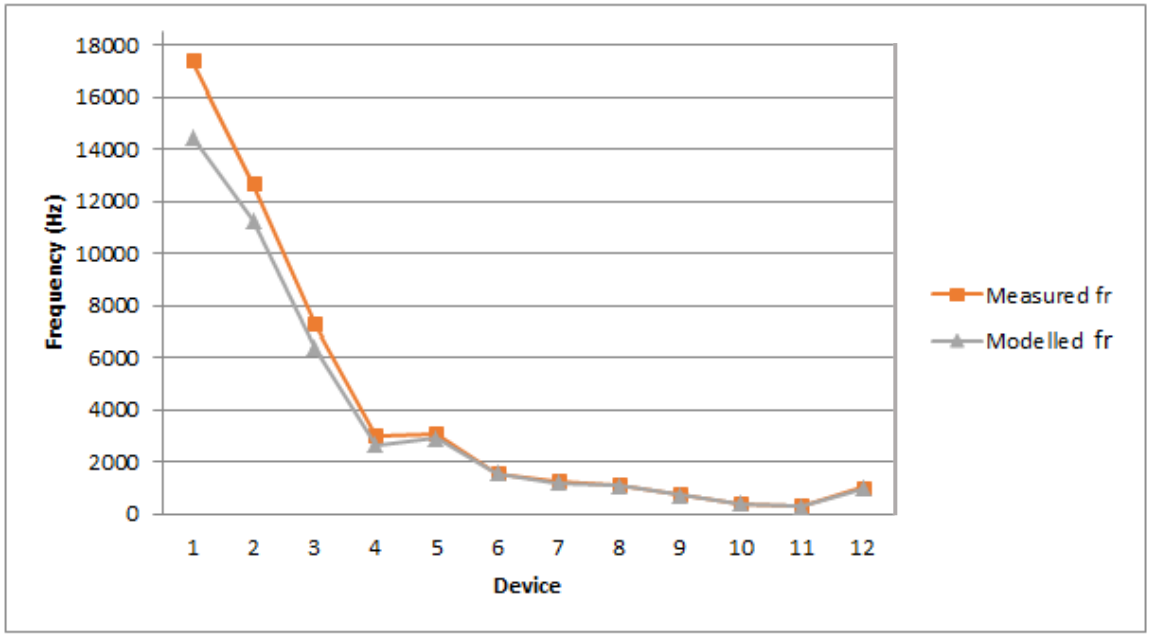


Figure 3.5: Initial Resonant Frequency Results

Figure 3.5 shows the results of the simulations in comparison with measurements made on the devices shown in Figure 3.4. Each device, simulated and measured, (1 – 12) is designed to operate at different resonant frequencies using formula (1.2) on page 9. For these calculations the mass was assumed to be a point mass and it was found from comparing the resonant frequency results of the fabricated devices to the results of this equation that this was not an accurate calculation of resonant frequency for these devices. The fabricated devices were tested using the LDV process previously discussed where a frequency sweep was applied to a speaker and the maximum deflection was measured. From the initial results a maximum discrepancy of 16.8% between the measured and modelled results was calculated. After optimising the model to better correspond to the measured results and improving the fabrication process of the devices another comparison was completed and from the results, shown in Figure 3.6, an improvement to a maximum error of 4.4% was achieved. Of interest here is device Number 12. All of the devices in this fabrication run were designed to operate between 80 and 120Hz. However, Device 12 is shown to have a resonant frequency of 22Hz and this is because it was designed and laid out as a doubly tethered beam but during fabrication one of the tethers broke. The model of this device was then re-run as a singly tethered device with the same dimensions as the broken Device 12

and the resonant frequency result from the model was 21.4Hz. This shows that the models are accurate when compared to real devices operating in air.

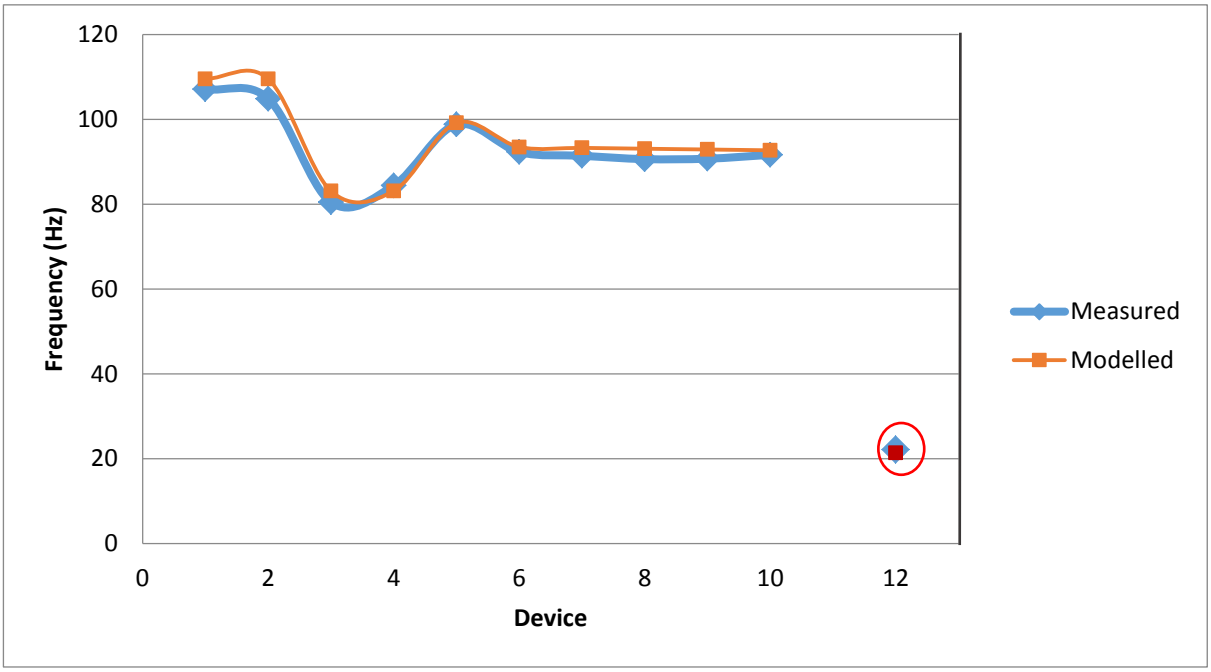


Figure 3.6: 2nd Generation Frequency Results

3.3. Broadening the Frequency Response

As discussed in Section 1.2.1 the bandwidth of the frequency response of the devices can be a critical feature. It was shown in Section 3.2 that devices can be modelled to predict the measured resonant frequency with a high degree of accuracy; however, the bandwidth of the frequency response of the MEMS devices was found to be very small (~1Hz). This means that even small differences from the expected frequency (which arise from variability in process tolerances in fabricated devices) could mean that the device will not work at the appropriate (design) frequency. Increasing the broadband response of the devices would mean that devices would operate over a wider range of frequency and the shifts away from the design specification seen in processed devices would not be so critical. To this end a number of different methods for increasing the bandwidth of the structures were examined. There are a number of factors which make this problem particularly challenging; firstly, low resonant frequencies are the subject of this work. However, the objective was to broaden the bandwidth without increasing the frequency. This is difficult to achieve with a combination of AlN and Si which both have high Young's modulus. Secondly, the Q factor (Q) of the device (i.e. the height of the

maximum deflection at resonant frequency which corresponds to maximum power output) is related to both the frequency and the bandwidth by:

$$Q = \frac{f_r}{\Delta f} \qquad (3.1)$$

where f_r is the resonant frequency and Δf is the bandwidth. From this equation it is seen that if the resonant frequency is kept the same but the bandwidth is increased then the Q factor is reduced. Here methods of increasing the bandwidth while maintaining a high Q factor will be discussed. Two methods will be discussed; the first is by broadening the bandwidth through layout and device geometry. The second is by using arrays of devices with a small frequency difference between each device.

3.3.1. Device Geometry for Bandwidth Broadening

Two methods for broadening the bandwidth response by altering the device geometry are discussed here. A number of resonant frequency modes are present in a material and when the resonant frequency is referred to in this work it is the first mode that is being addressed. However, the higher modes also produce a deflection (which is usually smaller than the first mode). If these modes could be brought closer together then, while the individual bandwidth of the modes would not be increased, the device could operate over all the frequencies in the range of the overlapping modes. This theory is shown in Figure 3.7 where the multiple modes, which don't overlap, are seen and Figure 3.8 which shows the effect of the overlapping modes.

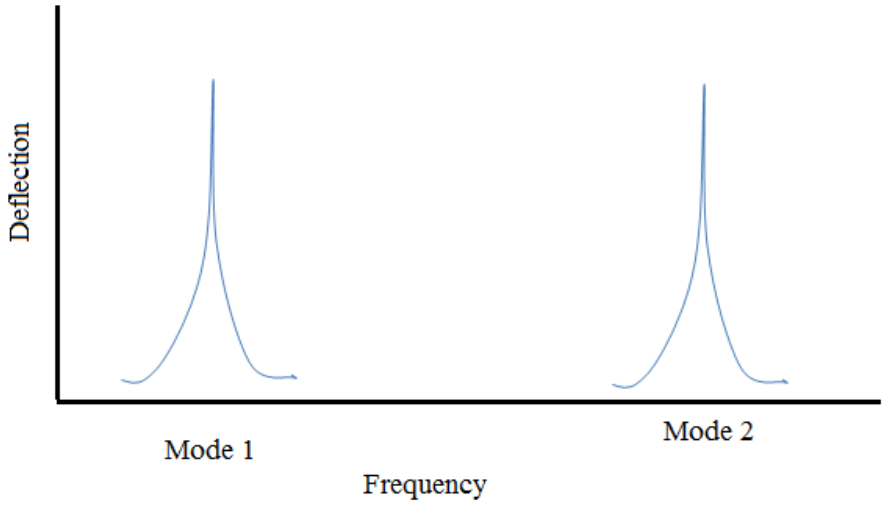


Figure 3.7: Example of multiple modes of resonant frequency of MEMS devices

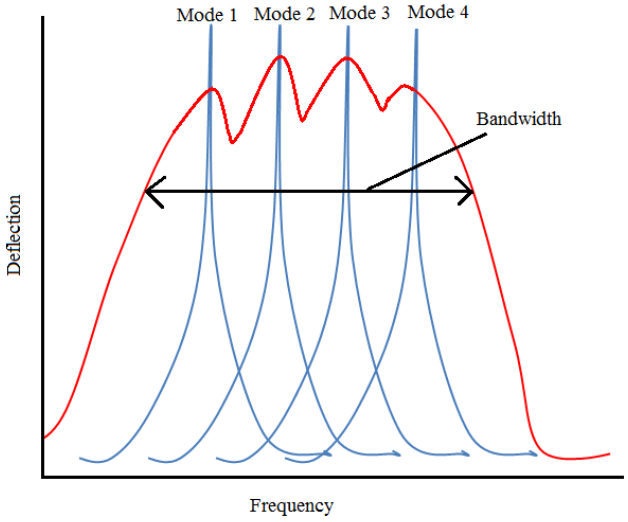


Figure 3.8: Example of increased bandwidth response with overlapping modes

To achieve this effect many different studies were conducted. In these studies a traditional cantilever design with known frequency is used and the effect of the changes in respect to the first two modes of vibration is examined. The first study examined the effect of a gap in the beam of the cantilever. This is shown in Figure 3.9 where the gap begins at the anchor (fixed) point and the length is increased along the length of the beam up to the mass and the gap width is extended from the centre of the beam to the outer edges so that the beam width is the same on both sides of the gap. In this image the colour variation shows the stress in the device with dark blue being the lowest stress and dark red the highest stress.

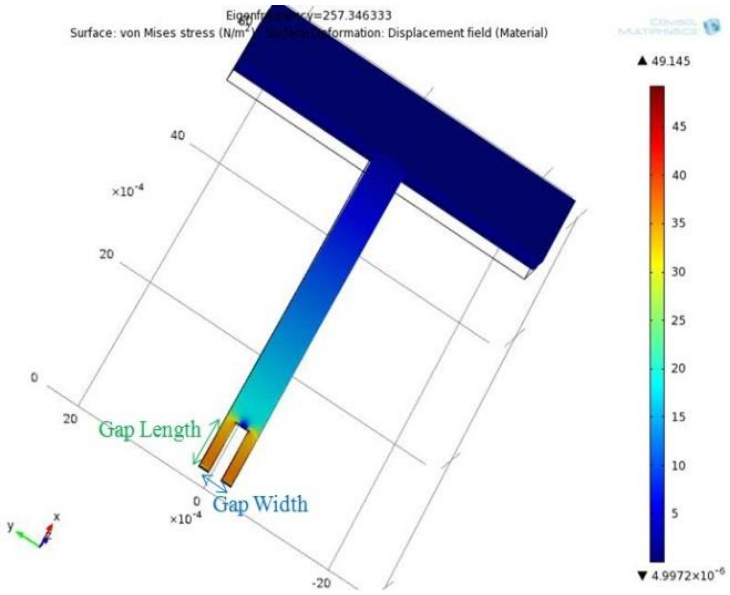


Figure 3.9: Cantilever with Gap on beam at anchor point. Colours indicate stress (in N/m^2) with red indicating maximum stress.

Figure 3.10 and Figure 3.11 show the results of these investigations. For the gap length there is a noticeable reduction in the difference between the resonant frequencies of the first and second modes for a gap of 5mm (which is the full length of the beam). The difference between the modes is still significant and it certainly doesn't fall within the 1Hz difference which would be required for multiple modes to overlap. The results for widening the gap are even less encouraging even though a drop is seen for a gap width of 0.45mm which is the maximum width allowed. This is partly due to the limited width specification of the device (500µm) but in any case increasing the width of the beam would also increase the resonant frequency of the device. Even with a combination of maximum gap width and maximum gap length the resonant frequencies of the modes remained hundreds of Hertz apart and removing this amount of the beam would also decrease the volume significantly which was shown from Equation (1.1) to affect the electrical storage for a device with the active layers.

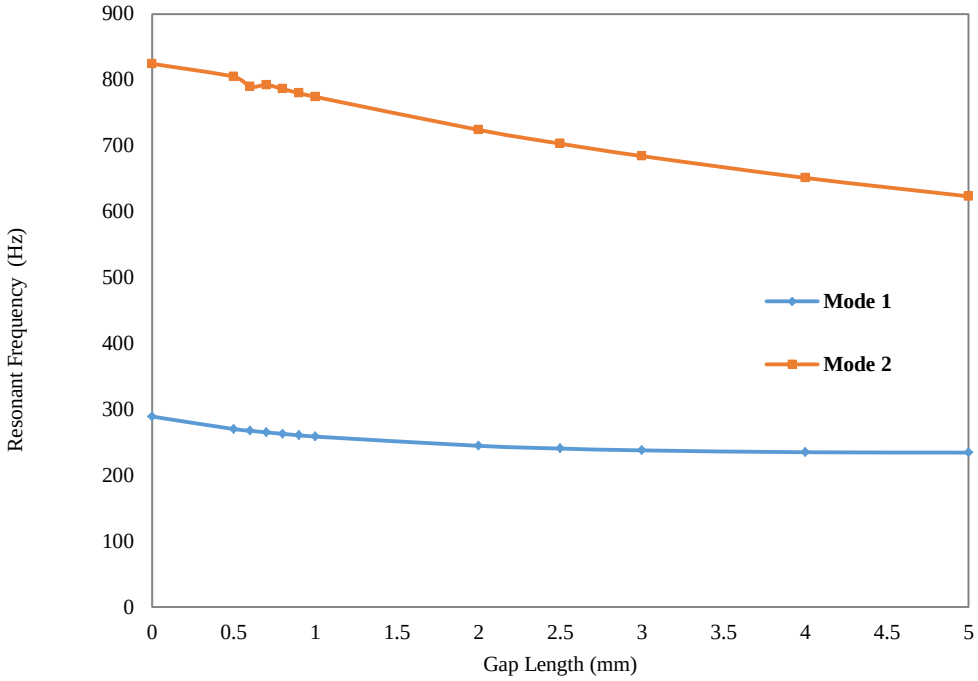


Figure 3.10: Resonant frequency vs. Gap length for Modes 1 and 2

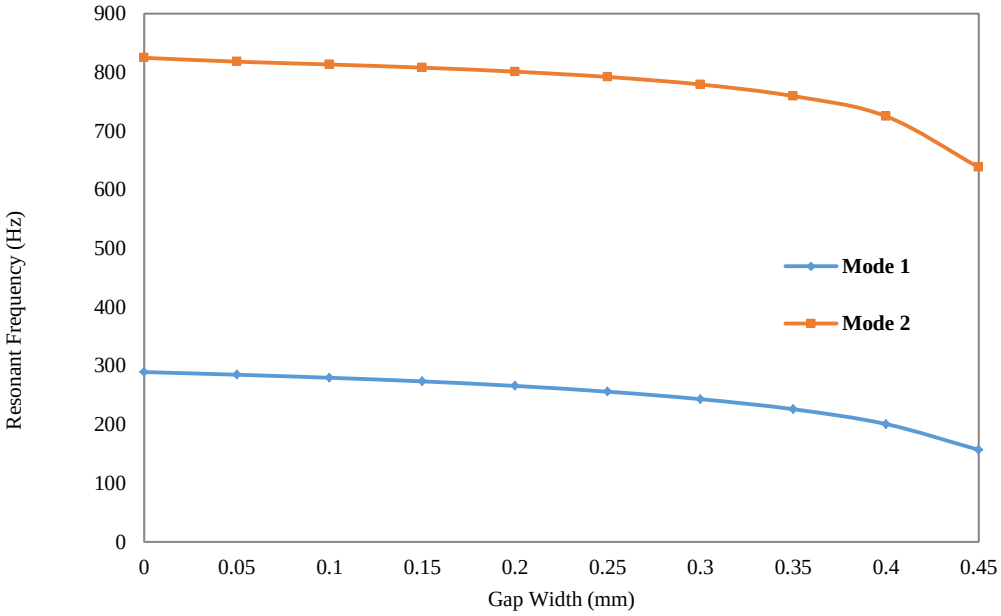


Figure 3.11: Resonant frequency vs. Gap width for Modes 1 and 2

These results can be compared to a structure with a spring at the anchor point (Figure 3.12) which was designed to activate the two modes simultaneously. Using this design the difference between Modes 1 and 2 was 207Hz which was the best

result obtained but this result confirms that this method cannot be used for devices with 1Hz bandwidth.

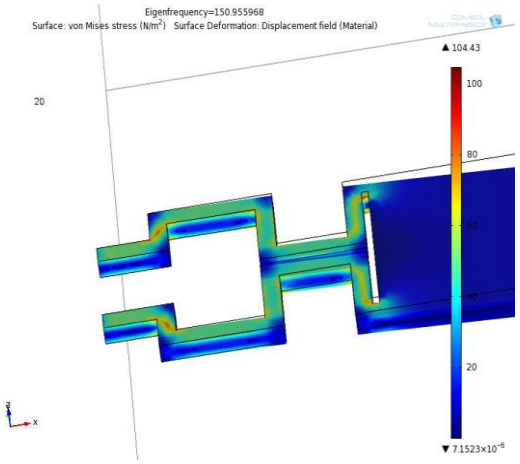


Figure 3.12: Cantilever beam with spring at anchor end. Colours indicate stress (in N/m^2) with red indicating maximum stress.

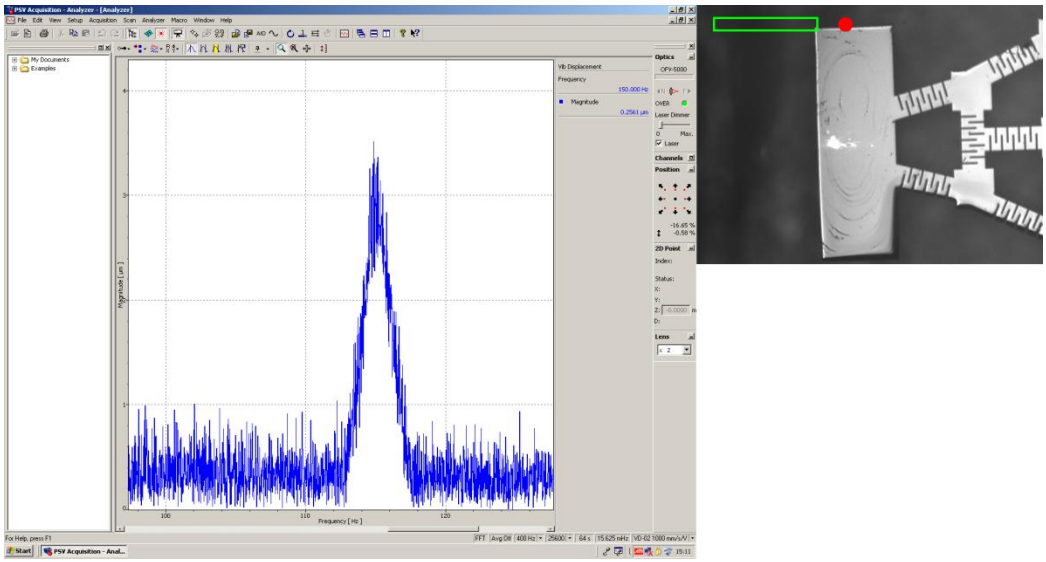


Figure 3.13: Spring network device LDV result

Another method to widen the bandwidth is to design novel structures with a wider bandwidth by using many springs as well as other designs. Figure 3.13 and Figure 3.14 show the results of LDV analysis on two devices using multiple springs. The LDV output is shown on the left in blue and the device is seen in the top right corner. The springs allow for more twisting and bending which brings the modes together and increases the bandwidth of the device. A schematic of the diaphragm with 4 springs is also provided in the bottom right. The spring network device (Figure 3.13) had a bandwidth of 4Hz centred at 115Hz and the diaphragm with 4

springs (Figure 3.14) had a bandwidth of approximately 30Hz centred at 450Hz but with a resonant frequency of 470Hz which is much higher than the targeted resonant frequencies and in both cases the power which could be extracted would be very low because using a spring system reduces the active piezoelectric device area to the surface area of the springs and therefore, the available area for piezoelectric material is very limited. It was also seen that the displacement of these devices was much smaller than that for the more traditional devices and this would also affect the power which would be available from it.

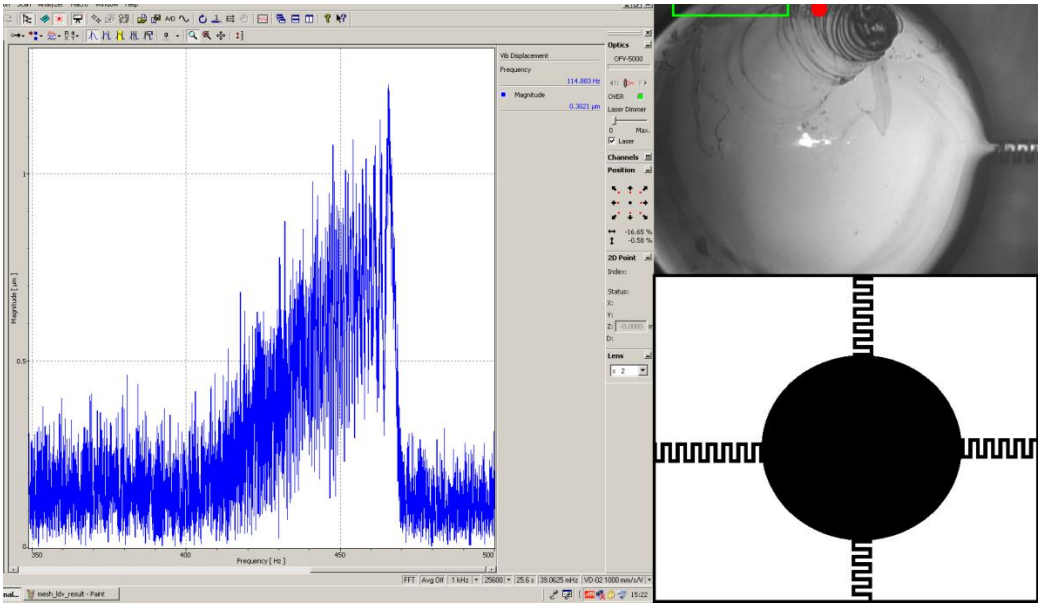
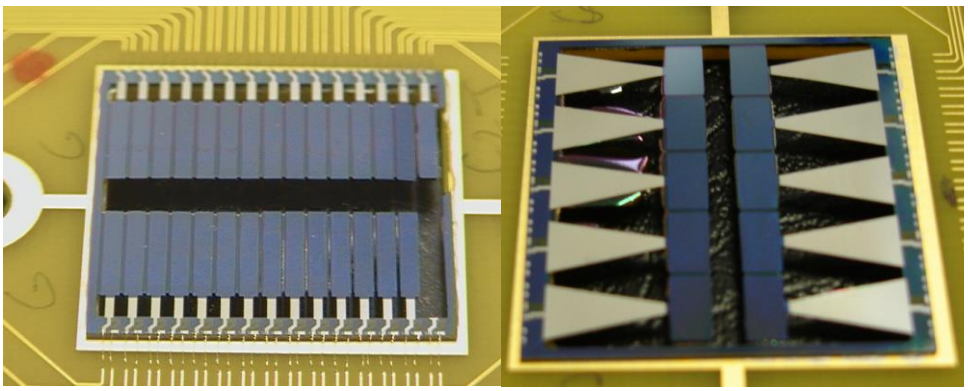


Figure 3.14: Diaphragm with 4 springs device LDV result

3.3.2. Device Arrays for Bandwidth Broadening

From the results in Section 3.3.1 it was seen that it is not feasible to move the first and second modes close enough to overlap and broaden the response. It was also shown that using multiple springs to tether the devices will produce a broadened frequency response but the reduction in the active region of the devices would mean that piezoelectric structures of these designs would not produce enough power to be useful. To address both of these issues, broadening the bandwidth by using an array of devices with a small frequency difference between each device was investigated. This is the same idea that was described in Section 3.3.1 but instead of using multiple modes of one device a single mode (Mode 1) of many devices are used. Figure 3.8 also illustrates this idea if each mode is considered to be a device. FEM simulations of cantilever type devices were created by varying the width and length

parameters of the devices to produce a 1Hz difference between each device. Figure 3.15 shows two examples of these arrays and Figure 3.16 shows a comparison of measured and modelled results for the traditional cantilever devices (a).



(a) **(b)**

Figure 3.15 Fabricated arrays of devices (a) traditional cantilevers (b) triangular beam cantilevers

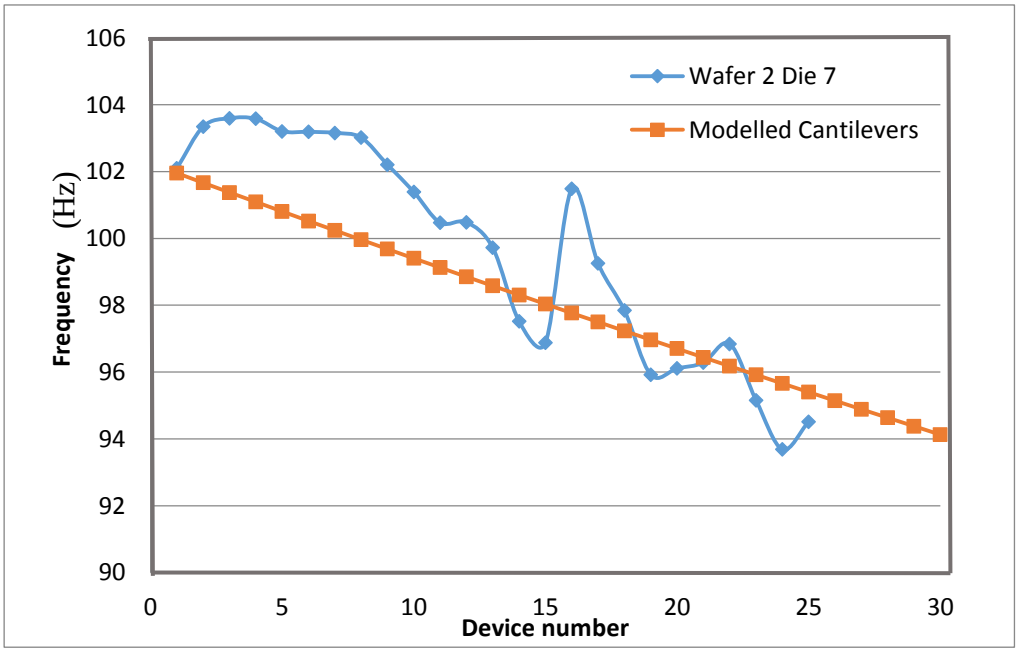


Figure 3.16: Frequency vs. mass length for modelled and fabricated cantilevers

Figure 3.16 shows the frequency result by mass length for modelled and fabricated devices. The mass length of the fabricated cantilevers was not measured so the mass lengths for these devices are based on the expected mass length for comparison. These results show that there is a discrepancy between the measured frequencies vs. those expected from the models. The devices were designed to have

a linear frequency range from 102Hz to 94Hz with a maximum of 0.5Hz difference. The fabricated devices do show an approximately linear dependency but the transition is not as smooth as the devices were designed to be and in some cases the difference in frequencies between adjacent devices would be outside the bandwidth of the devices. This was due to issues with the fabrication process which meant that some devices had more Si remaining on them than expected. The error bars for the frequencies of the fabricated devices could not be calculated because the fabrication errors were different for each device. Figure 3.17 shows how these process precision issues affect the device with areas of additional Si highlighted with red circles. This extra Si affects the resonant frequency because they increase the area of the device. However, a large number of the devices could still be tested for broadband response because the frequencies were within 1Hz of each other.

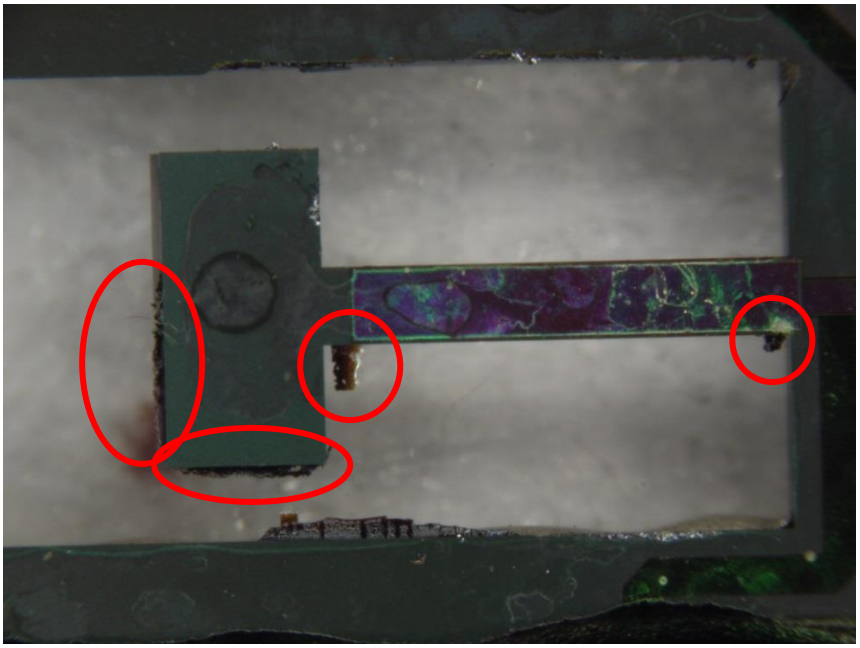


Figure 3.17: Fabricated device with silicon under etch

Figure 3.17 is the voltage response (measured by exciting the devices with a frequency sweep and reading the voltage between the top and bottom electrodes on a multimeter) vs. the frequency for 3 adjacent triangular beam cantilever devices from Figure 3.15(b). The voltage output from connecting each device is shown in purple, green and red for 3 different devices. The blue line corresponds to the voltage output of the three devices when a frequency sweep is applied to activate each device. From this result it can be seen that by using an array of devices a number of

frequency responses can be added together and the overall result provides more voltage as well as a broader bandwidth.

Three methods of broadening bandwidth have been examined and from the results it is seen that the only viable method is to use an array of devices each with overlapping frequency responses. This has consequences for the efficiency of the array per unit area because only one cantilever will be working at a specific frequency despite a lot of other silicon devices being present. These devices take up space but aren't functioning at that frequency.

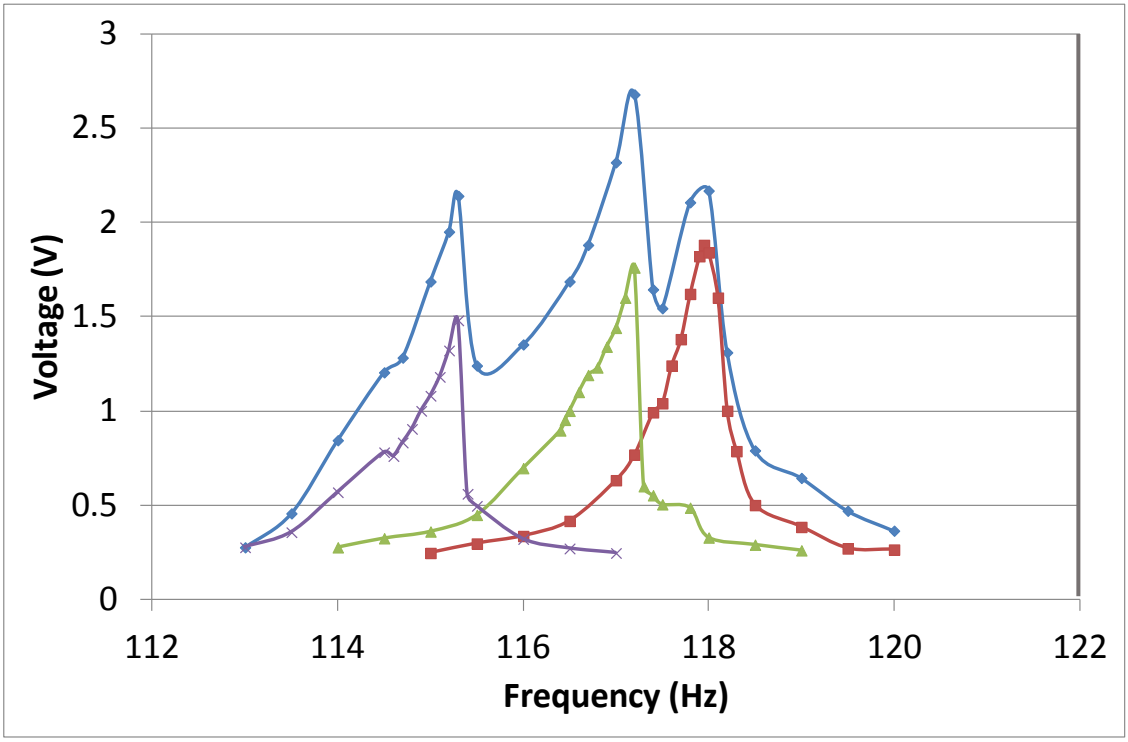


Figure 3.18: Output voltage vs. frequency for 3 triangular beam cantilever devices

3.4. Power Output Modelling

Previous work discussed in this chapter investigated the resonant frequency of the devices. The voltage output from some fully fabricated devices was shown in Figure 3.18 but otherwise the piezoelectric quality was not addressed. In this section modelled and fabricated devices are examined for the power available from the piezoelectric material. In the previous models the piezoelectric and electrode layers were not considered because only the mechanical properties of the devices were under observation. In the following section the devices modelled include these

active layers. For computational simplicity all layers apart from the piezoelectric (AlN) layer are considered to obey the linear elastic law and the Ti layer is considered to be the bottom electrode or ground with an Al layer as the top electrode.

3.4.1. Calculation of Device Output Power

The internal impedance of the energy harvester is a very important factor for the output power calculations. The internal impedance is intrinsic to the devices and is based on the device geometries and resonant frequency. To produce maximum power a resistive load circuit with impedance that is matched to the internal impedance of the device can be applied to the output of the energy harvester. The piezoelectric devices are basically capacitors with a dielectric (AlN) between two metal electrodes (Ti and AlN) and therefore to find the impedance the first step is to calculate the capacitance. The capacitance of the device is based on the material properties and device dimensions and is calculated using:

$$C = \varepsilon_r \varepsilon_0 \frac{A}{t} \tag{3.2}$$

where C is the capacitance, ε_r is the relative permittivity of the AlN, ε_0 is the permittivity of a vacuum, A is the surface area of the Al layer and t is the thickness of the AlN.

The resonant frequency (f) of the device, measured or modelled, is then used to determine the reactance (Z) using:

$$Z = \frac{1}{2\pi f C} \tag{3.3}$$

The power can then be calculated using:

$$P_{out} = \frac{V_{out}^2}{R_L} \tag{3.4}$$

where P_{out} is the output power, V_{out} is the measured RMS output voltage and R_L = Z for a load matched circuit. For the fabricated devices the power was calculated

using an array of resistors for the load and the resistance value was varied from 5MΩ to 200kΩ. The power for the modelled devices was calculated using a static analysis and was not coupled to the resistance. Therefore the equation was changed to:

$$P_{out} = \frac{V_{out}^2}{R_L+Z} \qquad (3.5)$$

3.4.2. Model Set-up

The anchor point of the devices, i.e. furthest point from the mass, was set as a fixed point and the rest of the device was allowed to move freely as shown in Figure 3.19. The load to provide an excitation of 1g (9.81m/s^2) was applied to the tip of the mass and allowed to propagate through the device to simulate the excitation experienced by the fabricated devices. Damping could be considered to be negligible due to the size of the devices. The assumption that the damping would be negligible was confirmed by comparing models which included damping to those without and it was found that the resonant frequency and voltage out was the same for both models.

The models were evaluated using the piezoelectric devices interface which is an interface offered by COMSOL. This interface provides the voltage output from the devices when they are stressed. The Ti layer is set to ground and the Al layer is a floating potential. This allows for the voltage of the device to be calculated. A static study using the piezoelectric interface provides information on the voltage. The voltage and frequency results from the models were then used to calculate the power output based on the modified power Equation (3.5).

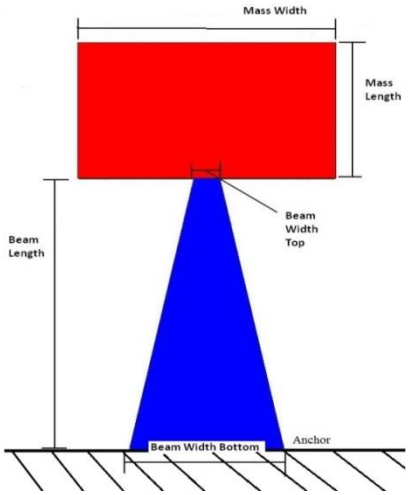


Figure 3.19: Triangular Beam showing Anchor at Base.

3.4.3. Device Testing

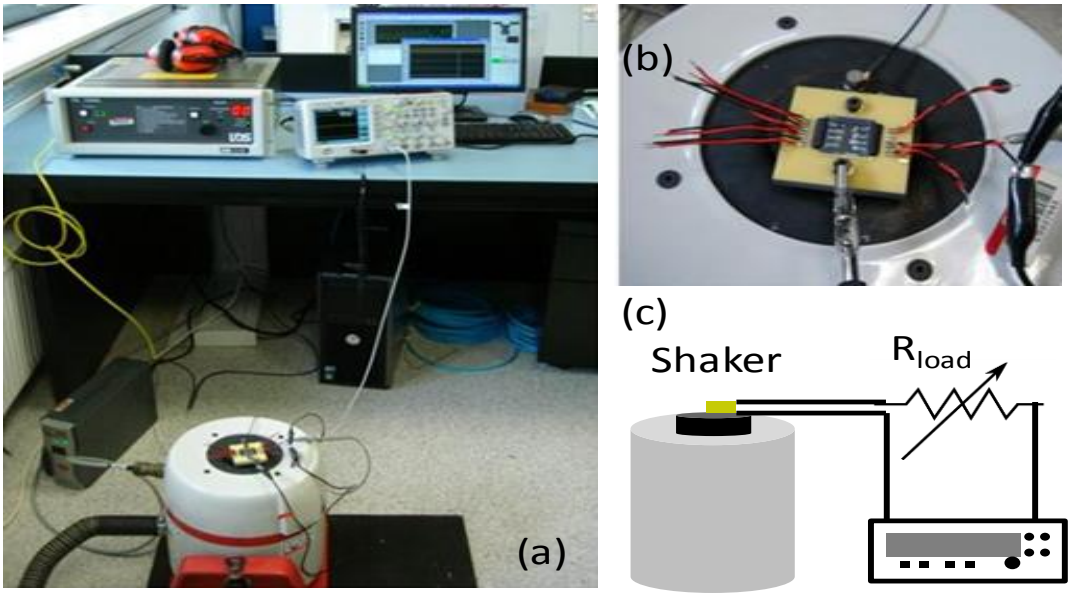


Figure 3.20: Electromagnetic Shaker Set-up. (a) Overview of full system showing magnet shaker and control hardware, (b) Device in place on shaker, (c) experimental set-up for measuring output power.

To test the power capabilities of the devices, they need to be excited at a known frequency and acceleration. To do this the devices were placed on an electromagnetic shaker and excited. This set up is shown in Figure 3.20 (a) and (b). The electromagnetic shaker could be set to a specific frequency and acceleration and feedback on these values was provided by an accelerometer secured to the shaker near the devices. The frequency response from the LDV was used and the acceleration was initially set to 0.1g. The voltage was then measured using an oscilloscope and a multimeter and the output was connected to an array of resistors so that the output power could be calculated using Equation 3.4.

The acceleration was also increased to determine the maximum acceleration possible before breakage as well as the response of the devices to increase in acceleration. The result of a device excited on the magnetic shaker is shown in Figure 3.21. The maximum power is achievable when the load resistance equals the resistance of the fabricated device as previously stated. For this reason the load resistance is swept so that the maximum power can be calculated. Figure 3.22 shows the relationship between power and acceleration. The thick blue line in this graph

corresponds to measured data from a cantilever device excited by the electromagnetic shaker and the thin black line is the relationship expected from the formula shown in the graph. It is clear that the measured data matches the result expected from the formula. From this graph it is clear that the maximum power output available from the devices is limited by their ability to withstand higher acceleration.

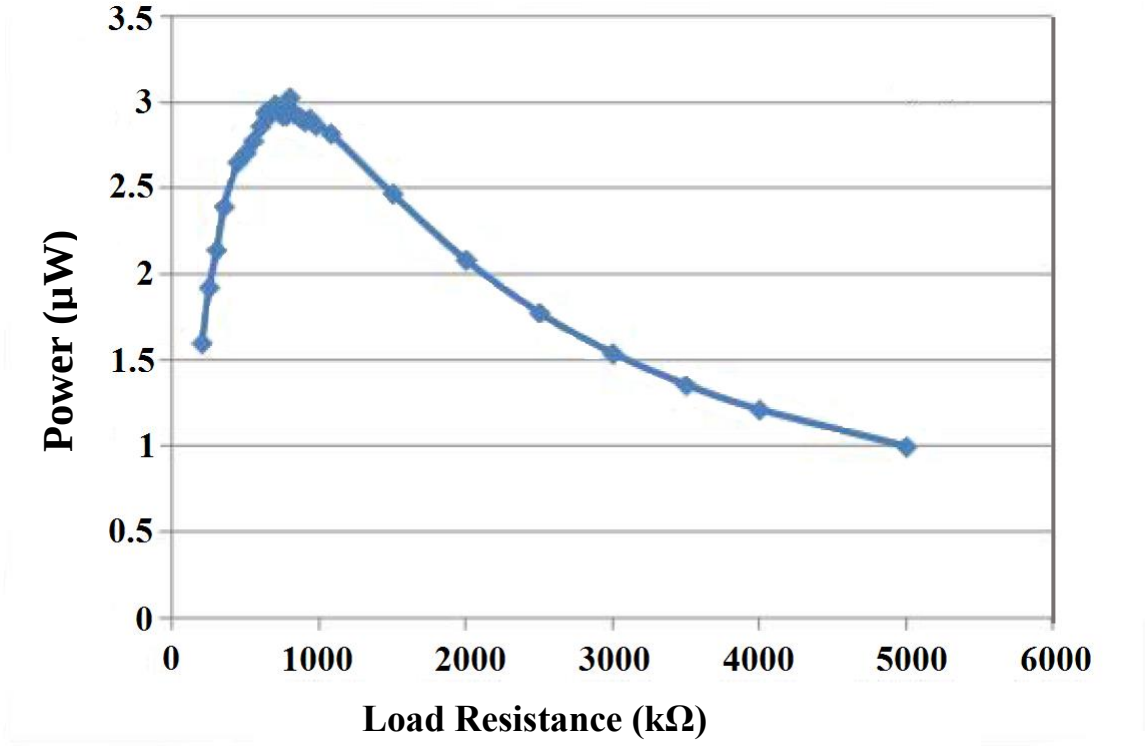


Figure 3.21: Power vs. Load Resistance for a device on a Magnetic Shaker

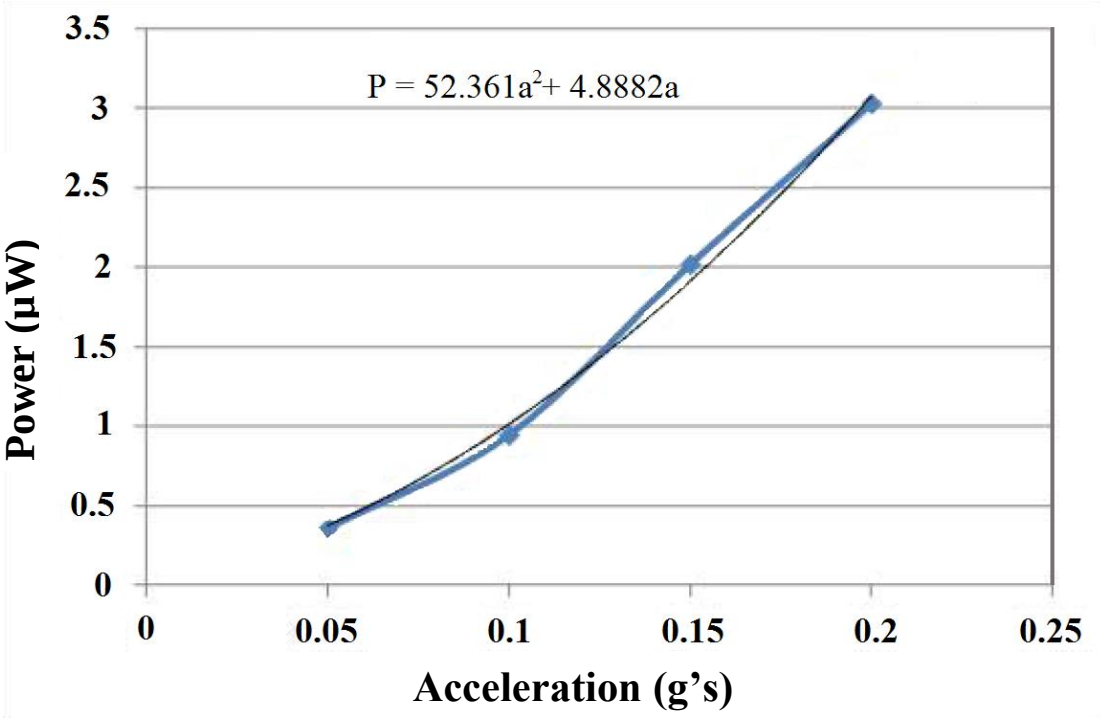


Figure 3.22: Power vs. acceleration for a single cantilever at resonance

3.4.4. Measured and Modelled Results Compared

Power results were obtained for cantilever type structures (similar to that in Figure 3.9) as well as the triangular structure shown in Figure 3.19. The displacement of the structures is shown graphically in Figure 3.23 and Figure 3.24. Here the red colour indicates areas of maximum displacement and areas of minimum displacement are shown in blue.

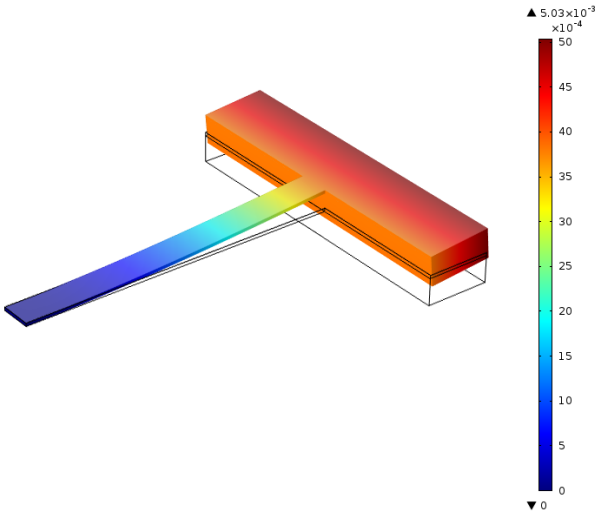


Figure 3.23: Cantilever device under excitation. Colours indicate displacement (in mm) with maximum displacement in red

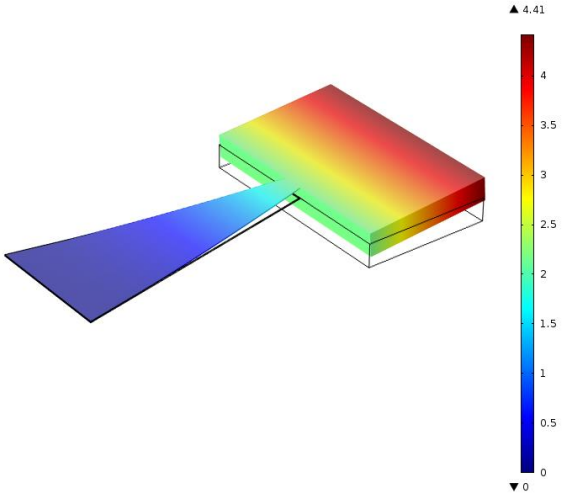


Figure 3.24: Triangular device under excitation. Colours indicate displacement (in mm) with maximum displacement in red

Three sets of power results comparing the modelled (COMSOL) simulation results with the measured data are presented in Figure 3.25, Figure 3.26 and Figure 3.29 for the devices shown in Figure 3.23 and Figure 3.24. The cantilever beam results for devices fabricated on two different wafers are shown for comparison. In all cases the point of maximum power and the general trend of the results are important features for the accuracy of these models and in all cases these results are comparable. Figure 3.25 shows agreement for lower resistance values and up to the maximum power point. However, for the modelled results a smoother tapering of the power at higher resistances is seen. Figure 3.26 has very similar results between modelled and measured but the measured results show some power spikes not seen in the models. This discrepancy can be explained by the measuring equipment. When the devices are excited the voltage across the device changes as the deflection is increased and decreased. The modelled devices are investigated at the maximum voltage at a known deflection of the devices. This deflection is based on the acceleration of the devices from the magnetic shaker results. A single value for voltage is obtained. In the measured data the value is read from an oscilloscope or a multimeter and it was found that the voltage reading can vary by a few mV during the reading time so that the result used is based on a non-static value. This also explains the more variable output from the measured results where sudden unexpected (but small) increases are seen. The two cantilever devices did produce

equivalent power at maximum deflection and load matching and this is expected from the piezoelectric material studies which were discussed in Chapter 2.

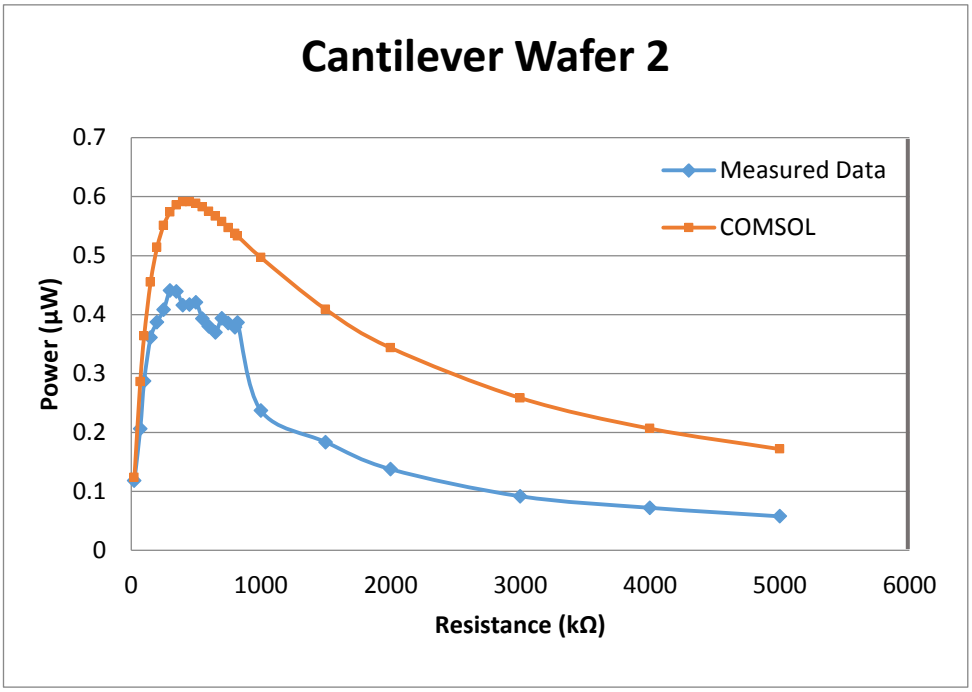


Figure 3.25: Power Measurement for Cantilever Device Wafer 2

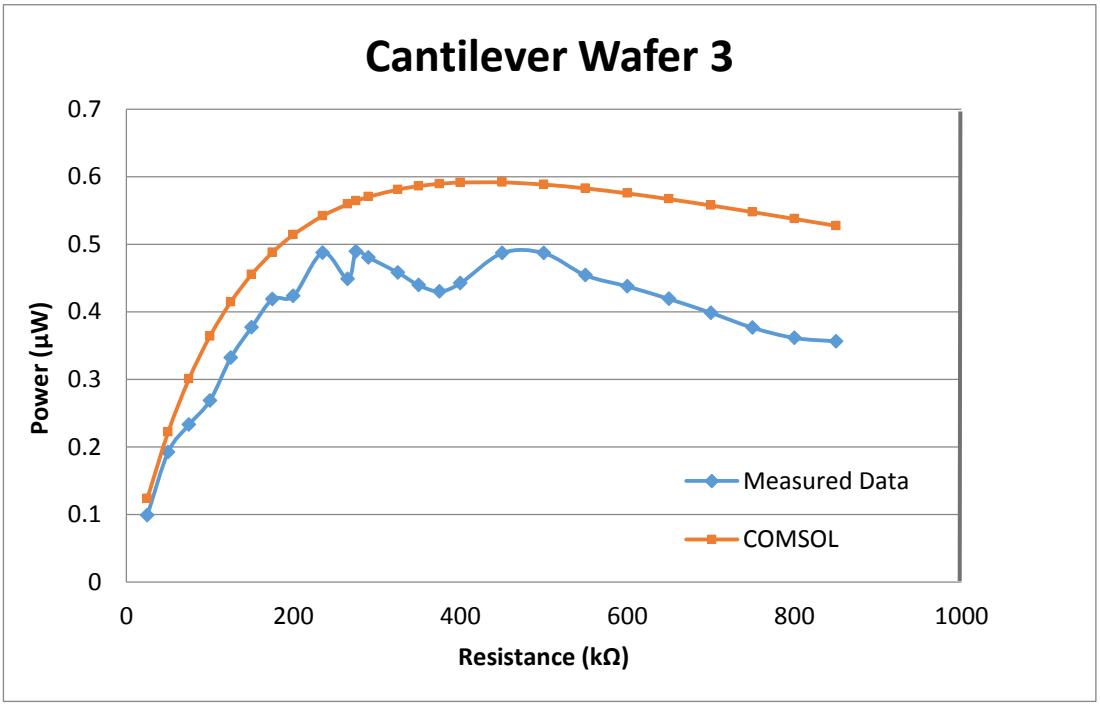


Figure 3.26: Power Measurement for Cantilever Device Wafer 3

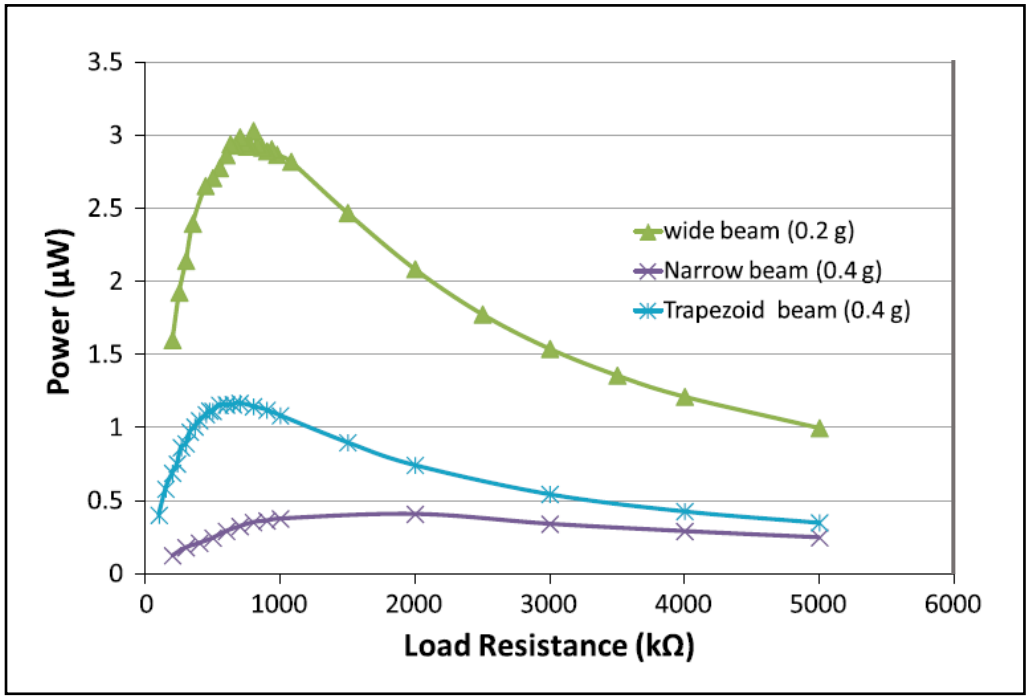


Figure 3.27: Experimental results showing the power generated vs. load resistance for 3 different cantilever structures operating at resonant frequency

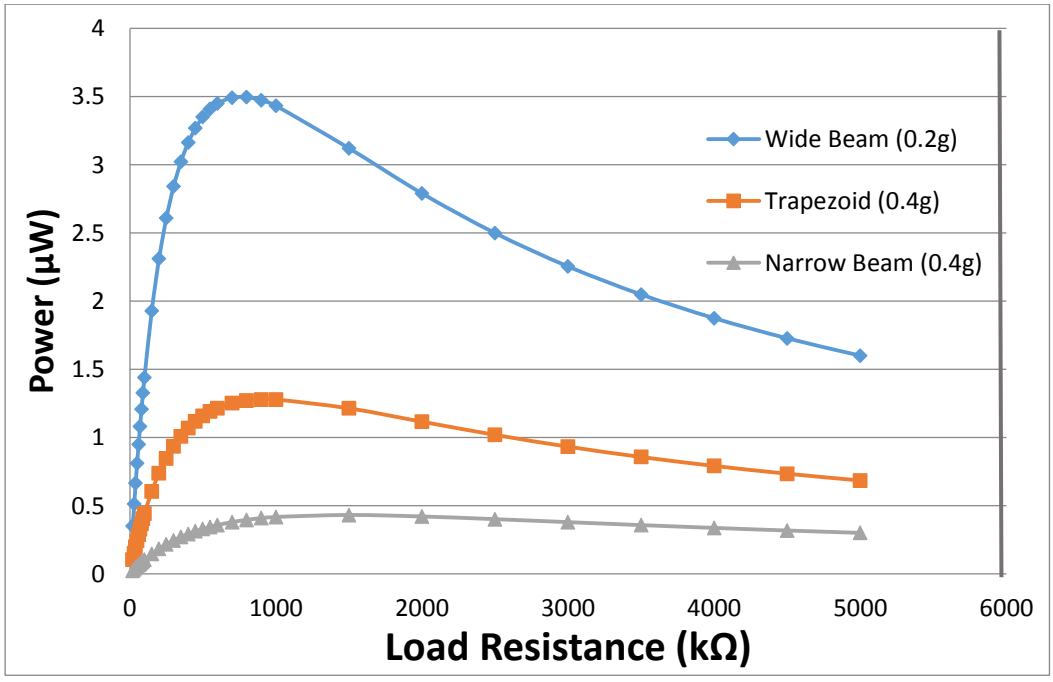


Figure 3.28: Modelling results showing the power generated vs. load resistance for 3 different cantilever structures operating at resonant frequency

Figure 3.27 and Figure 3.28 show the measured and modelled results for 3 different devices for comparison of their power generating ability. As is seen in all the power graphs the measured results are slightly lower than the modelled results

but in all these devices the results of both investigations are very similar. The wide beam is measured at a lower acceleration than the trapezoid and narrow beam because the wide beam broke at higher acceleration. The maximum power is shown in Table 3.1 for both measured and modelled devices.

Device (acceleration)	**Modelled Maximum Power (μW)**	**Measured Maximum Power (μW)**
Wide Beam (0.2g)	3.5	3
Trapezoid (0.4g)	1.25	1.15
Narrow Beam (0.4g)	0.4	0.35

Table 3.1: Measured vs. Modelled Power Results for 3 devices

To note here, is that the power was measured and modelled at different acceleration for the wide beam than the other two beams; and still the power output from the wide beam was much higher. This is due to the increased surface area of the wide beam which meant that a much larger amount of piezoelectric material was present on this beam. The trapezoid beam was also larger than the cantilever and this can explain the difference seen in the power capabilities.

The triangular beam results shown in Figure 3.29 have excellent correlation but in this case the resistance value for maximum power is slightly different. This could be due to the measurement issues discussed above. It may also be due to the fact that the resistance from the variable resistor array was also measured using a multimeter. Once a resistance within a few kΩ of the expected resistance was achieved the measurement was made. A more accurate result may have been achieved by using resistors of known values instead of the resistor array of variable resistors but the variable resistor array was the best solution for providing a wide range of resistance for all the devices under investigation.

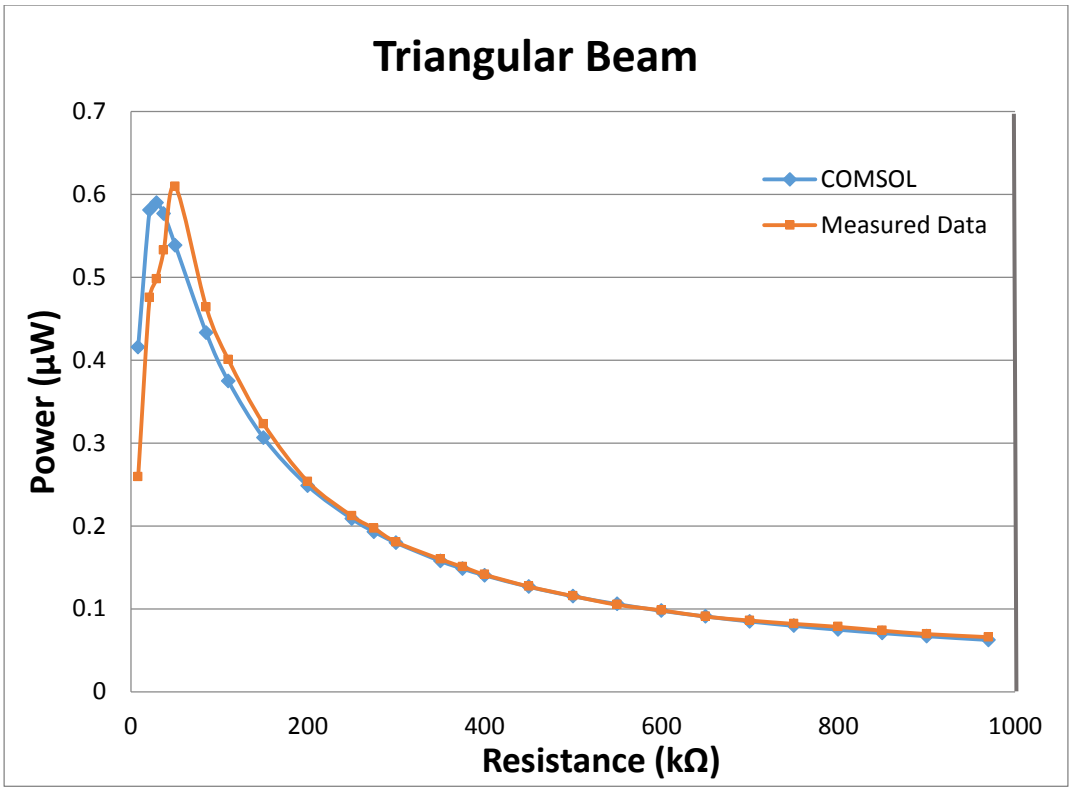


Figure 3.29: Power Measurement for Triangular Beam Device

Figure 3.30 shows the current measurements for the Wafer 2 cantilever. Here the measured data refers to measured voltage (V) and resistance (R) values which were used to calculate the current (I) using:

$$I = \frac{V}{R} \qquad (3.6)$$

The modelled results were found using the technique described in Section 3.4.1. Here it is seen that the modelled results are less than that for the measured data. As with previous models a number of factors contribute to the difference seen in the measured and modelled results and this is once again seen here.

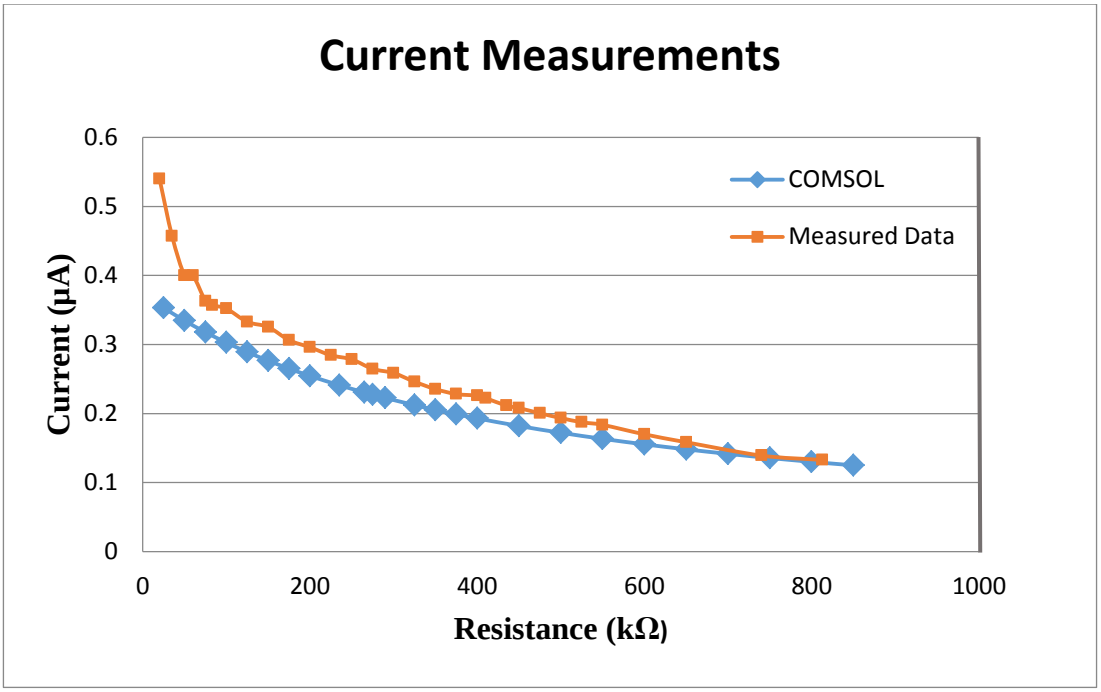


Figure 3.30: Current Measurements

3.5. Summary

In this chapter the abilities of COMSOL to model piezoelectric energy harvesting devices have been presented. Resonant frequency models were presented for many different types of device and the maximum difference between these models and the measured resonant frequency was reduced from 16.8% to 4.4% by suitable calibration of the simulator parameters. The ability to use COMSOL models to design MEMS devices for specific frequencies was also shown. The available bandwidth of the frequency response of MEMS devices was also investigated and three different schemes for broadening the bandwidth were examined. From these results it was shown that the only viable method to increase bandwidth while maintaining a high Q factor and power output was to design an array of devices with overlapping frequencies.

Here the limitation of the model to accurately predict real world conditions is seen. A model was created to determine the changes required to each cantilever to produce a change of 1Hz from a starting frequency. The measured results show that the expected linear dependence on the length of the mass was not achieved. This was due to limits in the precision of the fabrication techniques so that the small variation could not be accurately achieved.

However, it was found that due to this limitation on precision an array of cantilevers designed for a single frequency will have a range of frequencies within the bandwidth of the devices so that an array of bandwidth broadening devices can be fabricated.

Power results were also obtained for measured and modelled devices by increasing the complexity of the models to include all the active layers. These results were capable of determining the point of maximum power (i.e. matched load) and predicted the maximum power with a maximum error of 33%. For devices with less fabrication errors this error is reduced to 10% to 16% This error could be reduced by reducing the noise in the system and decreasing the fabrication errors. The accuracy of these models shows that COMSOL can be used to determine the power of MEMS devices and these models can be used to design future devices.

Several papers have been published based on work in this chapter including two journal papers in Microsystem Technologies [20] and [23]. Two conference papers presented in SMACD 2012 [101] and Eurosim 2013 [102].

Chapter 4:

Fluid-Actuated Energy Harvesting Devices

4.1. Introduction

Previous devices studied in this work examined how to tune resonant frequency and broaden the frequency response. These are very important parameters when looking at vibration-excited MEMS devices operating in air. In this chapter, devices for fluid-actuated energy harvesting are investigated. The final devices are expected to be actuated by blood flow and implanted into a human artery. This means that there are a number of limitations that must be considered. Blood is made-up of many suspended particles e.g. white and red blood cells (Figure 4.1). These particles remain suspended due to the force of the moving blood and reducing the velocity of the blood may cause particles to be dropped and arterial stenosis (plaque build-up) may occur. For this reason it is important to study the change in velocity of the fluid due to the presence of a MEMS device, using FEM. The turbulence of the flow is also studied because in a very turbulent system the particles will collide with each other and this could also cause particle build-up in the artery. These two parameters should give a good indication of the effect on the flow of the

various energy harvesting devices proposed in this work. The other study conducted is on the stress induced in the devices due to the blood flow and the resulting voltage across the devices. The stress results provide information on the reliability of the devices as well as the voltage output because if the stress is too high the devices could break free and travel through the artery. The FEM voltage results will be compared to experimental results.

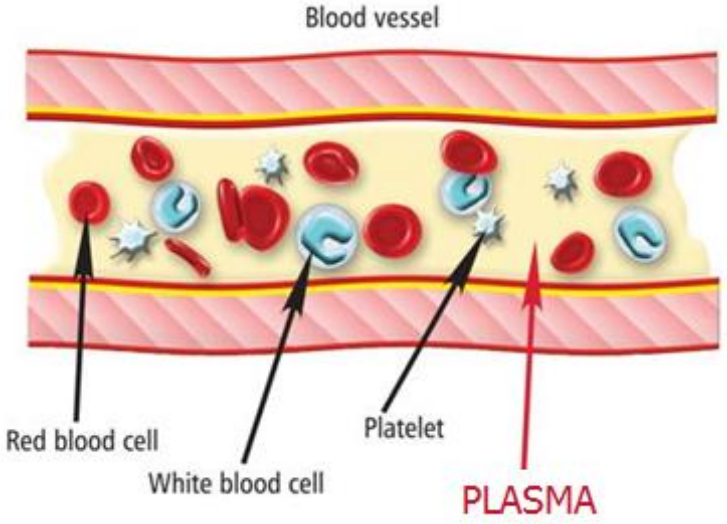


Figure 4.1: Suspended particles in blood [103]

4.2. Proposed Device Structures

For fluid actuated energy harvesting a number of device designs have been proposed as possible candidates. The list of these devices is shown in Table 4.1 and they are all described in the following text. The devices will be placed parallel or perpendicular to the flow as shown in Figure 4.2. In all of these devices it is assumed that the AlN will be deposited over the entire surface area of the device.

Figure 4.2 shows the proposed devices in the flow. In this figure the fluid flow is shown by the blue arrows and the placement of the devices in the flow is indicated with the free areas in green and the fixed areas in red.

Device	**Surface Area (μm^2)**
Cantilever	3.5
Diaphragm	15.9
Diaphragm (100μm hole)	15.8
Diaphragm (2000μm hole)	12.8
Fixed Beam	18
Diaphragm (cross)	15.3

Table 4.1: Proposed energy harvesting devices and surface area

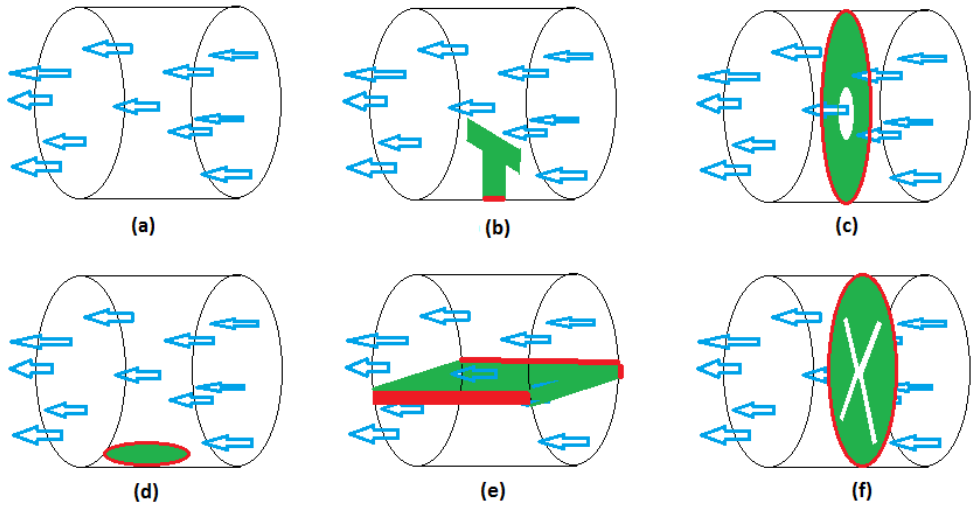


Figure 4.2: Fluid flow (blue arrow), fixed points (red) and free points (green) for (a) empty artery, (b) cantilever, (c) diaphragm with 2000μm hole, (d) diaphragm, (e) fixed beam and (f) diaphragm with cross cut out

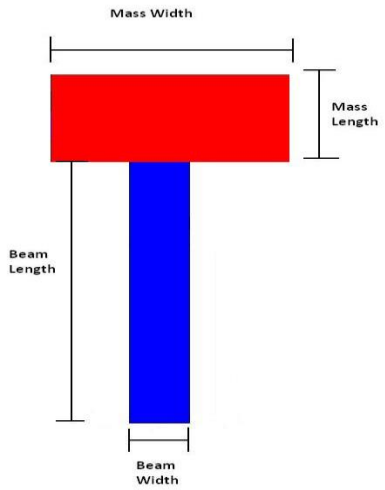


Figure 4.3: Cantilever Device

Dimension	Size (μm)
Beam Width	500
Beam Length	3000
Mass Width	1000
Mass Length	3000

Table 4.2: Dimensions of Cantilever

The cantilever shown in Figure 4.3 will be studied for its ability to act as a fluid actuated energy harvesting device. This is a typical layout for a resonant cantilever energy harvesting device. The small mass size allows movement due to blood flow and the dimensions were chosen to be comparable with other devices to be tested. This type of device is expected to cause a lot of disturbance to the flow and would not be ideal for environments where the flow of the fluid should not be impeded. The small surface area of the device and small anchor point also means that the amount of energy which could be harvested is expected to be less than that which could be achieved by the other devices. However, it should experience a lot of movement in the flow and this may compensate for its small surface area.

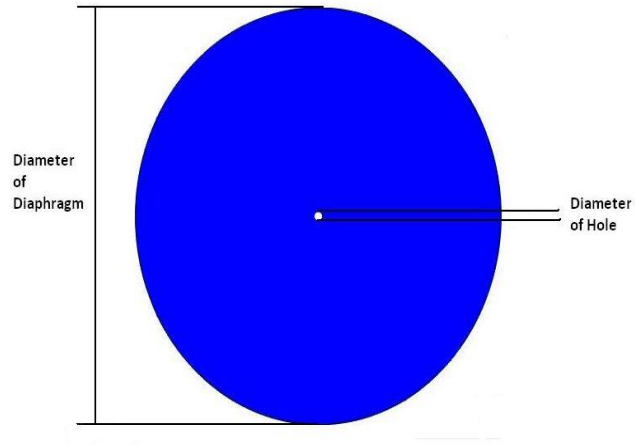


Figure 4.4: Diaphragm with 100µm hole

Dimension	Size (µm)
Diaphragm Diameter	4500
Hole Diameter	100

Table 4.3: Dimensions of Diaphragm

A complete diaphragm, as well as the diaphragm with the 100µm hole in it, Figure 4.4, will be placed in-line with the flow so the fluid flows on top of the round surface and the pressure of the fluid flow acts on the top, the side being shown, of the diaphragm as shown in Figure 4.2. This means that there is a minimal impact on the flow because the diaphragm will be placed along the vessel wall. However, possible issues could be that the device does not have a lot of space to expand and contract and also the device may contract under the pressure from the fluid and not be able to expand against this pressure as shown in Figure 4.5 (a) and (c). To combat this problem another diaphragm with a 100µm hole in the centre of the device has also been designed. This will allow flow into the underside of the device which will re-expand the diaphragm (Figure 4.5 (b) and (d)); it will also cause a pressure difference which may increase the stress over the device. The size of the hole was chosen as the minimum dimension to allow for the movement of small particles (blood cells) and large particles (platelets) to enter and leave the device unimpeded.

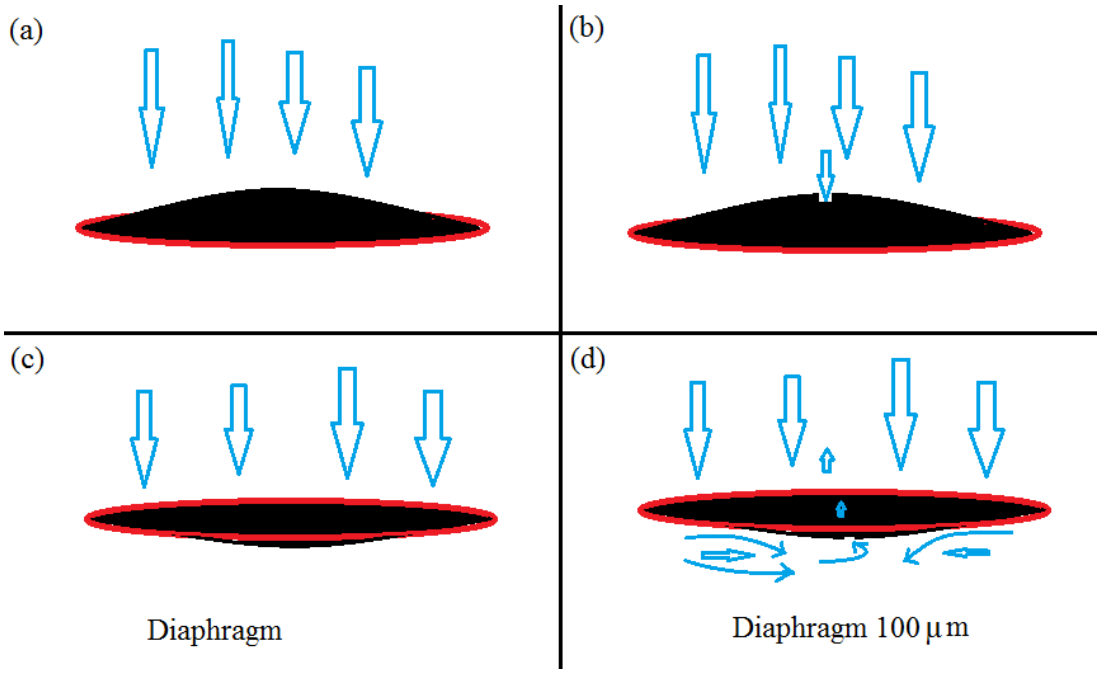
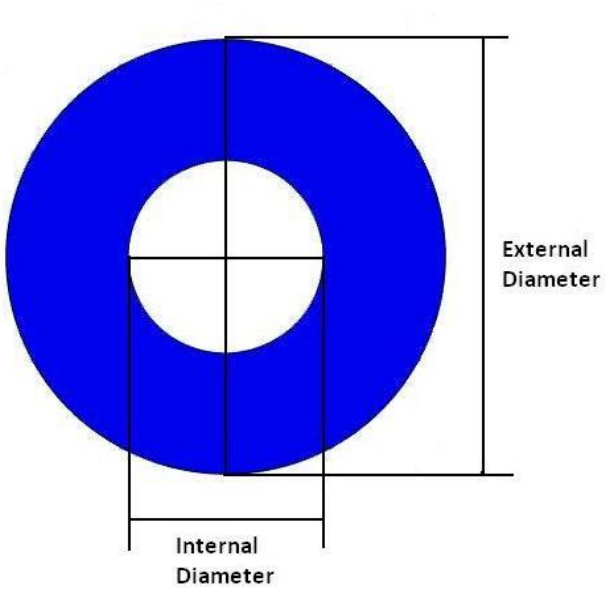


Figure 4.5: Diaphragm operation



Dimension	Size (µm)
Internal Diameter	2000
External Diameter	4500

Table 4.4: Dimensions of Diaphragm with 2000µm hole

Figure 4.6: Diaphragm with hole for placement in direct path of flow

Figure 4.6 shows a diaphragm device with 2000µm which will be placed perpendicular to the flow as shown in Figure 4.2. The external diameter is left the same as with the previous 2 diaphragms for comparison. This design simulates a contracted artery. The artery will be reduced to the external diameter of this diaphragm (4500µm) so that the device will be fixed to the walls of the artery. This means that a large proportion of the artery cross section (approximately 80%) will be covered by the device. These results will provide information on the maximum size of the device based on the size of the artery or vein in which it will be placed.

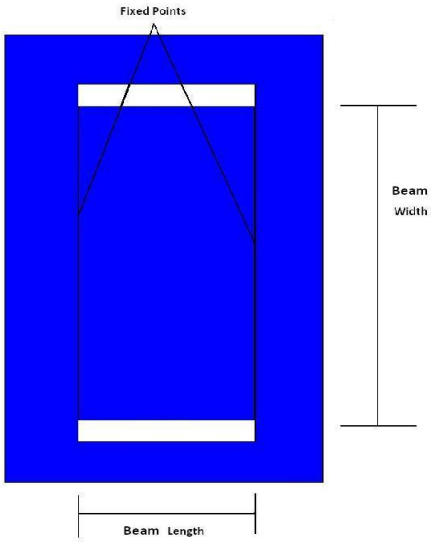


Figure 4.7: Fixed Beam Device

Dimension	Size (µm)
Beam Length	3000
Beam Width	6000

Table 4.5: Dimensions of Fixed Beam

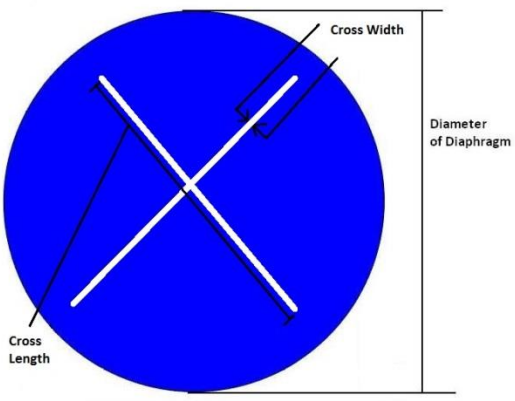


Figure 4.8: Diaphragm with cross

Dimension	Size (µm)
Diaphragm Diameter	4500
Cross Length	4000
Cross Width	100

Table 4.6: Dimensions of Diaphragm with Cross

The fixed beam device shown in Figure 4.7 is designed to be placed in the middle of the flow and in line with the flow so that the beam is fixed via the long sides to the vessel wall (Figure 4.2). The fixed long sides mean that the blood flows over the device and causes stress at different points. The fluid can then flow from above and below and cause pressure on both sides. This will cause extra stress (increased energy harvesting) with less impact on the blood flow. This would make it a useful geometry for the device if it works as anticipated. However, packaging it so that it can lie perpendicular to the flow is seen as a significant challenge at the moment.

The final design shown in Figure 4.8 is a diaphragm with a cross cut out and 4 masses, one on each section of the device. The diaphragm is designed to be perpendicular to the flow the same as the diaphragm with 2000µm hole in Figure 4.6. The big difference here is that the active area is very large but there is the potential for large displacement and that the fluid would still have a large area through which to flow when the sections deflect. Each of the four sections would be free to move in the flow so that the opening could become quite large when placed in the artery and fluid flows through it.

4.3. FEM Fluid Flow Results

4.3.1. Introduction

In these models the fluid used is water and the fluid flow is approximated based on the pressure of the flow. A sinusoidal waveform of the pressure was used to model the flow of blood using Equation 4.1, although the flow is not really sinusoidal in shape (Figure 4.9). This is an approximation of the pulsating flow of the blood in an artery described by Coppola *et al*. [104].

$$P_{in} = P_{min} + (P_{max} - P_{min}) \sin(\omega t) \qquad (4.1)$$

where P_{in} is the pressure in the artery, P_{max} is the systolic pressure (or maximum pressure) and P_{min} is the diastolic pressure (or minimum pressure) of the fluid in the artery, t is time, ω is the frequency in rad/s of the pulsating fluid and since the fluid is flowing at 60bpm (typical resting heart rate) the frequency is 1Hz and therefore ω = 2π. For normal adults typical blood pressures would be diastolic pressure, P_{min}, of

80mmHg (10670Pa) and systolic pressure, P_{max}, of 120mmHg (16000Pa). In this work a tube of 1cm diameter was chosen for the cantilever, diaphragm and diaphragm with 100µm hole models. This is typical of the dimensions of the aorta which is approximately 1cm in diameter. For the diaphragm with cross structure and diaphragm with 2000µm hole a tube size of 4500µm was used so that the device would fit exactly into the artery. For the same reason a diameter of 3000µm was used for the tube with the fixed beam. This reduction in the tube diameter was to allow for the devices to be designed with comparable size but work within the tube as if they were designed to fit the artery fully. The models discussed here were created using water as the fluid, but previous models completed for work on a smart stent [31], using blood show that without the inclusion of the suspended particles water is a good first approximation. The fluid flow in the artery (indicated by blue arrows), as well as the fixed (red lines) and free (green areas) points of the devices, are shown in Figure 4.2.

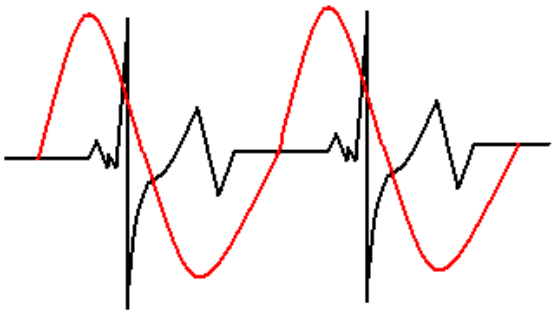


Figure 4.9: Typical artery pressure waveform and approximated waveform from equation for use in models

The resonant frequencies shown in Table 4.7 were obtained from simulations of the devices presented in Figure 4.2. It is interesting to note the difference from the previously examined resonant frequencies. In this table all the devices apart from the cantilever are in the kHz range which would be much too high for excitation through normal industrial or ambient vibrations but because here the fluid interacting with the devices will cause the deformation and movement of the structure, the resonant frequency is no longer a critical parameter because it is not

required to match a specific frequency for the devices to be excited and is presented here to show a full analysis of the devices was conducted.

Device	Resonant Frequency
Cantilever	258.1441 Hz
Fixed Beam	28.986 kHz
Diaphragm	22.823 kHz
Diaphragm with 100µm hole	22.815 kHz
Diaphragm with 2000µm hole	33.955 kHz
Diaphragm with Cross	16.524kHz

Table 4.7: Simulated resonant frequencies

4.3.2. Velocity Results

As previously stated, the velocity of the fluid flow in the pipe is a critical factor in blood flow due to the suspended particles requiring the force of the moving blood to remain suspended. In these models the blood will be modelled as water to reduce the complexity of modelling the suspended particles but also for comparison with experimental results which could only be conducted using water. It is important to note the result shown in Table 4.8 where the maximum velocity is measured at the same time in the simulation so that the same pressure is in the system and the results are comparable. The time was chosen as 0.6s as the frequency was set at 1Hz and the maximum pressure and therefore maximum deflection occurred at this time. These results show that the diaphragm structures are the best structures for maintaining the fluid velocity. However, the velocity profile must also be considered and for this reason the FEM models for the fluid velocity with each device in the flow and an empty artery are shown in Figure 4.10 to Figure 4.16. From the empty artery results, the velocity profile should have a minimum at the artery walls (as indicated by the blue colour) and a maximum at the centre of the artery (indicated in red). This velocity profile is shown for the diaphragm with a 2000µm, the fixed beam and the diaphragm with a cross structure.

Device	Maximum Velocity at t=0.6s (m/s)
No Device (Empty Artery)	0.4602
Cantilever	0.39018
Diaphragm (no hole and 100µm hole)	0.4707
Diaphragm (2000µm hole)	0.44
Fixed Beam	0.234323
Cross	0.00204

Table 4.8: Modelled fluid velocity for each device placed in flow

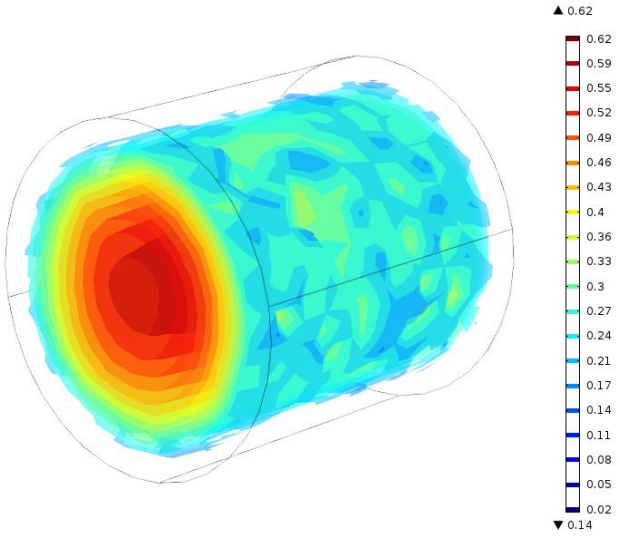


Figure 4.10: Empty Tube at t=0.6s. Velocity (in m/s) indicated by colours with maximum velocity in red

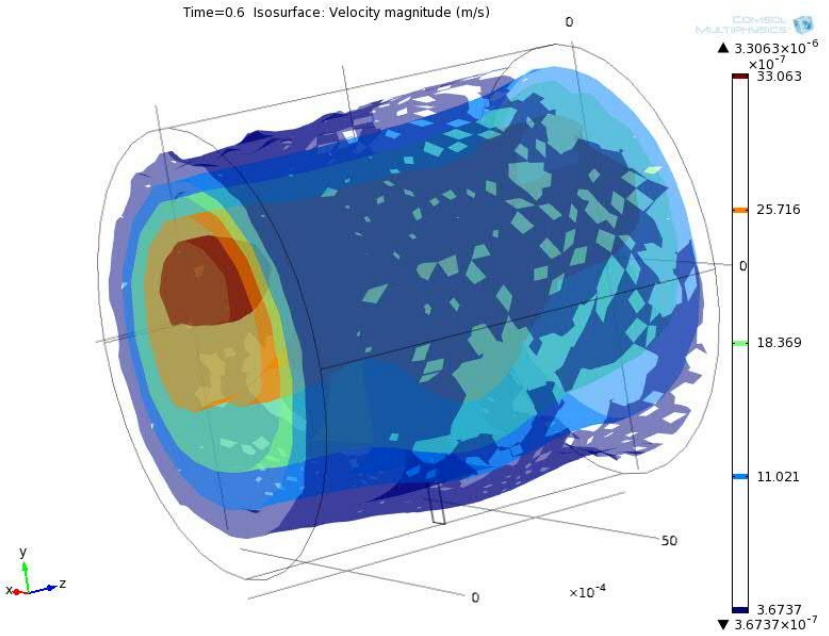


Figure 4.11: Cantilever at t=0.6s. Velocity (in m/s) indicated by colours with maximum velocity in red

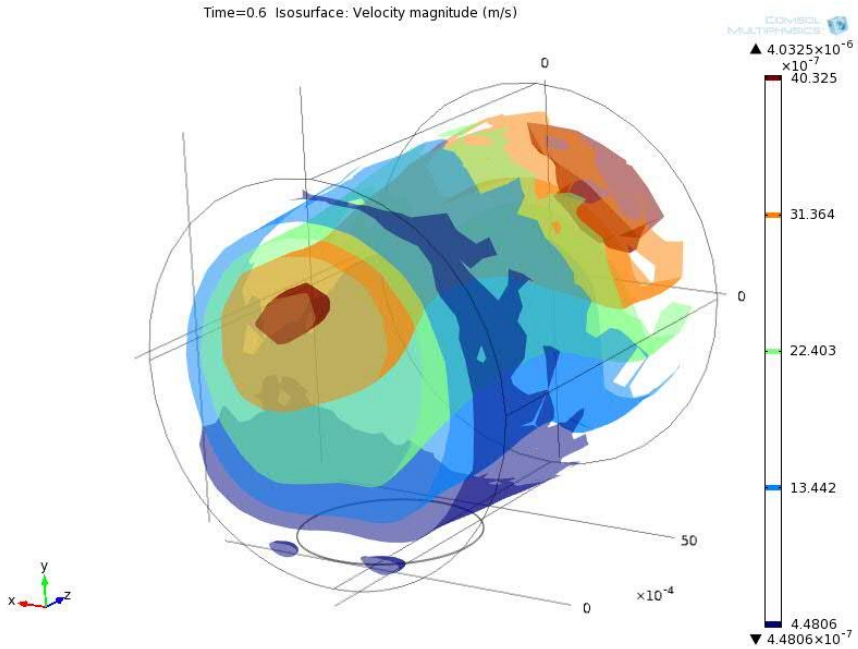


Figure 4.12: Diaphragm at t=0.6s. Velocity (in m/s) indicated by colours with maximum velocity in red

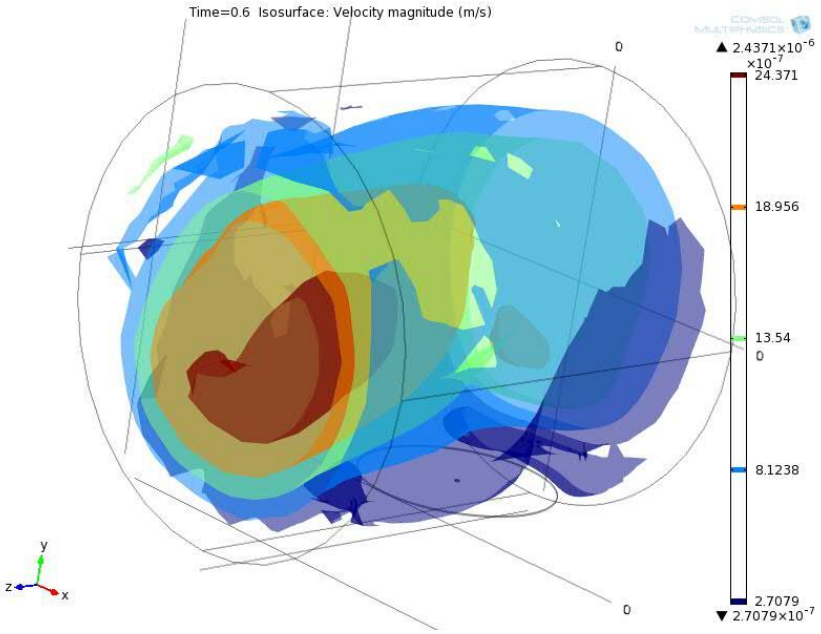


Figure 4.13: Diaphragm with 100µm hole at t=0.6s. Velocity (in m/s) indicated by colours with maximum velocity in red

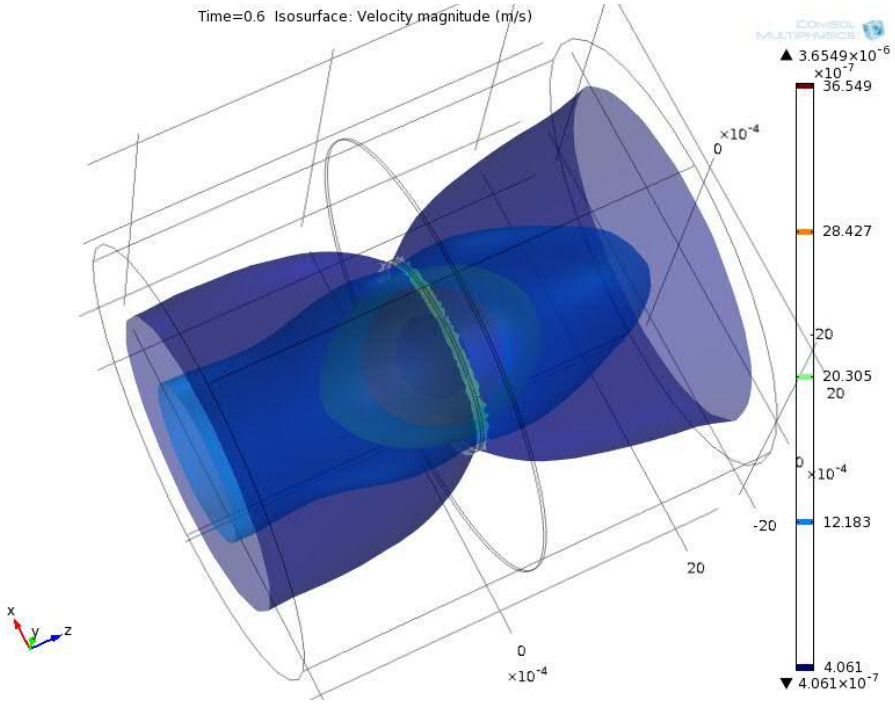


Figure 4.14: Diaphragm with 2000µm hole at t=0.6s. Velocity (in m/s) indicated by colours with maximum velocity in red

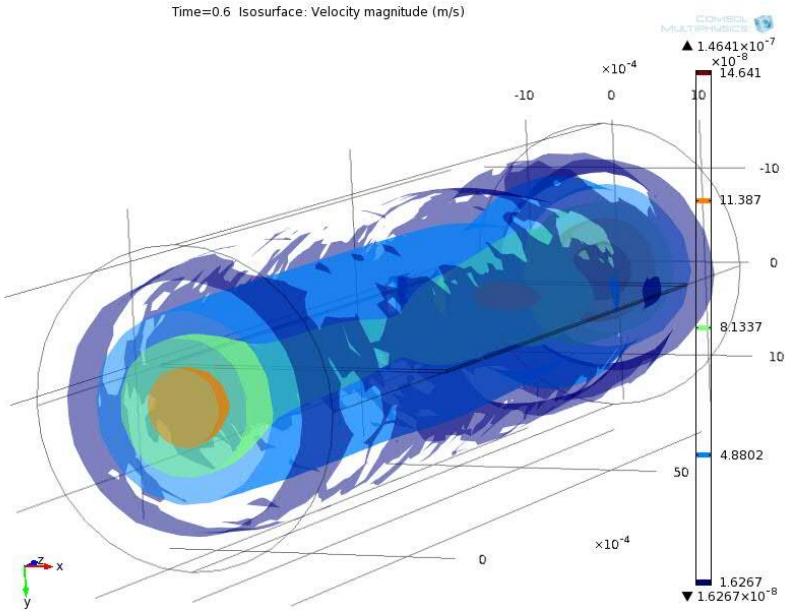


Figure 4.15: Fixed Beam at t=0.6s. Velocity (in m/s) indicated by colours with maximum velocity in red

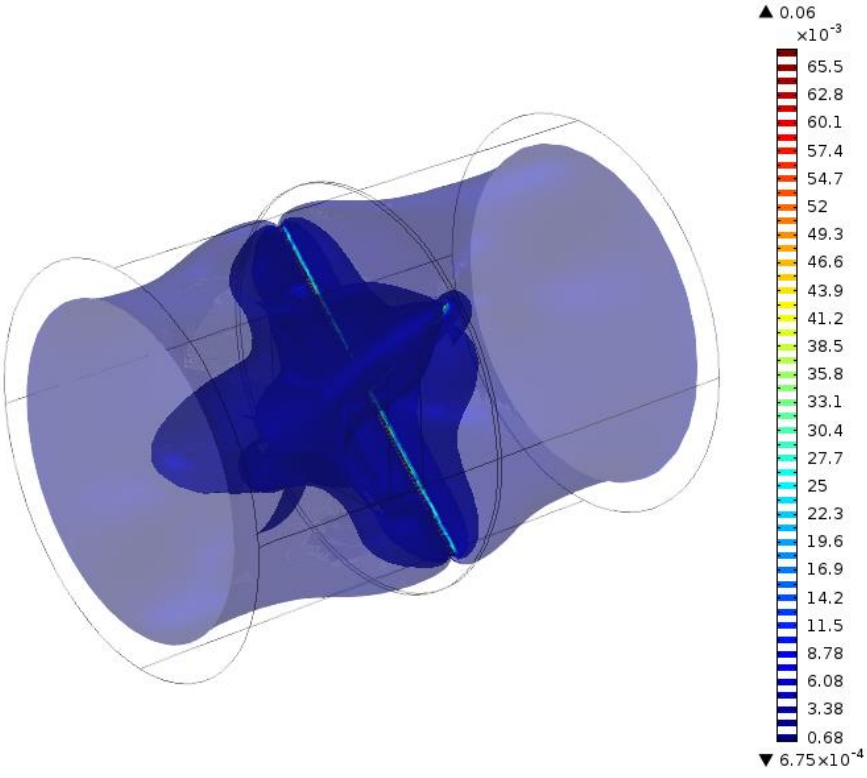


Figure 4.16: Diaphragm with Cross. Velocity (in m/s) indicated by colours with maximum velocity in red

4.3.3. Turbulence Results

The turbulence of the flow is an important parameter because in a turbulent flow the suspended particles will collide and interact more than in a laminar (smooth) flow. This interaction could cause the particles to slow down and become deposited on the artery walls. To investigate this, an empty artery was studied for its flow turbulence and the model compared to the results for the artery with each device included. As is seen in Figure 4.17 the flow is very smooth along the artery. The fluid moves very steadily. This is indicated by the arrows in regular rows along the artery. Comparing this to when the cantilever device is inserted (Figure 4.18) a big difference is seen. The arrows are now pointing in all directions and are of different sizes, which indicate areas of extra force. In this configuration the flow would be turbulent. Typical Reynold's number (Re) for blood calculated using Equation 4.2 [105] gives a value of 1951.24 which is expected from typical values stated for blood [105],

$$Re = \frac{2v\rho r}{\eta} \qquad (4.2)$$

where v is the effective velocity, ρ is the density of the fluid, r is the tube radius and η is the viscosity. Using this equation you get little information on the fluid turbulence with the effect of the devices because the equation assumes a pipe of known diameter but once the devices are inserted the fluid is no longer travelling through a circular pipe. For this reason the vortices created in the fluid are modelled and the results are used to determine the turbulent effect of the devices on the flow. The arrows in these simulations are compared to show where the fluid flow is interrupted due to the devices and turbulence is created. Figure 4.18 and Figure 4.19 show a much more similar turbulence profile to that of the empty artery and this is to be expected because these diaphragms would be seen as a minor reduction in the artery width. The wide beam and diaphragm with a 2000μm hole also show promising turbulence profiles. This may be due to the fact that they do not have large enough displacements in the flow to cause eddies and, in the case of the diaphragm with a 2000μm hole, would be seen by the flow as a smaller diameter artery. With the cross structured diaphragm there is more of a turbulent flow seen and this is to be expected due to the massive blockage that this would be caused

when the flow is not strong enough to deflect the walls to any great extent. This may be due to the use of silicon which is very stiff and therefore difficult to displace.

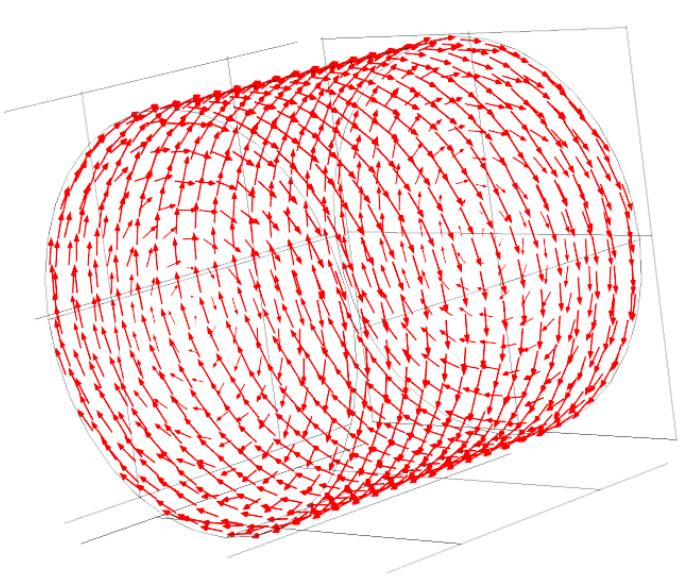


Figure 4.17: Empty Tube at t=0.6s. Arrows indicate disruption to flow

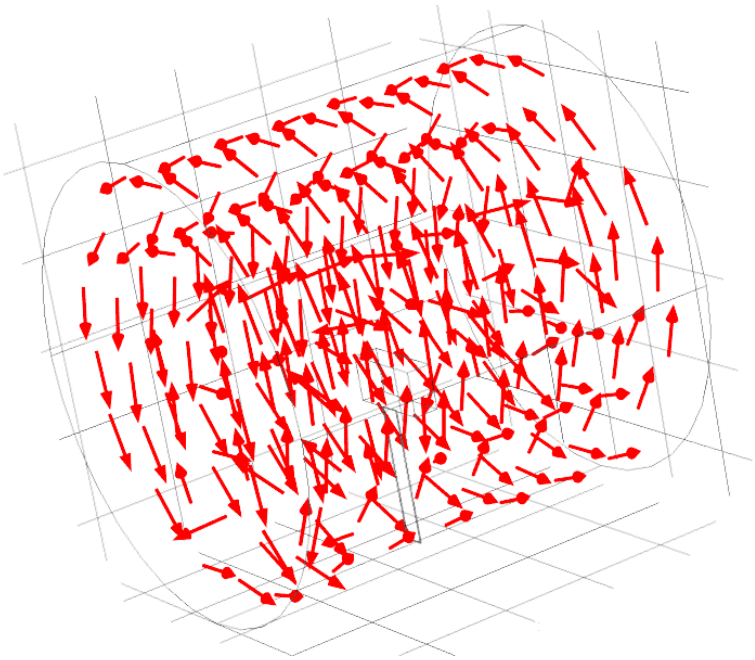


Figure 4.18: Cantilever at t=0.6s. Arrows indicate disruption to flow

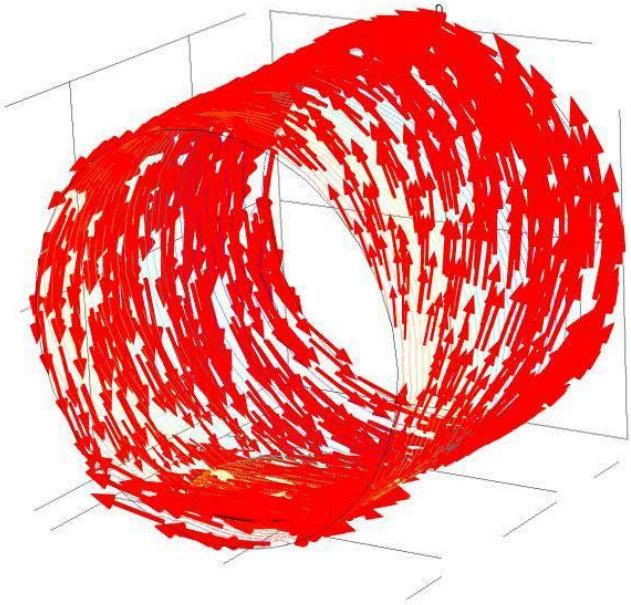


Figure 4.19: Diaphragm at t=0.6s. Arrows indicate disruption to flow

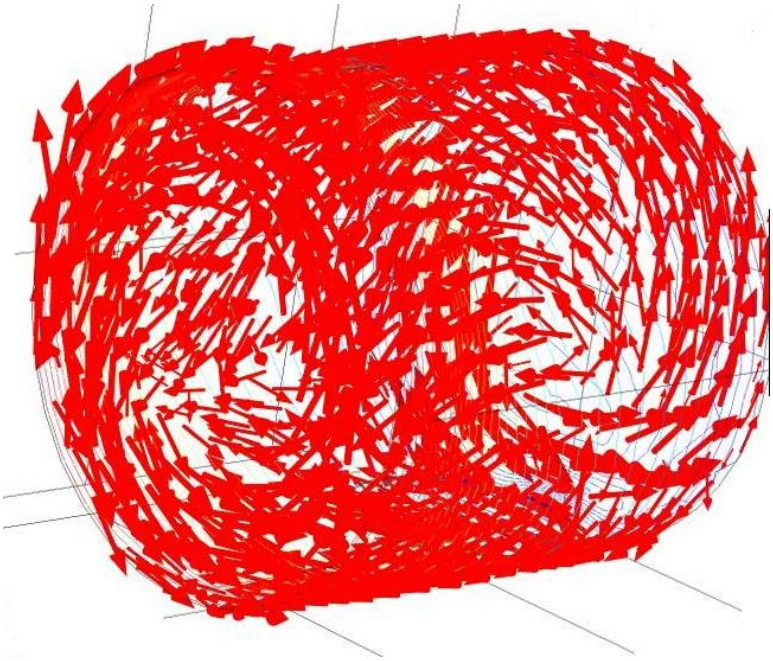


Figure 4.20: Diaphragm with 100μm hole at t=0.6s. Arrows indicate disruption to flow

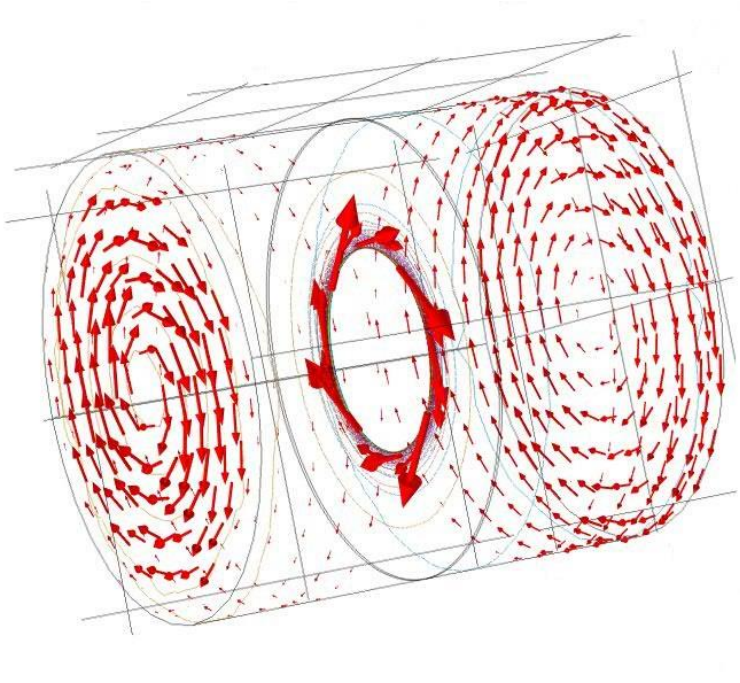


Figure 4.21: Diaphragm with 2000μm hole at t=0.6s. Arrows indicate disruption to flow

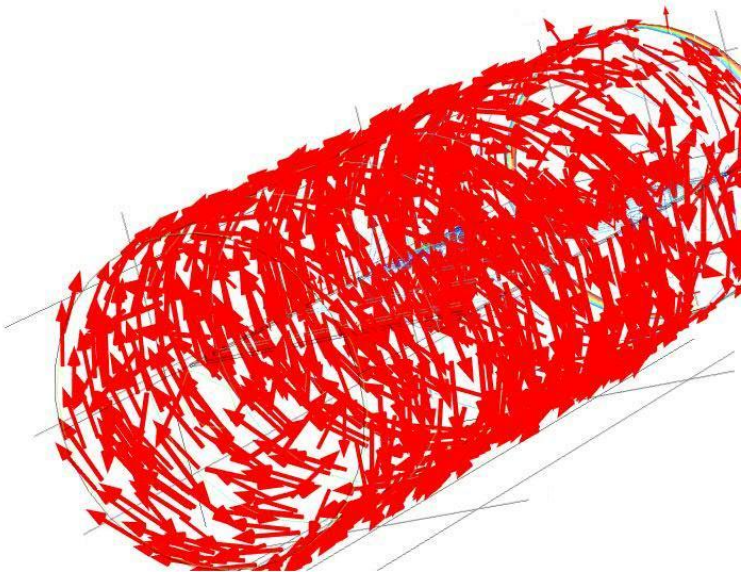


Figure 4.22: Fixed Beam at t=0.6s. Arrows indicate disruption to flow

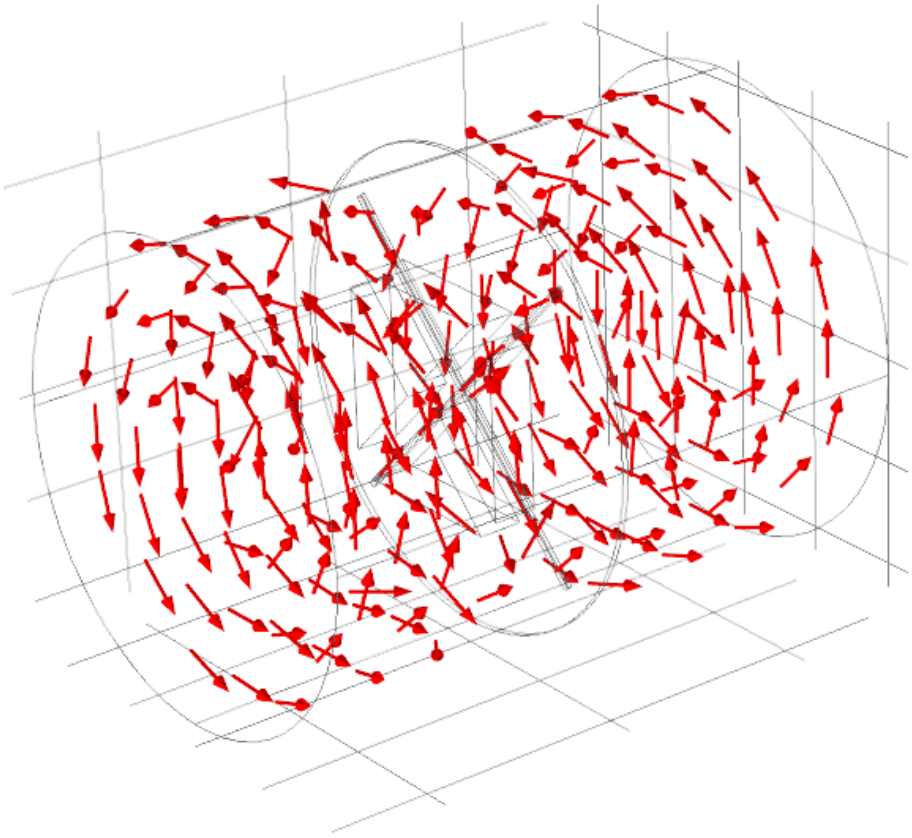


Figure 4.23: Diaphragm with Cross. Arrows indicate disruption to flow

4.3.4. Device Stress Results

The stress experienced by the devices when subjected to the flow of the fluid in the artery is studied to determine their reliability. The silicon is the thickest layer of the material and so if the stress is above the maximum stress which the silicon can withstand (5 to 9GPa) [23] then the devices will fail and could break off and become loose in the artery. Taking into account the worst case scenario of Si with a stress tolerance of 5GPa the maximum stress experienced by the devices when subjected to a pulsating flow of water is examined. The results of these studies are shown graphically in Figure 4.24 to Figure 4.29 where the maximum stress is shown in red and the minimum stress is shown in blue. As expected the maximum stress is experienced at the anchor points of each device. Table 4.9 shows the maximum stress of each of the devices. From this table it is seen that any of the devices should be able to operate in the bloodstream under normal pressure.

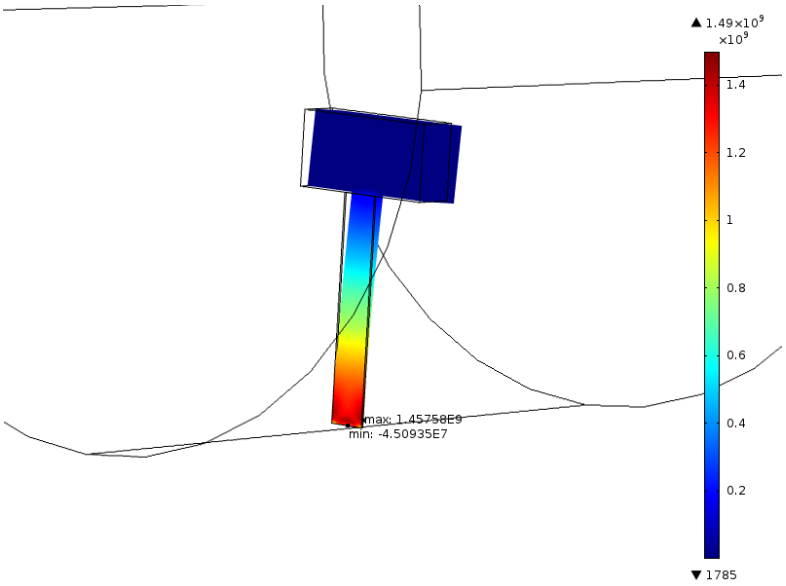


Figure 4.24: Cantilever. Stress (in N/m^2) indicated by colour with red indicating maximum stress

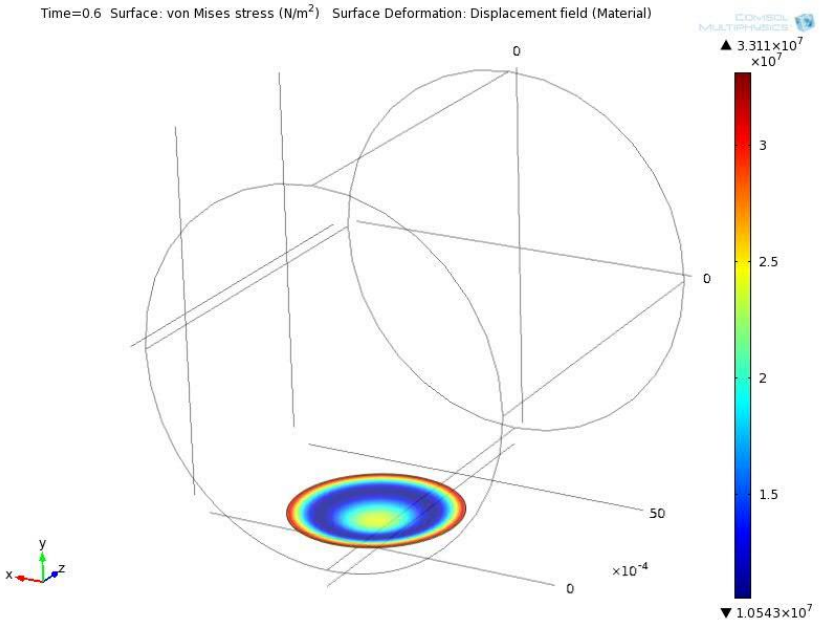


Figure 4.25: Diaphragm at t=0.6s. Stress (in N/m^2) indicated by colour with red indicating maximum stress

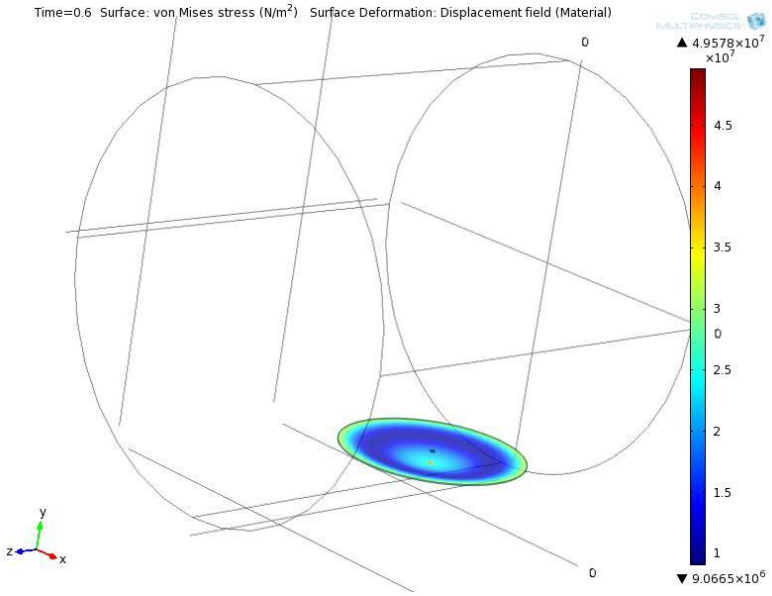


Figure 4.26: Diaphragm with 100µm hole at t=0.6s. Stress (in N/m^2) indicated by colour with red indicating maximum stress

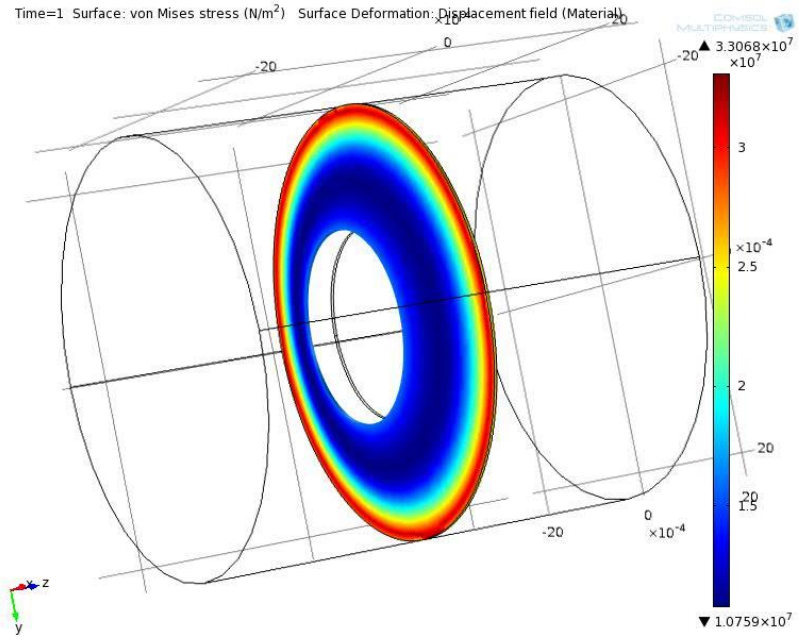


Figure 4.27: Diaphragm with 2000µm hole at t=0.6s. Stress (in N/m^2) indicated by colour with red indicating maximum stress

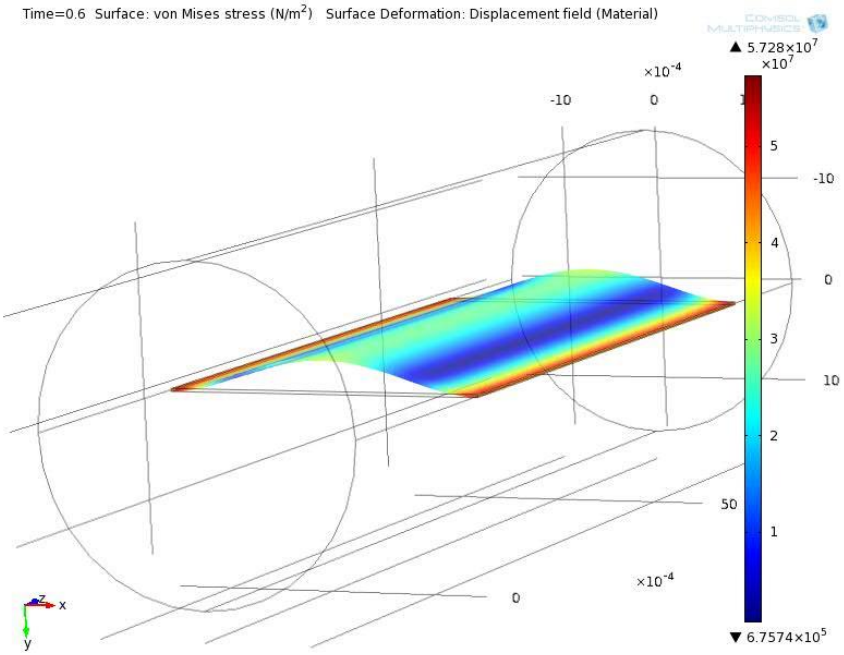


Figure 4.28: Fixed Beam at t=0.6s. Stress (in N/m^2) indicated by colour with red indicating maximum stress

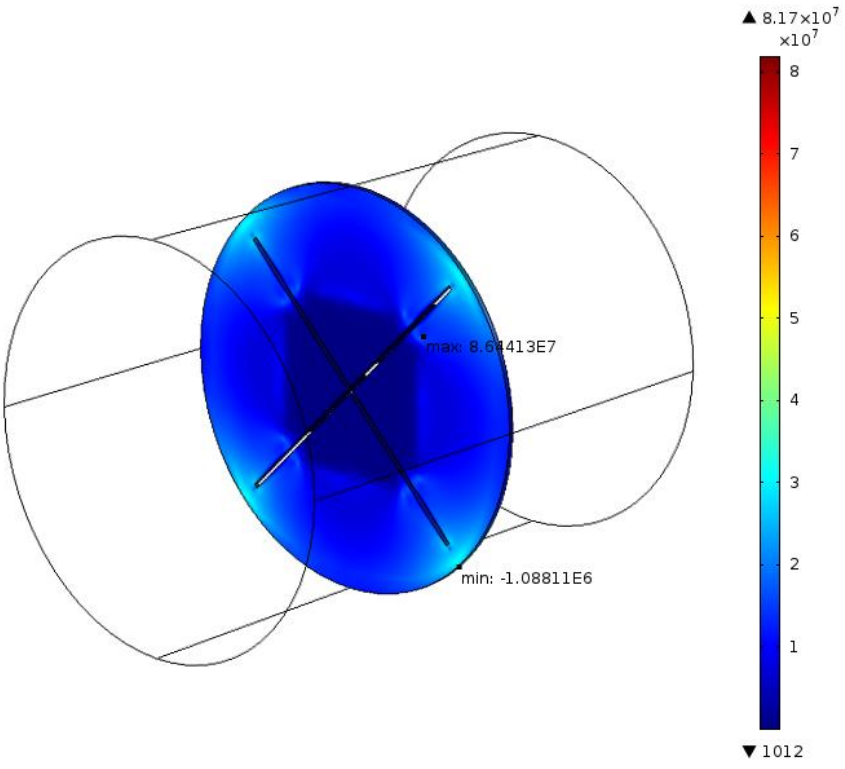


Figure 4.29: Diaphragm with Cross at t = 0.6s. Stress (in N/m^2) indicated by colour with red indicating maximum stress

Device	**Stress (GPa)**
Cantilever	1.46
Diaphragm (no hole)	0.043
Diaphragm (100µm hole)	0.0507
Diaphragm (2000µm hole)	0.023
Fixed Beam	0.053
Diaphragm with Cross	0.0864

Table 4.9: Maximum stress experienced by devices in flow

4.4. FEM Voltage Results

Table 4.10 shows the expected voltages for the devices in the flow at maximum velocity. These results show that the cantilever provides the largest voltage but it was shown from the flow results that there is an issue with this type of device placed in the artery due to the turbulence it introduces to the flow. The diaphragm device with and without the 100µm hole gave approximately the same value and this is a usable device for fluid actuated energy harvesting in an artery. However the velocity profile did show a small effect on the flow. The diaphragm with a 2000µm hole had a much lower voltage but proved to have less of an effect on the flow and therefore it is also considered to be a usable device. The fixed beam is a complicated structure to place in the artery and although the voltage is relatively high it is unlikely that this device would be a feasible option. The cross device provided a usable voltage of 0.4V but the silicon device was too stiff to deflect as expected and this caused a blockage to the flow which means that this device could not be used with a silicon substrate.

Device (AlN thickness = 500nm)	**Maximum Velocity at t=0.6s (m/s)**	**Voltage at t = 0.6s (V)**
No Device (Empty Artery)	0.4602	-
Cantilever	0.39018	5.5
Diaphragm (no hole and 100µm hole)	0.4707	1.8
Diaphragm (2000µm hole)	0.44	0.25
Fixed Beam	0.234323	0.9
Diaphragm with Cross	0.00204	0.4

Table 4.10: Maximum Velocity of Fluid and Voltage of Device at t=0.6s

4.4.1. Hole Diameter

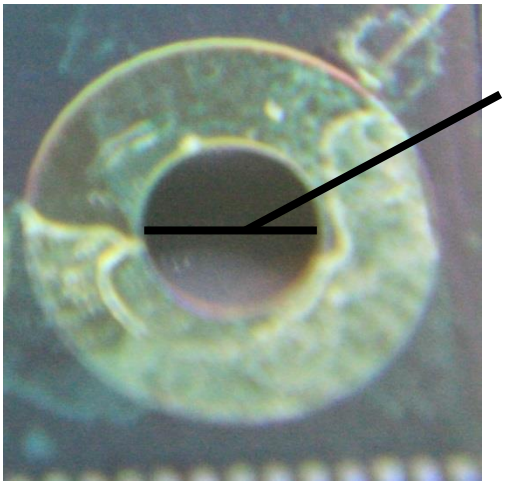


Figure 4.30: Hole Diameter from Device

Hole Diameter (µm)	Voltage Output (V)	Fluid velocity (m/s)
500	0.34	0.40
1000	0.31	0.42
1500	0.27	0.43
2000	0.25	0.44
2500	0.19	0.44
3000	0.11	0.44
Pipe with no device in it	N/A	0.46

Table 4.11: Effect on Fluid Velocity and Voltage Output for Varying Hole Diameters

The initial hole size for the diaphragm was chosen without consideration of other hole sizes. Since this design proved to be a good one for further testing it was necessary to investigate the hole diameter to determine the best size for the next generation of devices. The original hole diameter was 2000µm so models were tested with hole sizes of 500µm to 3000µm. The results are shown in Table 4.11 and it is clear here that the effect on the flow is negligible for increasing the diameter of

the hole beyond 2000µm where are the flow decreasing for smaller hole sizes. The voltage continues to increase as the hole size is reduced and the active area is increased which is expected. While this increase in voltage is good the resulting decrease in fluid speed means that it was determined that future devices based on this design will retain the 2000µm hole diameter.

4.5. Experimental Results

4.5.1. Introduction

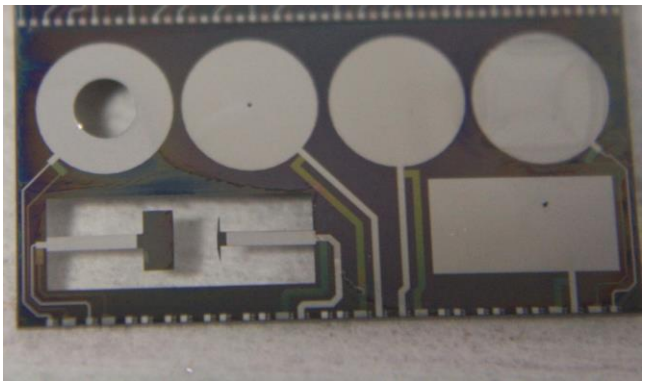


Figure 4.31: Fabricated Devices for Implantable Energy Harvesting

The fabricated devices (shown in Figure 4.31) were tested using a perfusion system which provided a pulsating flow to the fluid incident on the devices. Figure 4.35(c) shows the perfusion machine. It is a device which is used to simulate the pulsating flow of the blood. It does this by periodically compressing and releasing a tube while fluid flows through it. This is illustrated in Figure 4.32. The perfusion system allows the pressure and the velocity of the flow to be controlled so the devices can be tested under various conditions and stress levels.

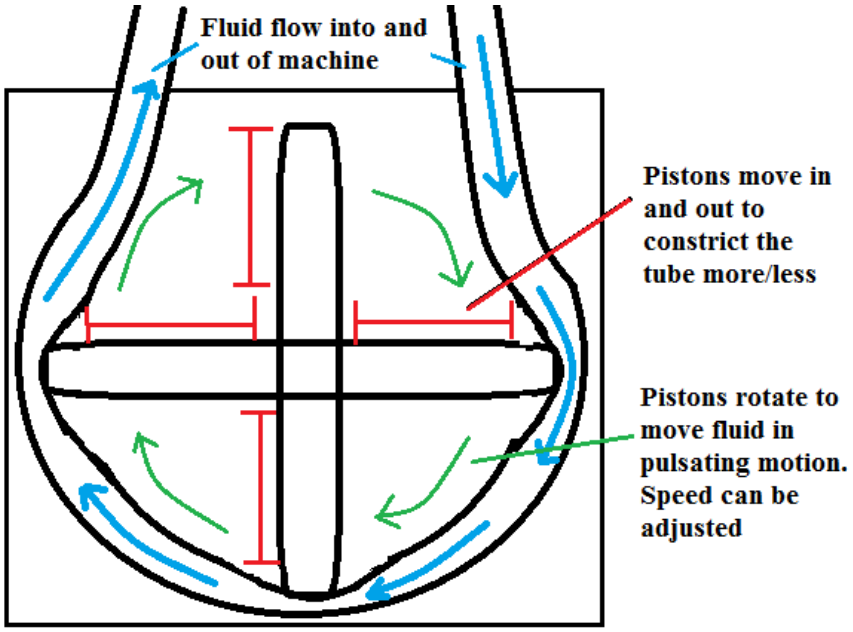


Figure 4.32: Perfusion machine operation

To insert the piezoelectric elements into the flow, two experimental set-ups were designed and fabricated in the mechanical lab. Two set ups were required because devices were designed to operate both perpendicular to the flow (Figure 4.33) and parallel to the flow (Figure 4.34). The devices were placed into the flow and the voltage and current generated were measured. From this, the power was calculated using the equations described in Chapter 3. Figure 4.35(a) shows the devices on a printed circuit board (PCB) placed into the flow fixture and (b) is the closed fixture with the devices on the PCB inside.

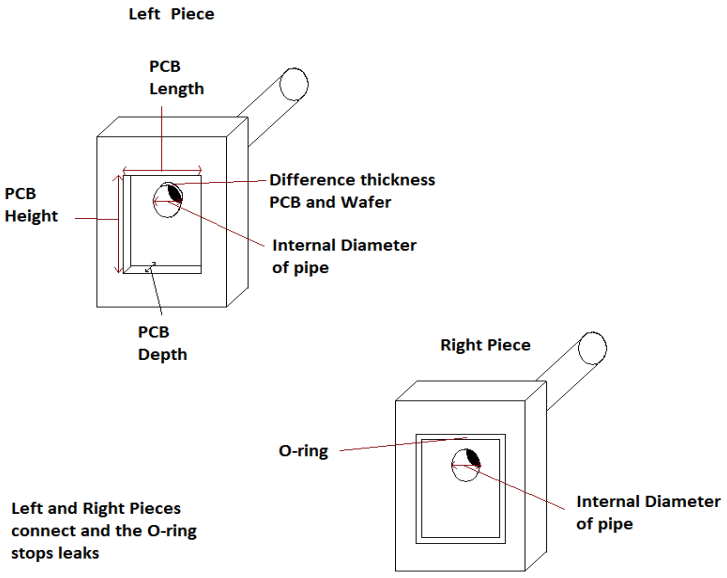


Figure 4.33: Set-up for Devices in-flow

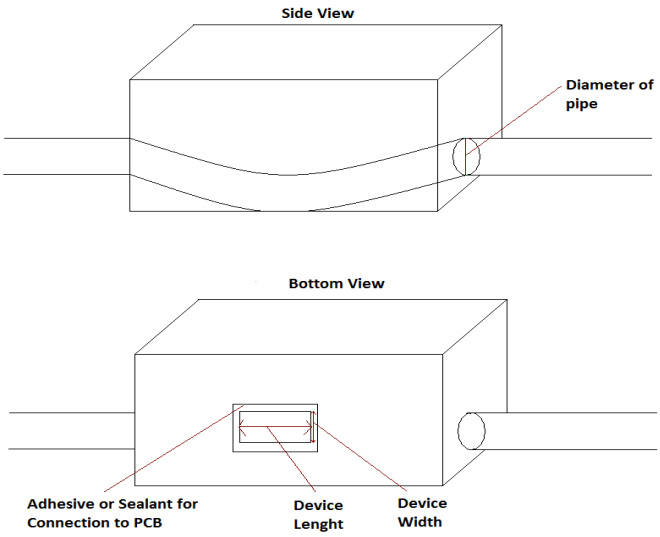


Figure 4.34: Set up for devices with flow on top

4.5.2. Perfusion Machine Results

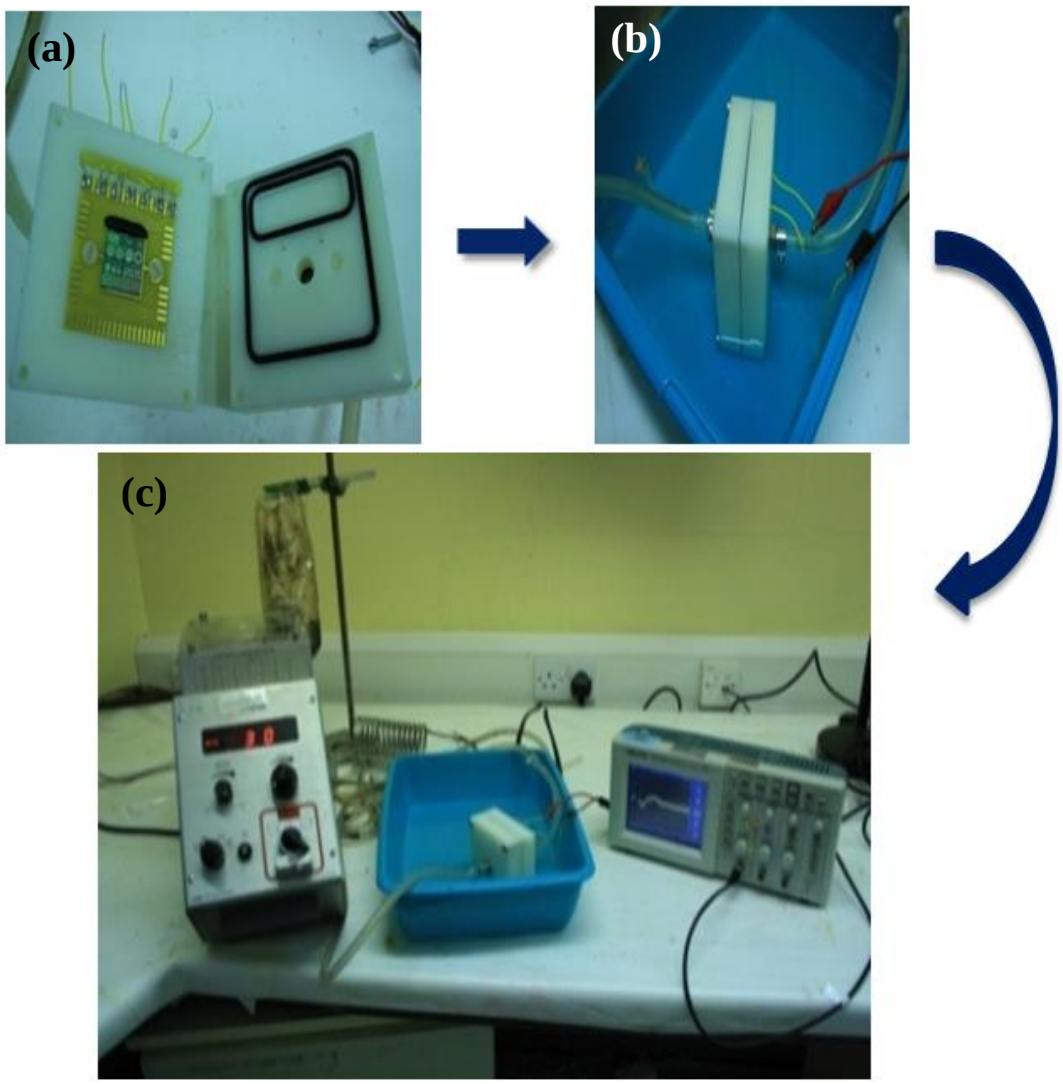


Figure 4.35: Perfusion Machine Set-up

Figure 4.35 shows the experimental set-up. The devices (full die on PCB) were placed in the holder. The two halves are connected and the holder is placed in water. The water flows into and out of the holder through the plastic tubing shown. This allows the fluid to flow over and through the various devices. The tubes are connected to the perfusion machine which provides the excitation of the devices by creating a pulsating flow. The velocity can be adjusted as well as, to a lesser extent, the pressure. The output voltage is read by connecting the wires (soldered to the PCB) to an oscilloscope.

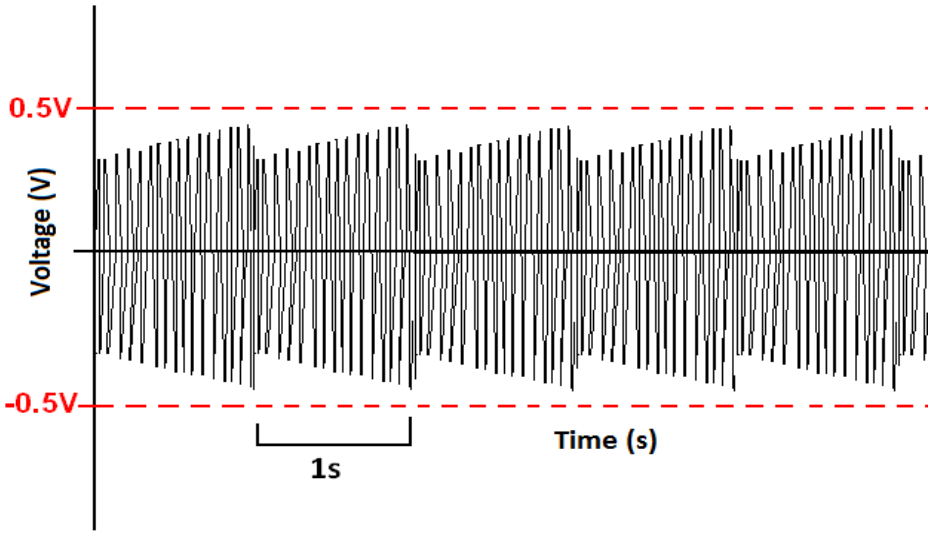


Figure 4.36: Example of Pulsating Flow

A range of test wafers were fabricated and results from two sample wafers, referred to as wafer 5 (AlN thickness 500nm) and wafer 6 (AlN thickness 1μm) are presented here. Wafer 5 gave an output of 900mVpp when the perfusion machine was operating at the highest pressure achievable. The noise in this case was 500mVpp which was taken from the noise in the system when the perfusion machine was turned off but the device was left in the flow. This result was the same for all devices which was not what was expected from the results of the models. Figure 4.36 shows a sketch of the output waveform obtained. Here 1s represents the time period for 1 beat so it is seen that over this period the voltage rises and then falls as the next period begins and the stress is lessened. Over a 1s period the output increases to a maximum and then returns to a minimum in the next second. This shows a periodic output of 1s which is to be expected. Also there is a significant amount of noise in the system and this is also to be expected due to the environment in which the device is placed. For Wafer 6 the output was 1.5Vpp with a noise level of 500mVpp. The noise level is the same in both cases which may be due to the relatively small difference in the thickness of the AlN compared to the full structure, even though the increase in AlN thickness is significant from the energy harvesting point of view. This increase in output is directly attributable to the increase in thickness of the AlN.

The experimental results are shown in Table 4.12: what is evident here is that the measured voltage is significantly different from the modelled results. Of

particular interest is the voltage measured on the Fixed Beam which is higher than that modelled. This slight increase is due to the effect of the coupling of the devices. This was seen previously with the array of structures. When devices are on the same die and are excited they have an effect on each other which can increase the measured voltage compared to a device which is excited individually. The lower voltage on the Cantilever and the Diaphragm which is the same measured voltage as on the Fixed Beam confirm this coupling between devices. This result shows that to properly test the individual devices they need to be tested separately so that this coupling does not occur.

Device (AlN thickness = 500nm)	**Maximum Velocity at t=0.6s (m/s)**	**Modelled Voltage at t = 0.6s (V)**	**Measured Voltage (V)**
No Device (Empty Artery)	0.4602	-	-
Cantilever	0.39018	5.5	1
Diaphragm	0.4326	1.8	1
Fixed Beam	0.234323	0.9	1

Table 4.12: Results of Measured vs. Modelled Voltage Results

A reason for the low output voltage could have been due to the pressure in the system. The pressure was set on the perfusion machine by decreasing the diameter of the tube as shown in Figure 4.32. The pressure is set to a particular value on the machine but there is no feedback to the machine so the pressure set by the machine considers a closed loop with no leakage or pressure drop throughout the length of the tube. There was a pressure monitor on the tube but this was placed near the profusion machine which was a significant distance along the tube from the location of the device holder and it was thought that this reading may not be accurate due to the leakage and non-ideal pressure in the tube. The assumed pressure was taken to be the pressure which was set on the perfusion machine. To test this assumption and to determine the accuracy of the models the pressure at the holder was tested.

4.5.3. Pressure Testing

To investigate the use of a polymer and determine an accurate reading of the pressure a PVDF film with a 2mm hole, as shown in Figure 4.37, was placed in the flow. The hole was made in the device so that fluid could flow though the device and therefore through the full perfusion system. The results from this were compared to those of an FEM (shown in Figure 4.38). The colours indicate the stress with the blue area being minimum stress and the red area the maximum stress. As seen previously the areas of maximum stress correspond to the anchor points.

The output from the PVDF was about 1.5Vpp and this corresponded to a pressure profile of 30mmHg to 25mmHg. This was also compared to the pressure sensor on the system and found to show the same value. As discussed above, it was thought that the pressure sensor may not be correct as it was placed very far away from the fixtures on the tube and was different from the pressure to which the perfusion machine was set. The FEM models however confirm that the pressure in the tube was the same as the pressure reading from the sensor. This is less than that which would be experienced by the device in the blood flow (typically 80 to 120mmHg). The perfusion machine was set to produce a pulsating flow at the pressures typically found in the bloodstream but these tests showed that that was not what was being experienced by the devices in the holder. This reduction in pressure could not be rectified by adjusting the perfusion machine because the maximum pressure was too low to compensate for the leakage in the system.



Figure 4.37: PVDF sample for measuring pressure

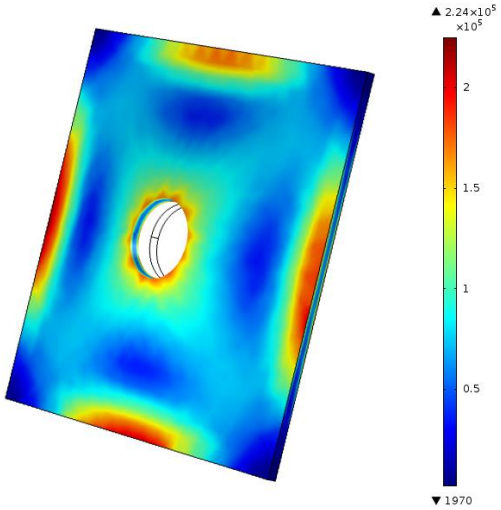


Figure 4.38: COMSOL model of PVDF sample. Colour indicates (in N/m^2) stress with maximum stress in red.

The reason for this is due to the fixtures which were leaking fluid during the experiment. The perfusion machine was expecting a perfect seal and without this the pressure could not reach the pressure set on the machine. There is no feedback to the perfusion machine and therefore the only way to determine the pressure was through the FEM and pressure sensor work. This reduction in pressure as well as the coupling of the devices explains the difference in the measured and modelled output voltages. For these reasons the fixtures had to be redesigned to reduce leakage and therefore maintain the pressure in the system. To do this extra O-rings and a recess on one side of the hold so that one section could fit into the next were suggested for future device testing. These changes to the holder would mean that the seal would be tighter and therefore the problem of leakage would be solved. The other problem highlighted was the coupling of the devices and to counteract this, the fabrication layout was redesigned so that the next generation of devices could be placed in the holder one at a time.

4.6. Summary

Various geometry devices for harvesting energy from fluid flow were examined including cantilever and diaphragm structures. FEM models provided information on the fluid characteristics of an empty artery and these models were used to compare the effect the various devices would have on the blood flow. These models were compared for the turbulence and fluid velocity that they introduce because

these were considered to be the vital characteristics which could contribute to particle deposition on the artery walls and devices. These results were also used to examine the stress experienced by the devices in flow and therefore the reliability of the silicon over normal pressure ranges. The stress results were also used to calculate the expected maximum voltage which would be available for each pulse.

The modelled voltage and modelled fluid results showed that the diaphragm designed to operate perpendicular to the flow was an excellent candidate for use as an energy harvesting device. The initial hole diameter (2000µm) was chosen at random and therefore it was necessary to examine this diameter further to optimise the device structure. From these results it was seen that for maximum voltage output and minimum effect on flow the best diameter for these devices was in fact 2000µm.

A test set-up was then designed using a perfusion machine to simulate the pulsating flow and from this the voltage was measured using an oscilloscope. However, the voltage results were inconsistent with the models as they were much lower than expected. To investigate the pressure of the system a PVDF device with a small hole to allow for fluid flow through the device was placed into the flow and the output was connected to an oscilloscope. The voltage results were compared to the voltage results of an FEM at standard blood pressure and it was found that the power output was significantly lower than expected. The model was then changed so that the voltage was set to the measured voltage from the device placed in the flow and excited by the perfusion machine. From this model it was found that the pressure equivalent was much lower than the pressure set on the perfusion machine. The reason for this was found to be the leakage in the fixtures. New fixtures were designed to be used for future testing.

This work has been presented in ICMTS [106].

Chapter 5:

Polymer Materials

5.1. Introduction

Due to the nature of Aluminium Nitride (AlN) it is usually deposited on a silicon substrate as has been described in Chapter 2. However, for biomedical applications it is usually preferable to use a polymer material because it is less stiff than Si and therefore mimics the human tissue more closely. Flexible piezoelectrics are used in a number of biomedical applications including artificial skin and muscles and tactile sensing [72]. Flexible piezoelectric material has also been used in wearable energy harvesters such as the shoe pressure devices discussed in Chapter 1 [65]. For fluid flow, in particular, it would be much closer to the material composition of an artery and therefore, it is necessary to investigate the use of such polymer materials for this application. Therefore, it is seen that flexible piezoelectric materials have a wide range of applications both inside and outside the body generating power using human motion. For the devices discussed in this work, the most important considerations are still the biocompatibility of the material and this chapter outlines

the use of a polyimide substrate for AlN growth as well as Polyvinylidene Fluoride (PVDF) because these materials are biocompatible. PVDF is a very useful material because it is highly flexible as well as biocompatible. However, it needs to be poled and it has a lower piezoelectric coefficient than AlN. AlN is a ceramic material and its piezoelectric constant is highly dependent on its crystal growth. Previous studies into growing piezoelectric materials have not obtained good quality piezoelectric AlN due to the amorphous polyimide material [107] it was deposited onto. In this chapter a new polyimide/AlN flexible material is studied using XRD to determine its piezoelectric quality. The use of a flexible material in the fluid for two devices (diaphragm with 2000µm hole and diaphragm with cross structure) are examined. Flexible materials provide less power for the same stress; however, it is more likely that a flexible material would be used for an implantable device because it is also less likely to crack and break. This is due to the fact that polymers are much less brittle than ceramics and can tolerate more stress [108].

5.2. AlN Growth on Polyimide

As previously discussed, the crystallinity as well as the crystal structure, is very important to the piezoelectric properties of AlN films. Single crystal (002) oriented AlN shows excellent piezoelectric qualities which are not seen for AlN grown in other orientations or for films with multiple orientations. A lot of work has been performed to optimise the growth of high quality AlN films on silicon substrates. However, it would be desirable to have AlN grown on a polymer substrate for biomedical devices. Polyimide is a very versatile material and has been used for commercially available printed circuit boards [109]. It is biocompatible and has a number of desirable qualities such as thermal stability, mechanical strength and chemical resistance. The polyimide used here is PI-2611[110]. Figure 5.1 shows an example of the AlN material grown on the polyimide. As can be seen in this image the material is very flexible and much less brittle than silicon.

AlN was grown on polyimide and the result was tested using X-ray Diffractometry (XRD), as discussed previously, and Piezoresponse Force Microscopy (PFM) to look at the piezoelectric qualities of the material. The XRD results are shown in Figure 5.2 to Figure 5.5. In all scans the substrate is polyimide onto which Ti was deposited and AlN was grown on top of the Ti.

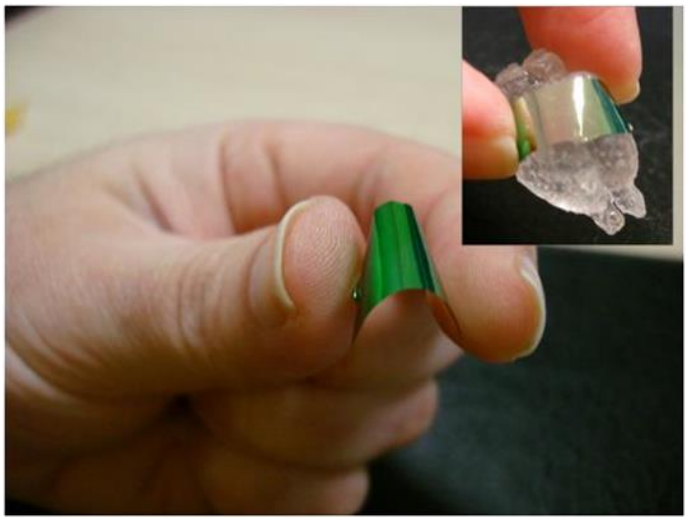


Figure 5.1: AlN deposited on flexible material for use in biomedical applications [72]

Figure 5.2 shows the 2Θ scan of the AlN grown on polyimide from 30° to 70°. The peak at 36º is AlN and the peak at 38º is Ti. It is clearly seen from this graph that there are no other peaks in the scan. This means that no other crystal orientations are present in the material. This is a huge benefit to the piezoelectric quality of the material. A previous study into the growth of AlN on a molybdenum underlayer by Petroni *et al*. [111], growing the material on commercial polyimide, showed additional peaks which would significantly affect the piezoelectric constant of the material. For comparison, the XRD results from the Petroni *et al*. AlN film are shown in Figure 5.3. In the work presented here the polyimide material was grown on a dehydrated Si (100) wafer as described by Jackson *et al*. [72] and it is the quality of this polyimide which effects the growth of the AlN to achieve the results shown here. The peaks also show that a crystalline structure of AlN (002) was achieved which is very important because amorphous AlN does not show good piezoelectric qualities [69].

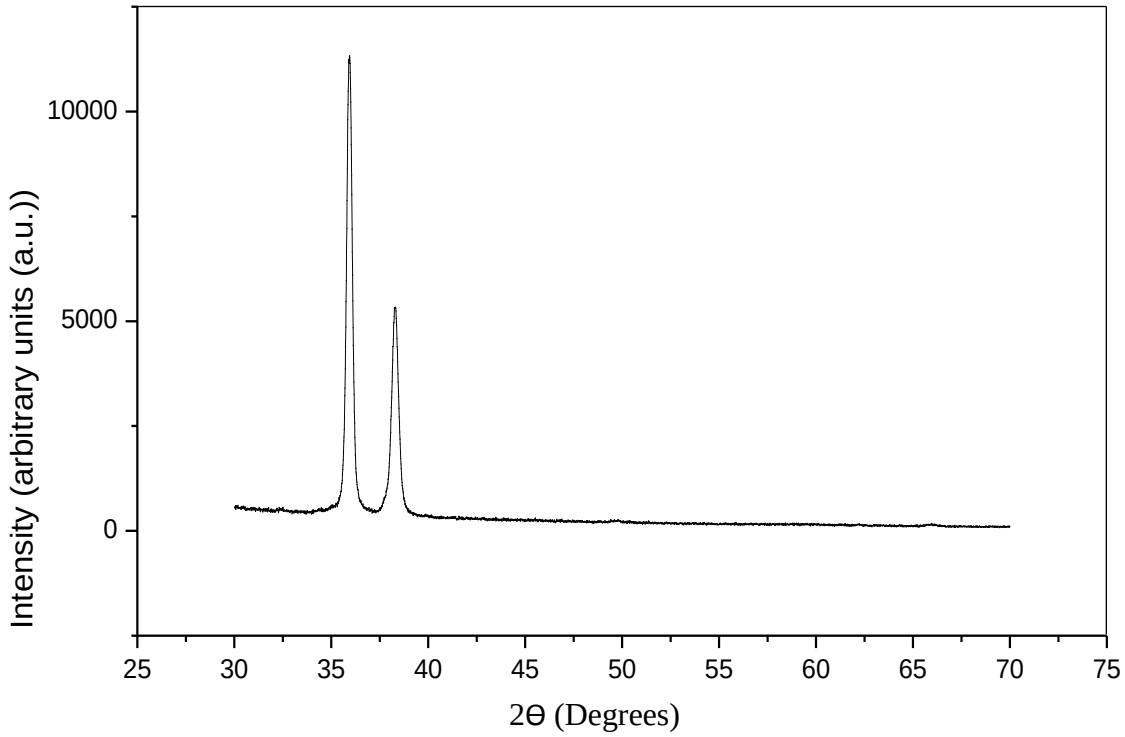


Figure 5.2: 2Θ Scan of AlN and Ti on Polyimide

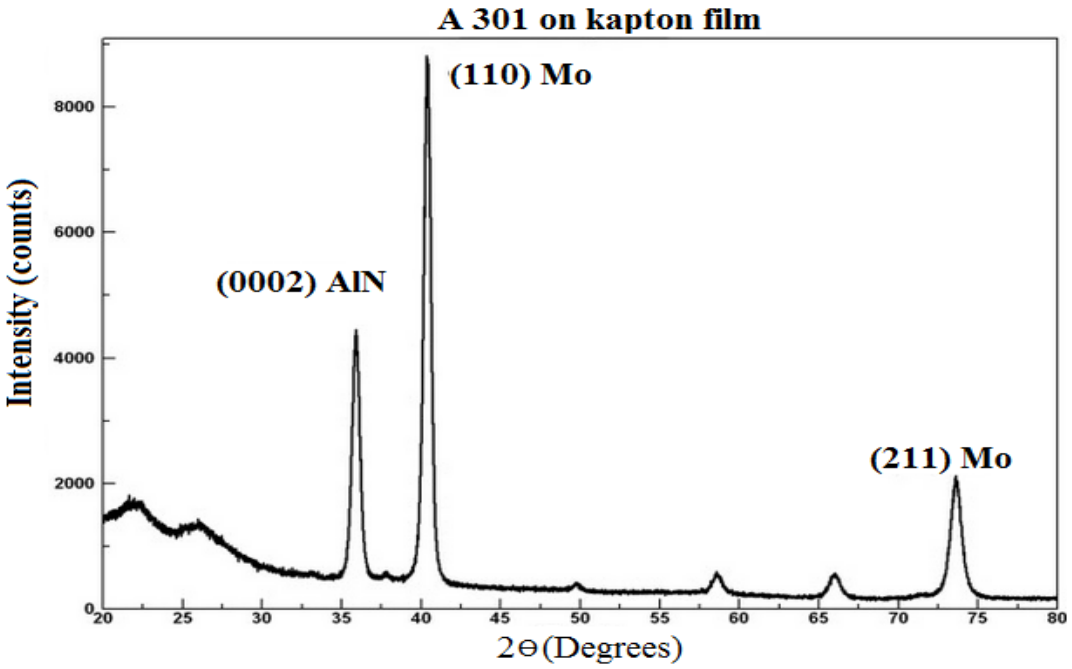


Figure 5.3: Results of Petroni *et al*. growth of AlN on polyimide [111]

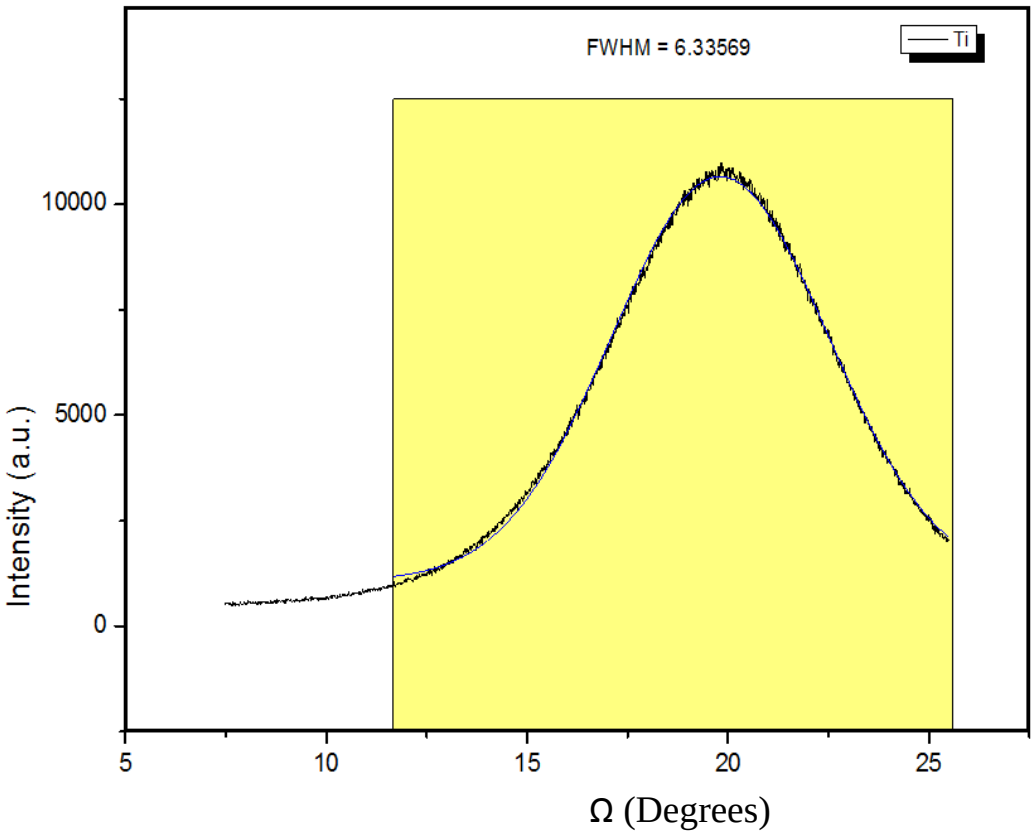


Figure 5.4: Relative Ω scan of Titanium grown on Polyimide

Figure 5.4 and Figure 5.5 are the relative Ω scans of Ti and AlN respectively. These scans show the full width half maximum (FWHM) of the materials, as described in Chapter 2, which is an indicator of the piezoelectric properties of the material. The smaller the value of the FWHM, the better the material. Previously published work by Akiyama *et al*. into depositing AlN on platinum/polyimide [112] showed a FWHM for the (002) AlN of 8.3° and depositing AlN on copper/polyimide [107] gave a FWHM of 9.1° A FWHM of 5.1° for AlN is shown in Figure 5.5 which is much better than either of these results. Examination of AlN grown on molybdenum/polyimide was presented by Petroni *et al*. [113] but the FWHM for the rocking scan analysis of the AlN is not presented.

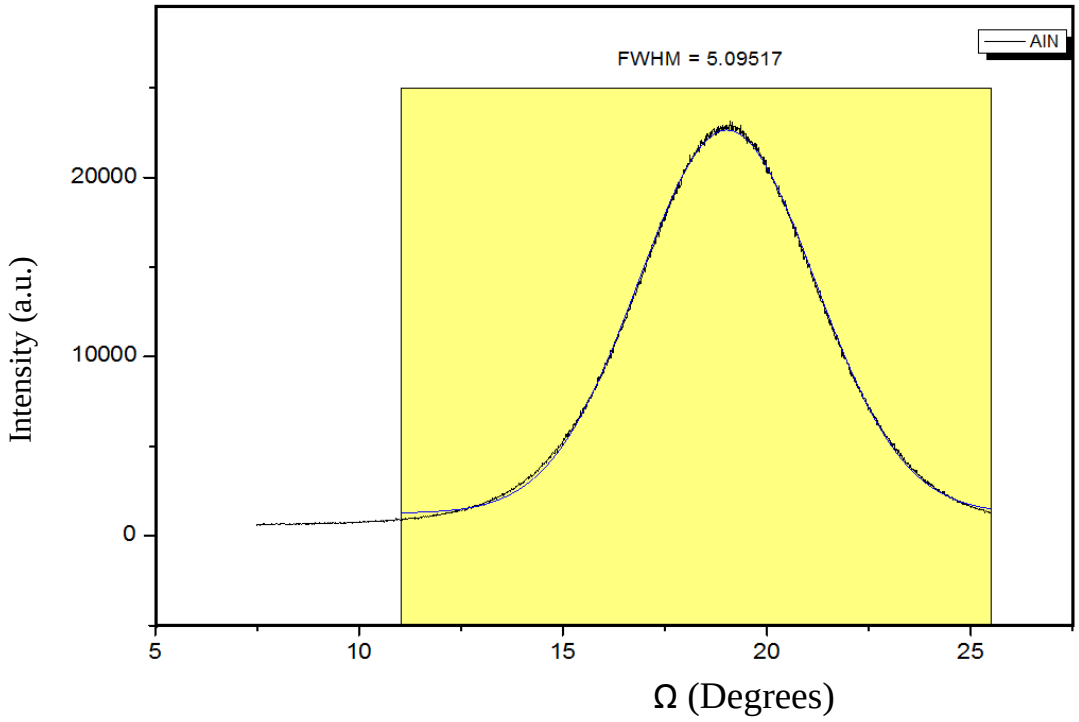


Figure 5.5: Relative Ω scan of Aluminium Nitride grown on Polyimide

Characteristic	SOA [107]	Tyndall [72]
FWHM (degrees)	9.1	5.1
d_{33} (pm/V)	0.56	1.12
Single Crystal Orientation	No	Yes

Table 5.1: Comparison of Tyndall AlN deposited on Polyimide and State of the Art (SOA)

Table 5.1 shows the results of XRD and PFM on the AlN material grown on polyimide. The state of the art results were achieved by Akiyama *et al*. [107]. This table shows that not only was a better FWHM achieved but also a high d_{33} coefficient was evident and this has a large effect on the piezoelectric properties of the material. The results presented here are better than the results achieved by Akiyama *et al*. when the rocking curve scan and piezoelectric constant are compared. The results also outperform the work of Petroni *et al*. where multiple orientations are shown in the 2Θ long scan. These results were for the first deposition of AlN on a polyimide substrate. This is very encouraging and means that while the piezoelectric results are not comparable to those for silicon, it is

possible that high quality AlN could be grown on polyimide and used in biomedical devices.

5.3. FEM Analysis of Polymer Material

In Chapters 3 and 4, silicon based MEMS devices were studied for resonant frequency response and response to fluid actuation as well as their effect on the flow of fluid through an artery. Here, two devices are studied for use with polymer material. The diaphragm with a 2000µm hole as well as the diaphragm with a cross structure were chosen because it was thought that these devices would benefit more from using a polymer substrate because due to their position perpendicular to the flow this would allow more deflection and less restriction of the flow. The cross structure on silicon substrate did not give good results because the silicon was too stiff and the fluid flow was significantly impeded. However, since the voltage results were encouraging, it is still considered that this structure might be viable when using a polymer substrate or polymer piezoelectric material because the displacement should be significantly increased.

The thickness of the AlN and the PVDF are equivalent to that of the AlN reported in Chapter 2, which is 500nm. The substrate thicknesses were chosen to be the same as the thicknesses of the Si substrate in the previous work (25µm). The same analysis as seen in Chapter 4 is presented here.

5.3.1. FEM of Diaphragm with 2000µm Hole

The results for polyimide and PVDF substrate with AlN as the piezoelectric material are discussed as well as the results of using PVDF as the piezoelectric material. PVDF is studied as the piezoelectric material as well as the substrate to provide a second polymer substrate which could be bought commercially or grown in house which is the case for polyimide. In the case of using PVDF as a substrate, poling would not be necessary because it is not required for it to be piezoelectric. Currently it is not possible to grow AlN on PVDF to test it as an AlN substrate but future work may include this. The results can be compared to the empty artery results found in Chapter 4. Figure 4.18 shows the turbulence and Figure 4.11 shows the velocity profile.

The turbulence modelled results for polyimide and PVDF diaphragm with a 2000µm hole are shown in Figure 5.6 and Figure 5.7, respectively. The turbulence is

indicated by the arrows and comparing this to the turbulence shown in Figure 4.18 in Chapter 4 shows that neither of these structures affects the turbulence to an unacceptable degree. The most interesting results are from the velocity profile. This has been identified as a critical factor already. It was thought that using a polymer would mean that the effect on the flow would be decreased. However, it is seen here that the effect is the same. Figure 5.8 and Figure 5.9 show the velocity profile with maximum velocity at the centre of the artery and minimum at the artery walls. In all cases the maximum velocity remained 0.44m/s for the diaphragm with a 2000µm hole devices.

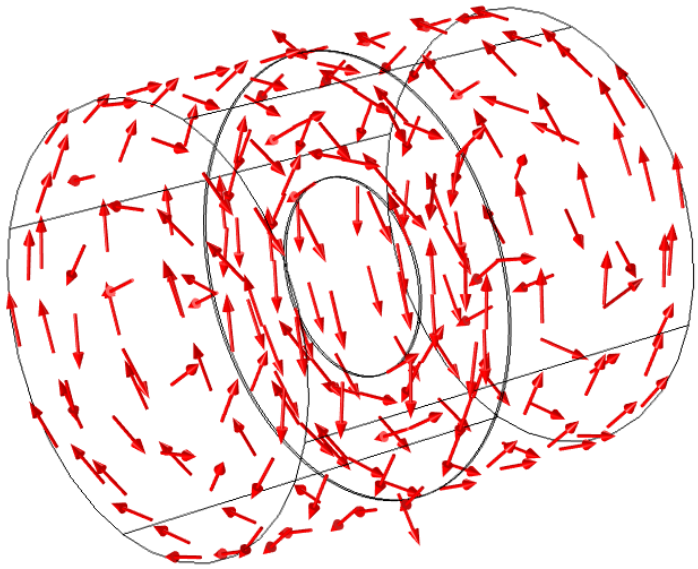


Figure 5.6: Diaphragm with a 2000µm hole, Polyimide. Arrows indicate disruption to flow

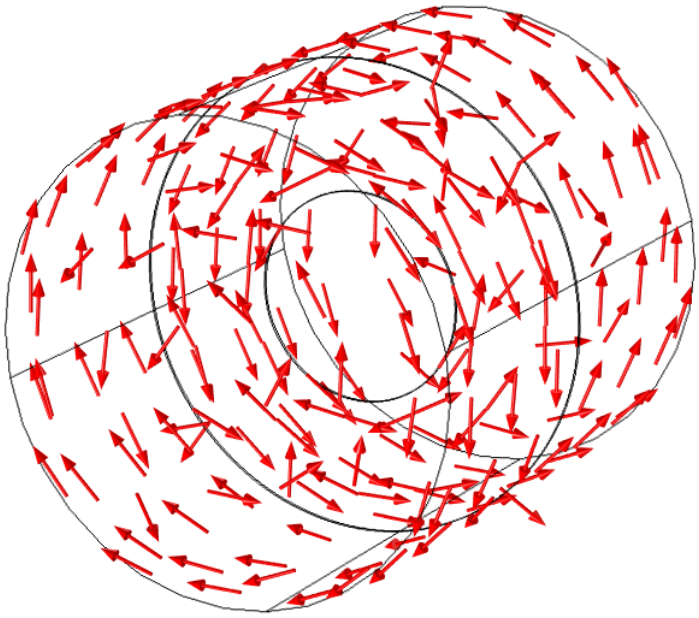


Figure 5.7: Diaphragm with a 2000µm hole, PVDF. Arrows indicate disruption to flow

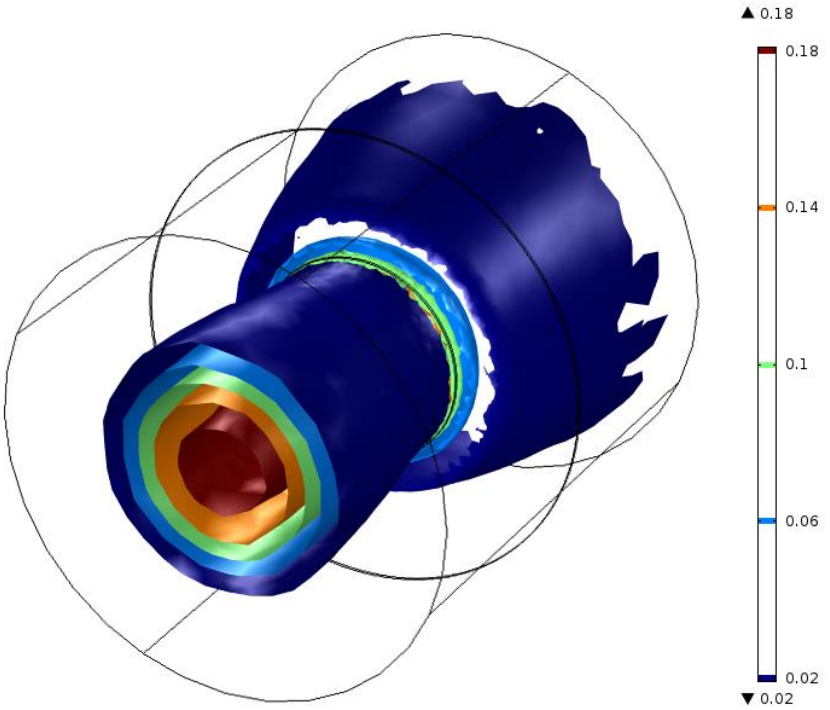


Figure 5.8: Diaphragm with a 2000µm hole, Polyimide. Velocity indicated by colours with maximum velocity in red

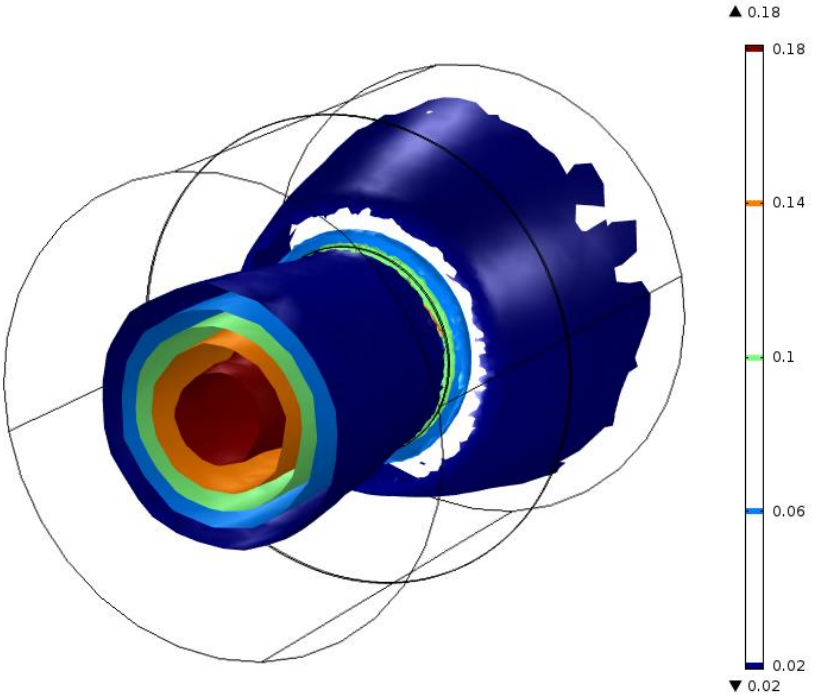


Figure 5.9: Diaphragm with a 2000µm hole, PVDF. Velocity indicated by colours with maximum velocity in red

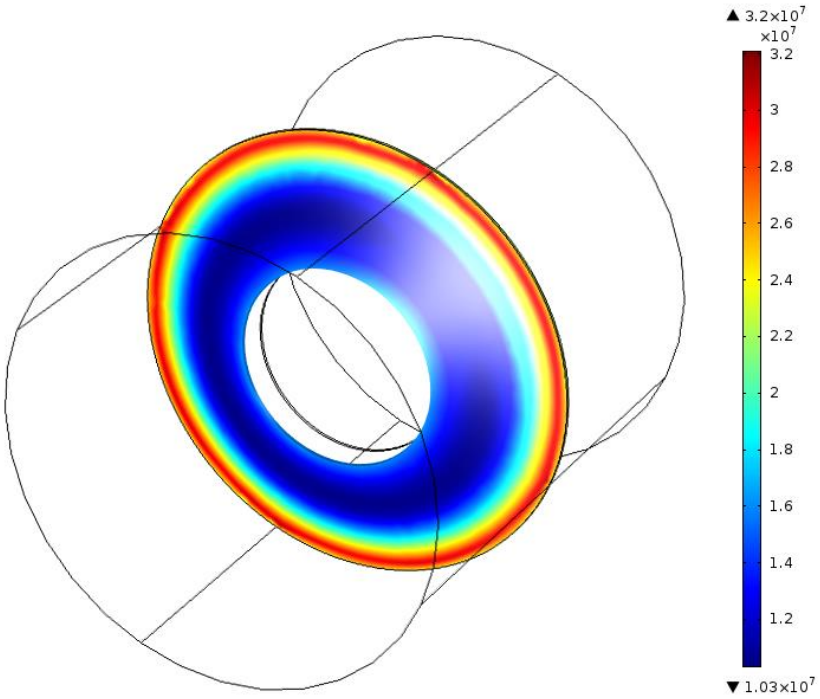


Figure 5.10: Diaphragm with a 2000µm hole, Polyimide. Stress (in N/m^2) is indicated by the colours with maximum stress in red

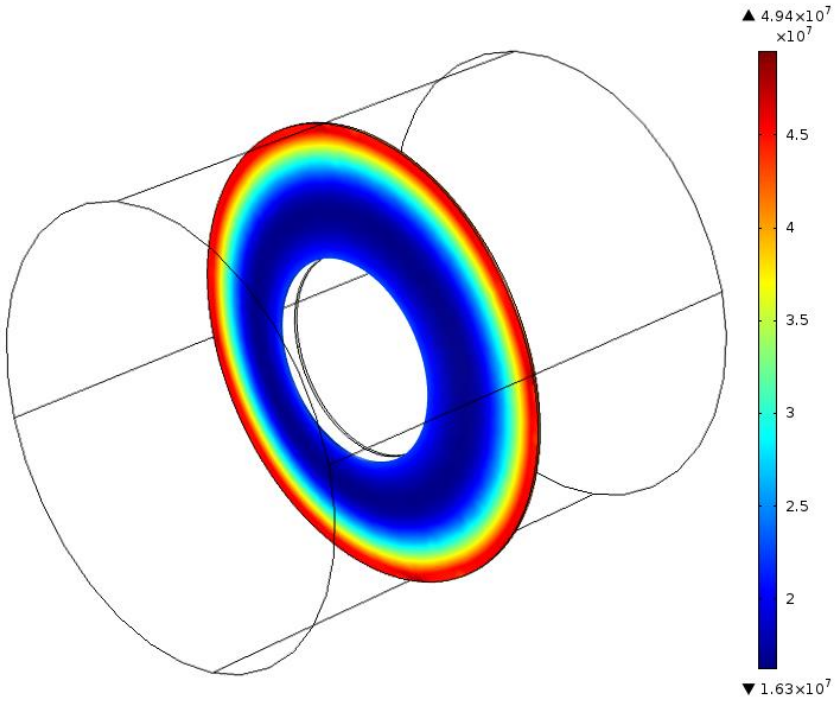


Figure 5.11: Diaphragm with a 2000µm hole, PVDF. Stress (in N/m^2) is indicated by the colour with maximum stress in red

Figure 5.10 and Figure 5.11 show the stress in the devices when excited by pulsating fluid. The stress in the device affects the voltage output. For the results of the voltage analysis the metal contacts were Ti and Al. In the case of the PVDF as both piezoelectric material and substrate the layers are PVDF substrate, then Ti as bottom electrode, PVDF as piezoelectric material and Al as top electrode so here the PVDF substrate is not electrically connected and is isolated from the PVDF piezoelectric material.

The electrical results of the simulation of the diaphragm device are shown in Table 5.2 where the voltage difference is the voltage output from the device. Using a polyimide or PVDF substrate can give better voltage results than seen for the Si device and this may be due to the more flexible material being deformed more than the Si under the same pressure. Here the material quality was assumed to be the same as that reported for the Si substrate and described in Chapter 2. XRD results presented in Section 5.2 show that this would not be the case for real material. From these results, as well as those of the fluid flow analysis, it would be recommended to use a polymer substrate for using AlN as the piezoelectric material if the AlN quality

can be increased to the quality reported for deposition onto Si. These results also show that PVDF would be a viable option for use as the piezoelectric material.

Diaphragm with hole Material	Voltage Max (V)	Voltage Min (V)	Voltage Difference (V)
Polyimide Substrate 26µm	0.941	-1.018	1.959
Polyimide Substrate 51µm	0.402	-0.978	1.380
PVDF Substrate 26µm	0.506	-0.941	1.447
PVDF Substrate 51µm	0.15973	-0.85639	1.061
PVDF no AlN PVDF substrate 26µm	0.618	-1.143	1.761
PVDF no AlN PVDF substrate 51µm	0.201	-1.054	1.255
PVDF no AlN Si substrate 51µm	0.095	-0.497	0.592

Table 5.2: Simulation voltage results for polymer material on diaphragm device

5.3.2. FEM of Cross Structure

The cross structure, shown in Chapter 4, using polyimide and PVDF is examined here. In the original design of the structure 4 masses of Si were placed on each section of the device and this was done to increase the likelihood of bending. For the polymer structures these masses have been removed because it would not be possible to grow the polymer material to the thickness of the masses and in these analyses there is no Si in the devices. The turbulence results for the cross structure using polyimide and PVDF are shown in Figure 5.12 and Figure 5.13, respectively. Comparing these results to the turbulence in an empty tube (Figure 5.6) it is seen that the PVDF structure is more similar to the flow of an empty artery and much less turbulence is seen in the flow. The polyimide material shows turbulence that could induce particle interactions and collisions which is undesirable.

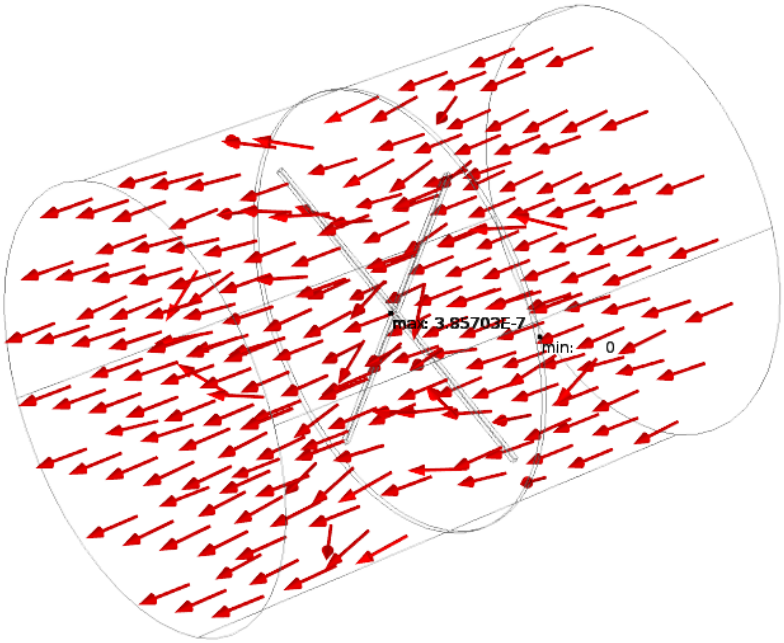


Figure 5.12: Diaphragm with a cross, Polyimide. Arrows indicate disruption to flow

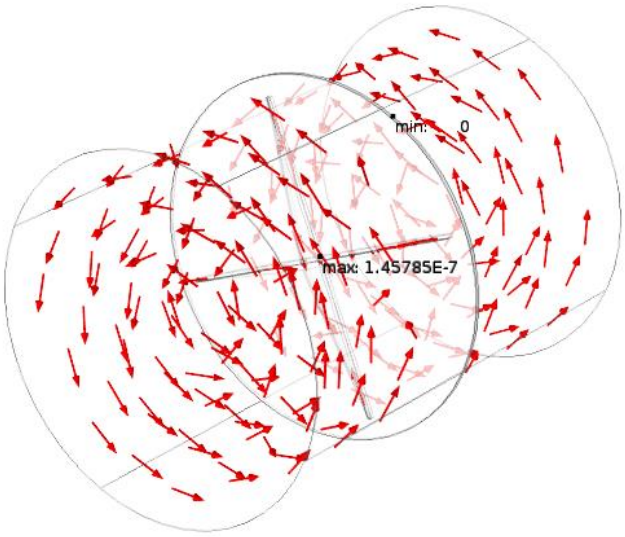


Figure 5.13: Diaphragm with a cross, PVDF. Arrows indicate disruption to flow

The velocity results are shown in Figure 5.14 and Figure 5.15 for polyimide and PVDF, respectively. The velocity profiles seen here are very different to that seen for the empty artery (Figure 4.11 in Chapter 4). The cross structure is blocking the artery and the pressure of the fluid is not enough to allow the fluid to flow unobstructed. The pressure in this system is not allowed to build-up over time because unimpeded flow is the optimum solution and hence, it is seen that for normal pressure this structure causes an obstruction in the artery. The velocity is also significantly decreased to only 0.08143m/s which is much too low for normal fluid flow (0.46m/s).

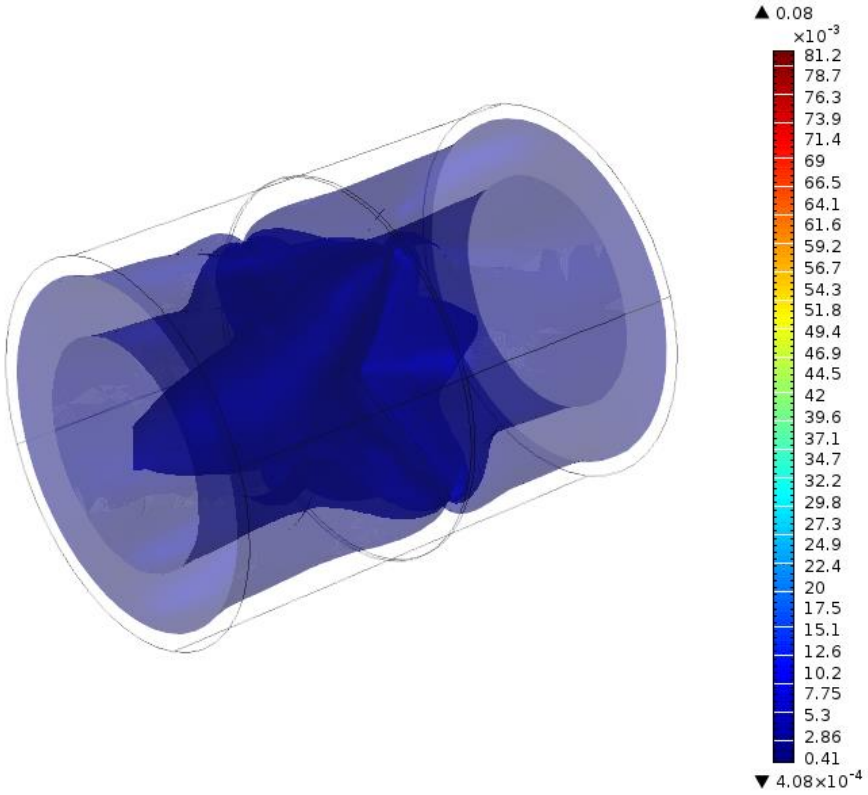


Figure 5.14: Diaphragm with a cross, Polyimide. Velocity (m/s) indicated by colours with maximum velocity in red

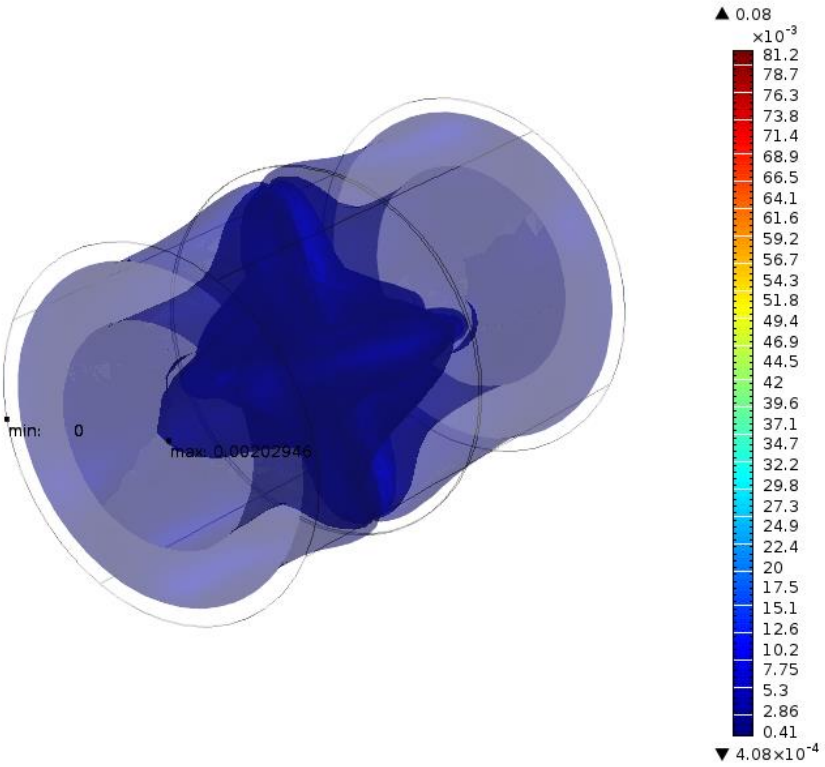


Figure 5.15: Diaphragm with a cross, PVDF. Velocity (m/s) with maximum velocity in red

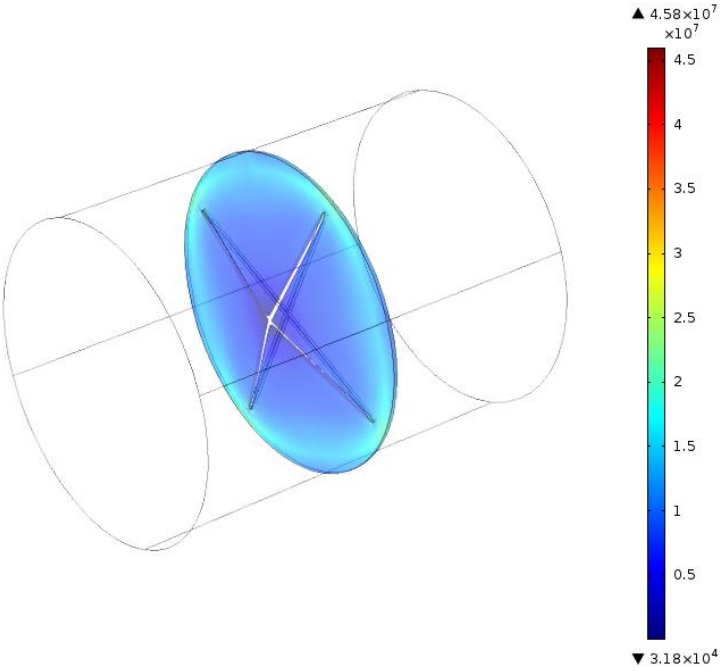


Figure 5.16: Diaphragm with a cross, Polyimide. Stress (in N/m^2) with maximum stress in red

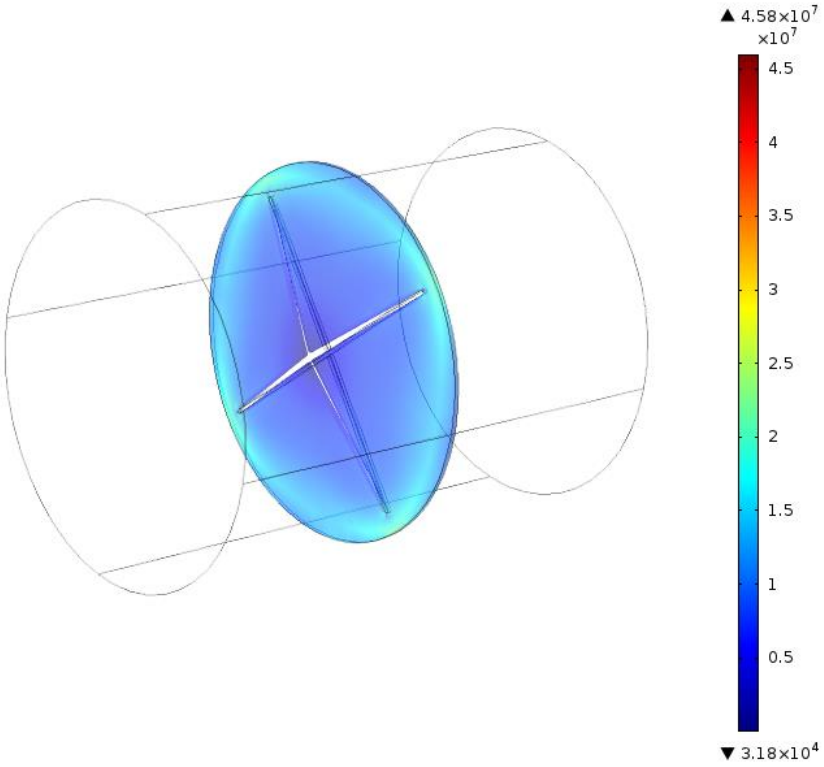


Figure 5.17: Diaphragm with a cross, PVDF. Stress (in N/m^2) with maximum stress in red

The stress results in Figure 5.16 and Figure 5.17 indicate the problem. For fluid flow at normal pressure the cross structure is not stressed enough to create a large enough opening for the fluid to flow unimpeded for either polymer material. The results from the electrical analysis of the cross devices is shown in Table 5.3. The increase in surface area has created an increase in the voltage possible. This is seen for all of the material types and thicknesses when the Si substrate is replaced by a polymer. This follows on from the fluid results where it was seen that the fluid was not powerful enough to cause a large displacement of the cross device even when using a polymer material as the substrate.

Cross Material	**Voltage Max (V)**	**Voltage Min (V)**	**Voltage Difference (V)**
Polyimide Substrate 26µm	0	-3.855	3.855
Polyimide Substrate 51µm	0	-3.093	3.093
PVDF Substrate 26µm	0	-2.628	2.628
PVDF Substrate 51µm	0	-2.381	2.381
PVDF no AlN PVDF substrate 26µm	0	-3.174	3.174
PVDF no AlN PVDF substrate 51µm	0	-2.590	2.590
PVDF Si substrate 51µm	0	-0.531	0.531

Table 5.3: Simulation voltage results for polymer material on cross device

5.4. PVDF Material Growth

An AlN film was grown on polyimide and its piezoelectric characteristics were studied. To further investigate flexible piezoelectric materials, PVDF was grown on silicon wafers. PVDF has four crystalline forms which are the nonpolar α form and the polar forms β, γ and δ [114]. To produce piezoelectric PVDF films, the β-phase needs to be induced during growth. This can be done using swelling agents which mechanically stress the material while it is being grown. To investigate the ability to grow β-phase PVDF, films of PVDF were prepared using two different recipes shown in Table 5.4. Recipe 1 was taken from He *et al*. [115] and Recipe 2 appears in work by Ma *et al*. [116]. These two recipes were chosen because the papers presented results which showed that the β-phase could be induced using these recipes. Here Dimethylformamide (DMF) is the solvent and Acetone with Magnesium Nitrate Hexahydrate

($Mg(NO_3)_2.6H_2O$) and Tetrahydrofuran (THF) are the swelling agents. The mixtures were prepared and then agitated until most of the PVDF was dissolved. Next the liquids were left for at least 24 hours at room temperature to make sure all the PVDF particles were completely incorporated into the mixture.

1. Acetone and DMF	**Recipe**
	50:50 DMF: Acetone
	0.2% wt. $Mg(NO_3)_2.6H_2O$
	10% wt. PVDF
	50:50 DMF: Acetone
2. THF and DMF	**Recipe**
	50:50 DMF: THF
	10% wt. PVDF

Table 5.4: Recipes for PVDF films

Once the PVDF was completely dissolved the fluid was deposited onto 0.4mm thickness silicon wafers slices ($1cm^2$ sections of wafer) and spun to create a uniform layer over the wafer using a Laurell Model WS-400BZ-6NPP/LITE spinner [117]. The spin speed was adjusted from 500rpm to 3000rpm to determine the effect on the film thickness. After spinning, a step was created by removing the film from half of the wafer slices using a squeegee before curing. The wafers were then cured on a hotplate for 30mins at 100ºC. The silicon wafers were used as a support structure during the fabrication process and when testing the films using the XRD and profilometer; but the films were removed from the wafers when testing the piezoelectric properties of the film using the piezometer.

The step height was measured using a KLA-Tencor AlphaStep 500 surface profilometer [118]. This is done by running a probe along the surface of the wafer from the area with no PVDF to the area with PVDF and measuring the deflection. Figure 5.19 shows the resulting step height which has an approximately linear dependency on spin speed as expected. Any defects or other particles on the material affect the height of the film. The results shown in Figure 5.18 are determined by taking the average height value of the wafer without PVDF from the average height measured at the wafer section coated in PVDF. The effect of the spin speed is significant when the speed is increased from 500rpm to 1000rpm and less

notable after this. This is explained by the relative difference in speed where here the speed is increased 100% and after this the relative increase in speed is smaller as the rpm are increased and therefore the relationship shown here is as expected. These results can be used to grow PVDF to different thicknesses. However, it must be noted that due to the limits of the profilometer and the roughness of the Si surface the exact thickness may differ by around 100 nanometres.

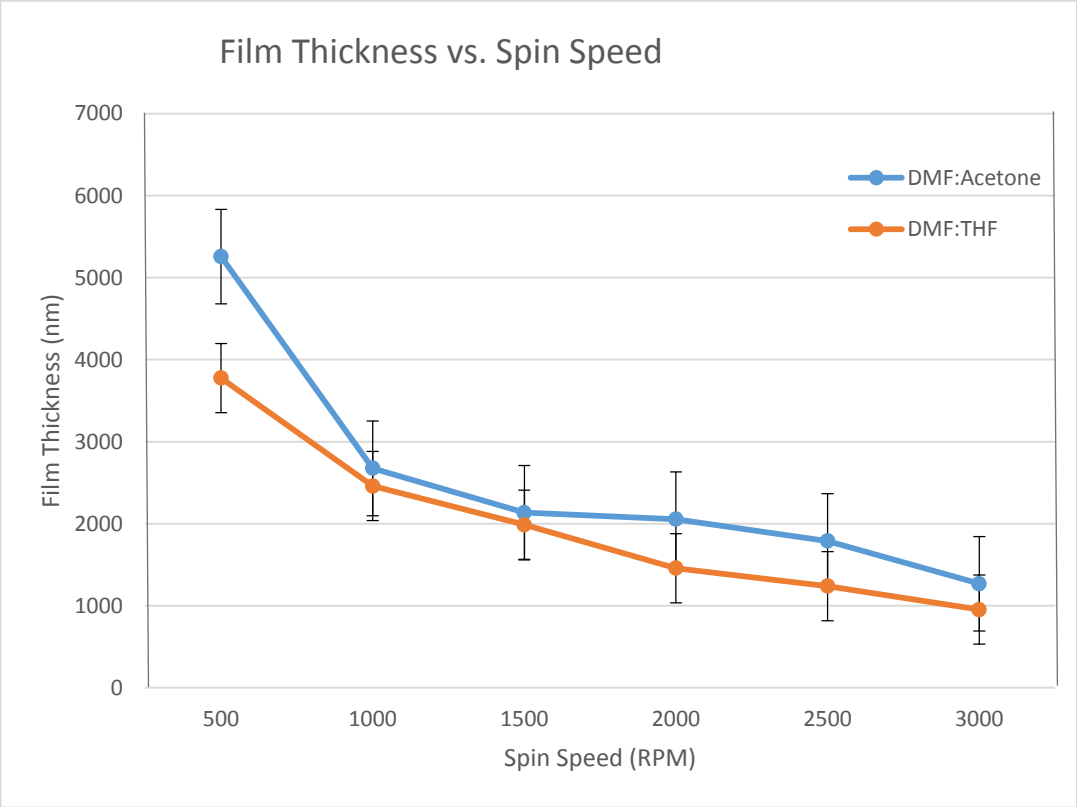


Figure 5.18: Film Thickness vs. Spin Speed

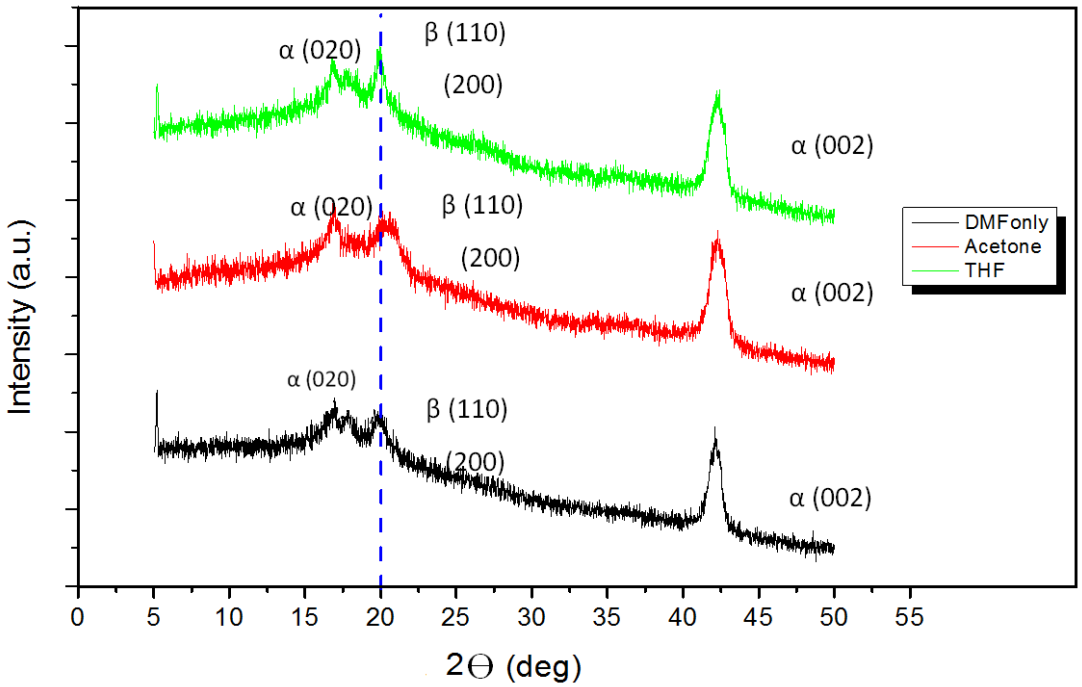


Figure 5.19: Comparison of PVDF fabricated with different Swelling Agents using XRD

Figure 5.19 shows the results from a wide angle XRD 2Θ scan of the PVDF films with the various swelling agents. To create a piezoelectric film the β-phase must be achieved. This is indicated by a peak around 20°. As is shown in this graph, β-phase is only achieved when using THF. In the paper by Ma *et al*. [116], the concentration of THF was investigated and as this was the only result that achieved β-phase it was necessary to determine the best concentration. To this end, more PVDF films were created using different concentrations of THF, namely 2:8 and 8:2 THF: DMF. In the work of Ma *et al*. [116] the best result was shown at a 5:5 concentration. It was only compared to concentrations above 5:5 though; so for this study, concentrations above and below were considered. It is shown in Figure 5.20 that β-phase is only reached for 5:5 concentration indicated again by a peak around 20°. In both figures, a number of α-phases are seen and this is consistent with the results of growing β-phase PVDF films in the literature.

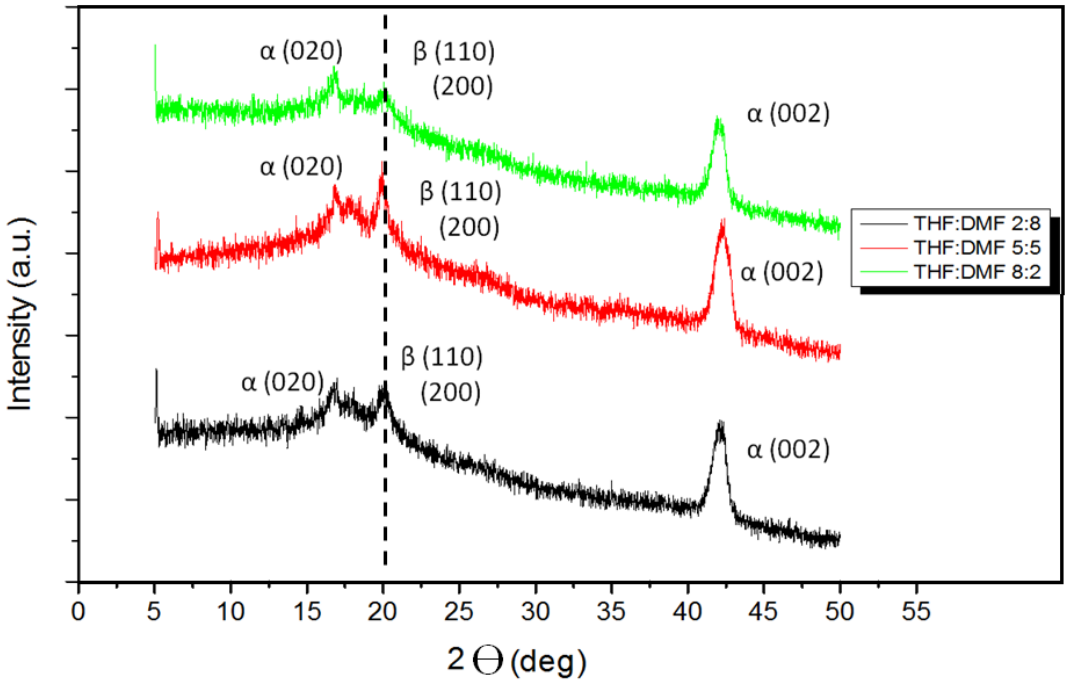


Figure 5.20: Comparison of sample with different THF Concentration

The XRD results for 5:5 THF:DMF (Figure 5.19 and Figure 5.20) show that it is possible to establish β-phase in PVDF films but to make it fully piezoelectric it must then be poled i.e. its molecular chains must be oriented by mechanical stretching. Because the equipment required to pole the film was not available, the piezoelectric nature of the film was tested without poling. The test was carried out using a piezometer (Piezotest d33 PiezoMeter System [119]) which applied a vibrating load of 2.5N at 110Hz. The response was measured through electrodes on the top and bottom faces of the material. For the AlN film which was deposited on Si this required the material to be etched through and a connection made to the Ti layer on the bottom. This means that the result is not ideal. The PVDF films were deposited on glass slides so that they could be peeled off and then a conducting ink was applied to the top and bottom so that the piezoelectric properties could be measured. The results are shown in Table 5.5 which compare with the results seen in Figure 5.19. The β-phase was only seen for the THF: DMF PVDF film and it is seen in Table 5.5 that the material is piezoelectric. The response is much less than that of the commercial material but this is to be expected when it has not been poled. The results for the commercial PVDF were measured from the piezometer and

compared to the value provided by the manufacturer and it was seen that these values matched so that the results here can be considered to be correct.

Material	**Piezoelectricity pC/N**
AlN (grown on Si)	4 - 7
PVDF THF: DMF (5:5)	5.4 – 5.6
PVDF Acetone: DMF (5:5)	0.1
PVDF (commercial) [110]	22

Table 5.5: Results from Piezometer

5.5. Summary

AlN grown on polyimide was investigated for its piezoelectric qualities using XRD and PFM and the results were compared to the current state of the art in the literature for commercial polyimide. The polyimide here was grown especially for use as an AlN substrate and it was shown that the achievable piezoelectric results are better than those presented in the literature to date. A (002) oriented AlN film with 5.1° FWHM and no other orientations was grown on polyimide with a Ti underlayer and the corresponding piezoelectric d_{33} of 1.12pm/V is twice that reported by other researchers.

The use of polymer substrates (PVDF and polyimide) instead of Si was investigated using FEM as well as the use of PVDF as the piezoelectric material to replace AlN. Two device structures were chosen to test the polymer substrates. The results indicate that a polymer substrate could be used for the diaphragm with a 2000µm hole and the power output would be improved compared to a Si structure. It was also shown that the cross structure is not viable even when using a polymer substrate as pressure would need to be allowed to build-up before it would deform enough to allow fluid to flow unimpeded.

Also, PVDF films were grown and tested to determine if it would be possible to create a reasonable piezoelectric material. Two recipes were examined and it was found that a good quality film could be grown and a piezoelectric response was seen without poling the material. The result of the piezometer was compared to the result obtained for AlN grown on Si and it was found that the unpoled PVDF material response was comparable to the AlN. Better results would be achieved for poled

PVDF and it is considered from these results that poling the PVDF material grown in this study would provide results comparable to commercially available PVDF films. However, since the equipment to pole the material is not available currently, the film could not be poled so the full piezoelectric response could not be determined. The results are encouraging though and it shows that even without poling a piezoelectric material was grown.

Chapter 6:

Review of Energy Harvesting Circuits

6.1. Introduction

Piezoelectric energy harvesters (PEH) generate an AC voltage which needs to be rectified before it can be used to power devices which usually require a DC bias. This rectification can be done in numerous ways and various rectification schemes have been investigated over the past decade. A good review of energy management circuits for PEHs was carried out by Szarka *et al*. in [120], as well as by Dicken *et al*. [121] where various circuits are evaluated over the same operating conditions. In this Chapter a review of energy harvesting circuits is provided for low power energy harvesting circuits with a view to identifying a design to be used in conjunction with the devices to build a fully working system in the future. Typical values for the devices with a silicon substrate for a half pulse at a frequency of 1Hz are provided in Table 6.1.

Device	**Voltage (V)**	**Reactance (MΩ)**	**Current (μA)**	**Power (μW)**
Cantilever	5.5	285.47	0.0193	0.11
Diaphragm	1.8	62.84	0.0287	0.052
Diaphragm with 100μm hole	1.8	63.24	0.0285	0.051
Diaphragm with 2000μm hole	0.25	78.06	0.0032	0.001
Fixed Beam	0.9	55.51	0.016	0.0146
Diaphragm with Cross	0.4	63.30	0.006	0.0025

Table 6.1: Device Electrical Parameters for a half pulse at 1Hz frequency

This table shows that for operating these devices off the resonance frequency the power is very low but for some of the devices the voltages are high enough so that voltage drops in the circuit would be acceptable. However, for other devices such as the diaphragm with 2000μm hole a voltage doubler might be necessary and for all of the devices the power is low and therefore low power circuit elements will have to be used. Considering this is the power for a half a pulse at a typical frequency of 1Hz or 60bpm then the available power will be usable but converting and storing such low power will provide a significant challenge. The low power available from an individual device shows that multiple devices will need to be used so that the overall power provided by the system will be increased for each pulse. For these reasons the energy harvesting circuit design will be an interesting challenge and an initial investigation into possible solutions is conducted in this Chapter.

For the devices discussed in this thesis average output voltages are around 1Vpp which means that voltage is high enough to be usable. However, the power available is very low because the current is typically in the order of μA. Typical values available from the energy harvesters discussed in the previous chapters are less than 0.1μW which is very low power and this means that the circuit power consumption is critical. In this chapter various methods for rectifying the input current of an energy harvester from AC to DC are discussed. As the power is very low for each individual device, it is considered that this scheme will need to use a number of devices operating concurrently with their outputs added together so that usable charge can be made available to the systems that needs it. Circuits which can achieve this addition of charge have been simulated and bread-boarded to investigate

their ability to cope with the circuit constraints. Circuits considered here include circuits based on Op-amp operation as well as investigations into circuits based on designs by Romani *et al*. [122] and Guilar *et al*. [123]. A voltage multiplier circuit is also presented because being able to increase the voltage is very useful for many forms of energy harvesting where the voltage is too small to be usable such as with solar power and also a voltage multiplier circuit could be used in conjunction with some of the devices previously discussed.

The most basic power management circuit is a diode based full wave rectifier, as shown in Figure 6.1. Since the output from the device excited by vibrations is not consistent or stable as a function of time, buck, boost or buck-boost converters are often used in conjunction with rectification to provide a constant voltage output. This is important for most electronic systems because they normally require a continuous operating voltage. Figure 6.2 shows the input and output waveforms from a full wave rectifier. This output can be used with the converters discussed in this work or with an output capacitor which can be used to smooth the output. This is the simplest form of rectification. However, a number of schemes have also been investigated for voltage management to increase the efficiency and output from piezoelectric transducers.

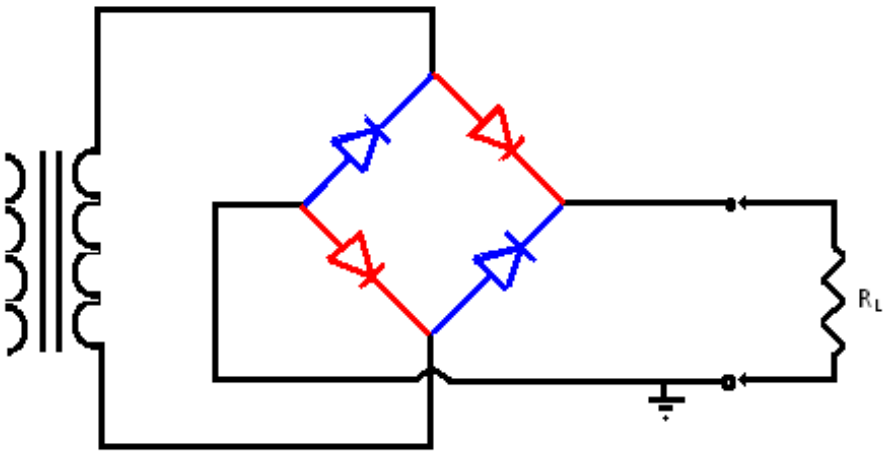


Figure 6.1: Full Bridge Rectifier

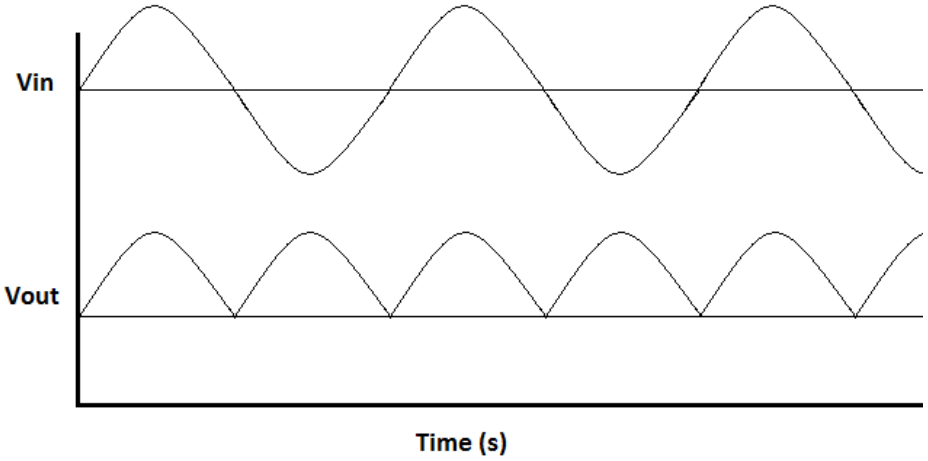


Figure 6.2: Input and Output voltages from Full Bridge Rectifier

Here the development of a flexible (bendable) energy harvesting circuit will not be discussed as it is out of the scope of this work. However, the final solution for these energy harvesting devices would be coupled with a flexible circuit which would respond to difference in the load impedance due to the changes in the blood flow when exercising, resting, etc.. A PEH circuit using a supercapacitor (Figure 6.3) was presented by Pörhönen [124] which only uses a simple diode rectifier circuit but the results show that a printed circuit would be possible in the future.

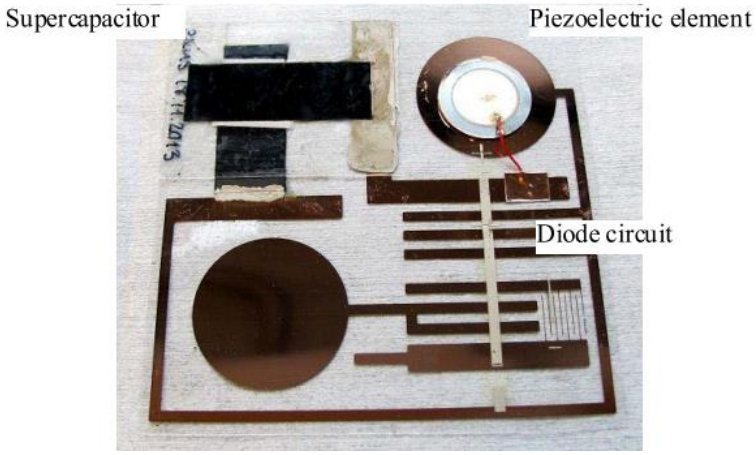


Figure 6.3: Flexible energy harvesting diode rectifier circuit with integrated supercapacitor and energy harvester [124]

6.2. Energy Harvesting Circuit Approaches

A very popular circuit for voltage management is to use a synchronous switch harvesting on inductor circuit (SSHI). The SSHI technique combines a switching circuit controlled by a maximum or minimum deflection of the piezoelectric device and an inductor. When a maximum or minimum occurs the switch is closed and a resonance circuit is created with the internal capacitance of the piezoelectric element and the inductor. This resonance is seen by the piezoelectric element as strain in the opposite direction to the deflection of the device which increases the stress in the device and therefore the voltage output. An example of this circuit designed by Chen *et al*. [125] is shown in Figure 6.4. Various forms of this circuit have been investigated and examples can be found in the work of Chen *et al*. [125] , Liang *et al*. [126] and Sun *et al*. [127]. Sun *et al*. [127] use MOSFETs instead of diodes. SSHI is used by Liang *et al*., [126], to reduce the loss of electrical energy being returned to the mechanical part of the system and therefore increase the overall efficiency. In the work of Chen *et al*. [125], velocity controlled SSHI is discussed. Here, the switching is controlled by a velocity control circuit instead of a peak detector which theoretically should address the phase lag issues associated with peak detection. A further advance on SSHI was made by Lallart *et al*. [128], where a buck-boost static converter is added to an SSHI configuration . This set up allows energy to be extracted independent of the load and leads to a harvested energy gain of over 500% compared with the traditional SSHI technique.

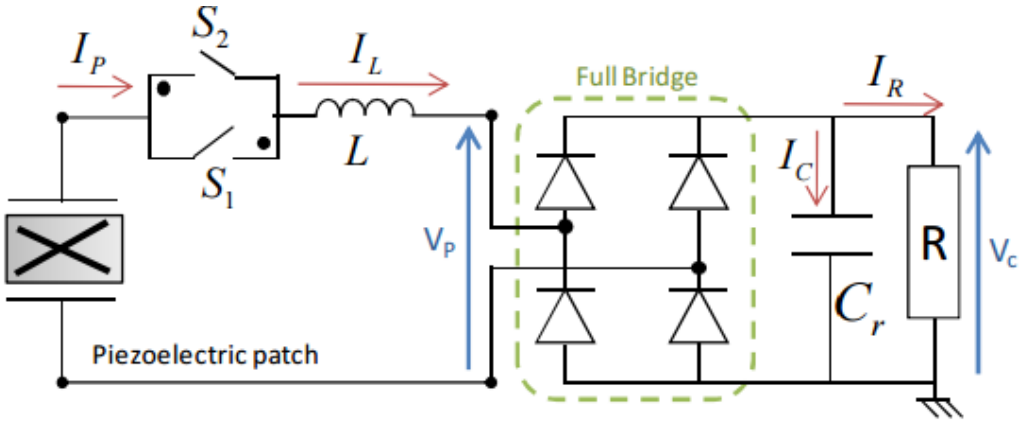


Figure 6.4: SSHI energy harvesting circuit [125]

A combination voltage doubler and switched inductor circuit is also seen in the work of Kushino *et al*. [129] where the combination provides approximately

320µW output power output compared to 250 µW for a voltage doubler circuit at the same voltage from simulations because of the increased mechanical strain on the piezoelectric element. This corresponds to a 28% increase in output power. Kushino *et al*. [129] also present an excellent comparison of full bridge rectifier circuits with half-wave voltage doubler circuits using theoretical and experimental results. A typical problem which is faced with these circuits is the issue of starting the circuit without an external power source. Self-powered devices usually use a combination of passive interaction to store the charge until it reaches a high enough voltage to power the active circuit. This issue was addressed by Vasic *et al*. [130] where the piezoelectric transducer was divided into 3 sections where one section was used to provide the initial power to drive the circuit. This is an elegant solution. However, it does require three transducers to provide the various required voltages to the different parts of the circuit. The schematic of this circuit showing the three circuit modules is presented in Figure 6.5. In this set-up P_2 and P_3 are used to power the SSHI interface and P_1 is connected to the interface and the output from P_1 is the harvested voltage.

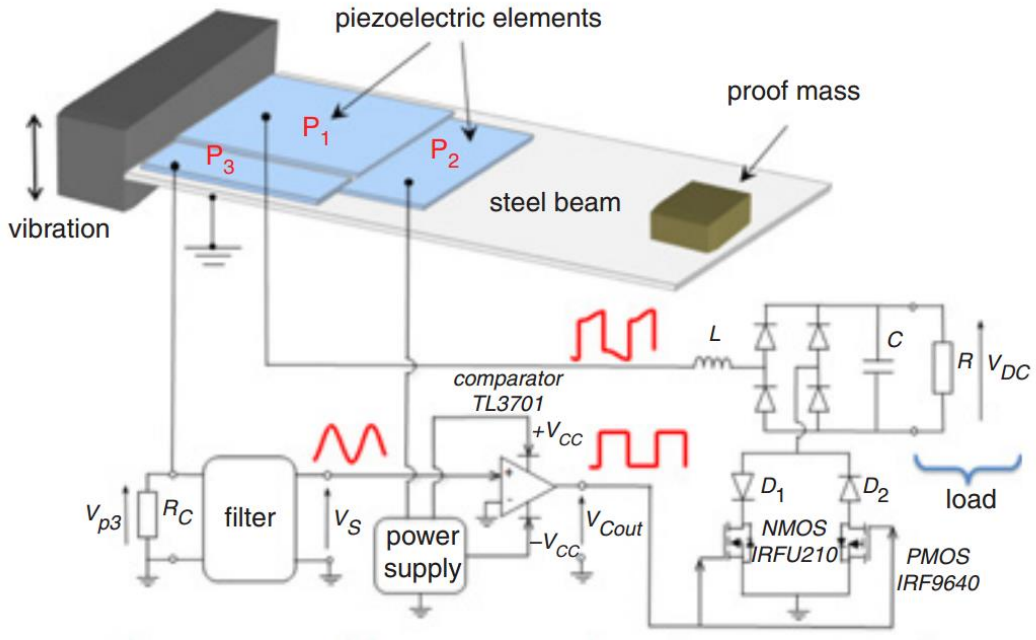


Figure 6.5: Schematic Diagram of Energy Harvester with Self-Powered SSHI Interface [130]

Other methods include the use of active diodes to reduce the forward voltage drop and reverse leakage as in the work of Cheng *et al*. [131], where a boosted DC

output was used to power the devices and eliminate the need for external power (i.e. power from an additional voltage source). An active voltage doubler powered by a fraction of the harvested energy was used by Dallago *et al*. [132]. Operational amplifiers were used to replace the comparators in the system and the efficiency was found to be 90% which meant a loss of only 10% of the harvested energy. Multifrequency arrays have been used in parallel to increase output voltage or in series to shorten battery charging time by Ferrari *et al*. [133]. Rao *et al*. powered a converter using energy harvested from the load [134] and Sangiorgi *et al.* used multiple transducers to increase the efficiency by up to 208% of the supplied voltage [135]. PMOS transistors were used instead of load resistors to create the rectifier and this increased the output power available to 99μW by Sun *et al*. [127]. An intermediate energy tank and non-linear energy harvesting provided a gain of over 30% of harvested power over a classical approach by Lallart *et al*. [136]. The use of a buck converter in parallel with a buck-boost converter provided a converter efficiency of 63.8% over the more classical approach by Dwari *et al*. [137].

Energy harvesting can often be from unpredictable sources and the amount of energy available is dependent on the conditions of the environment at that time, i.e. solar power increases on sunny days and is not available at night, blood flow increases when exercising etc. This means that management and storage of the harvested charge is necessary to increase the energy available. Harvesting aware power management (HAPM) systems consider periodicity, output signal, voltage/current characteristics, available energy as well as the system in which the power is being used [62, 138]. HAPM is concerned with the amount of energy available to the system and tries to adjust the needs of the system to match the harvester. This is an excellent method to increase the efficiency of a system because effective HAPM can also reduce the energy storage requirements by matching the available energy from the harvester to the device energy requirements and using the energy directly from the harvester. Using stored energy is less efficient than directly using harvested energy so there can be significant improvements through the use of HAPM.

An example of this is seen in the work of Rajasekaran *et al*. [139] where a pulse width modulation (PWM) controller is used which adapts to the different impedances of different energy harvesting devices. This is done by controlling the

switching frequency of the DC-DC converter based on the voltage output of the piezoelectric element so that the DC-DC converter impedance is changed to match the impedance of the harvester. Another scheme based on a water bucket fountain strategy is proposed by Teh and Mok [140] which provides input voltage protection as well as eliminating mechanical feedback due to isolating the voltage which is not desired unless using it to increase the stress on the piezoelectric element.

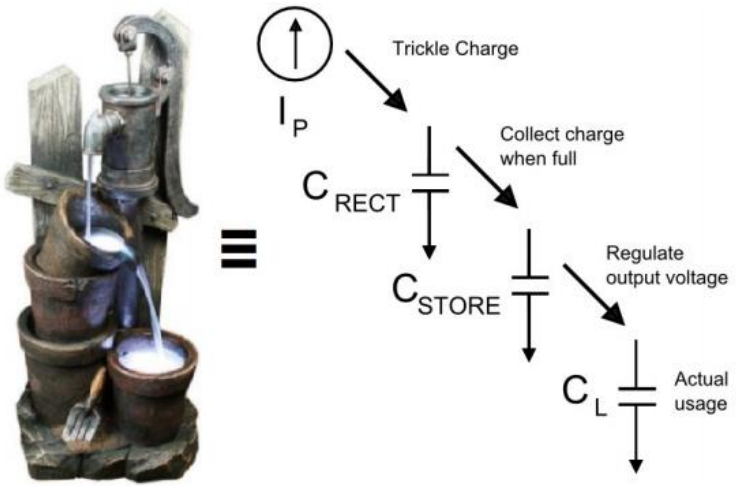


Figure 6.6: Water bucket fountain strategy overview [140]

It is not just the issue of rectifying the voltage that is important for ensuring that the largest possible amount of energy is harvested. The more efficient the energy harvesting circuit is, the more energy can be extracted so this is a great source of interest. One way to increase the efficiency of the circuit is to use low power elements and components with low power loss. However, another interesting concept is to increase the amount of energy extracted through the use of various techniques which increase the stress on the piezoelectric transducers and/or extract maximum power.

The concepts of maximum energy harvesting control (MEHC) and maximum power point tracking (MPPT) have been investigated to increase the usable energy which can be extracted from energy harvesters [61, 139, 141, 142]. These all look at how to increase the energy harvested in systems without a constant supply, i.e. solar power where harvesting is dependent on the sun and so the energy available changes during a 24 hour period and from day to day. Maximum power point tracking is used to tune the load to extract the maximum amount of energy possible through considering the previously available energy and adjusting the device accordingly.

Essentially, it evaluates past performance and uses that information to determine future performance. It is a closed loop system which can be used for solar energy harvesting because the energy has a seasonal and diurnal nature. It could also be of use for piezoelectric energy harvesting particularly in systems such as those proposed in this work where the number of beats per minute, and therefore the amount of blood flow and consequently charge generated, can change throughout the day. MEHC expands on this for vibration systems. The MEHC system adjusts the damping to the optimum for dynamic energy harvesting. Wang *et al*. [142] achieve this this by adjusting the voltage across solar cells based on a fraction of the open circuit voltage and the linear relationship between the maximum voltage and the open circuit voltage of solar cells.

One of the most recent advances in piezoelectric energy harvesting power management circuits involves the use of bias-flip rectifiers. In a traditional bias-flip circuit, like the one proposed by Ramadass and Chandrakasan [143], an inductor and a switch are placed in parallel with the energy harvester and a diode bridge rectifier is used in conjunction with this combination. The inductor is used to change the polarity of the voltage across the internal capacitor of the energy harvesting device. When the output voltage of an energy harvesting device changes direction a proportion of the output energy is lost when the voltage across the plates changes polarity. This proportion is shown in Figure 6.7 in the black shading of the current waveform (top right). The voltage output from the full-bridge rectifier (middle) and bias-flip rectifier (bottom) are also seen. From these it is seen that when using the bias-flip, a wider maximum voltage response is seen and therefore more power is made available. The inductor resistance limits the magnitude of this inversion and therefore the loss in power for each cycle. Further improvements were made by Vaddi *et al*. [144] where a similar enhanced bias-flip rectifier is discussed. In the enhanced scheme proposed by Vaddi [144] a capacitor is placed in series with the inductor and switch. When the capacitor is used the switching occurs closer to the point of maximum or minimum deflection, i.e. the delay is reduced. Therefore, the capacitor voltage remains at maximum for even longer than seen in the traditional bias-flip design. The power extracted by the circuit is 13 times that of a rectifier circuit and 3.25 times that of a traditional bias-flip circuit.

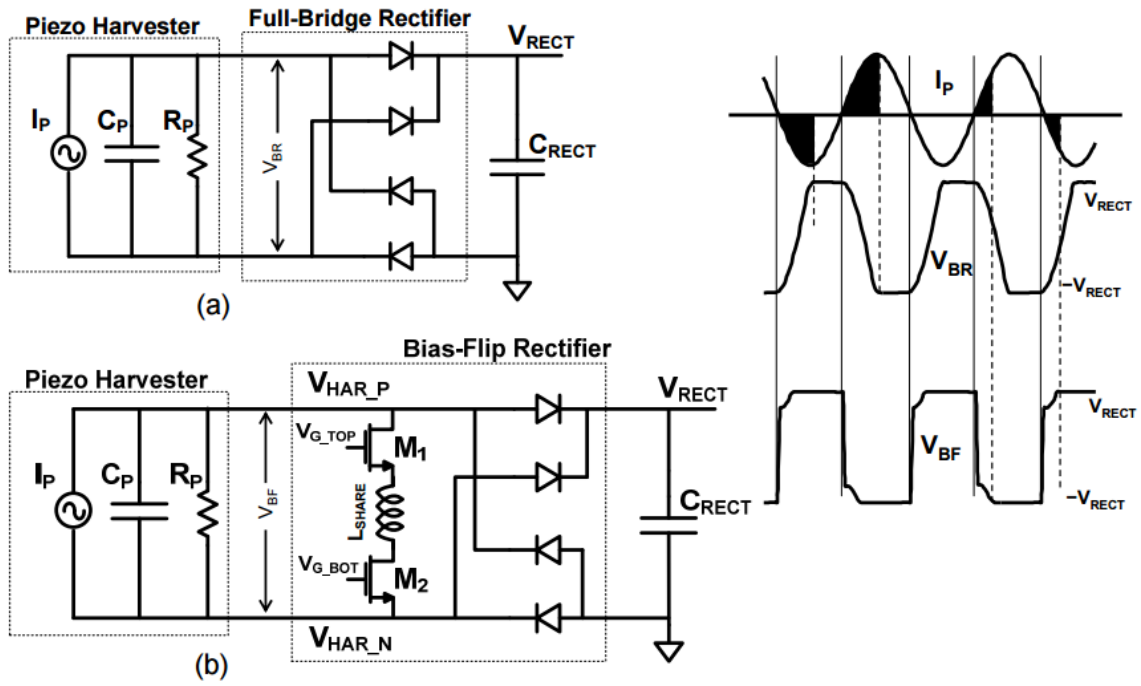


Figure 6.7: Full-Bridge Rectifier and Bias-flip circuit and output waveforms [143]

One further method for increasing the power efficiency of a PEH proposed by Hehn *et al*. [145] uses a modification on the synchronous electric charge extraction (SECE) technique. This technique operates by detecting the maximum and minimum peaks and the zero point (switching point). For each half of the voltage waveform output from the piezoelectric energy harvesters, the voltage is increasing to a maximum or a minimum and after it reaches this point it begins to decrease again to zero. SECE extracts the voltage at the maximum or minimum of the deflection when the maximum charge is available across the internal capacitor of the energy harvester. The output waveforms for SECE are shown in Figure 6.8.

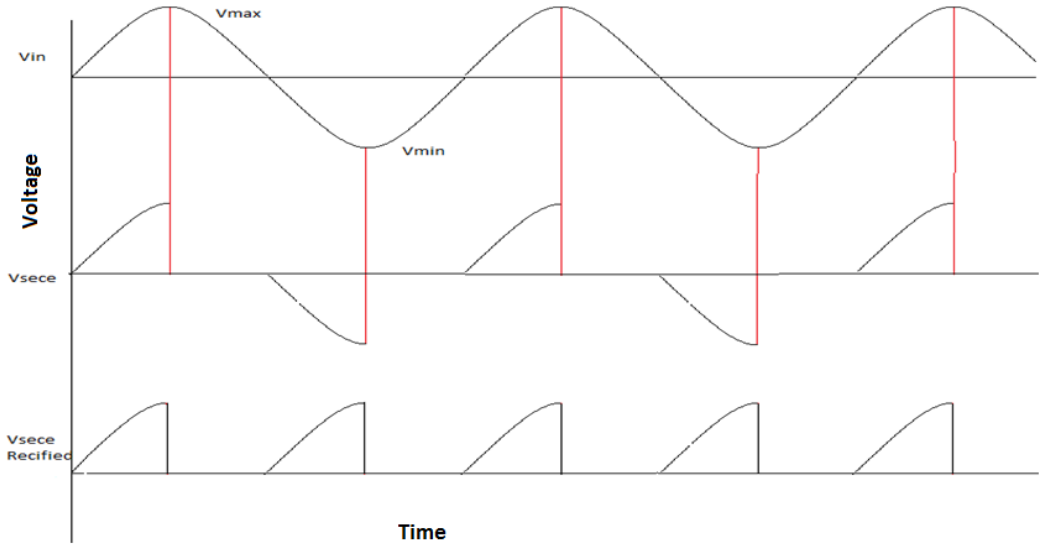


Figure 6.8: Synchronous Electric Charge Extraction (SECE) waveforms

The modified technique described by Hehn *et al*. [145], known as pulsed synchronous charge extraction (PSCE) uses combinations of the switches involved in SECE to increase the harvestable energy by increasing the damping. In SECE an inductor is used as temporary storage and the energy is transferred in short discrete bursts when the maximum deflection of the piezoelectric transducer occurs. This is done through the closing of three switches in the circuit. In PSCE a similar interface is used but a combination of two schemes of SECE is implemented so that the scheme is adapted for higher or lower voltages in the piezoelectric device. This system increases the efficiency by 123% at resonance and 209% at off-resonance when compared to a full-wave rectifier circuit. This design also incorporates start-up from an uncharged buffer capacitor so that the system can be fully autonomous. The chip, designed to be used with a macro scale PEH, was fabricated using a 0.35µm CMOS process. The PEH is connected via wires and the losses due to these are included in the analysis. This system also operated over a wide range of voltages from 1.3V to 20V.

A modified SSHI technique was also presented by Mohajer and Mahjoob [146]. This uses off the shelf components to create an efficient energy harvesting circuit which is fully self-powered. Mohajer and Mahjoob [146] used a modified SSHI technique where the circuit is completely self-powered. This is achieved by optimising the load, i.e. impedance matching as explained in Chapter 3. Optimising the load means that more power is available and therefore enough power could be

harvested to create a fully self-powered device. This represents an improvement of the output power of up to approximately 40% when compared to the standard technique for voltages over 2.28V due to the extra power required for powering the additional circuitry. The circuit is not effective under 2.28V because the additional circuitry needs to be powered.

Dongwon *et al*. [147] investigated a single inductor circuit, again, using a 0.35μm CMOS process. This system invests energy back into the energy harvester to increase the damping and therefore increase the output power. Using this system, a maximum conversion efficiency of 69.2% was achieved. Conversion efficiency for PEHs depends on the coupling factor and the Q-factor [148]. The coupling factor and the Q-factor are typically low for an unloaded PEH and it is typical to find efficiencies around 16% for a PEH.

Another technique for increasing the conversion efficiency called Single Supply Pre-Biasing (SSPB) is described by Elliott *et al*. [149]. SSPB is similar to SSHI because it provides a charge at the extremes of the piezoelectric transducer deflection which will increase damping and therefore increase power output. However, by using SSPB the rectification is achieved at the same time without the need for diodes. In this circuit, the charge is exchanged synchronously using an H-bridge configuration of switches with the PEH connected in series with an inductor across the centre as shown in Figure 6.9. An FPGA is used to control the switches in pairs. For one half of the resonant period, the element is discharged and the second pair of switches pre-biases the element with the opposite polarity for the second half of the period.

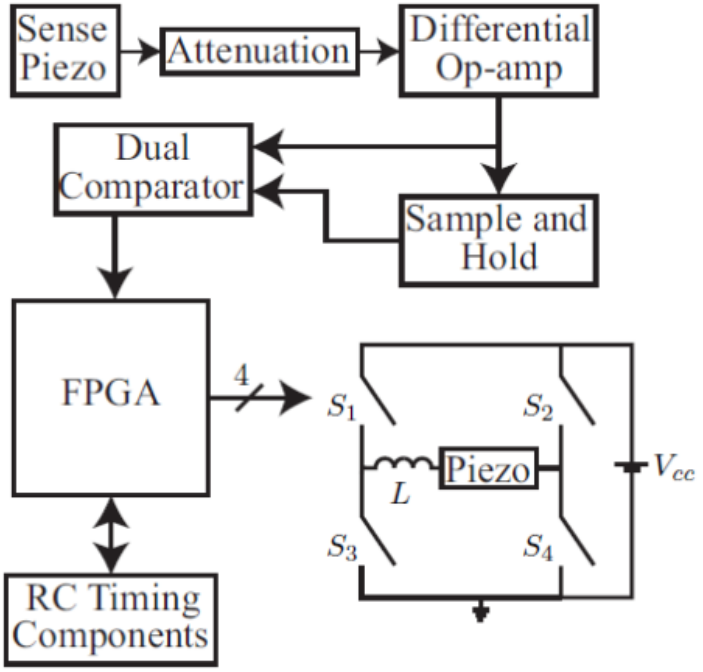


Figure 6.9: SSPB Circuit [149]

This technique outperforms SSHI by 14% and can extract 11.3 times as much energy as a bridge rectifier. However, this system does require the use of an FPGA which is a significant increase in the complexity of the circuit and a potential major drain on the available power. Van Liempd *et al*. [150] present a 94% efficient power management system using zero-bias active rectifiers. This system was able to achieve this high efficiency due to the elimination of static power loss by switching off the control current during non-conducting periods. This circuit is completely battery-less with start-up occurring when the vibrations generate enough voltage. The system by Van Liempd [150] operates from 1 to $5V_{pp}$ and was fabricated on a 0.25µm CMOS process.

Although there has been a significant increase in the conversion efficiency of energy harvesting circuits in the past decade there is still a great need for energy efficient circuits which can provide a continuous DC voltage output. The techniques discussed here represent the most recent advances and it can be seen that efficiency has been greatly increased but they generally concern a single transducer and do not consider efficient and effective ways of increasing or integrating the power output from multiple transducers. The various methods discussed above are summarised in Table 6.2. This table highlights an issue with current stands of energy harvesting

publications which is that not all information is provided to give a complete overiew of the effectiveness of the circuit.

Author	**Method**	**Input Voltage (V)**	**Maximum Power (µW)**	**η (%)**
Chen [125]	Velocity controlled SSHI	Over 2.5	200	
Liang [126]	Self-Powered SSHI	20	600	
Lallart [128]	Double SSHI	10	400	
Sun [127]	MOSFET SSHI		114	
Kushino [129]	Voltage doubler and switched inductor	6	400	
Cheng [131]	Voltage doubler using PMOST	>0.5	210	>80
Dallago [132]	CMOS voltage doubler with supply independent bias	>680m		>90
Dwari [137]	Buck converter in parallel with Buck-Boost	400m		>63.8
Teh [140]	Boost converter using water bucket fountain strategy	45m		75
Ramadass [143]	Bias flip recitifiers	2.4	32.5	85
Vaddi [144]	Enhanced Bias flip	1	26.4	
Hehn [145]	Modified SECE	1.4		85
Mohajer [146]	Modified SSHI	>2.28	25150	
Dongwon [147]	Single inductor	2		69.2
Elliot [149]	SSPB with FPGA	6.7	3500	
Van Liempd [150]	Zero bias rectifiers	5	940	94

Table 6.2: Summary of Energy Harvesting Circuit Literature Review

For most piezoelectric energy harvesters, an array of cantilevers, as seen in Figure 3.15 in Chapter 3, needs to be used because the output from a single transducer would not be sufficient. This is even more the case for piezoelectric energy harvesting from blood flow. The piezoelectric transducer must necessarily be small to fit into the artery without causing a large obstruction and the typical resting heart rate is 60bpm or 1Hz so the power available from a single transducer is quite small (typically less than 0.1µW). To compensate for this a number of transducers will need to be placed in series. As shown in Figure 3.17 in Chapter 3, when multiple devices activated at different frequencies are used, the total output voltage (shown in blue) is higher than the voltage of any one of the individual devices (shown in purple, green and red). This means that not only do arrays of energy

harvesters provide more power by adding the power of each harvester but also that using an array causes interactions within the harvesters that increases the voltage output of each individual harvester.

6.3. Simulated and Bread-boarded Circuits

In this section a number of different circuits for use with multiple inputs will be examined. The final system will require an IC to be designed. However, this was beyond the funding available for this work and so instead a number of circuits which could be later redesigned for an IC are simulated and bread-boarded here for analysis. In all of the simulations of multiple inputs the inputs are out of phase.

6.3.1. Op-Amp Circuits

For multiple input circuits a traditional solution is to use op-amps in conjunction with a summing node. This is based on the audio mixer set up of a summing amplifier which uses a summing amplifier and multiple resistors as shown in Figure 6.10. For resistances R_1 to R_n equal and independent of R_f the output of the amplifier is given by [151]:

$$V_{out} = -R_f \left(\frac{V_1}{R} + \frac{V_2}{R_2} + \cdots \ldots \ldots + \frac{V_n}{R_n}\right) \qquad (6.1)$$

This was the first solution considered and it was found that for a number of set-ups a rectified output could be achieved. Figure 6.12 shows a typical op-amp circuit tested in this work. The output from the summing amplifier becomes the input to a voltage doubler circuit which is indicated by a red circle. Figure 6.13 shows the results from the circuit and here it is seen that the output has increased from 0.1V to 1.1V. However this is largely due to the voltage multiplier circuit which is circled in Figure 6.11 and not the summing of the inputs. Another issue is that the op-amp requires 5V to operate which means a system such as this could never be self-powering for low voltage operation.

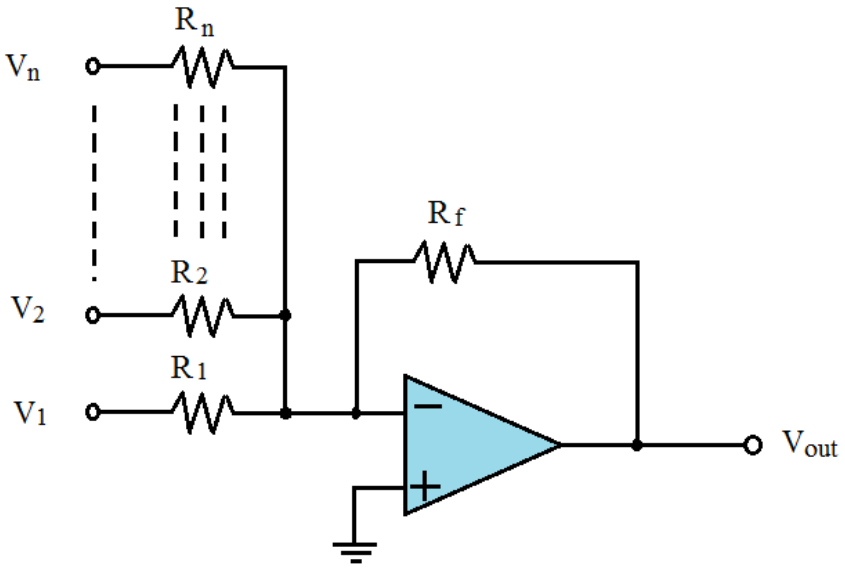


Figure 6.10: Summing Amplifier [152]

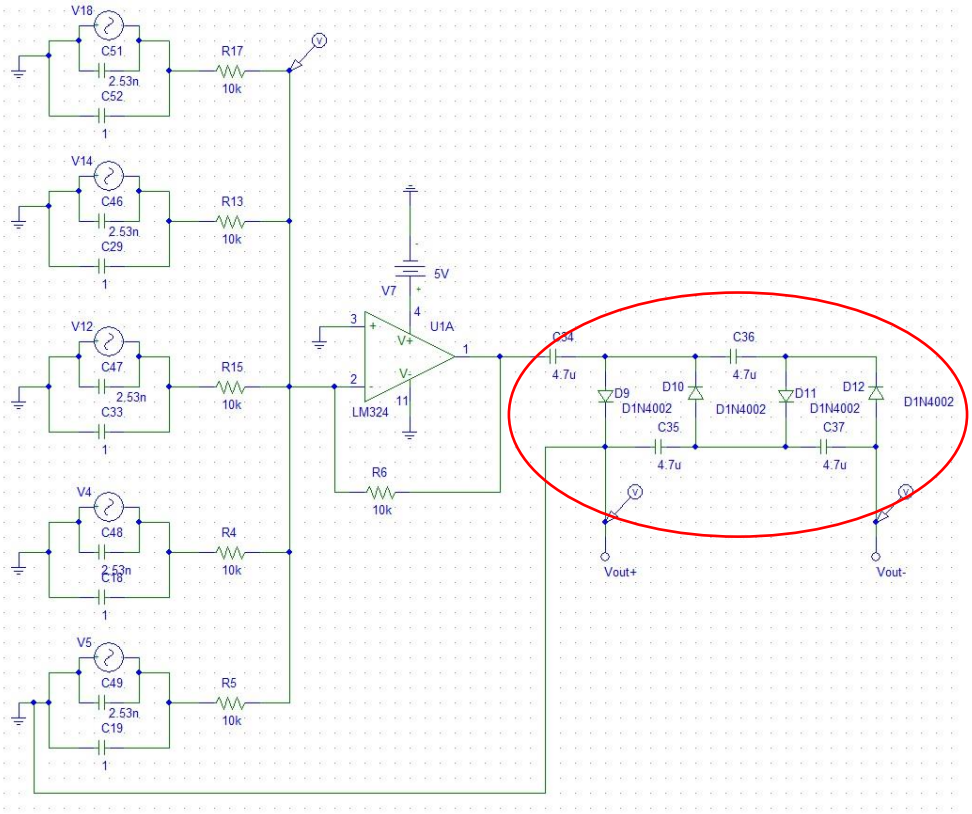


Figure 6.11: Example of a typical Op-Amp Circuit for Multiple inputs

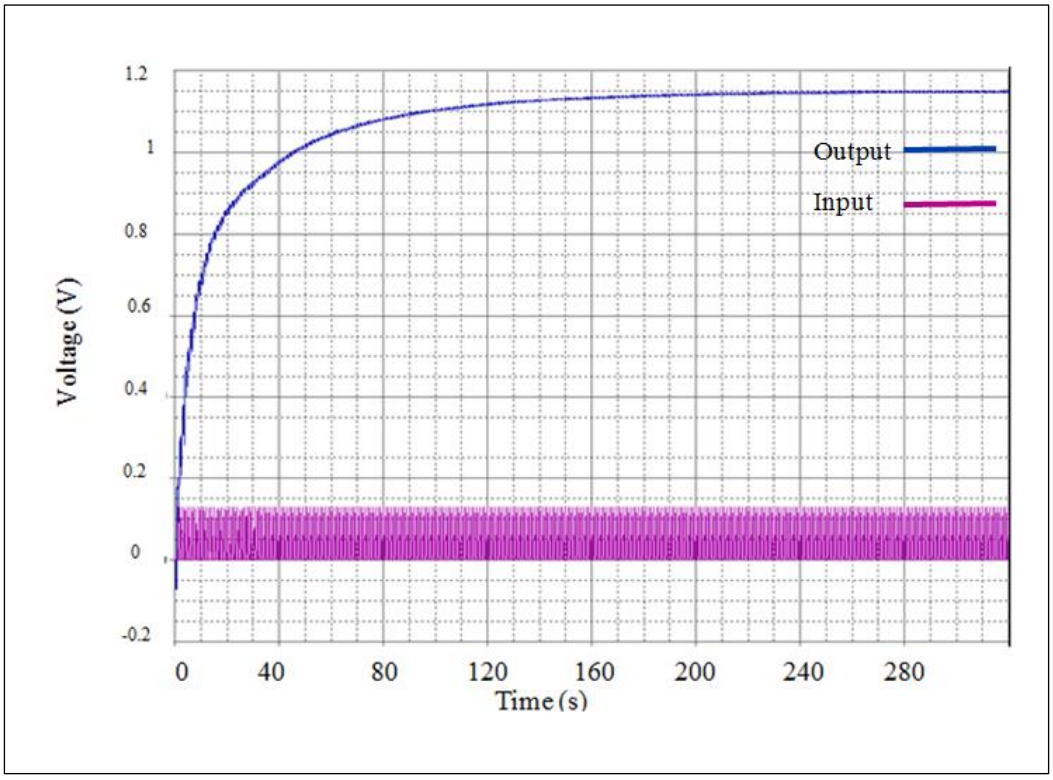


Figure 6.12: Output from Op-Amp Circuit (Blue) and Input (Pink)

6.3.2. Torah Circuit

Depending on the amount of power available, various methods of rectification can be used. A typical circuit used for rectifying and increasing available power is the voltage multiplier circuit. An example of this is shown in Figure 6.13. This circuit is based on the same circuit by Torah *et al*. [153]. The diodes are used to rectify in the same way seen in the traditional full bridge rectifier in Figure 6.1. The addition of the capacitors means that the charge is stored when the piezoelectric element is in the opposite polarity so that the voltage is captured and added at each half cycle.

This circuit was used by Cahill *et al*. [15] in a structural health monitoring device. This work examined a method to detect faults in concrete beams through the change in their resonant frequency. The resonant frequency of a beam was tested and then a fault was introduced and the change in resonant frequency was detected by a piezoelectric transducer placed on the beam. As the frequency of the beam changed the response of the transducer increased as the integrity of the concrete was compromised. This type of circuit is ideal for a situation where a high voltage is possible due to the large surface area of the transducer but increasing the voltage increases the difference in the voltage output from the

piezoelectric transducer as it responds to the different frequencies of the beam and so the change in the piezoelectric output is easier to detect.

This circuit [15] was designed and built using standard diodes and an LED was used as an indicator that a voltage was induced in the piezoelectric element and therefore there is a fault in the concrete. A 0.6V AC input will give an approximately 1.2V DC output (from simulation shown in the output diagram in Figure 6.14) which is enough to give a dim output from the LED. Figure 6.14 also shows that the voltage is not only multiplied but rectified. The multiplied voltage is enough to allow the diode to output a very dim light and if the input is higher the light intensity increases. Figure 6.15 shows that for increasing input voltages the output is increased. This means that this is an effective circuit for use as an indicator of increased stress across the piezoelectric transducer which indicates defects in the concrete.

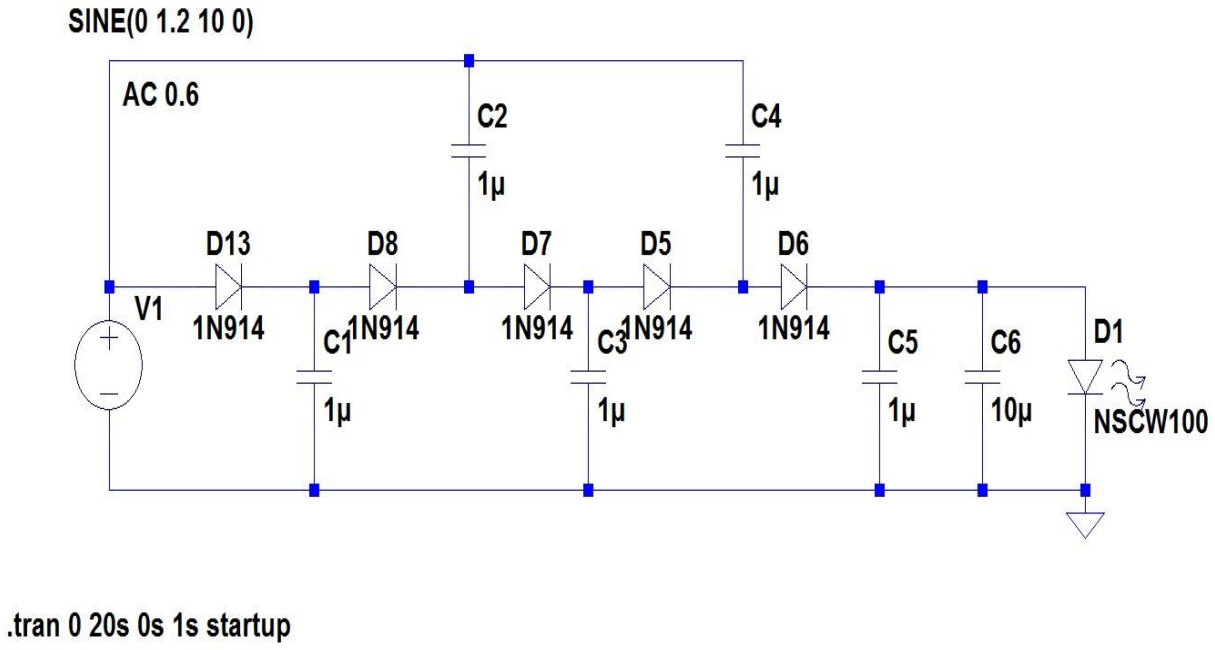


Figure 6.13: Voltage Multiplier Circuit Based on Torah *et al*. [153]

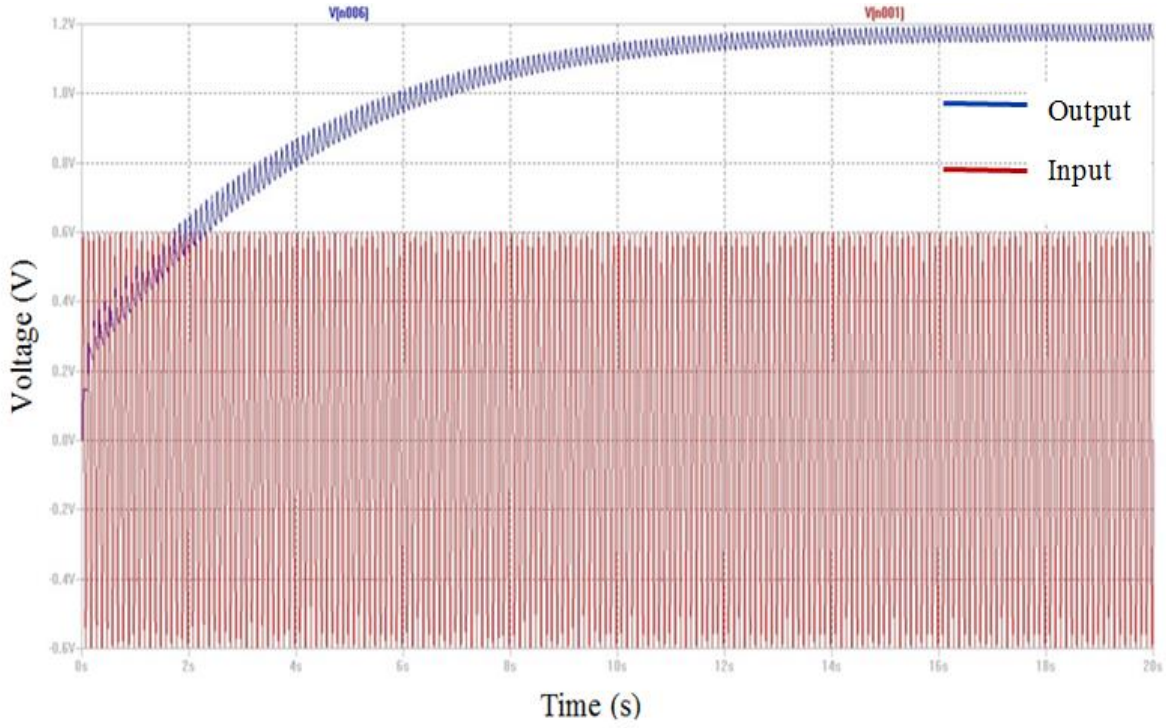


Figure 6.14: Simulated output from voltage multiplier circuit in blue. Input in red.

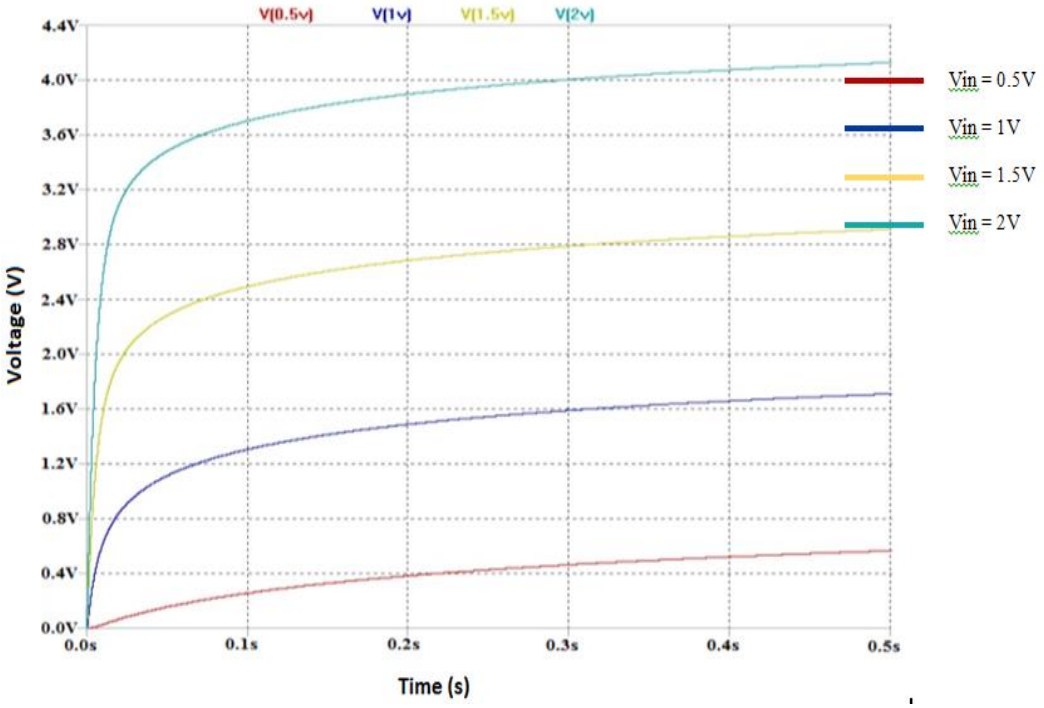


Figure 6.15: Output Voltage from Voltage Multiplier for Different Input Voltages

6.3.3. Guilar Circuit

Other circuits that provide the possibility of taking multiple inputs have been examined. Guilar *et al*. [123] propose to use a CMOS controlled rectifier (CCR) for each input. A CCR is the same as a full-bridge rectifier but instead of diodes MOSFETs are used. These are used to reduce the voltage drop in the circuit. The block diagram of this circuit is shown in Figure 6.16. Each piezoelectric transducer is connected to a CCR circuit through a resistor. For the positive half cycle of an AC input the voltage is transferred through the PMOS and for the negative half cycle the NMOS are activated and in this way the voltage is rectified in the same way as using a diode based rectifier. The CCR plays a particularly important role in this circuit and is shown in Figure 6.17.

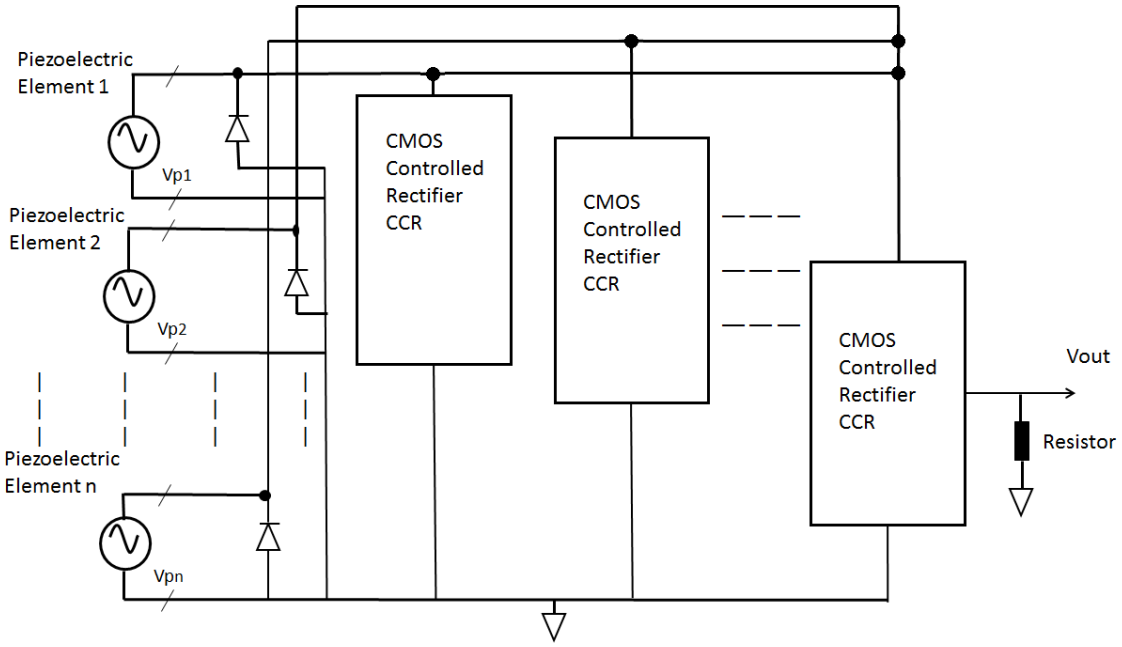


Figure 6.16: Block Diagram of Guilar *et al*. circuit for 3 inputs

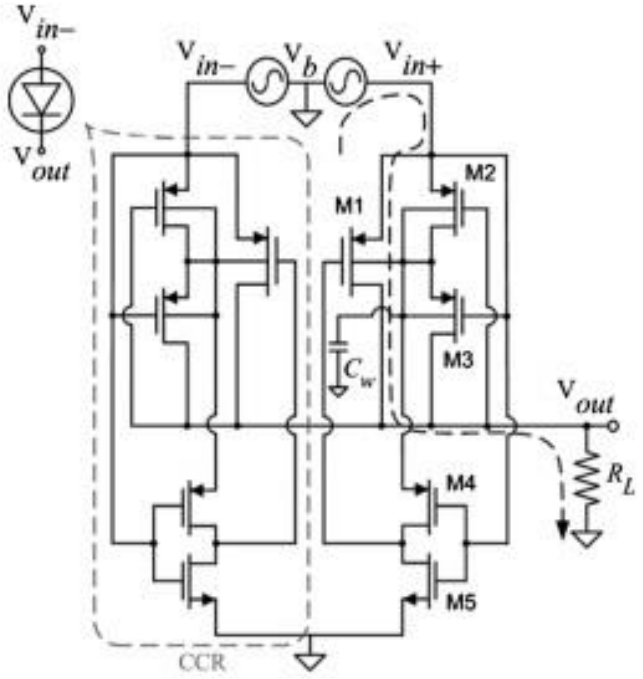


Figure 6.17: Dual Input Guilar Circuit. One CCR is highlighted by dashed light grey line [123]

This circuit does not use an inductor and doesn't require a microcontroller so that the circuit can be fully integrated in a CMOS process. Figure 6.18 shows the voltage output from a simulated circuit with 3 inputs of 1Vpp each. From this it can be seen that the voltages are summed and that a small amount of extra voltage (0.15V) was observed. To evaluate the possibility of increasing this voltage a more complex circuit which needs an inductor and a microcontroller to control the changing and discharging of the inductor was simulated. This is shown in Figure 6.19 and the voltage output is increased over the first 6s which is compared to Figure 6.18 but the voltage increase is minimal (3.15V for the circuit without the inductor and 3.8V for the circuit with the inductor). However, for the circuit without the inductor the output levels off at this point and does not increase further. To determine whether the same is true when an inductor is added a longer time step was used. It is clear that the voltage output continues to increase over time when an inductor is included in the circuit. This substantially increases the complexity of the circuit and an additional transducer is needed to power the control circuitry. It also means that the circuit is no longer CMOS compatible. Research by Wang *et al*.

[154] into incorporating inductors onto an IC have shown positive results for high frequencies but for the low frequencies required here the results are less encouraging for the size of the inductor required here.

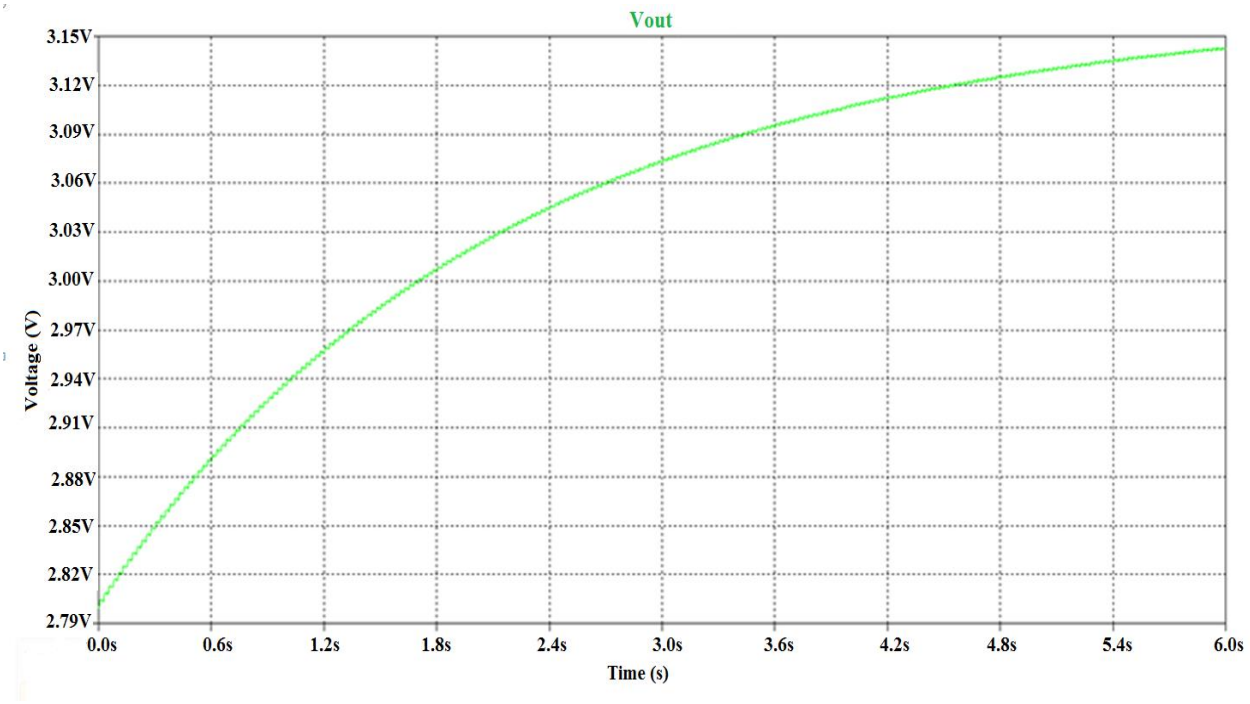


Figure 6.18: Simulated Output of Guilar *et al*. circuit for 3 inputs

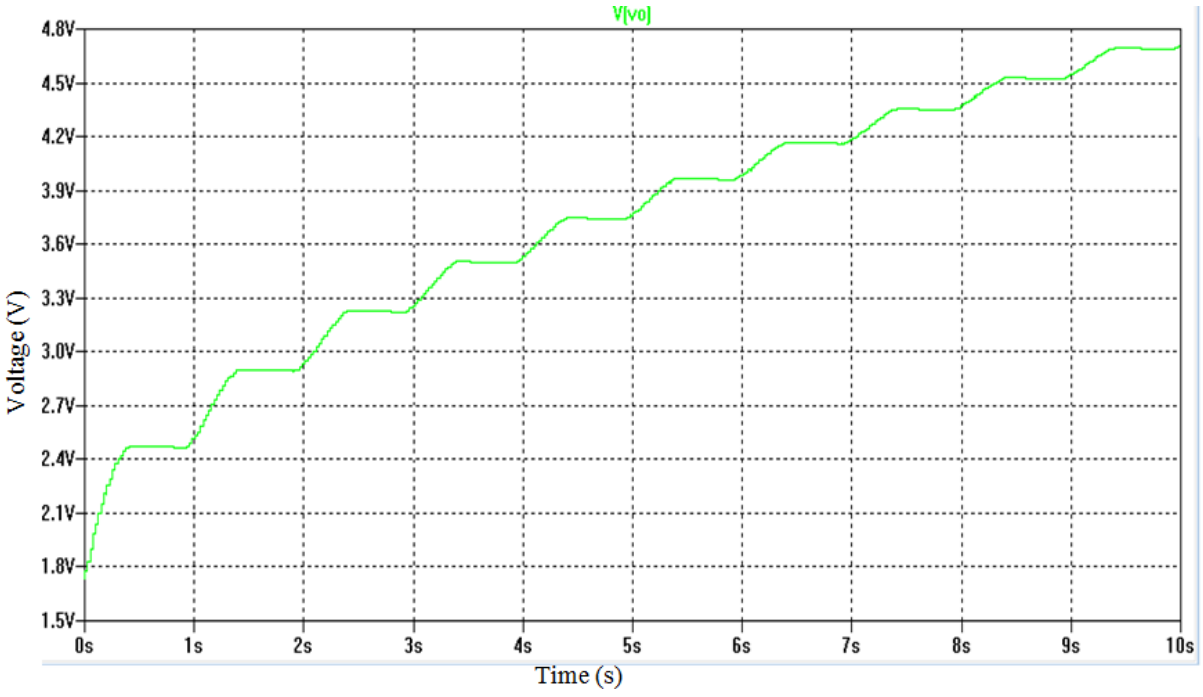


Figure 6.19: Guilar *et al*. circuit with microcontroller

6.3.4. Romani Circuit

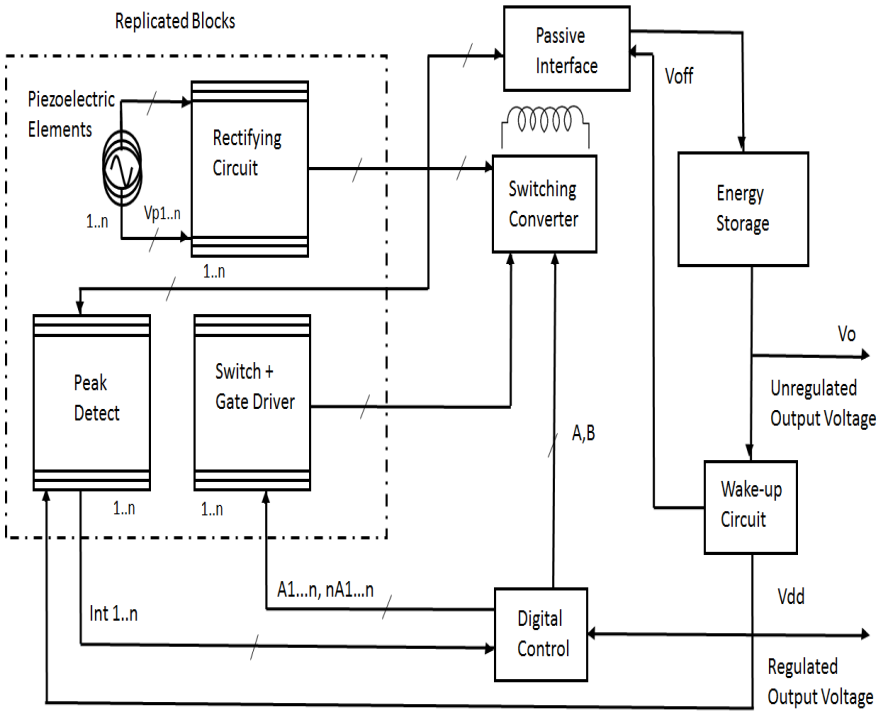


Figure 6.20: Romani *et al*. Circuit Block Diagram [122]

Another circuit which will be analysed was proposed by Romani *et al*. [122] to allow for multiple inputs. The block diagram is shown in Figure 6.20. This circuit combines passive and active elements that make it fully autonomous. This is very important for an energy harvesting circuit because if external power is required then the benefits of energy harvesting can be negated. Each piezoelectric transducer is connected to a full bridge rectifier and for low voltages the output of each rectifier is fed to Vo. This is the passive interface shown in Figure 6.21 and is activated when any of the transducers is providing voltage. A full bridge rectifier is required for each transducer because destructive interference can occur if the transducers are generating power out of phase with each other.

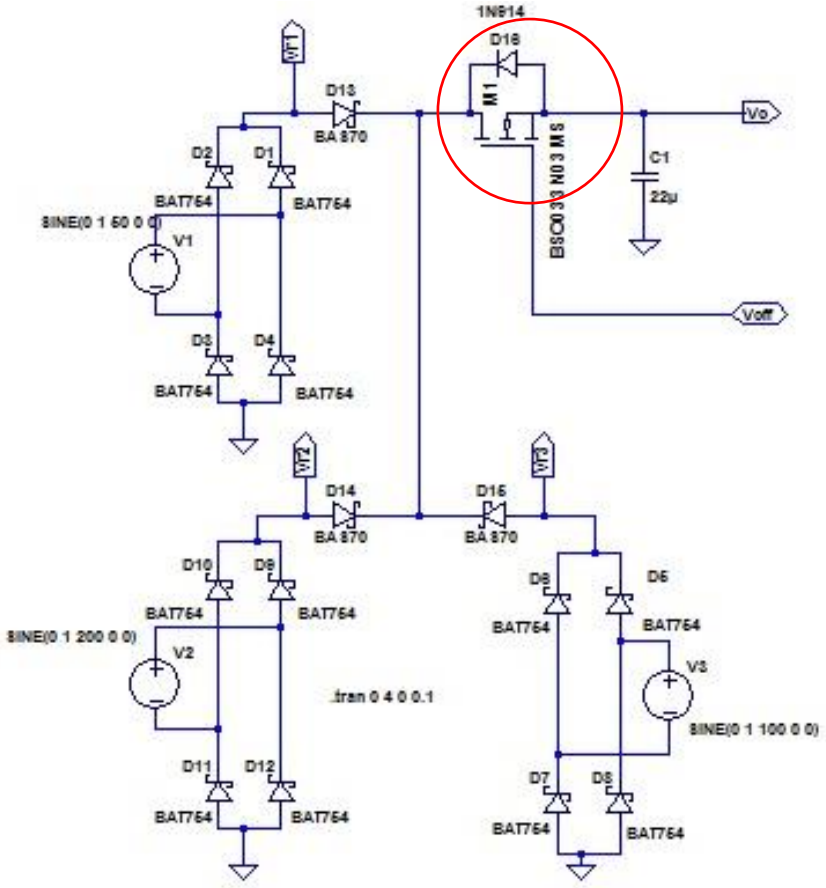


Figure 6.21: Passive Rectifying Circuit

Figure 6.21 shows the passive rectifying circuit for 3 inputs. The passive interface consists of a full-bridge diode rectifier for each input. This circuit is used to charge the output capacitor directly. The active circuit is only turned on when the charge from the passive interface is high enough. This is achieved by using the wake-up circuit and is based on the signal to Voff which is highlighted by the green circle in Figure 6.22. The wake-up circuit uses a voltage divider and when the output of the voltage divider is large enough to turn on D68 in Figure 6.22 (red circle) and turn off D18 in Figure 6.21 (red circle) the active circuit is turned on. The other feature of the wake-up circuit is the voltage regulator. This is used to provide a smooth voltage to the active circuit elements, particularly to the microcontroller. In this case the voltage regulator output is set to 1.8V which is the minimum voltage required to operate the microcontroller.

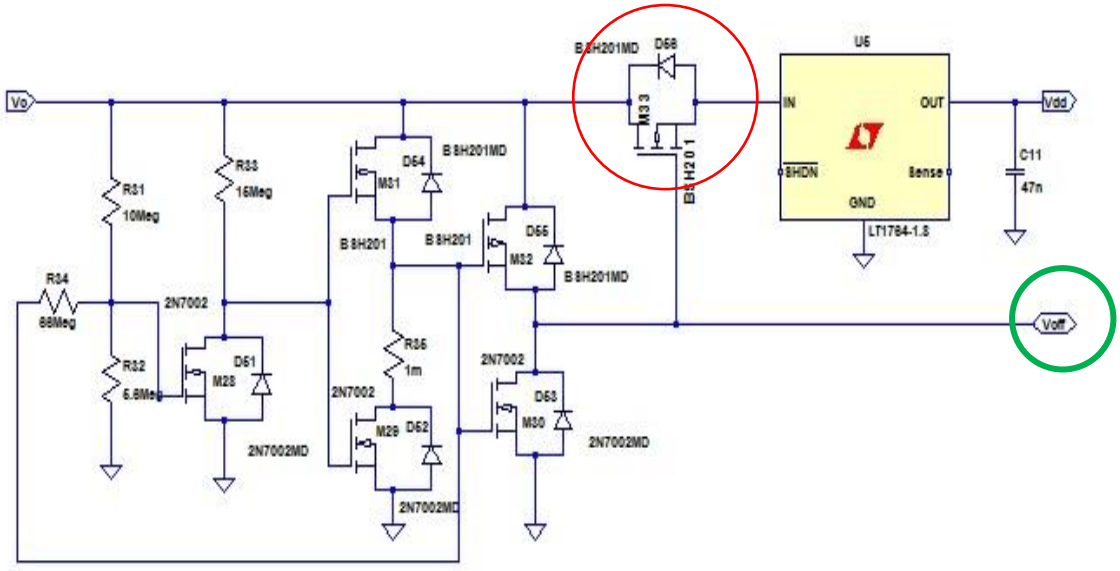


Figure 6.22: Schematic of Wake-up Circuit. Voltage Regulator in yellow box

The interface to and from the microcontroller is based on synchronous electric charge extraction which was described in Section 6.1. When a peak is detected an interrupt signal is sent to the microcontroller to open up the switch controller circuit for the corresponding input. This maximum voltage is then transferred to the output. As each maximum or minimum is detected for each input it is sent to the output and the maximum power is extracted. This scheme works well for multiple inputs because the maximum voltage is transferred from each input as it occurs. This is an ideal situation for energy harvesting from blood flow where the inputs will all be out of phase and maxima and minima may not occur at regular intervals depending on how the turbulence in the flow affects the piezoelectric transducers. The waveforms in Figure 6.8 show how this system works. The microcontroller is used to open and close the various switches and transfer the voltage.

The microcontroller is used to control the timing of the circuit. When an interrupt is detected from the interrupt circuit (shown in Figure 6.23) the microcontroller sends a signal to the appropriate switching circuit. A switching circuit is required to switch to the input on which a peak is occurring. This switching circuit is shown in Figure 6.24. This switching circuit provides the input to the inductor which is shown in Figure 6.25 The on signal for the switching circuit

Ai (where i is the input number 1 to n) is activated when a peak is detected. The on signal for transfer from the switching circuit to the inductor, A, is activated at the same instance and for the same length of time as Ai.

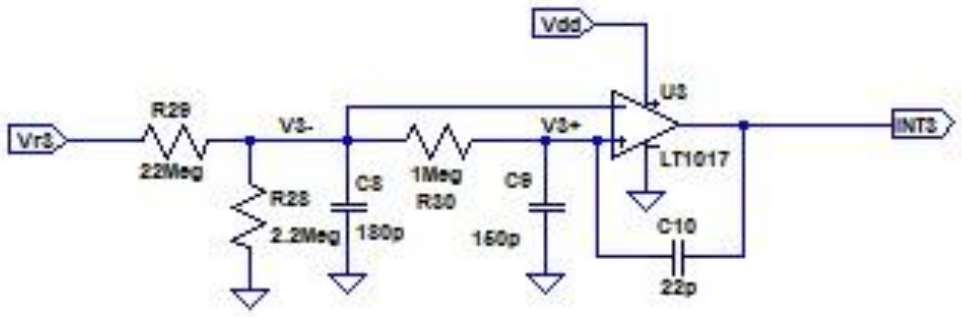


Figure 6.23: Interrupt Circuit

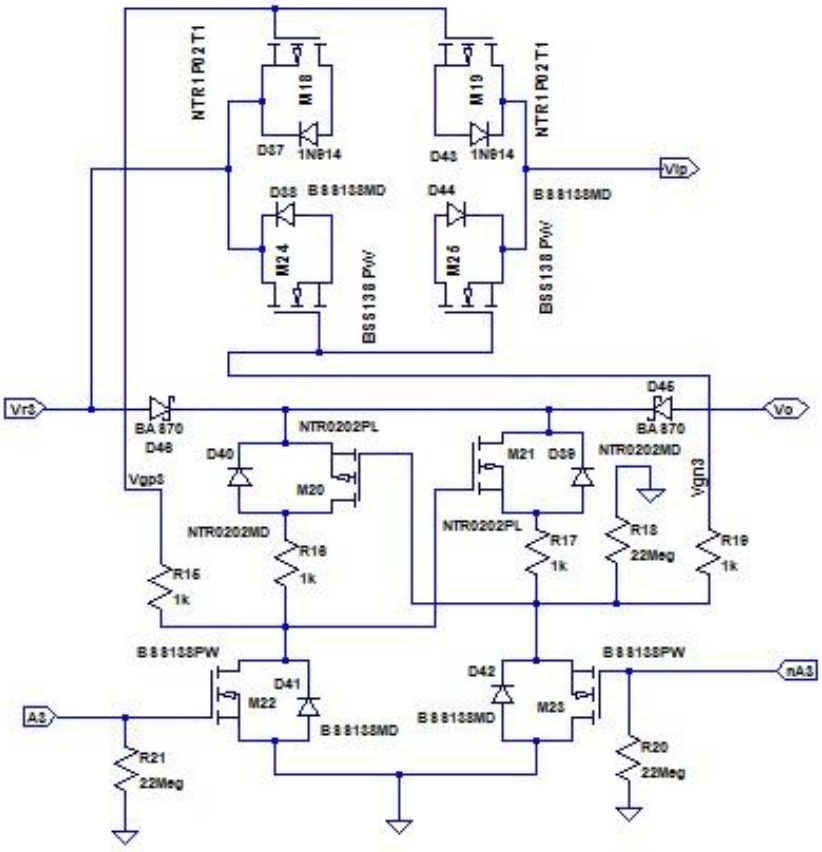


Figure 6.24: Main Switching Circuit.

The signal is transferred to an inductor and from this on to the output capacitor. First the input A is active and input B is off and the output is placed on the inductor. Then input B is active and the output is transferred to the output capacitor. This setup is shown in Figure 6.25 and the microcontroller control voltages are shown in Figure 6.26.

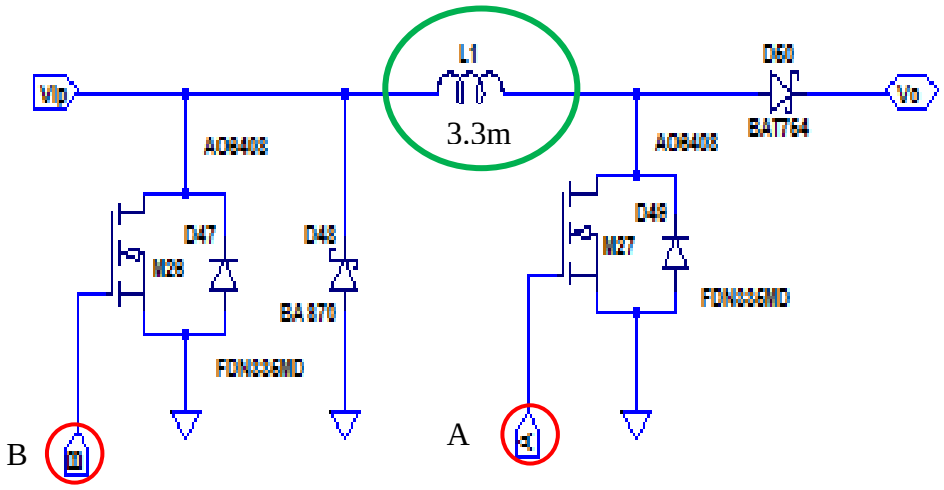


Figure 6.25: Voltage Control across Inductor

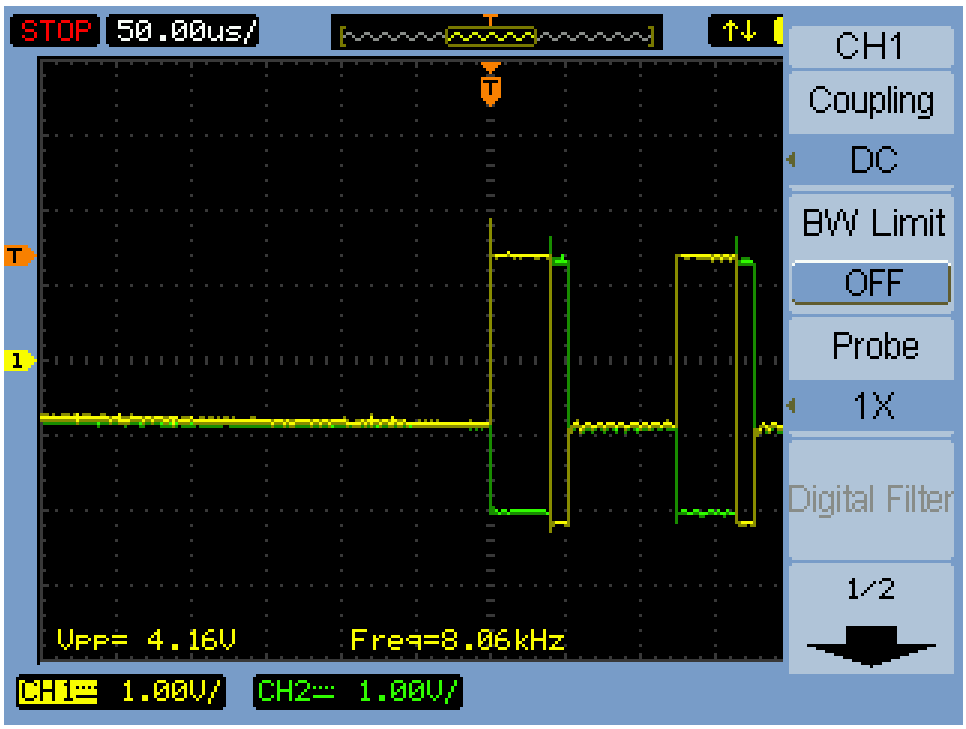


Figure 6.26: Voltage signal for A (yellow) and B (green) to control voltage across Inductor

6.3.5. Analysing and Redesigning the Romani Circuit

In the Romani *et al*. circuit [122] the output from the passive and active circuits are both connected to a single output, Vo, connected across a single output capacitor. From the paper it was shown that this caused the output voltage on the capacitor to increase and the voltage was stored over time so that the available voltage was more than the individual inputs at any single instant.

This circuit was simulated using LTSPICE [155] and the output from Vo was found not to charge up past the maximum voltage on any one of the inputs, i.e. if 3 transducers are used and each one supplies 2V peak to peak then the maximum voltage seen on Vo was 1V regardless of the length of time the circuit was activated. This issue was also seen when the circuit was bread-boarded (Figure 6.27). The results of the simulated and bread-boarded output when a single output is used are shown in Figure 6.28 and Figure 6.29 respectively. Figure 6.30 is a zoomed-in view of the simulated circuit so that the nature of the output can be seen. It is clear from the simulated and bread-boarded outputs that Vo follows a peak on any of the inputs but decreases until another peak is detected and the capacitor voltage never increases above 2V which is the rectified voltage from the inputs.

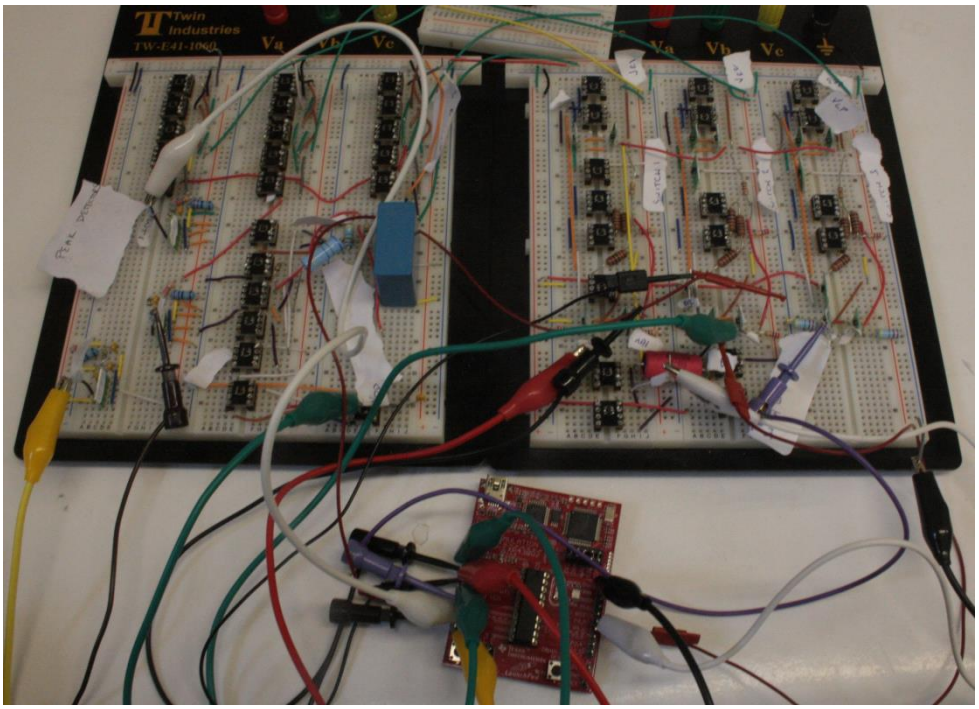


Figure 6.27: Bread-boarded Romani *et al*. Circuit

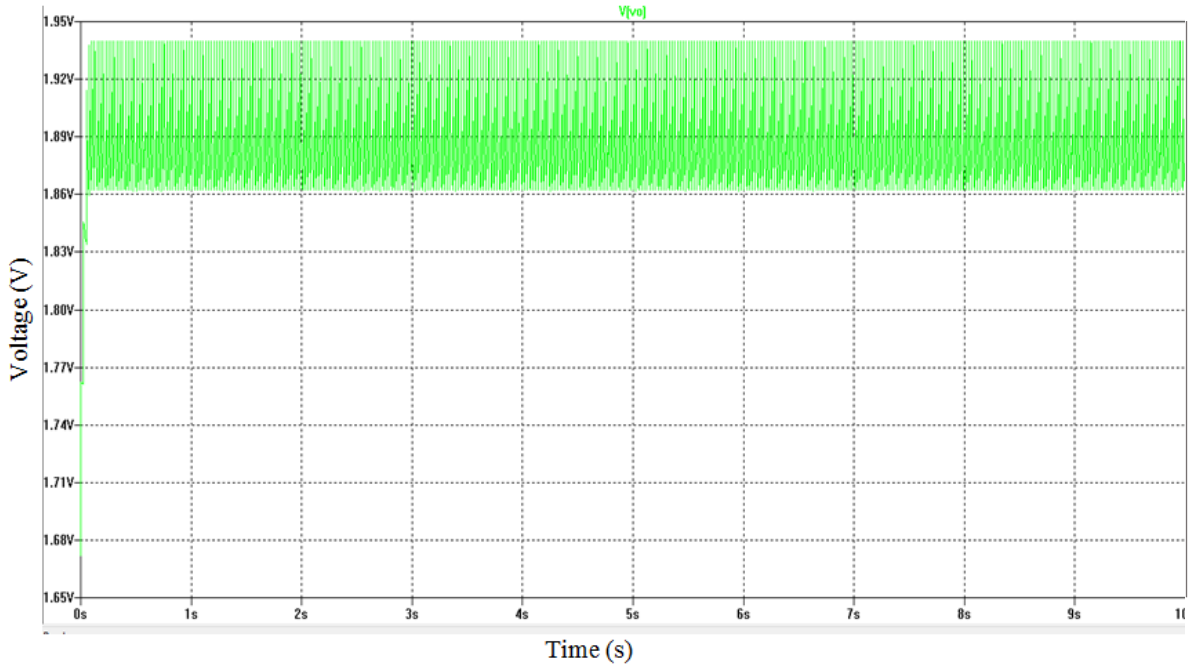


Figure 6.28: Vo Simulated Romani Circuit, 1 output

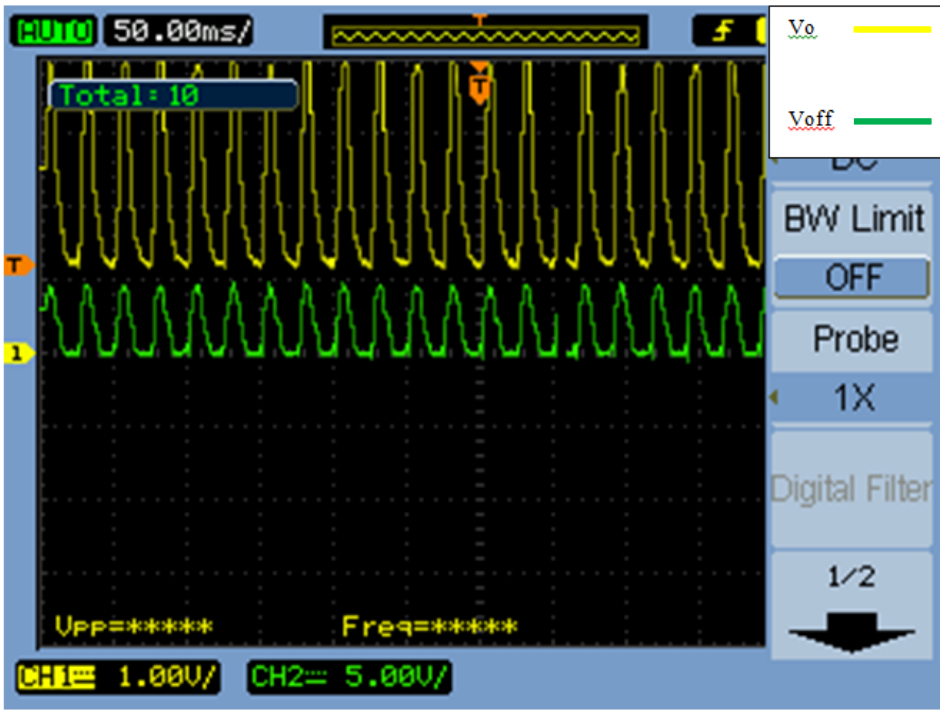


Figure 6.29: Vo (Yellow) and Voff (Green) from Bread-boarded Romani *et al.* Circuit, 1 output

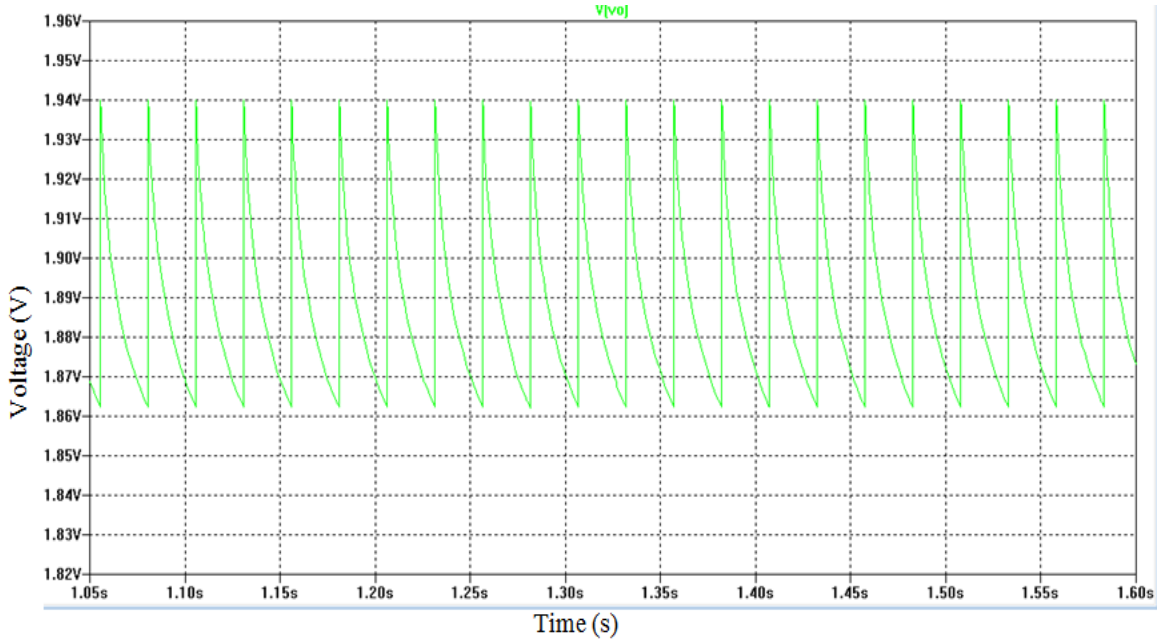


Figure 6.30: Vo, Simulated Romani *et al*. Circuit, 1 output, zoomed

These results show that the system does not perform as expected. Leakage in the capacitor is one major problem and there is no way that this system would provide usable energy for augmenting a battery. Due to this problem the circuit was re-examined and through simulation and bread-board analysis a solution which would allow multiple inputs and autonomous operation was found. During debugging the passive and active outputs were separated so that he outputs could be tested individually. The passive output was connected to the microcontroller to power the active circuit but the two outputs were not fully connected. This debugging provided the solution to the circuit charging issues. A second capacitor was added to the circuit so that the output from the passive circuit was smoothed by an output capacitor and when the voltage was high enough the active circuit was powered from the passive circuit and the output was used to charge the output capacitor connected to the output of the active circuit. The simulations show that this configuration does indeed charge the output capacitor and this was confirmed through the bread-boarded circuit. The output capacitor was charged to over 11V from two inputs of 2Vpp at 40Hz. This was measured using a multimeter in the physical circuit. The simulated circuit output is shown in Figure 6.31. When using two 1Vpp inputs at 1Hz (equivalent to what would be expected from piezoelectric elements excited from blood flow) the output of the capacitor dropped to 3V which is still useful for the application and better than the passive circuit alone.

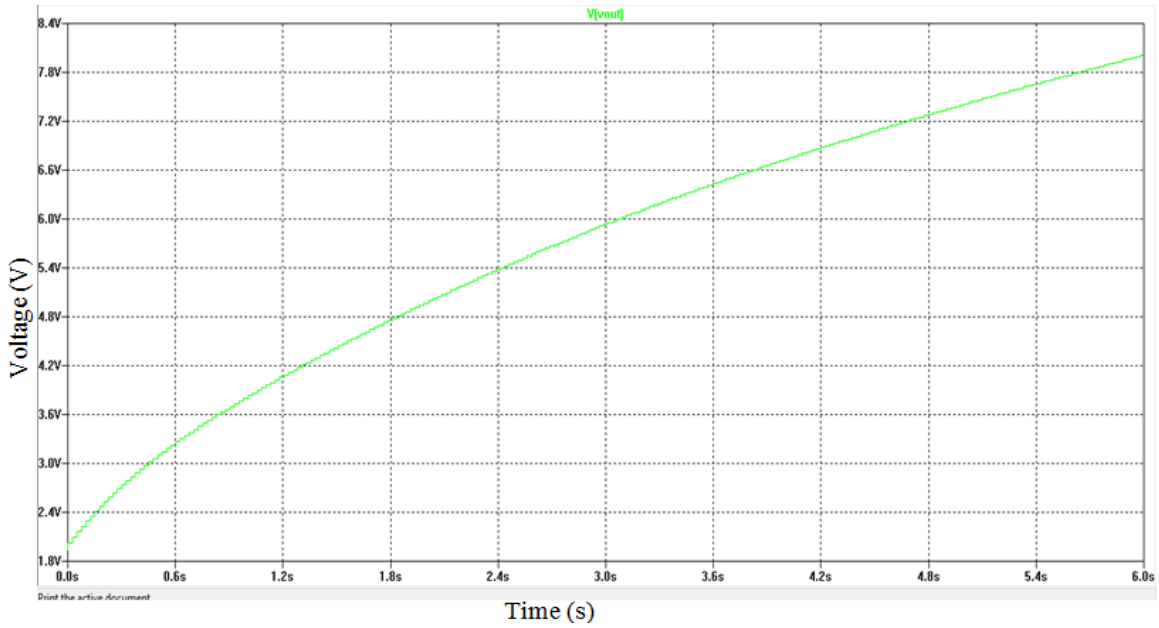


Figure 6.31: Simulation Results of altered Romani *et al*. circuit

The circuit would be further improved by matching the impedance of the circuit with that of the input transducers. However, this would need to be done for a PCB as the additional wires required for bread-boarding makes the correct calculation of the circuit impedance difficult. Another issue with the circuit is the very large inductor required by Romani *et al*. [122]. Larger inductors cannot be fabricated on a standard IC and therefore the smaller the inductor the more integratable the system becomes. An ideal solution requires no inductor but as was shown in the Guilar *et al*. [123] and the op-amp circuit simulations it appears to be challenging to design a multiple input rectifying circuit without an inductor.

In Romani *et al*. [122] the minimum inductor value presented was 3.3mH. In the new configuration proposed and studied in this work the inductor value was investigated to determine if a lower value of inductor would be possible. The results are shown in Table 6.3 and Figure 6.32. For maximum output voltage an inductor value of 0.05mH must be used. However, the inductor can be lowered to 0.005mH and the output is still significantly increased from the input of the individual devices (3 inputs with 1Vpp). From these results it is shown that the altered circuit presented here has some significant improvements over the circuit presented by Romani *et al*. [122].

Inductor size (mH)	Maximum Voltage Output (V)
10	5.76
3.3	9.59
1	15.6
0.5	20
0.1	30
0.05	30.3
0.01	30.2
0.005	14.4

Table 6.3: Inductor size and voltage output from 2 capacitor circuit simulations

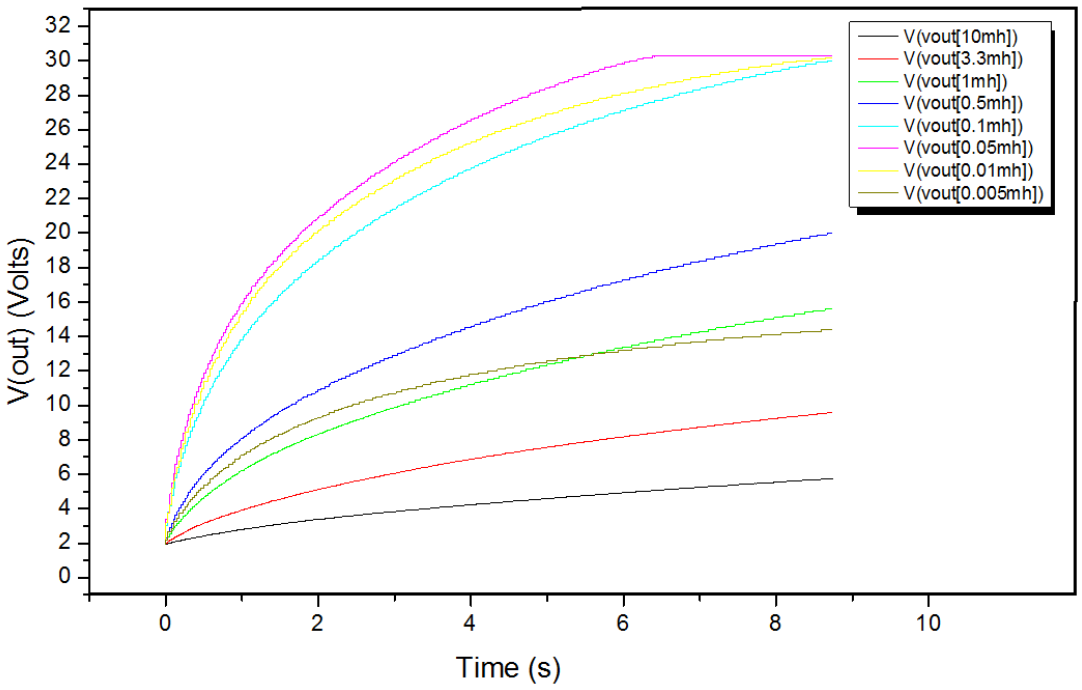


Figure 6.32: Voltage output from active circuit capacitor for different inductor voltages

Another factor in creating an IC for the circuit is the microcontroller, MSP430G2452. This is an excellent microcontroller but it is a very large circuit and there are a number of features which are not used to control the circuit. To examine the microcontroller and determine how to integrate the operation into an IC, the digital control waveforms have been investigated. These waveforms are shown in

Figure 6.33. The capacitances of the circuit will also be reduced for a circuit as was shown by Liqiang *et al*. [156] on an IC and this work provides an excellent platform for further research into this circuit and possible design of an IC.

The operation of the Outputs A, A_i and nA_i can be modelled using flip-flops. For the A inputs a JK flip-flop could be used (Figure 6.34). Typical output waveforms from a JK flip-flop are shown in Figure 6.35. The operation is controlled by J and K and triggered by the positive edge of a clock cycle shown in Figure 6.35. In the design discussed here, ΔT_A = 35µs and D_B=7µs. The clock will need to be triggered at the same time as the interrupt signal for the timing. The output from the latches controlling A can become the input to B so that the falling edge of A triggers B. A single clock can be used with a period of 7µs and when 5 cycles have been completed K would be set high and the output would be reset. Using a setup such as this and the small inductor identified already the circuit could be integrated into an IC with the inductor off chip.

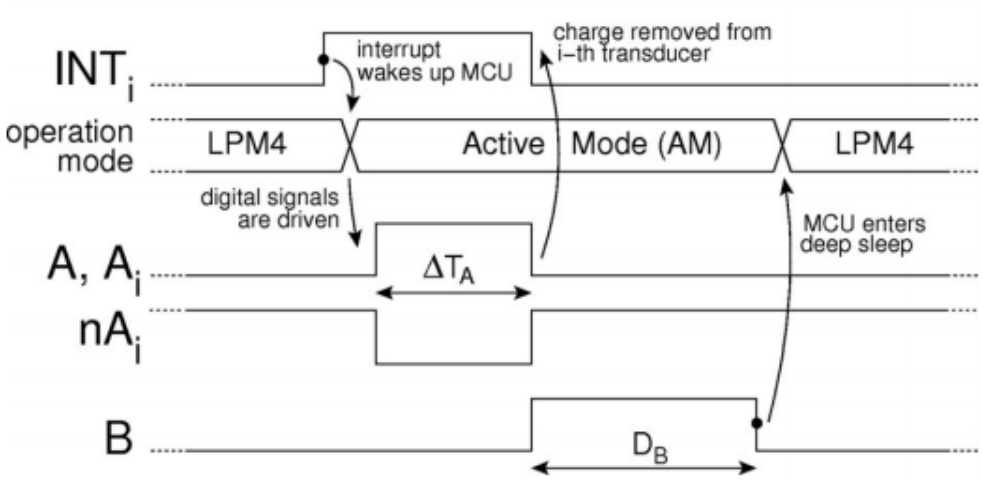


Figure 6.33: Control waveforms [122]

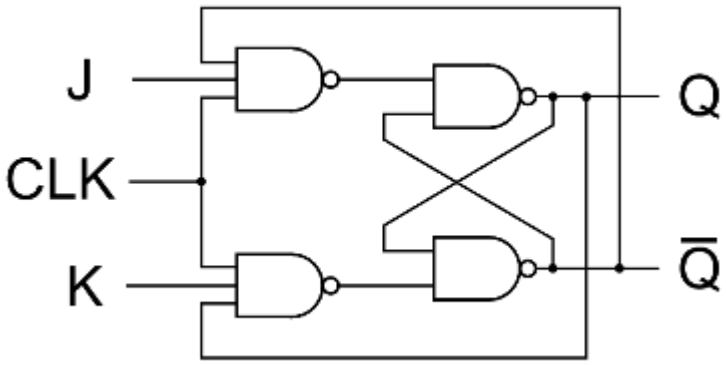


Figure 6.34: JK flip-flop using NAND logic gates [157]

J	K	COMMENT	Q	Q!
1	0	Set	1	0
0	0	Hold state	Q	Q!
0	1	reset	0	1
1	1	toggle	Q!	Q

Table 6.4: JK flip-flop operation

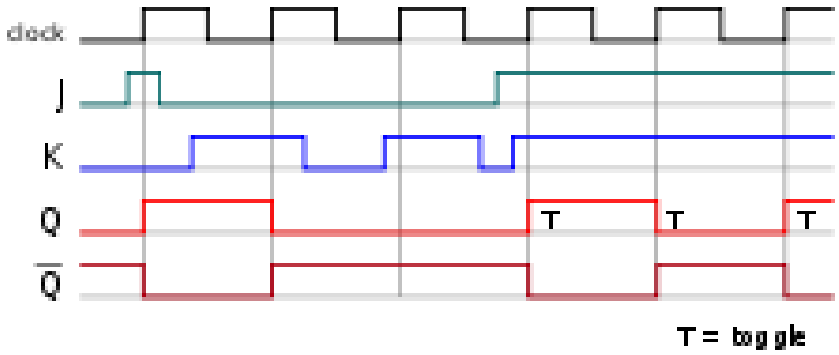


Figure 6.35: JK timing Diagram [158]

6.4. Summary

In this chapter an overview of energy harvesting circuits was presented and the advantages and disadvantages of these circuits were discussed. A large proportion of the energy harvesting circuits investigated only work for single input devices. For the devices discussed in this work the optimum approach would be to use an array of devices and harvest the power from all devices in the fluid flow. The possible circuits for rectifying and storing the output for multiple devices were investigated using SPICE [91] and LTSPICE [155] models and bread-boarded circuits.

Op-amp circuits were analysed using SPICE [91] and it was found that multiple inputs can be summed but the output voltage was very small and due to the power requirements of op-amps it was determined that these circuits would not be viable for use in a low power system such as the one proposed here. A voltage multiplier circuit was used in conjunction with the op-amp circuit and the results were still not enough to justify the 5V overhead of the op-amps. However, this circuit was shown to be useful for use with a piezoelectric transducer used to detect a fault in a concrete beam and this work was presented in EWSHM 2014 [15].

A multiple input circuit using CCRs which was fully CMOS compatible was also examined using LTSPICE and the results once again showed that the voltage was rectified and summed but the output of the circuit was still very low and it was considered that an inductor would need to be used to charge an output capacitor which would allow the voltage to be stored and the potential to be available on the capacitor; which is necessary for use with the proposed devices.

Finally, a circuit which combined active and passive elements based on work by Romani *et al*. [122] was investigated using both simulation results from LTSPICE and experimental results from a circuit built on a bread-board. These results showed that the capacitor was not storing charge in the method that was presented by the authors. The circuit was further analysed and from this it was determined that adding a second output capacitor allowed the capacitor to be charged and the output voltage increased to voltages far above the individual instantaneous voltages on the transducers.

This circuit was further examined to determine if the inductor could be reduced so that the circuit could be integrated into a CMOS process. These results showed that the modified circuit not only outperformed the circuit proposed by Romani *et al*. but also could be operated using a much smaller inductor which is a major advantage. In fact, from the results of the inductor study it was shown that the minimum inductor for the circuit for maximum voltage output proposed in this thesis was 66 times smaller than the smallest inductor proposed by Romani *et al*. Using flip-flops to provide the control circuit to implement the circuit as an IC has also been considered and it is seen that this solution could be useful as a control and storage system for the powering of external circuits. The creation of an IC which addressed this was also considered but it is outside the scope of this work to build it.

The results of the literature review as well as the circuit testing showed that there is still a large amount of work required in this area and some circuits are being published without full information or full analysis of the circuit. From the circuits which were testing in this Chapter it was seen that they did not perform as expected from the published work and this is a problem which needs to be addressed.

This Chapter provides the initial investigation into a multiple input circuit for use with low power and low frequency devices such as the proposed fluid-actuated devices investigated in this thesis. However, future work will need to be completed to design a full system with impedance matching to test the circuit fully and further investigation of the best way to integrate the circuit into an IC will also need to be completed. The results provided here show that there are options for a circuit which could operate with the restrictions of a low power system but there is a lot more work required.

Chapter 7:

Conclusions and Future Work

7.1. Introduction

This chapter summarises the major findings of this work and suggests possible future research.

7.2. Summary of this Work

The AlN material was analysed for piezoelectric properties using a number of different techniques including PFM, SEM, LDV and XRD. AlN films of 500nm grown on (100) Si with a Ti underlayer were used for this analysis. A matrix of deposition setups for DC and RF sputtering was conducted and the results were examined. The AlN material was analysed for test wafers as well as device wafers and tests were carried out on some of the fabricated devices. Process stability tests were also conducted to determine the effect of uncontrollable parameters on the process stability over time.

Three dimensional FEM models of MEMS devices for frequency analysis were created and the effect of different geometries on the frequency was investigated

and a number of possible solutions for bandwidth broadening were studied. Extremely accurate models were created and these models were used to provide input to a number of different MEMS energy harvesting devices for actuation using fluid and vibrations. The power generation capabilities of these devices were also studied using FEM models and the results compared to results from fabricated devices. The results of these studies showed that the power could be accurately predicted and the matched load could be identified which would be useful for designing the rectification and power management circuits.

A number of fluid-actuated energy harvesting devices were proposed and studied using FEM. The effect of the flow on the device as well as the impact of locating the device on the flow was examined. From this, information on the possibility of safely implanting a device of this nature was studied as well as the probable available power. The FEM was correlated with fabricated devices to provide accurate models. These results provided device geometries and dimensions which could be considered optimal for in-vivo energy harvesting. Tests were carried out on fabricated devices using a perfusion machine and the results showed usable voltage outputs from the devices.

Possible circuits for rectifying and storing the energy generated by the piezoelectric devices were researched. Promising candidates were simulated and bread-boarded. From these results it was seen the circuits provided in the literature would need to be modified to operate optimally. The redesigned circuit was then further examined to identify modifications which would facilitate the design of an IC although the design was outside the scope of this project.

The use of polymer material as a substrate for AlN as well as the piezoelectric material was investigated. Polyimide and PVDF were considered. The analysis was performed using FEM models of the most promising device geometries identified from previous analysis. The results show that the use of polymer material is a definite possibility. Two geometries were considered for this analysis, a diaphragm with a 2000µm hole and a diaphragm with a cross structure.

Optimal devices for energy harvesting using a ceramic and a polymer material were identified and the output results were used to test the circuit which was identified as the best possible circuit for use with multiple transducers which will

produce maximum power at unpredictable times due to the effect on the flow actuating the devices at different times and the turbulence created by the devices also acting on them.

7.3. Conclusions

From the material analysis a process which produces usable piezoelectric (002) AlN despite changes in the machine caused by target change and maintenance was identified and state of the art films were produced. The results of the DC and RF sputtering showed that DC sputtering produces higher quality films. Contrary to other published works it was found that the film quality was better when there was no interlayer in the process and no bias applied during processing. A state-of-the-art AlN film growth process was demonstrated and multiple wafers were fabricated which proved this process was repeatable. Single crystal (C-axis) orientation was confirmed to be a critical factor for growing high quality piezoelectric AlN material and XRD was also proven to be an excellent test method for these films. The results of the tests on the target distance, pressure, bias and power also showed that the best results occurred when there was no bias and no interlayer but the power seemed to have very little effect on the result and, in fact, the difference seen is within the precision limitations of the measurement.

The process which produced the highest quality film was destructive to the target. For the standard process it was decided to set the distance to 50mm and the pressure to 6mTorr because this would mean that multiple wafers could be deposited using the same target. This process was also used to grow AlN on polyimide and the state of the art for this material was also achieved. High quality piezoelectric material for silicon based and polymer based devices were grown for both AlN and PVDF. These results show that ceramic and polymer biocompatible materials can be grown for use in a fluid actuated energy harvester.

The FEM models have been tested compared to fabricated devices and the results show excellent correlation. This means that the models can be used to design future devices and also means that the results of the fluid analysis in this work can be considered a good first step in analysing the devices for proof of concept of the energy harvesting devices. The broadband and frequency results in this work have also been used to describe energy harvesting devices for vibration excitation as well

as for use with magnetic material for an AC sensor [159]. The FEM work shows that devices for fluid based energy harvesting can be designed such that the effect on the flow is minimised while still maintaining a high enough voltage output to charge an output capacitor.

For all of the devices tested the voltages were high enough for input into a rectifying circuit and storage for later use by implantable applications. These models also identified the best devices for fluid-actuated energy harvesting with the restrictions for blood flow previously identified. From these models it was seen that for silicon based devices a diaphragm placed along the wall with the flow over the surface provided good voltage output with minimum effect on flow and for a polymer based device a diaphragm with a 2000µm hole and placed perpendicular to the flow provided high voltage output and good fluid characteristics.

To rectify the output and store enough power for use in implantable devices a literature review of energy harvesting circuit was conducted and an initial design for a circuit for multiple inputs was developed and tested. These results showed that a device which can cause a charge to build up on a capacitor using the outputs from the piezoelectric devices designed from the FEM analysis could be created. Further analysis of this circuit also provided possible solutions to create an IC with a small off-chip inductor which was reduced in the circuit compared to a similar circuit identified in the literature. An investigation into replacing the microcontroller by a series of latches was also conducted and from this it was seen that an IC could be created.

Device testing in the perfusion machine proved difficult due to the leakage in the system and future work will need to be done to improve this setup. However the experimental results at low pressure were very encouraging and it was seen that usable power was available. These results confirm the results of the models and further show that this type of energy harvester may be useful in a real world scenario.

The aim of this thesis was to test the concept of energy harvesting from fluid flow for augmenting the battery of implanted devices. The work presented proves that it is possible to extract usable power from piezoelectric devices excited through blood flow. Three devices have been identified as possible energy harvesting

structures. Two diaphragm designs for placement along the artery wall would be excellent structures for use with a silicon substrate and the diaphragm with a 2000µm hole was identified as a possible structure for use with a polymer material. The results show that either of these designs would produce enough power and would not interfere with the flow. The results for the polymer diaphragm with a 2000µm hole need to be qualified for the AlN material because the quality of the material would not be as high as was modelled but these devices must still be considered as viable options.

A multiple input circuit which could operate with the identified structures has also been examined and these results show that a system for energy harvesting from fluid flow would be possible. This circuit could also be redesigned to be almost fully incorporated into an IC (the inductor would need to be off-chip) and the alterations to do this were studied and the results show that this is possible. The circuit would need to be made into an IC for it to be mounted on a flexible circuit which would be necessary for implantation.

A proof of concept for an energy harvesting system through fluid flow has been presented in this work where each aspect from the material, device design, fluid interaction and circuit optimisation have been considered. The work presented here provides an excellent first step in creating a blood flow excited energy harvester and it was seen that these devices could not only operate in a large artery but for an artery as small as 4500µm the results also proved that the flow of the blood could be maintained and usable voltages achieved.

Fifteen publications have resulted from the work presented in this thesis including three journal publications. The state of the art for AlN grown on Si and polyimide has been presented and accurate and versatile FEM models have been created which can be used to design future structures. A multiple input piezoelectric energy harvesting circuit has been optimised and studied for incorporating into an IC.

7.4. Recommendations for Future Work

Future FEM analyses of multiple devices with various distances between them need to be performed to examine the effect of multiple devices all being stressed at different points in the fluid. This would be expected in the final set-up as

a single device would not provide enough power. An examination of devices coupled with the electric circuit should also be conducted.

New devices are currently being fabricated and the new fixtures for the experimental set-up now allow for individual devices to be excited in the fluid flow from the perfusion machine. This set-up should provide better information on the power and effect on flow for the chosen devices. The fluid flow should also be analysed using an accelerometer. This type of analysis was previously conducted for examining stenosis in an occluded artery and has been proven to provide accurate information on the fluid.

The initial circuit design needs to be optimised and fully analysed. The devices should also be tested in conjunction with the energy harvesting circuit and a design for the circuit as a PCB should be considered. The full system needs to be tested to provide a complete picture of the circuit. Future optimisation of the circuit could be done once the full experimental setup has been established. Once the circuit if fully optimised an IC should be created and tested and the results used to design a flexible circuit.

Possible deployment scenarios for the devices have been considered and these should be tested. Currently the best option seems to be to use a stent which could be deployed and inflated in the artery and would help to keep the devices in place. A flexible circuit could also be incorporated into the stent so that the whole system is deployed together. This would need to be properly investigated but currently it is seen as the ideal option. For this sort of deployment the devices would need to be flexible so that they could be bent to fit into the stent and would be expanded to their intended shape when the stent is inflated.

Bibliography

[1] O. Aquilina. (2006, 09/09/2015). *A brief history of cardiac pacing*. Available: http://www.ncbi.nlm.nih.gov/pmc/articles/PMC3232561/

[2] C. F. Shakespeare, A. J. Camm, and A. J. Camm, "Benefits of the advances in cardiac pacemaker technology," *Clinical Cardiology,* vol. 15, pp. 601-606, 1992.

[3] 21st. Century Technology Blog. *Headlines: New Leadless Heart Pacemaker Making Debut in Europe*. Available: http://www.21stcentech.com/headlines-leadless-heart-pacemaker-making-debut-europe/

[4] V. S. Mallela, V. Ilankumaran, and N. Rao, "Trends in Cardiac Pacemaker Batteries," *Indian Pacing and Electrophysiology Journal,* vol. 4, pp. 201-212, Oct-Dec 2004.

[5] Battery University. (2015, 09/09/2015). *How to Make Batteries in Medical Devices More Reliable*. Available: http://batteryuniversity.com/learn/article/how_to_make_batteries_in_medical_devices_more_reliable

[6] J. D. Snell, "Method and apparatus for monitoring physiological data from an implantable medical device," Google Patents, 1998.

[7] A. Myers. (2012, 23/09/2015). *Swimming through the blood stream: Stanford engineers create wireless, self-propelled medical device*. Available: http://news.stanford.edu/news/2012/february/micro-device-implant-022212.html

[8] C. Cobelli, E. Renard, and B. Kovatchev, "Artificial Pancreas: Past, Present, Future," *Diabetes,* vol. 60, pp. 2672-2682, November 1, 2011.

[9] K. Mountfort, R. Knops, J. Sperzel, and P. Neuzil, "The Promise of Leadless Pacing," *Arrhythmia and Electrophysiology Review,* vol. 3, pp. 51-55, 2014.

[10] S. P. Beeby, M. J. Tudor, and N. M. White, "Energy Harvesting Vibration Sources for Microsystems Applications," *Measurement Science and Technology,* vol. 17, pp. 175-195, 2006.

[11] Y. K. Ramadass and A. P. Chandrakasan, "A Battery-Less Thermoelectric Energy Harvesting Interface Circuit With 35mV Startup Voltage," *IEEE Journal of Solid-State Circuits,* vol. 46, pp. 333-341, February 2010.

[12] K. A. Cook-Chennault, N. Thambi, M. A. Bitetto, and E. B. Hameyie, "Piezoelectric Energy Harvesting: A Green and Clean Alternative for Sustained Power Production," *Bulletin of Science, Technology & Society,* vol. 28, pp. 496-509, December 1, 2008.

[13] Y. K. Tan and S. K. Panda, "Review of energy harvesting technologies for sustainable wireless sensor network," in *Sustainable wireless sensor networks*, INTECH, pp. 1-30, 2010.

[14] Alternative Energy. (13/10/2015). *Common Types of Solar Cells*. Available: http://www.altenergy.org/renewables/solar/common-types-of-solar-cells.html

[15] P. Cahill, R. O'Keeffe, N. Jackson, A. Mathewson, and V. Pakrashi, "Structural Health Monitoring of Reinforced Concrete Beam Using Piezoelectric Energy Harvesting System," in *EWSHM - 7th European Workshop on Structural Health Monitoring*, Nantes, France, pp. 190-196 2014.

[16] H. Vocca and F. Cottone, "Kinetic Energy Harvesting," in *ICT - Energy - Concepts Towards Zero - Power Information and Communication Technology*, G. Fagas, Ed., InTech, pp. 25-48, 2014.
[17] F. Cottone. (2012, 22/09/2015). *Introduction to Vibration Energy Harvesting*. Available: http://www.slideshare.net/Energymotionsystems/introduction-to-vibration-energy-harvesting
[18] N. Elvin and A. Erturk, *Advances in Energy Harvesting Methods*: Springer New York, 2013.
[19] S. Priya, "Advances in Energy Harvesting using Low Profile Piezoelectric Transducers," *Journal of Electroceramics*, vol. 19, pp. 167-184, September 2007.
[20] N. Jackson, R. O'Keeffe, F. Waldron, M. O'Neill, and A. Mathewson, "Evaluation of low-acceleration MEMS piezoelectric energy harvesting devices," *Microsystem Technologies*, vol. 20, pp. 671-680, 2014.
[21] S. R. Anton and H. A. Sodano, "A Review of Power Harvesting using Piezoelectric Materials (2003-2006)," *Smart Materials and Structures*, vol. 16, pp. 1-21, 2007.
[22] Y. Qi and M. C. McAlpine, "Nanotechnology-enabled Flexible and Biocompatible Energy Harvesting " *Energy and Environmental Science*, vol. 3, pp. 1275-1285, 2010.
[23] A. Rivadeneyra, J. Soto-Rueda, R. O'Keeffe, J. Banqueri, N. Jackson, A. Mathewson, and J. López-Villanueva, "Tunable MEMS piezoelectric energy harvesting device," *Microsystem Technologies*, pp. 1-8, 2015.
[24] Precision Acoustics. (22/09/2015). *Guide to using Poled PVdf*. Available: http://acoustics.co.uk/wp-content/uploads/2013/12/Properties-of-poled-PVDF.pdf
[25] A. Townley, "Vibrational energy harvesting using MEMS piezoelectric generators," 2009. Available: http://www.seas.upenn.edu/sunfest/docs/papers/TownleyAndrew09.pdf
[26] D. Zhu, M. J. Tudor, and S. P. Beeby, "Strategies for Increasing the Operating Frequency Range of Vibration Energy Harvesters: A Review," *Measurement Science and Technology*, vol. 21, pp. 1-29, 2009.
[27] K. Swee-Leong, M. F. Ab Rahman, D. F. W. Yap, and Y. H. Ho, "Bandwidth widening strategies for piezoelectric based energy harvesting from ambient vibration sources," presented at *the IEEE International Conference on Computer Applications and Industrial Elelctroni*cs, Penang, Malaysia, 2011.
[28] S. A. Hariti, S. Hole, and J. Lewiner, "Broadening the potential bandwidth of piezoelectric transducers by partial depolarization," *Applied Physics Letters*, vol. 78, pp. 4037-4039, Jun 2001.
[29] E. O. Udo, N. M. van Hemel, N. P. Zuithoff, H. Nijboer, W. Taks, P. A. Doevendans, and K. G. Moons. (2013, 08/09/2015). *Long term quality-of-life in patients with bradycaria pacemaker implantation*. Available: http://www.ncbi.nlm.nih.gov/pubmed/23453871
[30] Dr. Chris. (2015, 22/09/2015). *Blocked Artery Signs, Symptoms and Effects*. Available: http://www.healthhype.com/blocked-artery-signs-symptoms-and-effects.html
[31] N. Jackson, R. O'Keeffe, R. O'Leary, M. O'Neill, M. Moriarty, and A. Mathewson, "Wireless Accelerometers for Early Detection of Restenosis," *Procedia Engineering*, vol. 25, pp. 563-566, 2011.

[32] Wikipedia. (2013). *Unimorph*. Available: http://en.wikipedia.org/wiki/Unimorph
[33] Q. Ou, X. Chen, S. Gutschmidt, A. Wood, and N. Leigh, "A Two-mass Cantilever Beam Model for Vibration Energy Harvesting Applications," presented at *the 6th Annual IEEE Conference on Automation Science and Engineering*, , Toronto, Ontario, Canada, pp. 301-306 2010.
[34] Y. Ting, G. Hariyanto, B. K. Hou, and C. Y. Huang, "Evaluation of Energy Harvesting by using Piezoelectric Unimorph Ceramics," presented at *the 2009 IEEE International Conference on Information and Automation*, Zhuhai/Macau, pp. 778-783, 2009.
[35] A. Erturk and D. J. Inman, "An experimentally validated bimorph cantilever model for piezoelectric energy harvesting from base excitations," *Smart Materials and Structures,* vol. 18, p. 025009, 2009.
[36] M. Ericka, D. Vasic, F. Costa, and G. Poulain, "Predictive Energy Harvesting from Mechanical Vibration Using a Circular Piezoelectric Membrane," presented at *the 2005 IEEE Ultrasonics Symposium*, Rotterdam, The Netherlands, pp. 946-949, 2005.
[37] I. Kuehne, M. Schreiter, H. Seidel, and A. Frey, "Optimum Design of a Piezoelectric MEMS Generator for Fluid-Actuated Energy Harvesting," presented at *the 2011 IEEE 24th International Conference on Micro Electro Mechanical Systems (MEMS)*, Cancun, Mexico, pp. 1317-1320, 2011.
[38] A. Khaligh, P. Zeng, and C. Zheng, "Kinetic Energy Harvesting Using Piezoelectric and Electromagnetic Technologies - State of the Art," *IEEE Transactions on Industrial Electronics,* vol. 57, pp. 850-860, 2010.
[39] P. Mane, K. Mossi, and C. Green, "Optimizing Energy Harvesting Parameters using Response Surface Methodology," *ICCC Transactions on Ultrasonics, Ferroelectrics and Frequency Control,* vol. 56, pp. 429-436, March 2009.
[40] WebMD. (2015, 08/09/2015). *Body Temperature*. Available: http://www.webmd.com/first-aid/body-temperature
[41] I. S. Bayer, M. K. Tiwari, and C. M. Megaridis, "Biocompatible Poly(vinylidene fluoride)/cyanoacrylate Composite Coatings with Tunable Hydrophobicity and Bonding Strength," *Applied Physics Letters,* vol. 93, pp. 1739021-1739023, 2008.
[42] European Commission. (2015, 08/09/2015). *Restriction of Hazardous Substances in Electrical and Electronic Equipment*. Available: http://ec.europa.eu/environment/waste/rohs_eee/events_rohs3_en.htm
[43] T. Sakai, S. Hoshiai, and E. Nakamachi, "Biochemical Compatibility of PZT Piezoelectric Ceramics covered with Titanium Thin Film," *Jounal of Optoelectronics and Advanced Materials,* vol. 8, pp. 1435-1437, August 2006.
[44] E. Nakamachi, H. Hwang, Y. Uetsuji, and H. Kuramae, "Three-Scale Process-Crystallographic Analysis of a new Biocompatible Piezoelectric Material MgSiO3 Generation," presented at *the 2010 2nd International Conference on Computer Technology and Development (ICCTD)*, Cairo, Egypt, pp. 206-210, 2010.
[45] CIDRA Precision Services, LLC. (2012, 22/09/2015). *Sapphire Machining and Grinding*. Available: http://www.cidraprecisionservices.com/products-services-crystalline-sapphire.html

[46] X.-H. Xu, H.-S. Wu, C.-J. Zhang, and Z.-H. Jin, "Morphological properties of AlN piezoelectric thin films deposited by DC reactive magnetron sputtering," *Thin Solid Films*, vol. 388, pp. 62-67, 2001.
[47] J. Xiong, H.-s. Gu, K. Hu, and M.-z. Hu, "Influence of Substrate Metals on the Crystal Growth of AlN Films," *International Journal of Minerals, Metallurgy and Materials*, vol. 17, pp. 98-103, 2010.
[48] T. Kamohara, M. Akiyama, and N. Kuwano, "Influence of Molybdenum Bottom Electrodes on Crystal Growth of Aluminium Nitride Thin Films," *Journal of Crystal Growth*, vol. 310, pp. 345-350, 2008.
[49] T. Kamohara, M. Akiyama, N. Ueno, K. Nonaka, and N. Kuwano, "Influence of Aluminium Nitride Interlayers on Crystal Orientation and Piezoelectric Property of Aluminium Nitride Thin Films Prepared on Titanium Electrodes," *Thin Solid Films*, vol. 515, pp. 4565-4569, 9 Apr 2007.
[50] A. Ababneh, U. Schmid, J. Hernando, J. L. Sánchez-Rojas, and H. Seidel, "The Influence of Sputter Deposition Parameters on Piezoelectric and Mechanical Properties of AlN Thin Films," *Materials Science and Engineering B*, vol. 172, pp. 253-258, 2010.
[51] Y. K. Tan and S. K. Panda, "A Novel Piezoelectric Based Wind Energy Harvester for Low-power Autonomonus Wind Speed Sensor," presented at *the 33rd Annual Conference of the IEEE Industrial Electronics Society*, pp. 2175-2180,Taipei, China, 2007.
[52] S. P. Matova, R. Elfrink, R. J. M. Vullers, and R. van Schaijk, "Harvesting energy from airflow with a michromachined piezoelectric harvester inside a Helmholtz resonator " *Journal of Micromechanics and Microengineering*, vol. 21, pp. 1-6, 19-July-2011.
[53] G. W. Taylor, J. R. Burns, S. M. Kammann, W. B. Powers, and T. R. Welsh, "The Energy Harvesting Eel: A Small Subsurface Ocean/River Power Generator," *IEEE Journal of Oceanic Engineering*, vol. 26, pp. 539-547, Oct. 2001.
[54] S. Pobering and N. Schwesinger, "A Novel Hydropower Harvesting Device," in *2004 International Conference on MEMS, NANO and Smart System*, pp. 480-485 *s*, 2004.
[55] A. D. Joseph, "Energy Harvesting Projects," *IEEE Pervasive Computing*, vol. 4, pp. 69-71, 2005.
[56] A. Delnavaz and J. Voix, "Electromagnetic micro-power generator for energy harvesting from breathing," in *IECON 2012 - 38th Annual Conference on IEEE Industrial Electronics Society*, pp. 984-988, 2012.
[57] E. Häsler, L. Stein, and G. Harbauer, "Implantable physiological power supply with PVDF film," *Ferroelectrics*, vol. 60, pp. 277-282, 1984/10/01 1984.
[58] R. Hoffmann, G. S. Mintz, G. R. Dussaillant, J. J. Popma, A. D. Pichard, L. F. Satler, K. M. Kent, J. Griffin, and M. B. Leon, "Patterns and Mechanisms of In-Stent Restenosis: A Serial Intravascular Ultrasound Study," *Circulation*, vol. 94, pp. 1247-1254, September 15, 1996.
[59] NHS. (23/09/2015). *Personalised Health and Care 2020*. Available: https://www.gov.uk/government/uploads/system/uploads/attachment_data/file/384650/NIB_Report.pdf
[60] J. Edmison, M. Jones, Z. Nakad, and T. Martin, "Using Piezoelectric Materials for Wearable Electronic Textiles," presented at *the International*

Symposium on Wearable Computers, Seattle, Washington, USA, pp. 41 -48 2002.

[61] J. Elmes, V. Gaydarzhiev, and A. Mensah, "Maximum Energy Harvesting Control for Oscillating Energy Harvesting Systems," presented at *the IEEE Power Electronics Specialists Conference*, Orlando, Florida, pp. 2792-2798, 2007.

[62] V. Raghunathan and P. H. Chou, "Design and Power Management of Energy Harvesting Embedded Systems," presented at *the International Symposium on Low Power Electronics and Design*, Tegernsee, Bavaria, Germany, pp. 369-374, 2006.

[63] X. Wei and J. Liu, "Power Sources and Electrical Recharging Strategies for Implantable Medical Devices," *Frontiers of Energy and Power Engineering in China*, vol. 2, pp. 1-13, 2008.

[64] P. D. Mitcheson, "Energy Harvesting for Human Wearable and Implantable Bio-Sensors," presented at *the International Conference of the IEEE EMBS*, Buenos Aires, Argentina, pp. 3432-3436, 2010.

[65] N. S. Shenck and J. A. Paradiso, "Energy scavenging with shoe-mounted piezoelectrics," *Micro, IEEE*, vol. 21, pp. 30-42, 2001.

[66] S. R. Platt, S. Farritor, K. Garvin, and H. Haider, "The use of piezoelectric ceramics for electric power generation within orthopedic implants," *Mechatronics, IEEE/ASME Transactions on*, vol. 10, pp. 455-461, 2005.

[67] J. L. González, R. Antonio, and F. Moll, "Human Powered Piezoelectric Batteries to Supply Power to Wearable Electronic Devices," *International Journal of the Society of Materials Engineering for Resources*, vol. 10, pp. 34-40, 2002.

[68] Y. Levron, D. Shmilovitz, and L. Martinez-Salamero, "A Power Management Strategy for Minimization of Energy Storage Reservoirs in Wireless Systems with Energy Harvesting," *IEEE Transactions on Circuits and Systems*, vol. 58, pp. 633-643, March 2010.

[69] S. Trolier-McKinstry and P. Muralt, "Thin Film Piezoelectrics for MEMS," *Journal of Electroceramics*, vol. 12, pp. 7-17, 2004.

[70] N. Jackson, R. O'Keeffe, F. Waldron, M. O'Neill, and A. Mathewson, "Influence of aluminum nitride crystal orientation on MEMS energy harvesting device performance," *Journal of Micromechanics and Microengineering,* vol. 23, p. 075014, 2013.

[71] B. Mohammadi, A. A. Yousefi, and S. M. Bellah, "Effect of tensile strain rate and elongation on crystalline structure and piezoelectric properties of PVDF thin films," *Polymer Testing*, vol. 26, pp. 42-50, 2007.

[72] N. Jackson, L. Keeney, and A. Mathewson, "Flexible-CMOS and biocompatible piezoelectric AlN material for MEMS applications," *Smart Materials and Structures*, vol. 22, p. 115033, 2013.

[73] G. F. Iriarte, J. Bjurstrom, J. Westlinder, F. Engelmark, and I. V. Katardjiev, "Synthesis of c-axis-oriented AlN thin films on high-conducting layers: Al, Mo, Ti, TiN, and Ni," *Ultrasonics, Ferroelectrics, and Frequency Control, IEEE Transactions on*, vol. 52, pp. 1170-1174, 2005.

[74] N. Jackson, R. O'Keeffe, M. White, M. O'Neill, F. Waldron, and A. Mathewson, "Influences of titanium underlayer (002) oriented aluminium nitride," presented at *the 2nd Int. Workshop on Piezoelectric MEMS,* Laussane, Switzerland, 2011.

[75] A. Sanz-Hervás, L. Vergara, J. Olivares, E. Iborra, Y. Morilla, J. García-López, M. Clement, J. Sangrador, and M. A. Respaldiza, "Comparative study of c-axis AlN films sputtered on metallic surfaces," *Diamond and Related Materials*, vol. 14, pp. 1198-1202, 2005.
[76] FEI. (27/10/2015). *Quanta SEM*. Available: http://www.fei.com/products/sem/quanta-sem/
[77] PANalytical. (27/10/2015). *X-ray diffractometers*. Available: http://www.panalytical.com/Xray-diffractometers.htm
[78] Hydrargyrum. (24/09/2015). *Bragg diffraction 2*. Available: https://commons.wikimedia.org/wiki/File:Bragg_diffraction_2.svg
[79] M. Akiyama, T. Kamohara, K. Kano, A. Teshigahara, and N. Kawahara, "Influence of oxygen concentration in sputtering gas on piezoelectric response of aluminum nitride thin films," *Applied Physics Letters*, vol. 93, p. 021903, 2008.
[80] L. Vergara, M. Clement, E. Iborra, A. Sanz-Hervás, J. García López, Y. Morilla, J. Sangrador, and M. A. Respaldiza, "Influence of oxygen and argon on the crystal quality and piezoelectric response of AlN sputtered thin films," *Diamond and Related Materials*, vol. 13, pp. 839-842, 2004.
[81] J. C. Doll, B. C. Petzold, B. Ninan, R. Mullapudi, and B. L. Pruitt, "Aluminum nitride on titanium for CMOS compatible piezoelectric transducers," *Journal of micromechanics and microengineering : structures, devices, and systems*, vol. 20, pp. 25008-25008, 2010.
[82] R. Elfrink, T. M. Kamel, M. Goedbloed, S. Matova, D. Hohlfeld, Y. v. Andel, and R. v. Schaijk, "Vibration energy harvesting with aluminum nitride-based piezoelectric devices," *Journal of Micromechanics and Microengineering*, vol. 19, p. 094005, 2009.
[83] H. Okano, Y. Takahashi, T. Tanaka, K. Shibata, and S. Nakano, "Preparation of c -Axis Oriented AlN Thin Films by Low-Temperature Reactive Sputtering," *Japanese Journal of Applied Physics*, vol. 31, p. 3446, 1992.
[84] H. Cheng, Y. Sun, J. X. Zhang, Y. B. Zhang, S. Yuan, and P. Hing, "AlN films deposited under various nitrogen concentrations by RF reactive sputtering," *Journal of Crystal Growth*, vol. 254, pp. 46-54, 2003.
[85] N. Matsunami, H. Kakiuchida, M. Sataka, and S. Okayasu, "XRD Characterization of AlN Thin Films Prepared by Reactive RF-Sputter Deposition," *Advances in Materials Physics and Chemistry*, vol. 3, pp. 101-107, 2013.
[86] S. Saravanan, E. Keim, G. Krijnen, and M. Elwenspoek, "Growth and surface characterization of piezoelectric AlN thin films on silicon (100) and (110) substrates," in *Microscopy of Semiconducting Materials*: Springer, pp. 75-78, 2005.
[87] A. Sanz-Hervás, M. Clement, E. Iborra, L. Vergara, J. Olivares, and J. Sangrador, "Degradation of the piezoelectric response of sputtered c-axis AlN thin films with traces of non-(0002) x-ray diffraction peaks," *Applied Physics Letters*, vol. 88, p. 161915, 2006.
[88] N. Jackson, R. O'Keeffe, R. O'Leary, M. O'Neill, F. Waldron, and A. Mathewson, "A diaphragm based piezoelectric AlN film quality test structure," in *Microelectronic Test Structures (ICMTS), 2012 IEEE International Conference on*, pp. 50-54, 2012.
[89] COMSOL Inc. (2015, 20/10/2015). *COMSOL.com*. Available: https://www.comsol.com/

[90] S. Roundy and P. K. Wright, "A piezoelectric vibration based generator for wireless electronics," *Smart Materials and Structures,* vol. 13, p. 1131, 2004.
[91] Berkeley. (09/28/2015). *The Spice Page*. Available: http://bwrcs.eecs.berkeley.edu/Classes/IcBook/SPICE/
[92] N. G. Elvin and A. A. Elvin, "A Coupled Finite Element—Circuit Simulation Model for Analyzing Piezoelectric Energy Generators," *Journal of Intelligent Material Systems and Structures,* vol. 20, pp. 587-595, March 1, 2009.
[93] Dassault Systemes. (2012, 20/10/2015). *ABAQUS Unified FEA*. Available: http://www.3ds.com/products-services/simulia/products/abaqus/
[94] M. Farnsworth, A. Tiwari, and R. Dorey, "Modelling, Simulation and Optimisation of a Piezoelectric Energy Harvester," *Procedia CIRP,* vol. 22, pp. 142-147, 2014.
[95] D. Ekeom and L. Buchaillot, "Thermoelastic FEM-BEM Model for MEMS Resonator Simulation," in *IEEE 22nd International Conference on Micro Electro Mechanical Systems (MEMS)* pp. 923-926, 2009.
[96] Z. Xin, W. Lei, W. Kai, and L. Guizhang, "Virtual Operation of MEMS Devices Based on FEM Simulation," in *2nd IEEE International Conference on Nano/Micro Engineered and Molecular Systems (NEMS),* pp. 122-126, 2007.
[97] MSC Software. (20/10/2015). *MSC Nastran*. Available: http://www.mscsoftware.com/product/msc-nastran
[98] PDE Solutions Inc. (20/10/2015). *FlexPDE 6*. Available: http://www.pdesolutions.com/
[99] Dassault Systemes. (20/10/2015). *SolidWorks*. Available: http://www.solidworks.com/
[100] MathWorks. (20/10/2015). *MATLAB*. Available: http://uk.mathworks.com/products/matlab/
[101] A. Rivadeneyra, J. A. Lopez-Villanueva, R. O'Keeffe, N. Jackson, M. O'Neill, and A. Mathewson, "Frequency response of variants of a cantilever beam," in *2012 International Conference on Synthesis, Modeling, Analysis and Simulation Methods and Applications to Circuit Design (SMACD),* pp. 177-180, 2012.
[102] R. O'Keeffe, N. Jackson, F. Waldron, M. O'Niell, K. McCarthy, and A. Mathewson, "Investigation into modelling power output for MEMS energy harvesting devices using COMSOL Multiphysics," in *14th International Conference on Thermal, Mechanical and Multi-Physics Simulation and Experiments in Microelectronics and Microsystems (EuroSimE),* pp. 1-6, 2013.
[103] biotestplasma. (28/09/2015). *What is plasma? What is its Function*. Available: http://biotestplasma.com/frequently-asked-questions/
[104] G. Coppola and K. Liu, "Study of Compliance Mismatch within a Stented Artery," in *COMSOL Conference*, Boston, MA, USA, 2008.
[105] R. Nave. (05/01/2016). *Renold's Number*. Available: http://hyperphysics.phy-astr.gsu.edu/hbase/pturb.html
[106] R. O'Keeffe, N. Jackson, A. Mathewson, and K. G. McCarthy, "Investigation of devices of in-vivo energy harvesting through blood-flow-like excitation," in *2013 IEEE International Conference on Microelectronic Test Structures (ICMTS),* pp. 19-24, 2013.

[107] M. Akiyama, Y. Morofuji, K. Nishikubo, and T. Kamohara, "Sensitivity enhancement in diaphragms made by aluminum nitride thin films prepared on polyimide films," *Applied Physics Letters*, vol. 92, p. 043509, 2008.
[108] R. Prehn, F. Haupert, and K. Friedrich, "Sliding wear performance of polymer composites under abrasive and water lubricated conditions for pump applications," *Wear*, vol. 259, pp. 693-696, 2005.
[109] PCB Board Online Marketplace. *Flexible PCB Board*. Available: http://www.chinapcbboard.com/pcb-1529347-polyimide-film-flexible-pcb-board-edhd-copper-0-5-oz-5-oz.html
[110] HD Microsystems. (2015, 02/06). *PI-2600 Series – Low Stress Applications* Available: https://snf.stanford.edu/SNF/materials-and-chemicals/specmat-requests/2014-prom-requests/20140205-p-wei-request-for-use-of-new-poly-imide-pi-2611-and-vm-651-in-snf/vm-2600-series-product-sheet/at_download/file
[111] S. Petroni, G. Maruccio, F. Guido, M. Amato, A. Campa, A. Passaseo, M. T. Todaro, and M. De Vittorio, "Flexible piezoelectric cantilevers fabricated on polyimide substrate," *Microelectronic Engineering*, vol. 98, pp. 603-606, 2012.
[112] M. Akiyama, Y. Morofuji, T. Kamohara, K. Nishikubo, Y. Ooishi, M. Tsubai, O. Fukuda, and N. Ueno, "Preparation of Oriented Aluminum Nitride Thin Films on Polyimide Films and Piezoelectric Response with High Thermal Stability and Flexibility," *Advanced Functional Materials*, vol. 17, pp. 458-462, 2007.
[113] S. Petroni, C. L. Tegola, G. Caretto, A. Campa, A. Passaseo, M. D. Vittorio, and R. Cingolani, "Aluminum Nitride piezo-MEMS on polyimide flexible substrates," *Microelectronic Engineering*, vol. 88, pp. 2372-2375, 2011.
[114] J. Liu, X. Lu, and C. Wu, "Effect of Preparation Methods on Crystallization Behavior and Tensile Strength of Poly(vinylidene fluoride) Membranes," *Membranes*, vol. 3, pp. 389-405, 2013.
[115] X. He and K. Yao, "Crystallization mechanism and piezoelectric properties of solution-derived ferroelectric poly(vinylidene fluoride) thin films," *Applied Physics Letters*, vol. 89, p. 112909, 2006.
[116] W. Ma, J. Zhang, and X. Wang, "Formation of poly(vinylidene fluoride) crystalline phases from tetrahydrofuran/N, N-dimethylformamide mixed solvent," *Journal of Materials Science*, vol. 43, pp. 398-401, 2008.
[117] Laurell Techology Corporation. (27/10/2015). *WS-400-6NPP-LITE Spin Processro*. Available: http://www.laurell.com/spin-coater/?model=WS-400-6NPP-LITE
[118] KLA Tencor. *Alpha-Step D-500*. Available: http://www.kla-tencor.com/Surface-Profiling/alpha-step-d-500.html
[119] Piezotest. (27/10/2015). *Piezotest d33 PiezoMeter System*. Available: http://www.piezotest.com/d33piezometer.php
[120] G. D. Szarka, B. H. Stark, and S. G. Burrow, "Review of Power Conditioning for Kinetic Energy Harvesting Systems," *Ieee Transactions on Power Electronics*, vol. 27, pp. 803-815, Feb 2012.
[121] J. Dicken, P. D. Mitcheson, I. Stoianov, and E. M. Yeatman, "Power-Extraction Circuits for Piezoelectric Energy Harvesters in Miniature and Low-Power Applications," *IEEE Transactions on Power Electronics*, vol. 27, pp. 4514-4529, Nov 2012.

[122] A. Romani, M. Filippi, and M. Tartagni, "Micropower Design of a Fully Autonomous Energy Harvesting Circuit for Arrays of Piezoelectric Transducers," *Power Electronics, IEEE Transactions on,* vol. 29, pp. 729-739, 2014.
[123] N. J. Guilar, R. Amirtharajah, and P. J. Hurst, "A Full-Wave Rectifier With Integrated Peak Selection for Multiple Electrode Piezoelectric Energy Harvesters," *Solid-State Circuits, IEEE Journal of,* vol. 44, pp. 240-246, 2009.
[124] J. Porhonen, S. Rajala, S. Lehtimaki, and S. Tuukkanen, "Flexible Piezoelectric Energy Harvesting Circuit With Printable Supercapacitor and Diodes," *Electron Devices, IEEE Transactions on,* vol. 61, pp. 3303-3308, 2014.
[125] Y.-Y. Chen, D. Vasic, F. Costa, W.-J. Wu, and C. K. Lee, "Self-powered Piezoelectric Energy Harvesting Device using Velocity control Synchronized Switching Technique," presented at *the IECON 2010 - 36th Annual Conference on IEEE Industrial Electronics Society* Phoenix, Arizona, USA, pp. 1785-1790, 2010.
[126] J. Liang and W.-H. Liao, "An Improved Self-Powered Switching Interface for Piezoelectric Energy Harvesting," presented at *the IEEE International Conference on Information and Automation*, Zhuhai/Macau, China, pp. 945-950, 2009.
[127] Y. Sun, I.-y. Lee, C.-j. Jeong, S.-k. Han, and S.-g. Lee, "An Comparator Based Active Rectifier for Vibration Energy Harvesting Systems," presented at *the International Conference on Advanced Communication Technology*, Gangwon-Do, South Korea, pp. 1404-1408, 2011.
[128] M. Lallart, L. Garbuio, L. Petit, C. Richard, and D. Guyomar, "Double Synchronized Switch Harvesting (DSSH): A New Energy Harvesting Scheme for Efficient Energy Extraction," *IEEE Transactions on Ultrasonics, Ferroelectrics and Frequency Control,* vol. 55, pp. 2119-2130, October 2008.
[129] Y. Kushino and H. Koizumi, "Piezoelectric energy harvesting circuit using full-wave voltage doubler rectifier and switched inductor," in *Energy Conversion Congress and Exposition (ECCE), IEEE,* pp. 2310-2315, 2014.
[130] D. Vasic, Y. Y. Chen, and F. Costa, "Design of self-powering part of SSHI interface for piezoelectric energy harvesting," *Electronics Letters,* vol. 49, pp. 288-290, 2013.
[131] S. Cheng, R. Sathe, R. D. Natarajan, and D. P. Arnold, "A Voltage-Multiplying Self-Powered AC/DC Converter with 0.35V Minimum Input Voltage for Energy Harvesting Applications " presented at *the IEEE Transactions on Power Electronics*, Forth Worth, Texas, USA, pp. 1311-1318, 2011.
[132] E. Dallago, D. Miatton, G. Venchi, V. Bottarel, G. Frattini, G. Ricotti, and M. Schipani, "Active Automonous AC-DC Converter for Piezoelectric Energy Scavenging Systems," presented at *the IEEE 2008 Custom Integrated Circuits Conference*, San Jose, California, pp. 555-558, 2008.
[133] M. Ferrari, V. Ferrari, M. Guizzetti, and D. Marioli, "Investigation on Electrical Output Combination Options in a Piezoelectric Multifrequency Converter Array for Energy Harvesting in Autonomous Sensors," presented at *the 2010 First International Conference on Sensor Device Technologies and Applications*, Venice/Mestre, Italy, pp. 358-263, 2010.

[134] Y. Rao and D. P. Arnold, "An Input-Powered Active AC/DC Converter with Zero Standby Power for Energy Harvestng Applications," presented at *the IEEE Energy Conversion Congress and Exposition*, Atlanta, Georgia, USA, pp. 4441-4446, 2010.
[135] E. Sangiorgi, A. Romani, and M. Tartagni, "Micro-power Converters for Energy Harvesting Devices," presented at *the 2010 8th International Conference on Advanced Semiconductor Devices & Microsystems (ASDAM)*, Smolenice, Slovakia, pp.259-262, 2010.
[136] M. Lallart, L. Garbuio, C. Richard, and D. Guyomar, "Low-Cost Capacitor Voltage Inverter for Outstanding Performance in Piezoelectric Energy Harvesting," *IEEE transactions on Ultrasonics, Ferroelectrics and Frequency Control*, vol. 57, pp. 281-291, February 2010.
[137] S. Dwari and L. Parsa, "An Efficient AC-DC Step-Up Converter for Low-Voltage Energy Harvesting," *IEEE Transactions on Power Electronics*, vol. 25, pp. 2188-2199, August 2010.
[138] D. Pimentel and P. Musilek, "Power Management with Energy Harvesting Devices," presented at *the Canadian Conference on Electrical and Computer Engineering*, Calgary, Alberta, Canada, pp. 1-4, 2010.
[139] A. Rajasekaran, A. Hande, and D. Bhatia, "Ultra-Low-Power Intelligent PWM Controller for Vibration Energy Harvesting Power Supplies," presented at *the IEEE Dallas Circuits and Systems Workshop*, Richardson, Texas, USA, pp. 1-4, 2009.
[140] T. Ying-Khai and P. K. T. Mok, "A piezoelectric energy harvesting interface circuit using one-shot pulse transformer boost converter based on water bucket fountain strategy," in *Circuits and Systems (ISCAS), 2014 IEEE International Symposium on*, pp. 1993-1996, 2014.
[141] J. W. Kimball, B. T. Kuhn, and R. S. Balog, "A System Design Approach for Unattended Solar Energy Harvesting Supply," *IEEE Transactions on Power Electronics*, vol. 24, pp. 952-962, April 2009.
[142] W. S. Wang, T. O'Donnell, N. Wang, M. Hayes, B. O'Flynn, and C. O'Mathuna, "Design Considerations of Sub-mW Indoor Light Energy Harvesting for Wireless Sensor Systems," *ACM Journal on Emerging Technologies in Computing Systems*, vol. 6, pp. 6:1-6:26, June 2010.
[143] Y. K. Ramadass and A. P. Chandrakasan, "An efficient piezoelectric energy-harvesting interface circuit using a bias-flip rectifier and shared inductor," in *Solid-State Circuits Conference - Digest of Technical Papers, 2009. ISSCC 2009. IEEE International*, pp. 296-297, 2009.
[144] R. Vaddi and S. Dasgupta, "Enhanced bias-flip rectifier with ultra-low power control for piezo electric energy harvester in the microwatt application scenario," in *Microelectronics and Electronics (PrimeAsia), 2012 Asia Pacific Conference on Postgraduate Research in*, pp. 132-137, 2012.
[145] T. Hehn, F. Hagedorn, D. Maurath, D. Marinkovic, I. Kuehne, A. Frey, and Y. Manoli, "A Fully Autonomous Integrated Interface Circuit for Piezoelectric Harvesters," *IEEE Journal of Solid-State Circuits*, vol. 47, pp. 2185-2198, Sep 2012.
[146] N. Mohajer and M. J. Mahjoob, "Modeling and electrical optimization of a designed Piezoelectric-based vibration Energy Harvesting System," in *Robotics and Mechatronics (ICRoM), 2013 First RSI/ISM International Conference on*, pp. 455-461, 2013.

[147] K. Dongwon and G. A. Rincon-Mora, "A single-inductor 0.35um CMOS energy-investing piezoelectric harvester," in *Solid-State Circuits Conference Digest of Technical Papers (ISSCC), 2013 IEEE International*, pp. 78-79, 2013.
[148] J. H. Cho, R. F. Richards, D. F. Bahr, C. D. Richards, and M. J. Anderson, "Efficiency of energy conversion by piezoelectrics," *Applied Physics Letters*, vol. 89, p. 104107, 2006.
[149] A. D. T. Elliott and P. D. Mitcheson, "Power density improvement of a piezoelectric energy harvester through use of a micropower switch-mode interface," in *Sensors, 2012 IEEE*, pp. 1-4, 2012.
[150] C. van Liempd, S. Stanzione, Y. Allasasmeh, and C. van Hoof, "A 1uW-to-1mW energy-aware interface IC for piezoelectric harvesting with 40nA quiescent current and zero-bias active rectifiers," in *Solid-State Circuits Conference Digest of Technical Papers (ISSCC), 2013 IEEE International* , pp. 76-77, 2013.
[151] DC/AC Circuit Reference. (28/09/2015). *Operational Amplifier Circuits*. Available: http://webpages.ursinus.edu/lriley/ref/circuits/node5.html
[152] Inductive load, "Op-Amp Comparator." Available: https://en.wikipedia.org/wiki/Operational_amplifier_applications
[153] R. Torah, P. Glynne-Jones, M. Tudor, T. O'Donnell, S. Roy, and S. Beeby, "Self-Powered Autonomous Wireless Sensor Node using Vibration Energy Harvesting," *Measurement Science and Technology*, vol. 19, pp. 1-8, 2008.
[154] N. Wang, T. O'Donnell, S. Roy, P. McCloskey, and C. O'Mathuna, "Micro-inductors integrated on silicon for power supply on chip," *Journal of Magnetism and Magnetic Materials*, vol. 316, pp. e233-e237, 2007.
[155] Linear Technology. (28/09/2015). *Design Simulation and Device Models*. Available: http://www.linear.com/designtools/software/
[156] Z. Liqiang, A. Mathewson, B. O'Flynn, M. Hayes, and C. O'Mathuna, "Design and implementation of the embedded capacitance layers for decoupling of wireless sensor nodes," in *Electronics Packaging Technology Conference (EPTC), 2010 12th*, 2010, pp. 687-690.
[157] DAE Notes. (06/01/2016). *Flip Flop*. Available: http://www.daenotes.com/electronics/digital-electronics/flip-flops-types-applications-woking
[158] S. Engvall, "JK timing diagram." Available: https://en.wikipedia.org/wiki/Flip-flop_(electronics)
[159] O. Z. Olszewski, R. Houlihan, R. O'Keeffe, M. O'Neill, F. Waldron, A. Mathewson, and N. Jackson, "A MEMS Silicon-based Piezoelectric AC Current Sensor," *Procedia Engineering*, vol. 87, pp. 1457-1460, 2014.

Author's publications highlighted in bold.